

**ENERGY HARVESTING FROM AN ELASTICALLY SUPPORTED  
CRUCIFORM STRUCTURE**

**AHMAD ADZLAN FADZLI BIN KHAIRI**

**UNIVERSITI TEKNOLOGI MALAYSIA**

**DECLARATION OF THESIS / UNDERGRADUATE PROJECT REPORT  
AND COPYRIGHT**

Author's full name : \_\_\_\_\_

Date of Birth : \_\_\_\_\_

Title : \_\_\_\_\_

Academic Session : \_\_\_\_\_

I declare that this thesis is classified as:



**CONFIDENTIAL**

(Contains confidential information under the Official Secret Act 1972)\*



**RESTRICTED**

(Contains restricted information as specified by the organization where research was done)\*



**OPEN ACCESS**

I agree that my thesis to be published as online open access (full text)

1. I acknowledged that Universiti Teknologi Malaysia reserves the right as follows:
2. The thesis is the property of Universiti Teknologi Malaysia
3. The Library of Universiti Teknologi Malaysia has the right to make copies for the purpose of research only.
4. The Library has the right to make copies of the thesis for academic exchange.

Certified by:

---

SIGNATURE OF STUDENT

---

SIGNATURE OF SUPERVISOR

---

MATRIC NUMBER

---

NAME OF SUPERVISOR

Date:

Date:

NOTES : If the thesis is CONFIDENTIAL or RESTRICTED, please attach with the letter from the organization with period and reasons for confidentiality or restriction

“We hereby declare that we have read this thesis and in our opinion this thesis is sufficient in terms of scope and quality for the award of the degree of Doctor of Philosophy in Mechanical Engineering”

Signature : \_\_\_\_\_  
Name of Supervisor I : Associate Professor Dr Mohamed Sukri Bin Mat Ali  
Date : September 8, 2021

Signature : \_\_\_\_\_  
Name of Supervisor II : Dr Nurshafinaz Binti Mohd Maruai  
Date : September 8, 2021

*Replace this page with the Cooperation Declaration form, which can be obtained from SPS or your faculty. This page is **OPTIONAL** when your research is done in collaboration with other institutions that requires their consent to publish the finding in this document.*

ENERGY HARVESTING FROM AN ELASTICALLY SUPPORTED  
CRUCIFORM STRUCTURE

AHMAD ADZLAN FADZLI BIN KHAIRI

A thesis submitted in fulfilment of the  
requirements for the award of the degree of  
Doctor of Philosophy

Malaysia-Japan International Institute of Technology  
Universiti Teknologi Malaysia

DECEMBER 2020

## **DECLARATION**

I declare that this thesis entitled "*Energy Harvesting from an Elastically Supported Cruciform Structure*" is the result of my own research except as cited in the references. The thesis has not been accepted for any degree and is not concurrently submitted in candidature of any other degree.

Signature	:	_____
Name	:	Ahmad Adzlan Fadzli Bin Khairi
Date	:	September 8, 2021

## **DEDICATION**

My dearest wife and children. Respected supervisor and colleagues at the WEE  
iKohza. This is for all of you.

## **ACKNOWLEDGEMENT**

I would like to first express my highest sense of gratitude to my supervisor Dr. Mohamed Sukri Mat Ali. His knowledge and proficiency in computational fluid dynamics have made my entry into this field of study a little bit more bearable and has since been an excellent tool in making novel discoveries and conclusions. His open stance in receiving ideas and suggestions to strengthen the foundations of this research has been fundamental to the preservation of the originality and timeliness of this work. I have learned a lot from him about the value of logical continuity and how to achieve it throughout the course of completing this work. The relentless effort for logical continuity throughout the thesis has been, in my opinion, crucial towards a manuscript that not only is easily accessible but helps target audiences to build upon this work in the future, hence advancing the field as a whole.

As for my beloved family, especially my wife and two babies, I really cannot think of any way to repay your hardships and understanding throughout the years of my study. Even a lifetime of unconditional love and devotion towards all of you squares only but a small fraction of what you have given up making my studies a reality. To that end I can only trust the Most Merciful to fully even the debt and make all of you among those who are most beloved by the Most Gracious. I pray to the Almighty to accept the fruit of our jihad in finding knowledge and may all the trials and tribulations we have encountered together, physically, psychologically and financially, will stand witness in the hereafter that we have answered His call towards submission, and His call towards success. Aamin ya Rabbal 'alamin.

## ABSTRACT

From off-grid charging of electronic devices to energising independent wireless sensor networks, the demand for stand-alone, low-power generators from renewable energy sources is becoming ever more prevalent. This study aims to address this need, by numerically investigating a cruciform energy harvester that comprises of an elastically supported circular cylinder, and a downstream strip plate at right angles in the Reynolds number range  $1.1 \times 10^3 \leq \text{Re} \leq 14.6 \times 10^3$  and Scruton number 9.94. The continuity and three dimensional, unsteady Reynolds-averaged Navier-Stokes equations are solved on the numerical domain using a free and open-source C++ library called OpenFOAM. The Spalart-Allmaras turbulence model is used to provide closure to the governing equations. Previous studies on the power output from a 10 mm diameter cylinder show that meaningful power generation only begins when the reduced velocity  $U^*$ , exceeds 15 and produces a consistent output in the order of 1 mW over the whole observation window. To improve upon this, a more fundamental understanding of why this observation takes place is indispensable. This is done by investigating the temporal evolution of the lift and displacement signals using the Hilbert-Huang transform, leading to the discovery of a route through which a significant quantity of energy is lost during energy harvesting. To eliminate said route, this work examines energy harvesting of a generalised cruciform structure, with varying cruciform angles, and discovered the following. For steep-angled cruciforms ( $45^\circ \leq \alpha(\circ) \leq 67.5^\circ$ ) this study found asymmetries in the vortical structures that prevents lock-in and thus high-amplitude vibrations from taking place. However, for shallow-angled cruciforms ( $0^\circ \leq \alpha(\circ) \leq 22.5^\circ$ ), this work discovered a high degree of symmetry in the distribution of vortical structures, leading to the onset of meaningful power generation as early as  $U^* = 9.1$  up to the upper limit of observation, with a maximum mechanical power that is one order of magnitude larger than the highest reported by similar studies in the literature. Finally, the mechanical power and efficiency of the generalised cruciform energy harvester are presented as a map in cruciform angle-reduced velocity ( $\alpha(\circ) - U^*$ ) parameter space, thus making it possible for future engineers to tailor the design of their cruciform energy harvester to their specific power and efficiency needs.

## ABSTRAK

Daripada pengecasan peranti elektronik di luar grid sehingga pentenagaan rangkaian sensor tanpa wayar, permintaan untuk sistem penjana berkuasa rendah dari sumber tenaga boleh diperbaharui adalah semakin meningkat. Kajian ini bertujuan untuk memenuhi keperluan tersebut, dengan cara menyelidik sebuah sistem pemungut tenaga jenis krusiform yang terdiri daripada sebuah silinder bulat yang disokong secara elastik, dan sekeping plat jalur yang diletakkan pada sudut tegak di hilirnya dalam julat nombor Reynolds  $1.1 \times 10^3 \leq Re \leq 14.6 \times 10^3$  dan nombor Scruton 9.94. Persamaan keselanjaran dan Navier-Stokes purata Reynolds tidak stabil tiga dimensi diselesaikan dalam domain numerikal menggunakan OpenFOAM, sebuah pustaka C++ yang percuma dan bersumber terbuka. Model gelora Spalart-Allmaras digunakan untuk melengkapkan persamaan tersebut. Kajian terdahulu tentang kuasa dari silinder berdiameter 10 mm menunjukkan penjanaan kuasa yang signifikan bermula apabila halaju terturun  $U^*$  melebihi 15, seraya menghasilkan kuasa dalam julat 1 mW secara konsisten. Kefahaman yang lebih mendalam tentang pencetus respon mekanikal tersebut adalah diperlukan untuk membolehkan penambahbaikan terhadap keputusan ini. Ini dilakukan dengan mengkaji evolusi temporal bagi daya angkat dan sesaran menggunakan penjelmaan Hilbert-Huang, yang membawa kepada penemuan proses yang membazirkan jumlah tenaga yang signifikan dalam aktiviti penjanaan kuasa. Bagi merencat proses tersebut, tinjauan dilakukan terhadap pemungut tenaga daripada bentuk krusiform yang lebih umum, sekaligus membawa kepada penemuan-penemuan berikut. Bagi krusiform bersudut tinggi ( $45^\circ \leq \alpha(\circ) \leq 67.5^\circ$ ), kajian ini mendapatasi asimetri dalam struktur vorteks yang menghalang kejadian frekuensi terkunci, serta penghasilan amplitud getaran yang tinggi, daripada berlaku. Di sudut yang lain, bagi krusiform bersudut rendah ( $0^\circ \leq \alpha(\circ) \leq 22.5^\circ$ ), kajian ini mendapatati darjah kesimetrian yang tinggi dalam taburan struktur vorteks di sekeliling krusiform tersebut, yang memberarkan pemungutan tenaga yang signifikan bermula seawal  $U^* = 9.1$  sehingga batasan tertinggi pemerhatian dalam penyelidikan ini, dengan penghasilan kuasa maksimum satu peringkat magnitud lebih tinggi daripada yang tertinggi pernah dilaporkan dalam kajian yang setara. Akhir sekali, tulisan ini memetakan kuasa dan kecekapan mekanikal bagi krusiform terubahsuai tersebut dalam ruang parameter sudut krusiform-halaju terturun ( $\alpha(\circ) - U^*$ ), sekaligus membolehkan penyesuaian rekabentuk pemungut tenaga mengikut perincian kuasa dan kecekapan yang diperlukan.

## TABLE OF CONTENTS

	<b>TITLE</b>	<b>PAGE</b>
<b>DECLARATION</b>		<b>ii</b>
<b>DEDICATION</b>		<b>iii</b>
<b>ACKNOWLEDGEMENT</b>		<b>iv</b>
<b>ABSTRACT</b>		<b>v</b>
<b>ABSTRAK</b>		<b>vi</b>
<b>TABLE OF CONTENTS</b>		<b>vii</b>
<b>LIST OF TABLES</b>		<b>x</b>
<b>LIST OF FIGURES</b>		<b>xi</b>
<b>LIST OF ABBREVIATIONS</b>		<b>xvi</b>
<b>LIST OF SYMBOLS</b>		<b>xvii</b>
<b>LIST OF APPENDICES</b>		<b>xviii</b>
<b>CHAPTER 1 INTRODUCTION</b>	<b>1</b>	
1.1    Background	1	
1.2    Problem Statement	4	
1.3    Research Questions	4	
1.4    Thesis Objectives	5	
1.5    Significance of Study	6	
1.6    Thesis Scope	7	
1.7    Thesis Organisation	9	
<b>CHAPTER 2 LITERATURE REVIEW</b>	<b>11</b>	
2.1    Vortex Shedding from a Cylinder	11	
2.1.1    Karman Vortex Shedding	12	
2.1.2    Streamwise Vortex Shedding	15	
2.2    Vortex-induced Vibration of a Cylinder	21	
2.2.1    Single Cylinder Oscillator Unit	21	
2.2.2    Cruciform Oscillator Unit	24	
2.3    Energy Harvesting from a Vibrating Cylinder	29	
2.3.1    Single Cylinder System	29	

2.3.2	Pure Cruciform System	32
2.4	Chapter Summary	35
<b>CHAPTER 3 METHODOLOGY</b>		<b>39</b>
3.1	Problem geometry	39
3.2	Numerical method	40
3.3	Dynamic mesh motion	47
3.4	Open flow channel experiment	48
3.5	Ensemble empirical mode decomposition and Hilbert transform	52
3.6	Phase lag between Cl and normalised cylinder displacement	55
3.7	Estimation of Power	55
3.8	Grid Independence Study	56
3.8.1	The grid convergence index (GCI) and Richardson extrapolation	58
3.9	Chapter Summary	59
<b>CHAPTER 4 RESULTS AND DISCUSSION</b>		<b>61</b>
4.1	The GCI Study	61
4.2	The pure cruciform	64
4.2.1	The amplitude and frequency response	69
4.2.2	Main vibration-driving vortical structure	73
4.2.3	Temporal evolution of the lift coefficient	76
4.2.3.1	The KVIV regime (reduced velocity below 13.6 )	76
4.2.3.2	Transition to SVIV (reduced velocity between 15.9 and 18.2)	83

4.2.3.3	The stable SVIV regime (reduced velocity greater than 20.5)	89
4.2.4	Harnesseable power	91
4.2.5	Possibility for increasing fluid power	97
4.2.6	Section Summary	99
4.3	Steep-angled cruciforms	100
4.3.1	The amplitude and frequency response	101
4.3.2	Main vibration-driving vortical structure	103
4.3.3	Phase lag between Cl and normalised cylinder displacement	108
4.3.4	Section Summary	117
4.4	Shallow-angled Cruciforms	118
4.4.1	The amplitude and frequency response	119
4.4.2	Main vibration-driving vortical structure	122
4.5	Phase lag between Cl and normalised cylinder displacement	133
4.5.1	Power characteristic in cruciform angle - reduced velocity parameter space	133
4.5.2	Section Summary	137
<b>CHAPTER 5</b>	<b>CONCLUSION</b>	<b>140</b>
5.1	Research Outcomes	141
5.2	Future Works	145
<b>REFERENCES</b>		<b>146</b>
<b>LIST OF PUBLICATIONS</b>		<b>164</b>

## LIST OF TABLES

TABLE NO.	TITLE	PAGE
Table 2.1	Summary of findings in literature and key takeaways.	37
Table 3.1	Empirical constants used in the Spalart-Allmaras turbulence model.	45
Table 3.2	The list of conditions investigated in this study, i.e. the research matrix	46
Table 3.3	The specifications of the HP Z420 workstation	47
Table 3.4	Summary of experimental parameters in contrast to those used in the experimental work of Koide <i>et al.</i> (2013).	49
Table 4.1	Summary of grid independency study.	64

## LIST OF FIGURES

FIGURE NO.	TITLE	PAGE
Figure 1.1	Number of publications with keywords ["vortex induced vibration" energy]. Retrieved from SCOPUS.	2
Figure 1.2	Apparent power $P_a$ (W) versus reduced velocity $U^*$ for cases of KVIV and SVIV. Adapted from Koide <i>et al.</i> (2013).	3
Figure 2.1	Schematic of the base configuration of the oscillator system used in this study, i.e. the pure cruciform. In this configuration, the axis of the cylinder and the strip plate are perpendicular to each other.	27
Figure 2.2	The pyramid of knowledge for the cruciform energy harvester.	36
Figure 3.1	The computational domain: three-dimensional overview and cross-sections.	41
Figure 3.1	The computational domain: three-dimensional overview and cross-sections.	42
Figure 3.2	The cruciform variations studied in this thesis.	43
Figure 3.2	The cruciform variations studied in this thesis.	44
Figure 3.3	Sketch of the experimental system used in this study.	50
Figure 3.4	Side view schematic of the openflow channel.	51
Figure 3.5	Experimentally measured $y^*(t)$ , which is the normalised cylinder displacement time series.	52
Figure 3.6	The flowchart encapsulating the sum total of research activities in this study.	57
Figure 4.1	The course, medium and fine mesh used in the grid independency study.	62
Figure 4.1	The course, medium and fine mesh used in the grid independency study.	63
Figure 4.2	Richardson extrapolation of $y_{\text{RMS}}^*$ and the corresponding drop in error.	65
Figure 4.3	Richardson extrapolation of $f^*$ and the corresponding drop in error.	66

Figure 4.4	Richardson extrapolation of $Cl_{RMS}$ and the corresponding drop in error.	67
Figure 4.5	Evolution of the normalised root-mean-square amplitude of cylinder displacement $y_{RMS}^*$ , with respect to reduced velocity $U^*$ , in the streamwise vortex-driven vibration regime.	69
Figure 4.6	Comparison between the evolution of $y_{RMS}^*$ with respect to $U^*$ of a pure cruciform system from the numerical and experimental work. The filled square represents the numerical, while the filled circle represents the experimental results.	70
Figure 4.7	Evolution of the normalised cylinder displacement frequency, $f^*$ , with respect to reduced velocity $U^*$ , for the pure cruciform case.	72
Figure 4.8	Evolution of the lift coefficient root-mean-square amplitude ( $Cl_{RMS}$ ) and normalised frequency of lift coefficient ( $f_{Cl}^*$ ), with respect to reduced velocity $U^*$ , for the pure cruciform case. The dashed line in Fig. 4.8b visualises the shedding frequency of Karman vortex computed from Eq. 4.4.	74
Figure 4.9	Distribution of normalised frequency of vortex shedding, along the span of the cylinder of the pure cruciform at $U^* = 22.7$ .	75
Figure 4.10	Dominant vortical structures at $U^* = 22.7$ observed in the pure cruciform case.	77
Figure 4.11	The Q-criterion for the $90^\circ$ cruciform at $U^* = 22.7$ : the isometric (4.11a) and plan view (4.11b).	78
Figure 4.12	The Q-criterion for the $90^\circ$ cruciform at $U^* = 6.8$ : the isometric (4.12a) and plan view (4.12b).	79
Figure 4.13	Temporal analysis of $Cl$ and $y^*$ at $U^* = 4.5$ .	80
Figure 4.13	Temporal analysis of $Cl$ and $y^*$ at $U^* = 4.5$ .	81
Figure 4.14	Temporal analysis of $Cl$ and $y^*$ at $U^* = 6.8$ .	82
Figure 4.14	Temporal analysis of $Cl$ and $y^*$ at $U^* = 6.8$ .	83
Figure 4.15	Temporal analysis of $Cl$ and $y^*$ at $U^* = 13.6$ .	84
Figure 4.15	Temporal analysis of $Cl$ and $y^*$ at $U^* = 13.6$ .	85

Figure 4.16	Temporal evolution of $y^*$ and Cl at $U^* = 15.9$ .	86
Figure 4.17	Temporal analysis of the lift coefficient and normalised cylinder displacement signal at $U^* = 15.9$ .	87
Figure 4.17	Temporal analysis of the lift coefficient and normalised cylinder displacement signal at $U^* = 15.9$ .	88
Figure 4.18	Temporal analysis of the lift coefficient and normalised cylinder displacement signal at $U^* = 18.2$ .	90
Figure 4.18	Temporal analysis of the lift coefficient and normalised cylinder displacement signal at $U^* = 18.2$ .	91
Figure 4.19	The instantaneous phase lag $\phi$ of $C_{Cl,y^*}$ in the range $20.5 \leq U^* \leq 29.5$ .	92
Figure 4.19	The instantaneous phase lag $\phi$ of $C_{Cl,y^*}$ in the range $20.5 \leq U^* \leq 29.5$ .	93
Figure 4.20	Variation of $\theta_{y-Cl}$ with respect to $U^*$ .	93
Figure 4.21	Estimation of $P_{Mech.,RMS}$ and $P_{Fluid,RMS}$ and comparison with available data.	94
Figure 4.22	The HHT spectrogram of Cl between $20.5 \leq U^* \leq 29.5$ . The solid and dashed line white boxes delineate the distribution of the streamwise and Karman components of lift, respectively.	95
Figure 4.22	The HHT spectrogram of Cl between $20.5 \leq U^* \leq 29.5$ . The solid and dashed line white boxes delineate the distribution of the streamwise and Karman components of lift, respectively.	96
Figure 4.23	Evolution of $C_{F_L,Karman,RMS}$ and $C_{F_L,streamwise,RMS}$ with respect to $U^*$ .	98
Figure 4.24	Evolution of the normalised root-mean-square amplitude of cylinder displacement $y_{RMS}^*$ , with respect to reduced velocity $U^*$ , for the $67.5^\circ$ and $45^\circ$ cruciform.	102
Figure 4.25	Evolution of the normalised cylinder displacement frequency, $f^*$ , with respect to reduced velocity $U^*$ , for the $67.5^\circ$ and $45^\circ$ cruciforms.	104

Figure 4.26	Evolution of the normalised Cl root-mean-square amplitude, $Cl_{RMS}$ , with respect to reduced velocity $U^*$ , for the $67.5^\circ$ and $45^\circ$ cruciforms.	105
Figure 4.27	Evolution of the normalised Cl frequency, $f_{Cl}^*$ , with respect to reduced velocity $U^*$ , for the $67.5^\circ$ and $45^\circ$ cruciforms. The dashed lines outline $f_{v,Karman}$ from Eq. 4.4.	106
Figure 4.28	Distribution of normalised frequency of vortex shedding, along the span of the cylinder of the $67.5^\circ$ and $45^\circ$ cruciforms at $U^* = 22.7$ .	109
Figure 4.29	Dominant vortical structures at $U^* = 22.7$ observed in the $67.5^\circ$ and $45^\circ$ cases.	110
Figure 4.29	Dominant vortical structures at $U^* = 22.7$ observed in the $67.5^\circ$ and $45^\circ$ cases.	111
Figure 4.30	The Q-criterion for the $67.5^\circ$ cruciform at $U^* = 22.7$ : the 4.30a isometric and 4.30b plan view.	112
Figure 4.31	The Q-criterion for the $67.5^\circ$ cruciform at $U^* = 4.5$ : the 4.31a isometric and 4.31b plan view.	113
Figure 4.32	The Q-criterion for the $45^\circ$ cruciform at $U^* = 22.7$ : the isometric (4.32a) and plan view (4.32b).	114
Figure 4.33	The Q-criterion for the $45^\circ$ cruciform at $U^* = 4.5$ : the isometric (4.33a) and plan view (4.33b).	115
Figure 4.34	Phase lag $\theta_{y-Cl}$ ( $^\circ$ ) between Cl and $y^*$ when $67.5^\circ$ and $45^\circ$ .	116
Figure 4.35	Evolution of the normalised root-mean-square amplitude of cylinder displacement $y_{RMS}^*$ , with respect to reduced velocity $U^*$ , for the $22.5^\circ$ and $0^\circ$ cruciform.	120
Figure 4.36	Evolution of the normalised cylinder displacement frequency, $f^*$ , with respect to reduced velocity $U^*$ , for the $22.5^\circ$ and $0^\circ$ cruciforms.	121
Figure 4.37	Evolution of the normalised Cl root-mean-square amplitude, $Cl_{RMS}$ , with respect to reduced velocity $U^*$ , for the $22.5^\circ$ and $0^\circ$ cruciforms.	123
Figure 4.38	Evolution of the normalised Cl frequency, $f_{Cl}^*$ , with respect to reduced velocity $U^*$ , for the $22.5^\circ$ and $0^\circ$ cruciforms. The dashed lines outline $f_{v,Karman}$ from Eq. 4.4.	124

Figure 4.39	Distribution of normalised frequency of vortex shedding, along the span of the cylinder of the $22.5^\circ$ and $0^\circ$ cruciforms at $U^* = 22.7$ .	125
Figure 4.40	Dominant vortical structures at $U^* = 22.7$ observed in the $22.5^\circ$ and $0^\circ$ cases.	126
Figure 4.40	Dominant vortical structures at $U^* = 22.7$ observed in the $22.5^\circ$ and $0^\circ$ cases.	127
Figure 4.41	The Q-criterion for the $22.5^\circ$ cruciform at $U^* = 22.7$ : the isometric (4.41a) and plan view (4.41b).	128
Figure 4.42	The Q-criterion for the $22.5^\circ$ cruciform at $U^* = 4.5$ : the isometric (4.42a) and plan view (4.42b).	129
Figure 4.43	The Q-criterion for the $45^\circ$ cruciform at $U^* = 22.7$ : the isometric (4.43a) and plan view (4.43b).	130
Figure 4.44	The Q-criterion for the $45^\circ$ cruciform at $U^* = 4.5$ : the isometric (4.44a) and plan view (4.44b).	131
Figure 4.45	Phase lag $\theta_{y-\text{Cl}}$ ( $^\circ$ ) between Cl and $y^*$ when $22.5^\circ$ and $0^\circ$ .	134
Figure 4.46	Isocontours describing the map of the normalised RMS amplitude of cylinder displacement, $y_{\text{RMS}}^*$ in the cruciform angle - reduced velocity ( $\alpha-U^*$ ) parameter space.	135
Figure 4.47	Isocontours describing the map of the estimated mechanical power in the cruciform angle - reduced velocity ( $\alpha-U^*$ ) parameter space.	136
Figure 4.48	Isocontours describing the map of the estimated mechanical power in the cruciform angle - reduced velocity ( $\alpha-U^*$ ) parameter space.	137

## **LIST OF ABBREVIATIONS**

ANN	-	Artificial Neural Network
PC	-	Personal Computer
SVM	-	Support Vector Machine
UTM	-	Universiti Teknologi Malaysia
XML	-	Extensible Markup Language

## **LIST OF SYMBOLS**

Re	-	Reynolds number
St	-	Strouhal number
$U^*$	-	Reduced velocity
Cl	-	Lift coefficient

## LIST OF APPENDICES

APPENDIX	TITLE	PAGE
Appendix A	Temporal Evolution of Lift in a Pure Cruciform System for Energy	162
Appendix B	OpenFOAM Implementation for The Study of Streamwise Vortex-Induced Vibration-Based Energy Harvester for Sensor Networks	163

# CHAPTER 1

## INTRODUCTION

Vortex-induced vibration (VIV) is a type of vibration that grows from instabilities in fluid flows moving past a solid object, i.e. bluff body. When the flow exceeds a critical velocity, the flow develops vortices that are shed alternately downstream the bluff body. This triggers the onset of unsteady lift and drag forces that initiate and sustain its vibration (Bukka *et al.*, 2020). Numerous occurrences of VIV are readily observable in the field of engineering. In the ocean, marine currents give rise to the vibration of risers and offshore drilling platforms (Liu *et al.*, 2020; Zhang *et al.*, 2020; Meng *et al.*, 2020). Up in the sky, aeroplane wings vibrate, and high-rise buildings experience sway as strong gusts blow around the mighty structures (Arul *et al.*, 2020; Hao and Yang, 2020; Gao *et al.*, 2020). Closer to the ground, power transmission lines vibrate as the result of wind blowing over them (Wang *et al.*, 2019; Gómez-Ortega *et al.*, 2019).

The common denominator for all these examples is the potential damage to the engineering construct experiencing it. Thus, methods are devised and implemented to mitigate the effects of the vibrations by dissipating the vibrational energy or delaying/aborting its onset in the first place.

However, the past decade has seen efforts to do exactly the opposite: purposely maximising the vibration induced by the vortices, with the aim to generate electrical power. The simplicity of design and scalability attracts many to contribute to this multidisciplinary field of study, along with the prospect of successful development and subsequent commercialization of a new generation of energy harvester.

### 1.1 Background

The term “flow-induced vibration” refers to a wide range of phenomena: flutter (Doare and Michelin, 2011; Xia *et al.*, 2015a,b), galloping (Kluger *et al.*, 2013;

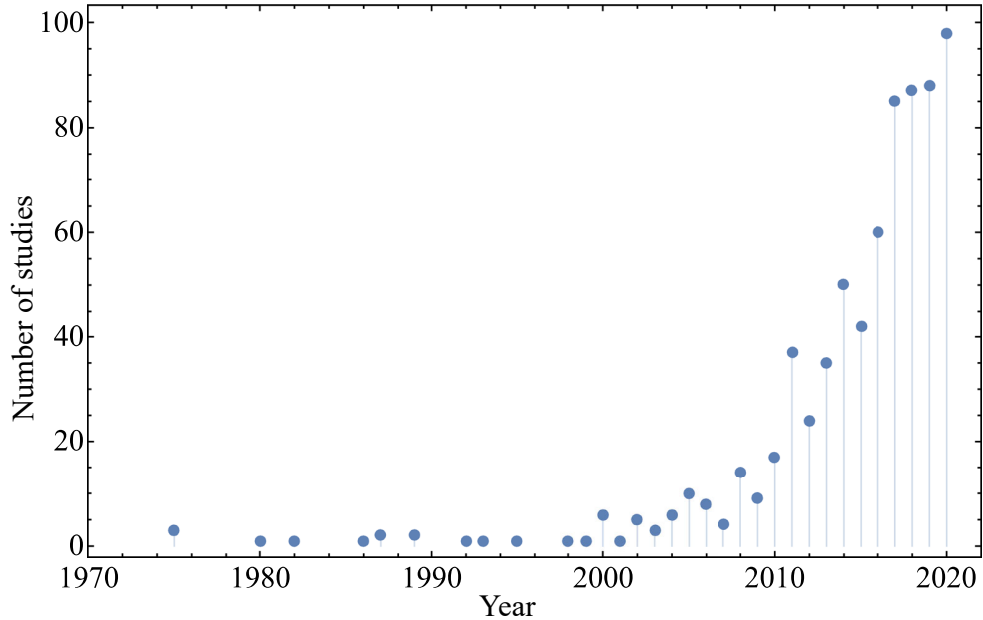


Figure 1.1: Number of publications with keywords ["vortex induced vibration" energy]. Retrieved from SCOPUS.

Barrero-Gil *et al.*, 2010; Luo *et al.*, 2003; Chen *et al.*, 2012), turbulence-induced vibration (Nakamura *et al.*, 2013), wake-induced vibration (Ogink and Metrikine, 2010; Bearman, 2011; Derakhshandeh *et al.*, 2014), and VIV of various kinds, which are the main object of study in this proposal. The study of VIV is traditionally motivated by the potential failure of engineering structures resulting from the fluid moving around them (Shiraishi *et al.*, 1988; Nakamura and Nakashima, 1986; Larsen and Halse, 1997; Khalak and Williamson, 1999). Nevertheless, technical publications since the 2000s saw a surge in contributions toward the subject from the perspective of energy harvesting. A simple search in SCOPUS shown in Fig. 1.1 reveals this trend for keywords ["vortex induced vibration" energy] for the last 4 decades.

At the cutting edge of this field of research is a group at The University of Michigan, that has already built prototypes of the energy harvester, named VIVACE. They compared the cost of power production in USD/kWh between VIVACE and a wide selection of common (pulverised coal, integrated gasification combined cycle, natural gas combined cycle, etc.) and new power generation technologies (anaerobic digester, landfill gas, solar, etc.). The result of this comparison demonstrated how VIVACE is on par in terms of power production cost with most of the technologies it was contrasted to Bernitsas *et al.* (2008).

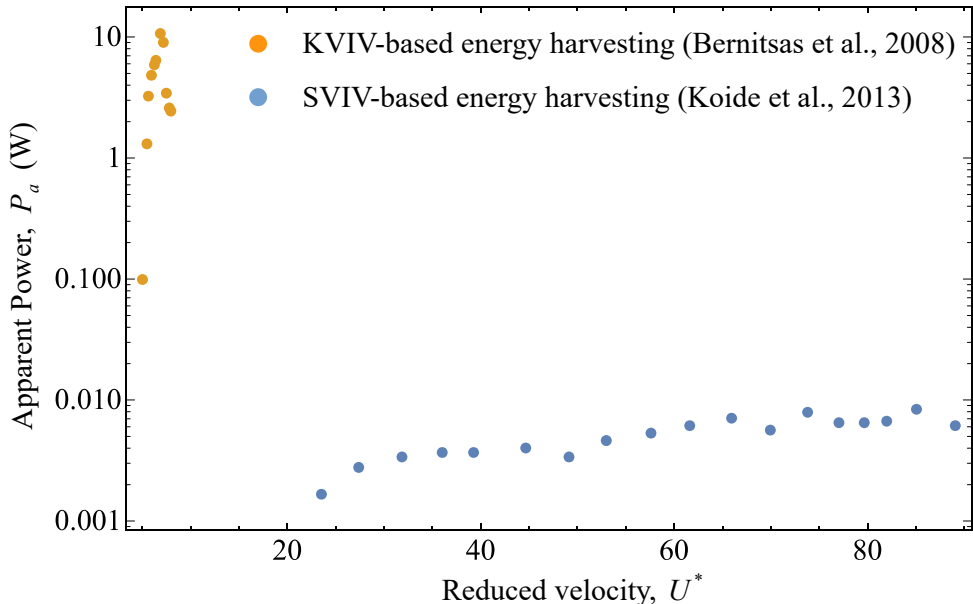


Figure 1.2: Apparent power  $P_a$  (W) versus reduced velocity  $U^*$  for cases of KVIV and SVIV. Adapted from Koide *et al.* (2013).

The VIV phenomenon utilised by the team at the University of Michigan is of the Karman VIV type (KVIV), capable of producing power in the order of MW when installed as a large-scale energy farm (Raghavan, 2007). However, as pointed out by Koide *et al.* (2013) the reduced velocity ( $U^*$ ) range within which KVIV can be relied upon for power generation is about one order of magnitude smaller than what can be expected from another form of VIV namely the streamwise VIV (SVIV). Reduced velocity  $U^*$  is a nondimensional form of characteristic velocity that allows comparison of results between similar systems of differing dimensions. Since SVIV power generation is possible for a large range of  $U^*$ , it is better suited for deployment in flows with large velocity changes.

Despite this, the main shortcoming of SVIV is its maximum power output which is demonstrated at this stage of development to cap at a mW scale for a single-cylinder setup. An isolated cylinder setup for KVIV produces a maximum power in the order of 10 W (Bernitsas *et al.*, 2009). The apparent power  $P_a$  (W) for both KVIV and SVIV is shown in Fig. 1.2. Following this present limitation of the unoptimized SVIV energy harvesters, their application is currently limited to mW electronics e.g., sensors and signal transmitters.

## 1.2 Problem Statement

The preceding section has established the viability of harnessing energy from a flow by exploiting the VIV phenomenon. Multiple modes of VIV have been observed, and SVIV stands out as better oriented for deployment in fluid flows that vary greatly in terms of free-stream velocity. Even with very rudimentary optimisations, SVIV has demonstrated its ability to generate power in the order of mW consistently over a large range of free-stream velocities. This can be harnessed to develop a self-contained power source for off-grid electronics charging, or to power independent sensor networks.

To achieve this, the problems outlined below must be addressed to close relevant gaps in the current body of knowledge.

1. A lack of understanding on the transition mechanism from Karman to streamwise vortex-induced vibration.
2. A paucity in the knowledge on what contributes to the magnitude of the alternating lift force acting on the cylinder, and its vibrational frequency components.
3. A deficiency of new methods to control the flow perturbation which gives rise to a strong, stable and periodic forcing of the cylinder vibration, sustainable over the desired operating range of  $U^*$ .

Addressing the above problems will provide a better understanding on the origins of the streamwise vortex pairs, uncover new perspectives on variables that affect the alternating lift force in the context of streamwise vortex pairs, and generate novel insight on new flow regimes, which can enlighten the research community to a better configuration of the energy harvester, i.e. producing more power than ever before.

## 1.3 Research Questions

The answer to several questions is sought in this proposed study. These questions are meant to drive the study towards its objectives.

1. How does the lift signal evolve as the flow transitions from being driven primarily by Karman vortex to streamwise vortex?
2. How does the ratio of energy transferred from the flow to the lift components evolve with respect to  $U^*$ ?
3. What deviations do the modified cruciform configuration impose on the vortical structure, against the vortical structure observed around a pure cruciform?
4. How do the deviations mentioned in 3 affect the lift magnitude, and by extension the frequency-amplitude response?
5. Where in the power envelope can maximum (minimum) power be obtained with the largest (narrowest) operability range, and how does this translate into a new mode of flow control to suit the operating conditions of the cruciform energy harvester?

#### **1.4 Thesis Objectives**

Following the problems outlined in the previous section, the objectives that define the scope of work in this proposal are listed below.

1. To identify what takes place when the dominant vortical structure forcing the vibration changes from Karman to streamwise vortex-induced vibration (SVIV) in terms of lift and vibration signals for the pure cruciform ( $90^\circ$ ) oscillator.
2. To distinguish the lift signal in terms of its components and how the components interact to modify the frequency-amplitude response of the cylinder.
3. To synthesise the system responses of a variable-angle cruciform and chart how the mechanical power and efficiency evolve in cruciform angle - reduced velocity parameter space.

The aim of objective item 1 is to get a better understanding of how the advent of streamwise vortical structures perturb the lift acting on the cylinder, which directly modifies the vibration signal of the cylinder. Objective 2 is an attempt to identify the footprint of dominant vortical structures in the flow in the lift signal and relate those to the resulting vibration signal. Finally, objective 3 seeks to recommend and evaluate a modified version of the cruciform structure that alters the vortical structure in the

flow, thus modulating the lift signal acting on the cylinder and its frequency-amplitude response. The power envelope will provide a more generalised operability condition for the energy harvester, and holds the key as to how the cruciform configuration should be varied to cater to a particular flow environment.

### **1.5 Significance of Study**

Structural efforts to put flash floods in check are almost always very costly - RM443 million allocated in the 2020 Malaysia Budget alone (Kementerian Kewangan Malaysia, 2019). However, the rationale for structural solutions to the floods becomes increasingly suspect considering the worsening climate change in recent decades. However, the allocation for non-structural methods of reducing flood damages such as flood forecasting and warning protocols, was not highlighted in this budget, despite them being part of the 2016-2020 Civil Service ICT Strategic Plan (Unit Pemodenan Tadbiran dan Perancangan Pengurusan Malaysia, 2016) and 2016-2020 Department of Irrigation and Drainage Strategic Plan (Department of Irrigation and Drainage Malaysia, 2016). This fact, along with the decreasing effectiveness of structural efforts highlights the need to develop an inexpensive, simple, yet reliable non-structural system to tackle the flood problem.

Against this background, this study is able contribute significantly towards the development of an in-situ device to power water level and flow velocity/discharge sensors for a given river/drainage system using vibration energy harnessed from the flow itself. The minimalist and self-powered feature of the device allows installation of as many of the devices as necessary along the river/drainage system for adequate monitoring.

Off-grid charging of electronics is also another area to which the results of this study is able to improve. Both civilian and military activities in remote areas can benefit from the power generated to charge essential electronic devices necessary for a successful operation in said area. Improvement in terms of power output means that usage of more complex and resource intensive electronic equipments will gradually be possible in off-grid locations. This gives the deployed personnel an added advantage over their peers in performing his or her civilian or military duties in such locations.

The most significant contribution is however, to facilitate the widespread adoption of independent, wireless sensor networks. Sensor networks have wide-ranging applications in the field of monitoring; from wildlife (Gazis and Katsiri, 2020; Pathak, 2020) to forests (Kadir *et al.*, 2019; Zellweger *et al.*, 2019) to civil structures (Ni *et al.*, 2020; Sadeghi Eshkevari *et al.*, 2020; Mao *et al.*, 2020), these networks are low-power by design and is expected to operate around the clock. To increase the coverage and resolution of the monitoring task, the obvious solution is to increase the overall quantity and concentration of sensors in a particular area of interest. Nevertheless, the impracticality of connecting such a network to the national grid thrusts them in a unique position to benefit from VIV-based energy harvesters that this study seeks to improve upon.

## 1.6 Thesis Scope

This work is mainly a computational fluid dynamics (CFD) study of a particular version of VIV-based energy harvester that comprise of an elastically supported, horizontally constrained smooth circular cylinder of diameter 1 cm and a passive flow control mechanism that is a strip of rectangular plate at a right angle downstream the cylinder, forming a cruciform. The range of Reynolds number investigated in this thesis is between  $1.1 \times 10^3 \leq Re \leq 14.6 \times 10^3$  and the mass-damping parameter, expressed by the nondimensional Scruton number  $Sc$ , is 9.94. This work limits itself to examining a cruciform where the width of the strip plate is equal to the diameter of the cylinder  $D$ , and the primary data collected from the simulation runs are the time evolution of the cylinder displacement and the corresponding lift coefficient  $C_l$ .

The baseline numerical results, i.e. results from a pure cruciform (a cruciform where the cylinder and strip plate are  $90^\circ$  to each other) are validated against experimental results of a similar system in a custom-made recirculating open flow channel. Although analogous systems have been studied experimentally in the past (Koide *et al.*, 2017; Zhao and Lu, 2018), in the author's opinion it is best to test the extent of reproducibility of the results in these studies first before attempting any sort of comparison with the numerical results of this work. Furthermore, having a system similar to the numerical model studied in this thesis physically available allows for

rapid consistency checks to be made between the two, thus increasing the credibility of the results.

The first part of this study looks to elucidate the relationship between the vortical structures present in the flow, especially when the ambient fluid power is high (high flow velocity region), and how they modulate the resulting lift acting on the cylinder. This is done by conducting a time-series analysis of both cylinder displacement and lift coefficient signals using the Hilbert-Huang transform (HHT). The motivation behind this is to understand why the amplitude of cylinder displacement is limited to the order of magnitude observed not only by the author, but also in numerous studies within the last ten years. This part of the study concludes with the discovery of a particular route through which a significant amount of energy from the freestream is lost during the energy harvesting process, and the amount by which the power output can be improved if this loss is eliminated.

The second part of this thesis is the author's attempt to eliminate the loss mentioned previously. This is done by generalising the cruciform system, through the variation of the relative angle between the cylinder and the strip plate. The study then proceeds to investigate the generalised cruciform system by examining the vortical structures present in the flow, how they affect the resulting lift acting on the cylinder, the amplitude of cylinder displacement itself, and ultimately the power output. The dynamics between the lift and cylinder displacement are explained through the computation of instantaneous phase lag between the two, which in turn is made possible by HHT.

The thesis concludes with the unveiling of a mechanical power and efficiency map, within a parameter space consisting of the cruciform angle and flow velocity. Useful recommendations can be deduced from the map, which highlights regions of high and low power output, and also regions of high and low efficiency, in order to obtain the desired power output and efficiency for any given power consumption requirement.

## **1.7 Thesis Organisation**

This thesis is organised into eight chapters. The author introduces the study and gives a general overview of the research in Chapter 1. In Chapter 1, gaps in the research are identified and thesis objectives are formulated based on those gaps. Chapter 1 also outlines the questions the author seeks to address, details the scope of this study and provide concrete examples as to the significance and merit of this work. Chapter 2 reviews relevant literature that gives an overview of the progress made up to the present day, on the subject of VIV energy harvesting, by exploiting an isolated circular cylinder as the oscillator. The chapter then introduces the cruciform oscillator and the studies on the vibration characteristics of a number of variations of the cruciform oscillator.

Chapter 3 discusses the methodology taken by the author to attain the objectives listed in Chapter 1. In Chapter 3, the author details the numerical model implemented in the CFD undertaking and this includes the domain size, critical dimensions of the cruciform, boundary conditions and solution method to the unsteady, three-dimensional (3D) Reynolds-averaged Navier-Stokes equation governing the flow. Apart from that, the author also discusses the turbulence modelling adhered to in the numerical studies. The author also introduces the Hilbert-Huang transform (HHT) and explains the ensemble empirical mode decomposition (EEMD) algorithm that drives the decomposition of a time series signal into a finite number of orthogonal components. Finally, the author explains the Hilbert transform and how the transform is able to compute instantaneous phase or frequencies of a decomposed component of the signal.

Chapter 4 takes into account the validation of the numerical setup in two ways: by way of a grid independency study, and by way of experimental comparison. The grid independency study utilises the Richardson extrapolation and grid convergence index (GCI) as the primary tool to ensure spatial convergence of the numerical results. In the experimental validation, this work showcases a simple contactless method of measuring the cylinder displacement using a camera and an open-source image tracking software. After the processing of the experimental data to compute the uncertainty and present them as error bars, the author concluded that the numerical results of the pure cruciform

( $90^\circ$  cruciform) is in fair agreement with the experimentally obtained values, providing an added layer of confidence in the numerical results.

Chapter 5 deals with the vibration characteristics of a pure cruciform. In this chapter, the author studies in detail the lift-displacement dynamics that results from the kind of vortical structures that appear in this setup. This chapter concludes with the discovery of a path to energy loss that has never been considered before in the literature and estimated the amount of improvement possible for the power output if said loss is eliminated. Chapter 6 discourses about the vortical structures and lift-displacement dynamics of a steep-angled cruciform ( $45^\circ \leq \alpha^\circ \leq 67.5^\circ$ ), while Chapter 7 covers the vortical structures and lift-displacement dynamics of a shallow-angled cruciform ( $0^\circ \leq \alpha^\circ \leq 22.5^\circ$ ). Here, the study found out that for shallow-angled cruciforms, the onset of meaningful power generation is brought down significantly to from  $U^* = 18.2$  in the pure cruciform, to  $U^* = 9.1$  when the cruciform angle is  $0^\circ$ . At  $\alpha = 0^\circ$ , the maximum power also improves by approximately a power of two.

Finally, in Chapter 8, the author computes the mechanical power and efficiency of each of the cruciform variants for all flow velocities studied. From it, this work is able to produce a mechanical power and efficiency map, in essentially a cruciform angle-flow velocity parameter space.

## CHAPTER 2

### LITERATURE REVIEW

The alternate shedding of vortices from opposing sides of a cylinder introduces an alternating lift and drag which, unless constrained, will induce the vibration of the cylinder. This vibration energy can be converted into electrical power via the piezoelectric effect or electromagnetic induction. This is the basis of vortex-induced vibration (VIV) energy harvesting, and in this chapter, the author goes through the body of work done on the subject of vortex shedding, vortex-induced vibration and finally energy harvesting from the many variants of cylindrical oscillators, to determine the limits of the current knowledge and pinpoint where this work resides within the web of research done by the community.

#### 2.1 Vortex Shedding from a Cylinder

In this work, a cylinder is defined as an elongated three-dimensional (3D) object with a well-defined axis, and whose cross-sectional shapes are the same at any arbitrary location along the axis. Flow around a cylinder is one of the phenomenon that, although abundantly occurring in nature and in man-made settings, remains impervious to rigorous and analytical description of the phenomenon. Key to this elusiveness is the fact that for a flow pattern to manifest itself in the physical world, the solution to the governing equations of fluid mechanics must not only exist, but must also be stable to ambient random excitations for it to be sustainable. Thus far, the Navier-Stokes equation remains unsolved on the list of Millennium Problems by the Clay Mathematics Institute, prompting researchers to rely heavily on experimental and numerical techniques in the push for breakthroughs in this field of study. Vortex shedding from a cylinder is one such interest in this field - and as the reader will see in the following subsections - whose advances are greatly driven by experimental and numerical research.

### 2.1.1 Karman Vortex Shedding

In the study of Karman vortex shedding, seldom is the case where one does not find reference being made to a chart on lift and drag coefficients for a stationary circular cylinder between  $10^0 < \text{Re} < 10^8$  in Zdravkovich (1997). The observation that both lift and drag coefficients ( $C_l$  and  $C_d$ ) have their high and low regions within  $10^0 < \text{Re} < 10^8$  is of extreme utility to engineers. From the preservation of risers to the improvement of power output for VIV-based energy harvesters, the chart in Zdravkovich (1997) gives a rough outline to the range of Reynolds number suitable for a particular engineering operation. That being said, the chart remains silent on why  $C_l$  and  $C_d$  evolve the way they do with respect to  $\text{Re}$ , leaving the gap to be filled by later researchers.

For example, Desai *et al.* (2020) tackled the question why is there a reduction in  $C_l$  and  $C_d$  as the cylinder goes through the upper boundary of subcritical flow ( $1.49 \times 10^5 < \text{Re} < 3.55 \times 10^5$ ). Their study is experimental, using tools such as particle image velocimetry (PIV) for a quantitative visualisation of the two-dimensional (2D) flow field, and proper orthogonal decomposition (POD) for identification of dominant flow structures. In doing so, they have identified two modes of shedding - the antisymmetric and symmetric modes - which takes place one after another, albeit in no well-defined cycle. The antisymmetric mode corresponds to the “normal” shedding of Karman vortices while the symmetric mode a weaker form of shedding with a higher energy level in its low-frequency components. The symmetric mode gains strength with increasing  $\text{Re}$ , which entails a weaker form of shedding taking over the flow. This ultimately reduces the magnitude of  $C_l$  and  $C_d$  of the cylinder. Depending on which side of the divide one is, an engineer may opt to amplify the symmetric mode to protect the integrity of a structure, or augment the antisymmetric mode to improve the conversion efficiency of energy from the freestream into cylinder vibration. In other words, a deeper understanding into the mechanics of Karman vortex shedding invariably leads to better strategies in cylinder motion control.

Expanding on the topic of flow control, Durhasan *et al.* (2019) conducted an experimental study of the shedding process under the following setup: the circular cylinder is placed in a larger hollow cylinder with varying pore spacing - quantified

by their porosity -  $\beta$  - and submerged in a water flow at Reynolds number  $Re = 5000$ . What they found out is the stunting of the wake from the inner cylinder when  $\beta \leq 0.5$ , while for porosities  $\beta \geq 0.6$ , a reduction of 21% to 87% in drag is observed.

Another exploitation of porous material in the control of Karman vortex shedding is in the work of Geyer (2020). In Geyer (2020), they work to test a method of noise reduction by wrapping certain parts of the cylinder surface with a porous material. This is because, at velocities in the order of  $O(10^1)$  m/s, Karman vortex shedding also exacerbates the level of noise generated by the cylinder. They discovered that the higher the air resistance of the material, and the higher the porosity, the bigger the improvement will be in terms of noise reduction. In addition, the porous wrapping reduces turbulence intensity in the wake near-field, hence making it more uniform.

In studying a flow around a solid object, one quickly finds that experimental methods employed in the investigation is never absolutely independent of the phenomenon being studied. The use of probes, for example, means that the researcher is introducing additional elements into the flow that cannot be fully isolated from affecting the flow, however careful the design of the experiments are. To compensate this shortcoming, studies have employed numerical methods to model the flow under consideration, and track the evolution of quantities of interest in the flow to a degree of resolution limited only by the computational power available. Taking note of the expediency of porous media buffering the cylinder to temper flow behaviour, Ledda *et al.* (2018) made use of numerical methods to simulate Karman vortex shedding from a square cylinder to gain a deeper insight on how the flow interacts with the porous media to produce the flow responses discussed previously. In this study, the authors observed the efficacy of a porous cylinder surface in not only detaching the recirculation region in the near-wake, but in purging it altogether, at higher porosity values. If a technique can be found to vary the porosity of the surface, perhaps through the use of smart materials (Arsh, 2020), an engineer can basically switch Karman vortex shedding on and off at will.

Other than the usual methods of numerical investigation that work to solve the continuity and Navier-Stokes equations directly (DNS) (Xiong *et al.*, 2018; Alves

Portela *et al.*, 2020), or those that employ some form of simplification (Deloze *et al.*, 2016; Shao and Li, 2016), methods that model molecular dynamics (MD) have also found their way in the arsenal of tools available to researchers in the field of fluid-structure interaction. One such example is the study by Asano *et al.* (2020). In it, the authors employed the Lennard-Jones potential to model represent the molecular dynamics of a flow around one or two circular cylinders. The Lennard-Jones potential models the fluid particle distribution, and all physical quantities are then expressed in terms of energy, length and time. What they discovered was, cavitation, although undesirable in normal operation of turbomachineries, can be a determining factor in the onset of Karman vortex shedding. As they decreased the fluid temperature, the cavitation bubbles interact with the shear layer of the cylinder in a manner that pushes the wake further downstream than usual. Eventually, wake where the vortex shedding resides is pushed far enough downstream that the alternating lift that normally acts on a cylinder during Karman vortex shedding vanishes.

Another method for Karman vortex shedding control that imposes some form of modification to the shear layer of the cylinder is through the affixing of fairings on the surface of the cylinder. A recent example of this can be found in the work of Kang *et al.* (2020). In Kang *et al.* (2020), the fairings affixed to the cylinder surface caused a reduction in both lift and drag acting on the cylinder, although the strength of this effect varies with respect to the actual flow velocity being imposed on the cylinder.

Apart from tempering the shear layer of the cylinder, one can also - similar to Yokoi (2016) - alter the downstream region of the cylinder to achieve a desired response. In their study, Yokoi (2016) introduced a splitter plate on the trailing edge of a circular cylinder and discovered a rich collection of flow patterns that one can achieve simply by varying the following variables: splitter plate length, cylinder forcing amplitude and cylinder forcing frequency. By doing this, one can even achieve a symmetric shedding of Karman vortices from the top and bottom surfaces of the cylinder. To appreciate the significance of this result, one simply needs to recall that alternating  $C_l$  and  $C_d$  acting on the cylinder is the consequence of Karman vortices shedding alternately from the top and bottom of the cylinder. The fact that one can force the shedding to take place

simultaneously from the top and bottom of the cylinder means that the amplitude of both  $C_l$  and  $C_d$  can be significantly diminish, if not altogether.

To be clear, the splitter plate method is not particularly new in near-wake control; splitter plates have been studied in the past under a similar setup (Mat Ali *et al.*, 2011; Mat Ali *et al.*, 2012), although under completely different flow conditions and cylinder geometry. However, one may find it difficult not to rely to some extent on the studies by Mat Ali *et al.* (2011); Mat Ali *et al.* (2012), since unlike Yokoi (2016), they study flow patterns that are self-induced and does not rely on external forcing. This is particularly pertinent as in nature and man-made settings, self-induced vibrations is the norm rather than the exception.

### 2.1.2 Streamwise Vortex Shedding

In the real world, Karman vortex shedding is almost never a two-dimensional phenomenon. Three-dimensionality dominates the flow field and streamwise vortices appear alongside the Karman vortices once  $Re$  exceeds 150. Among the seminal studies on Karman vortex three-dimensionality are the works of Williamson (1996b,a). The author discusses two main modes of three-dimensionality: modes A and B. Mode A has a spanwise wavelength of three to four diameters and appears at  $Re = 200$ . However, as  $Re$  is increased, another mode with a smaller wavelength appears, designated as mode B. The modes consist of vorticities that point in the streamwise direction. The shedding of these modes are therefore a simple representative case of streamwise vortex shedding.

Noticeably, a lot of studies on streamwise vortex shedding discuss the process as a secondary process that is the offspring of the vortical structure that actually dominates the flow field - the spanwise Karman vortex. This trend in viewing streamwise vortex shedding as a secondary process is also found in Agbaglah and Mavriplis (2019). In their numerical study of an isolated square and circular cylinder, they considered two Reynolds number,  $Re = 205$  and  $Re = 225$ , and noted that the shedding frequencies of the two cylinders are quite similar. The Strouhal number  $St$  for the square cylinder is 0.152 and is 0.149 for the circular cylinder. It is interesting to note that not only do they differ from each other only by two percent, but also that they differ by less than

20% from the empirical equation (see, Eq. 2.1) describing the shedding frequency of Karman vortices from a smooth circular cylinder (Blevins, 1990).

$$St_{\text{Karman}} = 0.198 \left( 1 - \frac{19.7}{Re} \right) \quad (2.1)$$

The fact that  $St$  for the square and circular cylinders of Agbaglah and Mavriplis (2019) differs less than 20% of the value estimated using Eq. 2.1 indicates that the shedding process of streamwise vortex is overshadowed by Karman vortices, which are larger in scale. Perhaps this is an artefact of using an isolated cylinder, and as long as one uses a similar system, Karman vortex shedding will remain the primary process governing the flow.

More recent works on streamwise vortex shedding have shifted away from a simple isolated circular cylinder configuration to slightly more complex layouts, perhaps to recreate models that are more faithful to real engineering situations. For example, in Gibeau *et al.* (2018), an elongated body is studied in the range  $3.5 \times 10^3 \leq Re \leq 7.0 \times 10^3$ . Through this study, Gibeau *et al.* (2018) found that the average strength of the streamwise vortices in the upstream boundary layer is ten times smaller than in the wake. They also observed that the wavelength reaches between 0.7 and 0.8 of the elongated plate thickness,  $h$ .

In another study, Gibeau and Ghaemi (2019) swapped the isolated circular cylinder for a blunt trailing edge body. This blunt trailing edge (BTE) body is made from a leading edge that is a 5:1 ellipse connected to a plate with thickness  $h$ . This experimental study in the range  $2.6 \times 10^2 \leq Re \leq 2.58 \times 10^4$ , reveals that the rotational direction of the streamwise vortices are conserved during the shedding cycle, and their wavelength is close to mode B of Williamson (1996b).

Knowledge on the spatial distribution and key dimensions of streamwise vortices may be insufficient to highlight how one can exploit them to one's advantage. To exploit streamwise vortex shedding to fulfil engineering objectives, one needs insight on the effects of streamwise vortex shedding on the flow. This is demonstrated in the work by

Rai (2018), in which the author published numerical results of flow around a flat plate with a circular trailing edge. The Reynolds number varies from  $250 \leq \text{Re} \leq 10000$ . Rai (2018) discovered that streamwise vortices are responsible for generating steep spanwise velocity gradients that affect the strength of the dominant vortical structure of the flow, i.e. the Karman vortex. The author also found that fluctuations in the streamwise velocity within the boundary layer leads to variation in the shedding period of the dominant Karman vortex. Finally, streamwise vortex shedding is observed to affect the shedding frequency of the spanwise Karman vortices through the speed of their streaks in the boundary layer.

In an evaluation of a passive method to control flow around a circular cylinder, Lin *et al.* (2018) inserted the cylinder inside a conical shroud and assessed its effect on the vortical structures shed around it. They chose a very low  $\text{Re} = 100$ , to keep the flow as two-dimensional as possible. Lin *et al.* (2018) tested two types of conical shroud. One shroud is with perforations of varying diameter and placement angle along the peak of the cone, and the other without. The authors also varied the wavelength and outer diameter of the conical shroud. By doing so, the study essentially discovered a method to prevent the energising of Karman vortex when the disturbance brought about by the conical shroud is large enough. Energy from the freestream is redirected away from Karman vortices, to form strong  $\Omega$ -shaped vortices in the neighbourhood of the conical valley. This results in partial to full suppression of Karman vortex shedding. The ability to refocus energy to a vortical structure of choice is indispensable, especially to engineers who may either want to minimise cyclic force acting on a structure, or maximise it to improve vibration energy harvesting potential of the structure.

Other examples of energy redirection can be found in Zhang *et al.* (2016) and Zhang *et al.* (2019). In these studies, the authors examined two methods to control Karman vortex shedding from a model bridge. The first method in Zhang *et al.* (2016) employs suction on the bottom of the bridge to disrupt the homogeneity of the Karman vortex along the span of the bridge. When suction is applied, streamwise vortex - which is considered a secondary process by the authors - becomes energised. The energised streamwise vortex then destabilises the primary vortical structure - the Karman vortex - hence reducing the net force resulting from it.

Providing suction on the bottom of the bridge is an active flow control method. This is because an active supply of energy is required to power the suction from the designated holes. As an alternative, Zhang *et al.* (2019) proposed using vortex generators affixed similarly to the bottom of the bridge, and evaluates the degree to which a similar result can be achieved. In the final analysis, they demonstrated that the disruption of Karman vortex homogeneity is possible through the use of vortex generators. However, they did not specify quantitatively how much weaker does the Karman vortices get in expense of stronger streamwise vortices.

Attachment of a plate (Gibeau and Ghaemi, 2019) or placement of the cylindrical object inside a conical casing (Lin *et al.*, 2018), even the deployment of vortex generators on the surface of the cylinder (Zhang *et al.*, 2019) are all methods of flow control that add another layer of complexity to the cylindrical object. In situations where an engineer seeks to retrofit a flow control method to existing systems with cylindrical objects, direct modification of the cylinder can be difficult and downright undesirable. What if there exists an accessible flow control method that requires only a minimum amount of effort from the end used to install, but is still powerful enough to significantly alter the dominant vortical structures of the flow? The deployment of another cylindrical object downstream the main cylinder seems to be a promising technique.

Flow control using a secondary cylinder placed downstream the main cylinder dates back nearly three decades. Originally, the authors investigating it (Shirakashi *et al.*, 1989) is focussed on reducing the magnitude of cyclic forces acting on an isolated circular cylinder system. They placed a secondary circular cylinder downstream the original circular cylinder and explored how, among others, root-mean-square lift coefficient of the original cylinder varies as the gap between the original and secondary cylinders are varied. The secondary cylinder is placed downstream the original in a way such that the axes are perpendicular to each other, creating a cruciform. In doing so, they discovered that while the root-mean-square of lift coefficient can be reduced as the downstream cylinder is brought closer to the original one, when the normalised gap between two cylinders  $g/D$  is  $< 0.25$  the lift coefficient rises again and peaks close to  $\approx 0.7$  before dropping off again as  $g/D \rightarrow 0$ . This is a significant finding in that it

demonstrates how the flow around an existing isolated cylinder system can be altered in hindsight by simply forming a cruciform structure with another cylinder.

The dominant vortical structure in such a cruciform when  $0 < g/D < 0.5$  is dominated by a pair of streamwise vortices, shed alternately from the top and bottom of the primary cylinder (Koide *et al.*, 2017). Two types of streamwise vortices are observed, the necklace vortex when  $0.25 < g/D < 0.5$ , and the trailing vortex when  $0 < g/D < 0.25$ . Although both types of vortices form close to the cruciform juncture, the necklace vortex dominates a region that is closer to the juncture than the trailing vortex (Takahashi *et al.*, 1999), which forms a little further away from the juncture. The streamwise vortex pair that forms due to the cruciform does not seem to be secondary to the Karman vortex that is also shed from the upstream cylinder. Instead, the streamwise vortices seem to have its own mechanics which is independent from the cycle of Karman vortex shedding.

One obvious example is the deference to Eq. 2.1. Streamwise vortices such as those discussed earlier (Zhang *et al.*, 2016; Rai, 2018; Agbaglah and Mavriplis, 2019; Zhang *et al.*, 2019) develop as three-dimensional instabilities of Karman vortex shedding, and as such, have a base shedding frequency that loosely obeys Eq. 2.1. However, streamwise vortices in Takahashi *et al.* (1999), and even in Shirakashi *et al.* (2001) and Bae *et al.* (2001) do not. Streamwise vortices from these studies are shed at an increasing St as Re is increased within the region  $Re < 10000$ . When  $Re > 10000$ , St for the streamwise vortex becomes more or less constant with  $St \approx 0.04$  for the necklace vortex and nearly twice that value for the trailing vortex.

Domination of the cruciform flow field by the streamwise vortex pair does not imply that the Karman vortex completely disappears from the experimental domain. This is demonstrated in Koide *et al.* (2006) and Kato *et al.* (2006). According to the frequency spectra of the upstream cylinder vibration, the Karman shedding frequency still exist in the system, only far smaller in magnitude compared to the amplitude attained by the streamwise vortex structures. The flow field is thus dominated by the streamwise vortex pair close to the cruciform juncture, while the influence of the Karman vortex only grows as one moves towards the ends of the upstream cylinder. This begs the

question whether the streamwise vortex-dominant flow is simply a consequence of two circular cylinders at right angles to each other - placed some distance away from each other - or is it something universal to cruciform structures?

To answer this, Kato *et al.* (2007) and Nguyen *et al.* (2010) tested several variations of the cruciform, to see whether a similar occurrence of streamwise vortex shedding can be observed. For example, Kato *et al.* (2007) swapped the downstream circular cylinder with a strip plate, and observed that similar streamwise vortices do appear in the flow. They are shed at very similar values of St as the two-cylinder cruciform, but the frequency spectra of velocity fluctuations revealed a noisier pattern with less discernable peaks compared to the frequency spectra computed from a two-cylinder cruciform. More recent flow visualisations suggest that the noisier pattern is due to an increased turbulence level in the flow as streamwise vortices are produced from the circular cylinder-strip plate system (Koide *et al.*, 2017). Streamwise vortices produced from the two-cylinder system however, is less turbulent and thus one finds less distortion in the vortical structures compared to the circular cylinder-strip plate cruciform.

Distortion of the vortical structures discussed in Kato *et al.* (2007) and Koide *et al.* (2017) are self-induced: the result of an increasing level of turbulence in the flow. An increased level of turbulence is something that is internal to the flow being considered. It remains to be seen whether external factors such as the type of medium used as the ambient fluid, or configuration of the experimental rig can affect the shedding behaviour of the streamwise vortices. The work by Nguyen *et al.* (2010) partially answers this question. In their study, the two-circular cylinder cruciform is tested under various settings. They tested the system in wind and water tunnels of various sizes and ascribing different dimensions to the cruciform. The dimensions Nguyen *et al.* (2010) vary in their experiments are the circular cylinder diameter, cylinder length and aspect ratio. At the end of their study, Nguyen *et al.* (2010) concluded that nearly all major characteristics of streamwise vortex shedding are observed under the various test conditions. There are, however, some discrepancies namely reduction by 30% to 50% of streamwise vortex shedding St in the largest wind tunnel, and the vanishing of the necklace vortex in the water tunnel as  $Re > 22400$ .

Clearly, streamwise vortex shedding that results from the deployment of a cruciform structure is robust and induces as much force on the upstream cylinder as Karman vortex shedding on an isolated cylinder, if not more. This makes the cruciform structure a good oscillator candidate for the purpose of converting energy from the free stream in to vibration energy. In the next section, the author reviews the recent developments in VIV and discusses how a cruciform oscillator ties into the overall work done to induce a larger, but predictable vibration from fluid flows, including that which depends on Karman vortex.

## 2.2 Vortex-induced Vibration of a Cylinder

### 2.2.1 Single Cylinder Oscillator Unit

Since Karman vortex shedding has been demonstrated to produce alternating lift and drag on an isolated cylinder system, replacing motion constraints with elastic supports allows oscillatory motion to take place. Typically, the oscillation is constrained to a one-dimensional transverse motion against the direction of the free stream. Following the success of Raghavan (2007) and Bernitsas *et al.* (2008); Bernitsas and Raghavan (2008a) in achieving a high amplitude response from an isolated circular cylinder oscillator, experimental studies for such an oscillator are increasingly done in the  $2 - 4 \times 10^4 \leq Re \leq 1 - 2 \times 10^5$  range.

Numerical studies provide a non-intrusive method to collect high-resolution data on flow quantities. Following the trend in experimental studies of VIV, an increasing number of works have been pushing through the  $Re \sim O(10^5)$  barrier, and collect time-resolved flow quantities that lay the groundwork for advancing VIV flow theory. Additionally, if one is able to develop a working numerical model of VIV at a particular range of  $Re$  that is in good agreement with experimental findings, scholars can then use that model to automate the variation of parameters. This automation enables efficient exploration of the parameter space of interest and rapid product prototyping.

However, for numerical works to accurately depict what is going on in the flow at  $Re \sim O(10^5)$ , investigators need to abandon one of the most commonly made assumption to simplify the KVIV phenomenon: that the flow is two-dimensionally reducible. Reducing KVIV to a two-dimensional domain greatly reduces computational

requirements and allows the researcher to focus the computational effort on resolving the shear layer of the cylinder and the near-wake region. However, three-dimensional effects exists throughout the flow field as soon as  $Re > 150$ , and an accurate representation of KVIV necessitates taking these effects into account.

*Kinaci et al.* (2016) proposed a tip-flow correction factor to reduce deviation of a two-dimensional CFD simulation from experimental results. The tip-flow correction factor is computed from three-dimensional simulation of flow around a cylinder within the  $Re$  range of interest, in essence providing the reader with a new “effective length” of the cylinder. The success of this method is however quite limited as it only scales the lift magnitude from a two-dimensional simulation, but not the phase lag between the lift and cylinder displacement. This means that to conduct a meaningful study of KVIV in the TrSL3 regime ( $2 - 4 \times 10^4 \leq Re \leq 1 - 2 \times 10^5$ ) one must rely on experiments and three-dimensional simulations to explore the bulk of parameter space.

One of the recent developments in the control of KVIV is by affixing passive turbulent stimulations on the surface of the cylinder. For example, *Park et al.* (2016) deploys surface roughness on the cylinder and observed their effect on KVIV. They identified several location on the cylinder that produces weak to high reduction in the amplitude response. They reasoned that this is due to the reduction of vorticity in the shear layer that forestalls vortex roll-up, hence trim the vibration amplitude by at least a factor of three. This forestalling of vortex shows that surface roughness on the scale of the shear layer thickness can alter the vorticity and thus the lift production process of the cylinder.

The altering of vorticity in the shear layer is also what enables the bridging of KVIV and galloping in single cylinder systems with surface roughness. At low angles of attachment of the roughness strip (*Chang et al.*, 2011; *Park et al.*, 2013), the flow separates at the strip upstream but reattaches further downstream the cylinder surface. At high angles of attachment, there is not enough distance along the cylinder surface for the separated flow to reattach, hence vorticity cancellation between Karman vortices shed from the top and bottom of the cylinder becomes comparatively more aggressive. The absence of this aggressive cancellation of spanwise vorticity is the

reason why placement of the roughness strip is able to, in contrast to Bernitsas and Raghavan (2008b) and Park *et al.* (2016), enhance KVIV and improve the amplitude response of the single cylinder oscillator.

In §2.1.2, this work discussed how the cruciform system has its origin as a simple method that can be retrofitted to an existing single cylinder oscillator unit to control Karman vortex shedding. As such, the effect of the downstream cylinder/strip plate is targeted towards the upstream cylinder and not itself. However, within the last five years, the VIV research community has increasingly realised that there is no reason for the conversion of energy from the free stream into vibration to strictly be a one-stage process. Excess energy that is not eludes capture by a single cylinder should simply be recovered with another cylinder downstream.

Bearing this in mind, Ding *et al.* (2017) investigated the system response of a two-circular cylinder system, one in front of the other and with their axes parallel to each other. Then, they measured the amplitude/frequency responses of the system and observed the following, compared against a single cylinder system with passive turbulence control (PTC). The amplitude response of the upstream cylinder seems to improve in this serial arrangement of cylinders, and they experience only a small influence from centre-to-centre distance variation. On the other hand, the downstream cylinder experiences a reduction in the amplitude response compared to a single cylinder system and is more sensitive to the centre-to-centre distance between the two cylinders. The reduced amplitude response of the downstream cylinder is the result of the acquisition of downstream cylinder vorticity by the upstream cylinder in proximity. Proximity between the two cylinders determine how much downstream cylinder vorticity is carried away by the upstream vortex, and this reduces the net lift acting on the downstream cylinder. The reduction of lift finally results in the reduction of downstream vibration amplitude.

There is however, a countermeasure to improve the amplitude response of the downstream cylinder. The improvement is achieved by imposing a smaller damping on the downstream cylinder (Xu *et al.*, 2017). When Xu *et al.* (2017) reduced damping for the downstream cylinder, the amplitude response of the downstream cylinder becomes

more similar to the amplitude response of the upstream cylinder. Nevertheless, because harnessed power is proportional to damping - specifically damping in the mechanical to electrical power converter - a reduced total damping just to achieve a higher amplitude vibration is simply contrary to the engineer's main objective of energy harvesting Bernitsas *et al.* (2008, 2009).

Spacing between the two cylinders play an important role in obtaining maximum vibration amplitude from both the upstream and downstream cylinders. This much is already known from the works of Park *et al.* (2016) and Ding *et al.* (2017). However, recently, Yuan *et al.* (2020) utilised the Hilbert transform on the cylinder displacement time series of both upstream and downstream cylinders. In doing so, they identified five major responses of the two-cylinder oscillator that depends primarily on the centre-to-centre distance between the two cylinders, and secondarily on other parameters such as spring coefficient and total damping.

The use of Hilbert transform enabled Yuan *et al.* (2020) to compute instantaneous frequency and phase lag between the upstream and downstream cylinders and identified the five major response regimes of the system. Although Yuan *et al.* (2020) have essentially demonstrated the utility of Hilbert transform in analysing complex and interdependent systems of vibration, the signals they analysed are for the most part monocomponent signals with more or less a symmetrical signal envelope. For signals that lack these features, the pre-processing step of empirical mode decomposition (EMD) or ensemble empirical mode decomposition (EEMD) is necessary to produce meaningful physical results (Huang, 2014; Chen *et al.*, 2019).

### 2.2.2 Cruciform Oscillator Unit

Streamwise vortex-induced vibration (SVIV) is a type of vortex-induced vibration (VIV) driven by vortical structures whose vorticity vector points in the direction of the free stream. In its early days, the cruciform oscillator is nothing but two circular cylinders perpendicular to each other, overlapping at their midpoints (Zdravkovich, 1981, 1983, 1985).

A cruciform oscillator unit derives its vibration from the streamwise vortex pairs discussed in §2.1.2. Investigators observed the upstream cylinder acquiring significant vibrations in the order of  $O(10^{-1}D)$ , as the reduced velocity of the flow  $U^*$  exceeds 14. Here  $D$  denotes the diameter of the upstream cylinder and the reduced velocity is defined in Eq. 2.2 as

$$U^* = \frac{U_\infty f_n}{D}, \quad (2.2)$$

where  $U_\infty$  and  $f_n$  refers to the freestream velocity and the natural frequency of the system, respectively. Interestingly, however, the latest published research on a zero-gap circular cylinder cruciform system between  $300 \leq \text{Re} \leq 1800$  revealed that no streamwise vortex cell are formed and shed from the structure (Tang *et al.*, 2021). This work by Tang *et al.* (2021) was a numerical one, employing large eddy simulation (LES) with the dynamic  $k$ -equation subgrid-scale (DKSGS) model. Even the time history of the drag and lift coefficients did not show significant levels of periodicity, similar to those found in Deng *et al.* (2007), although they both simulate flow in the same Reynolds number magnitude of  $O(10^2)$ . In fact, Deng *et al.* (2007) simulated the flow around a circular cylinder cruciform at a much lower Re and still were able to observe the formation of the streamwise vortex cells and their footprint, manifesting themselves as the periodic oscillation of the drag and lift coefficients. What can be deduced from this is the gap between two cylinders forming a cruciform is essential for the formation of streamwise vortices and ultimately the vibration induced by it.

In their study of the two-circular cylinder cruciform, Shirakashi *et al.* (2001) observed the vibration of the upstream cylinder hitting the top boundary of the wind tunnel between  $20.5 \leq U^* \leq 35.9$ . The height of the wind tunnel in Shirakashi *et al.* (2001) is 320 mm and the diameter of both upstream and downstream cylinders are 26 mm. The fact that the reported vibration amplitude reaches the top extent of the wind tunnel means that it is able to achieve at least  $(320 \text{ mm}/2)/26 \text{ mm} = 6D$  within  $20.5 \leq U^* \leq 35.9$ . This alone is far bigger than any of the amplitude attained by the single cylinder oscillator units reviewed in §2.2.1. However, there seems to be a finite range within which the cruciform oscillator is able to sustain this high

amplitude response, which is approximately 15 units of  $U^*$ . Past this, the amplitude of the cylinder drops to about  $0.1D$  and stayed there up to the maximum  $U^*$  tested. In contrast, single cylinder oscillators of §2.2.1 is able to sustain its vibration through galloping for seemingly an infinite range of  $U^*$ .

More recent iterations of the system (Koide *et al.*, 2007; Kato *et al.*, 2007) employs a thin, rectangular plate of width  $w = D$  in place of the fixed downstream cylinder, and showed that the region of high-amplitude vibrations of the system is enlarged from 15 units of  $U^*$  for a two-circular cylinder cruciform to approximately 40 units of  $U^*$  for the circular cylinder-strip plate oscillator studied in Koide *et al.* (2007). Nevertheless, the shortcoming of this configuration is a lower amplitude of vibration, which attains only a maximum of close to  $y_{\text{RMS}}^* = 0.35$ . The vibration amplitude in (Koide *et al.*, 2007; Kato *et al.*, 2007) is given as the root-mean-square of nondimensionalised vibration amplitude  $y_{\text{RMS}}^* = y_{\text{RMS}}/D$ . Here,  $y$  denotes the coordinate pointing in the transverse direction of the flow, i.e. the direction of cylinder vibration. The effect of circular cylinder-strip plate gap  $g/D$  on  $y_{\text{RMS}}^*$  was also examined, and the results were consistent with the trend of high lift generation discussed in §2.1.2:  $y_{\text{RMS}}^*$  jumps to a high-amplitude regime as  $g/D$  is decreased to  $< 0.5$ , especially when  $g/D < 0.25$ .

However, at  $G = g/D = 0.16$ , researchers have found that the circular cylinder-strip plate oscillator managed to sustain its vibration over a very large range of  $U^*$ . In relative terms, the vibration of this variant of the cruciform is sustained over a range of  $U^*$  15 times the width observed in an isolated, smooth circular cylinder oscillator of similar diameter (Koide *et al.*, 2009, 2013). The reason behind this is the vortical structure driving the vibrations: vibration of the cruciform is driven by a pair of counter-rotating streamwise vortex shed a short distance from the cruciform juncture (refer Fig. 2.1), while vibration of the isolated, smooth circular cylinder is driven by Karman vortices shed alternately from the top and bottom surface of the cylinder.

The upside of this discovery is the fact that this wide synchronisation range is due to vortex shedding i.e., vortex-induced vibration (VIV) instead of galloping, as in Sun *et al.* (2019), Xu *et al.* (2019) and Ding *et al.* (2019), as VIV-based energy

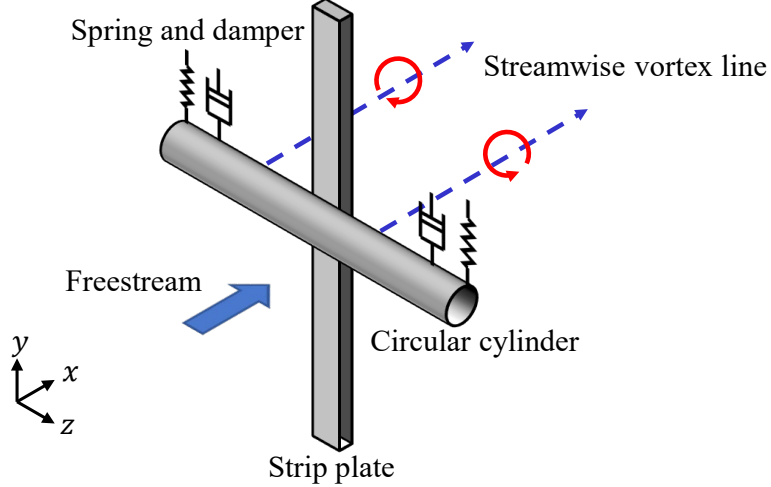


Figure 2.1: Schematic of the base configuration of the oscillator system used in this study, i.e. the pure cruciform. In this configuration, the axis of the cylinder and the strip plate are perpendicular to each other.

harvesters of similar scale operate at higher efficiencies compared to galloping-based ones (Sun *et al.*, 2016; Ma *et al.*, 2016).

In their study, Deng *et al.* (2007) examined the flow field of a twin circular cylinder cruciform using computational fluid dynamics (CFD). Their domain stretches  $28D$  in the streamwise direction,  $16D$  in the transverse direction and  $12D$  in the spanwise direction. They studied an  $Re$  range yet another order of magnitude smaller than that studied by Koide *et al.* (2017), possibly to get an even clearer visualisation of the vortical structures with less turbulence, and to ease computational requisites. At a fixed  $Re = 150$ , streamwise vortices form even at a gap ratio of 2. This result differs quite strikingly from Koide *et al.* (2006, 2007), conducted at an  $Re$  twice the order of magnitude of Deng *et al.* (2007), an indication that the minimum gap ratio needed for the onset of streamwise varies with respect to  $Re$ .

They also observed that when the gap ratio  $G$ , which they denote as  $L/D$  in their paper, increases from 3 to 4, the maximum amplitude of the lift coefficient increases by almost threefold. This can be attributed quite easily to the current vortex pair shed by the upstream cylinder. The downstream cylinder immediately disturbs the pair shed from the upstream cylinder when  $G = 3$ . The lift coefficient increases by about a factor of 3 when this immediate disturbance diminishes at  $G = 4$ . The visualisation

of three-dimensional (3D) vorticity isocontours enables the present work to quickly establish this link vis-à-vis the lift coefficient signal. The authors use of CFD made this possible.

A similar study in the order of magnitude  $\text{Re} \sim O(10^2)$  by Zhao and Lu (2018) particularly highlighted the immense utility of CFD as a tool to research SVIV or flow around a cruciform in general. They computed the sectional lift coefficient along the upstream cylinder, and the time history of this sectional lift coefficient revealed two different modes of vortex shedding, namely, parallel and K-shaped. They also paid attention to the local flow patterns that vary along the length of the upstream cylinder such as the trailing vortex flow, necklace vortex flow and flow in the small gap (denoted as SG flow). The discontinuities in the phase angle of the sectional lift coefficient along the upstream cylinder seems to suggest the inadequateness of attributing the lift coefficient to streamwise vortex shedding alone, particularly when Karman vortex streamlines were also observed some distance away from the junction of the cruciform.

Shirakashi *et al.* (1989) also made a similar observation in their experimental work. These observations lead the present author to hypothesise that the lift signal is more appropriately viewed as the streamwise and Karman vortex-induced composite lift signal. The present work, nevertheless, could neither find studies that took this viewpoint, nor work out its consequence on power generation. It is worth mentioning that there was a recent development in this field of study, which investigated a square cylinder and a square plate downstream of it (Mohamed *et al.*, 2021). This is essentially a variant of the canonical cruciform structure where the upstream circular cylinder is swapped for a square one, and the downstream strip plate is shortened to the same height of the upstream square cylinder. From all the experimental conditions tested, Mohamed *et al.* (2021) found only one setup that enhances the KVIV amplitude of the system, which is when the side ratio and gap ratio of the system is  $(B/D, g/D) = (1.0, 1.17)$ , while other setups cut down the KVIV amplitude by a factor of two. Galloping however, receives a boost in the root-mean-square amplitude at  $(B/D, g/D) = (1.2, 1.15)$  and  $(1.4, 1.15)$ , making this setup a galloping-oriented oscillator and ultimately, energy harvester.

## 2.3 Energy Harvesting from a Vibrating Cylinder

The field of energy harvesting has witnessed exponential growth in the past two decades, particularly those which are based on alternating lift mechanisms. Following the same method used in the previous §2.2, the author reviews the progress in the single cylinder energy harvesting unit first, followed by the recent advances in the cruciform systems.

### 2.3.1 Single Cylinder System

Recent advances in energy harvesting from a single cylinder system builds upon the body of work done on single cylinder oscillators. One of the overarching themes in power output improvement from a single cylinder system is the operating range of  $Re$ . Ever since the work done by Bernitsas *et al.* (2008) and Bernitsas *et al.* (2009), prototyping studies have planted their foot firmly in the high lift regime of TrSL3. In doing so, studies such as Ding *et al.* (2019) and Park *et al.* (2017) managed to demonstrate an amplitude response with an upper branch sustained over a wider range of  $U^*$  compared to amplitude responses of single cylinder systems in TrSL1 or TrSL2. A higher vibration amplitude will elicit a higher harnessed power from the harvester.

Here, TrSL1, TrSL2 or TrSL3 refers to the classification system in Zdravkovich (1997) to characterise the flow around a smooth circular cylinder. The classification system uses abbreviations of the flow description as labels for different flow behaviours. For example, the flow around the circular cylinder undergoes a number of transitions in the shear layer between  $350 - 500 \leq Re \leq 1 \times 10^5 - 2 \times 10^5$ . The first transition in the shear layer, occurring between  $350 - 500 \leq Re \leq 1 \times 10^3 \times 2 \times 10^3$ , is the development of transition waves. Zdravkovich (1997) labeled this regime as TrSL1, formed by joining the abbreviations of “transition”, “shear”, “layer”, and the numerical equivalent of “first”, which is the number one (1). Similarly, the second transition in the shear layer occurring between  $1 \times 10^3 - 2 \times 10^3 \leq Re \leq 2 \times 10^4 - 4 \times 10^4$ , which is the formation of free vortices, is labeled as TrSL2. The shear layer becomes fully turbulent between  $2 \times 10^4 - 4 \times 10^4 \leq Re \leq 1 \times 10^5 - 2 \times 10^5$ . This regime is thus labeled TrSL3.

Now with the single cylinder system firmly planted in the TrSL3 regime, researchers worked to push the single cylinder harvesting system even further by tweaking its mechanical parameters. For example, Sun *et al.* (2018) and Ma *et al.* (2018) used as the restorative force, i.e. springs, of the nonlinear variant. So instead of modelling the spring linearly as

$$F(t) = kx(t), \quad (2.3)$$

where  $F(t)$  is the restorative force,  $k$  the spring coefficient and  $x(t)$  the displacement of the object fixed to the end of the spring, they experimented with  $F(t)$  that is given as a cubic function and an  $F(t)$  that is given as a piecewise linear function. The cubic spring

$$F(t) = ky(t) + ky(t)^3, \quad (2.4)$$

is found to significantly improve energy harvesting in all branches of amplitude response. Most significantly, however, is the improvement in the transition from VIV lower branch to galloping branch. In systems with a linear restorative force, the VIV lower branch is out of sync with the lift and also vortex shedding. This causes the net power harnessed in this regime to drop up to a factor of three, compared to the power harnessed in the upper branch of VIV (Sun *et al.*, 2018; Ma *et al.*, 2018). In contrast, when a cubic restorative force is applied to the system, energy harvesting improves by up to 78% during the transition from lower branch to galloping. Furthermore, once the system enters the galloping regime, the cubic restorative force improves energy harvesting up to 12%. In fact, the only branch where the original linear restorative force outperforms the cubic spring system in terms of energy harvesting is the upper branch.

Differently, a piecewise linear spring such as in Eq. 2.5, in essence enables switching of system stiffness and natural frequency according to the cylinder displacement.

$$F(t) = \begin{cases} k_1 y(t), & \text{if } |y(t)| \leq y_0 \\ k_1 y(t) y_0 + k_2 (y(t) - y_0), & \text{if } |y(t)| > y_0. \end{cases} \quad (2.5)$$

Through this modification, the system is able to automatically switch to a lower stiffness when the lift acting on the cylinder is small, and to a higher stiffness otherwise. A higher stiffness results in a higher system natural frequency. Consequently, when the system is in sync with the alternating lift and vortex shedding, thus producing a large vibration amplitude, the frequency of vibration also switches to a larger value. This switch to a larger value is valuable as the harnessed power from such a system is proportional to the square of its angular frequency (Ma *et al.*, 2018).

Apart from this, the piecewise linear spring is able to harness energy even when  $Re < 25000$ , which is lower than the usual linear spring system of Eq. 2.3 (Sun *et al.*, 2016). In terms of damping, although it is proportional to the net harnessed power (Ma *et al.*, 2018), there is a trade-off with the size of the stall zone during transition from VIV to galloping. The width of the stall zone increases with increasing system damping, and this reduces the system's range of operability. Furthermore, in a single cylinder system with a linear spring, simply increasing the damping reduces the maximum vibration amplitude.

Interestingly, this suppression effect on vibration amplitude due to increased damping can be kept in check when one uses the in-tandem arrangement of cylinders. The in-tandem system is similar to that discussed in §2.2.1, and Sun *et al.* (2019) observed that the amplitude reduction is not as severe in the in-tandem system compared to the single cylinder unit. This highlights the potential of exploiting the synergy between the two cylinders to counter vibration amplitude reduction that is otherwise striking, provided that the two cylinders are optimally spaced. The results also brought

attention to the concept of synergy between single cylinder oscillators in order to harness more energy from the flow.

Kim and Bernitsas (2016) took the idea of synergy and investigated a four-cylinder system for energy harvesting. Overall, what they found out was the net energy harvested by the four-cylinder system can exceed the total energy harvested by four isolated cylinder, provided that the four-cylinder system adhere to the optimised system parameters of centre-to-centre cylinder spacing, mass ratio, spring stiffness and damping. They also postulated an energy harvesting unit that consists of stacked arrays of single cylinder oscillators, thus maximising the footprint of the unit and increase power-to-volume density of the system. In summary, Kim and Bernitsas (2016) highlighted the need for the research community to widen their perspective and pay greater attention to multi-component energy harvesting systems as there is a high chance that one can discover practical arrangement of the components that increases the net harnessed energy. The next subsection explores one such system: the pure cruciform energy harvester.

### 2.3.2 Pure Cruciform System

A pure cruciform (Zou *et al.*, 2021) system is an example of a multicomponent energy harvester where the presence of the downstream plate perpendicular to the upstream cylinder alters the flow such that the vibration response of the upstream cylinder becomes different from the single cylinder oscillator. In such an energy harvesting system, there exists two vortical structures regulating the flow around the cruciform: the Karman and streamwise vortices. However, as the present study discussed in §2.1.2, only the shedding of streamwise vortex is able to synchronise with the alternating lift and cylinder displacement, thus producing a cylinder response fit for energy harvesting.

An example the cruciform system is given in Fig. 2.1. In broad terms, the literature on SVIV-based energy harvesting from pure cruciform oscillators are either one of these two categories: studies that investigate how the mass ratio, spring stiffness and damping affect the system response, and studies that put into the spotlight the details of flow that regulates the lift acting on the elastically supported cylinder, hence its

amplitude/frequency response, which directly influences the system's energy harvesting capabilities.

For example, Koide *et al.* (2009) investigated such an energy harvesting system by varying a number of parameters defining the vibration-to-electrical energy converter. Damping, similar to single cylinder systems in §2.3.1, decreases the magnitude of amplitude attained by the cylinder during vibration. They pointed out the possibility of reduced harnessed power due to this reduction in vibration amplitude. Koide *et al.* (2009) also measured the power and current generated by their pure cruciform system. From these measurements, they computed the phase angle between power and current to estimate the power factor of the system. The evolution of the power factor, however, seems to indicate that there is a lot of room for improvement for their vibration-to-electrical energy converter as the power factor varies significantly from reduced velocity to reduced velocity without any prominent trend.

In Nguyen *et al.* (2012), the authors attempted to unravel the effect of mass ratio and damping on a pure cruciform oscillator. However, since they are unable to independently vary either of the two parameters, the conclusions one can draw from their study is fairly limited. Taking this handicap into account, they proposed a crude model of the system response with respect to  $U^*$  by assuming a strong linearity underpinning the cylinder vibration. According to this model, the synchronisation range of an oscillator is larger when the total damping is higher. This seems to contradict the experimental observations of Sun *et al.* (2016), whose data indicates that an increased total damping diminishes the range of  $U^*$  capable of sustaining VIV and delays the onset of galloping. Furthermore, only the experimental data from the single cylinder oscillator of Nguyen *et al.* (2012) showed some semblance of agreement with the model, but even this agreement is objectively poor as it incapable in capturing the actual trend and magnitude of the experimentally measured amplitude responses. The study did, however, confirm that resonance in VIVs are highly nonlinear, while also suggesting the nonlinearity of SVIV to be qualitatively higher than KVIV.

Such a shortcoming can be overcome using a host of techniques such as the sensor-based virtual spring and damper system (Garcia and Bernitsas, 2018; Sun *et al.*,

2018), application of machine learning to fill in the gaps missing from a full factorial study (Wu *et al.*, 2018; Ren *et al.*, 2019; Raissi *et al.*, 2019; Hu and Kwok, 2020), and quite conventionally through the use of computational fluid dynamics (CFD) (Wu *et al.*, 2011; Zhang *et al.*, 2018b).

In the second focus area, investigators turned their attention to the details of the flow where streamwise vortex shedding occurs. One such study carefully shot motion pictures of the dye-injected flow (Koide *et al.*, 2017) at Reynolds number in the order of  $\text{Re} \sim O(10^3)$ . A lower Reynolds number ( $\text{Re}$ ) reduces the amount of turbulence in the flow, allowing a clearer shot of the vortex structures. Their study also highlights the higher level of turbulence produced by the circular cylinder-strip plate cruciform in contrast to the twin circular cylinder cruciform, which diminishes the periodicity of vortex shedding.

Although visually enlightening, this and other more qualitative studies contribute little towards improving the understanding of the relationship between vortex shedding and the resulting lift. Deng *et al.* (2007) demonstrated a way to overcome such a shortcoming. In their study at Reynolds number 150, they changed the natural frequency of the system at certain points in their transient simulation and observed how the cylinder amplitude and the force coefficients evolve with respect to the changes. In doing so, the authors found that a higher lift amplitude does not simply translate into a higher amplitude in cylinder displacement. Other factors such as the phase lag between the lift and cylinder displacement plays a significant role in predicting the outcome amplitude of the cylinder. They also verified the previous findings of Shirakashi *et al.* (1989), Koide *et al.* (2009) and Koide *et al.* (2017), that points to the coexistence of both Karman and streamwise vortex shedding in a cruciform system. The fact that only one of the two vortex shedding mechanisms actually govern the cylinder's vibration is viewed by this present work as hinting towards an untapped potential in improving the output and efficiency of the cruciform energy harvester.

Despite this, there is a marked lack in efforts to propose and evaluate new types of cruciform oscillators, particularly on the hidden potential of the strip plate as an effective vortical structure regulator. There are, however, some recent studies on the

generalisation of the strip plate in the effort to produce steady lift over the surface on the cylinder (Hemsuwan *et al.*, 2018a,d,b,c). In these studies, there are not one, but two circular cylinders placed at the ends of a small rod. The two cylinders placed just upstream the ring plate, with the centre of the small rod coinciding with the centre of the ring plate. The result of the steady lift acting on the cylinders is the rotation of the rod with the two cylinders at its ends and the centre of the ring plate as its centre of rotation - creating essentially a turbine for fluid energy harvesting.

A lot of studies on this new type of energy harvester focuses on exploring the parameter space of variables that are hypothesised as having some significant degree of influence on the resulting torque or power. For example the study of Hemsuwan *et al.* (2021) explored the parameters ring plate width and exposed blade length, while Sakamoto *et al.* (2021) the gap between the circular cylinder blade and ring plate, and flange separation length. All these variables investigated exhibits optimum points that are typical in the study of turbine performance. Although this is a novel variation on the cruciform-type harvesters and seems very promising, the power output and efficiency is still far behind conventional wind turbines by several orders of magnitude.

Apart from these studies, the present work is not aware other attempts to generalise the cruciform oscillator system and further unlock the vortical structure and cylinder vibration-regulating potential of the strip plate, which might hold the key to further improving its power output and efficiency.

## 2.4 Chapter Summary

This chapter reviewed studies that contribute towards the advancement of vibration energy harvesting from alternating lift mechanisms, in particular the advancement of energy harvesting from cruciform systems. Figure 2.2 illustrates how the status quo of knowledge concerning energy harvesting from a cruciform is akin to the tip of the pyramid. Improving the performance of the cruciform energy harvester is heavily dependent on advances in other fields that are more fundamental, such as vortex-induced vibration and vortex shedding. Figure 2.2 also exemplifies the relative number of studies between the subjects, with the most number of studies over the years investigating the phenomenon of vortex shedding, especially Karman

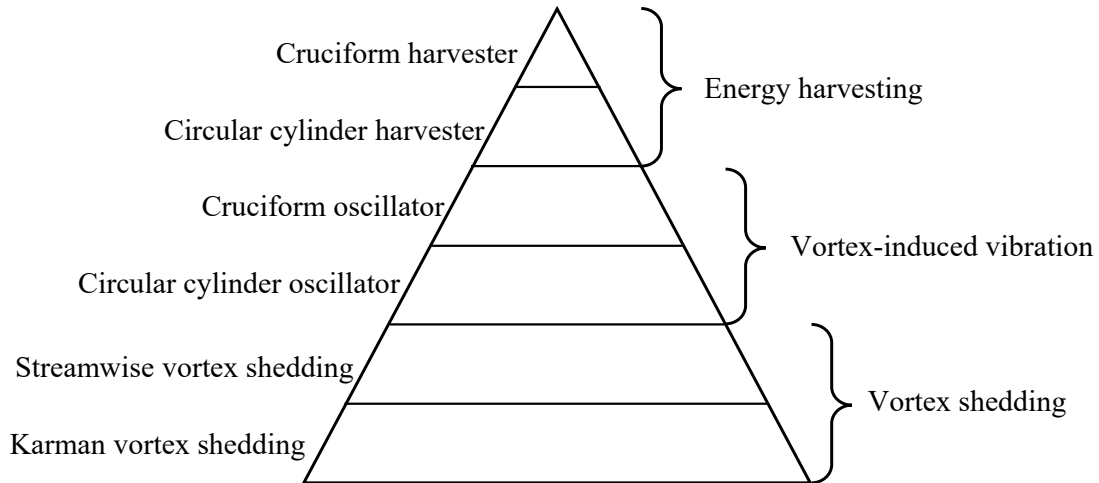


Figure 2.2: The pyramid of knowledge for the cruciform energy harvester.

vortex shedding, followed by studies on the vibration responses of circular cylinder and cruciform oscillators, and finally, studies on energy harvesting using cruciform oscillators and the circular cylinder oscillator which they are based upon.

The main takeaways from each literature reviewed in this chapter is summarised in Table 2.1. The state-of-the-art of Karman vortex shedding studies inform this thesis of the controllability of the vortex shedding through the modulation of the shear layer around the circular cylinder. Then, this work is informed that the three-dimensionality of Karman vortex brings about the formation of streamwise vortices of a scale smaller than the diameter of the circular cylinder, and whose dynamics are heavily influenced by the shedding of Karman vortices.

Table 2.1: Summary of findings in literature and key takeaways.

Literature	Type of study	Key takeaway
Asano <i>et al.</i> (2020)	Numerical	
Ledda <i>et al.</i> (2018), Durhasan <i>et al.</i> (2019), Geyer (2020), Kang <i>et al.</i> (2020)	Experimental	Karman vortex shedding can be controlled by modulating the shear layer of the circular cylinder. This is achieved through various methods, e.g., porous surface/outer layer and cavitation bubbles.
Gibeau <i>et al.</i> (2018), Gibeau and Ghaemi (2019), Rai (2018)	Experimental	Small scale streamwise vortices originate from the three-dimensionality of Karman vortices, and the temporal dynamics of these streamwise vortices are dictated by the shedding dynamics of the Karman vortices.
Lin <i>et al.</i> (2018), Zhang <i>et al.</i> (2019), Koide <i>et al.</i> (2017)	Experimental	Flow control due to placement of a downstream body is able to induce the shedding of large scale streamwise vortices, and the temporal dynamics of these streamwise vortices are independent of the shedding dynamics of coexisting Karman vortices.
Ding <i>et al.</i> (2017), Xu <i>et al.</i> (2017), Yuan <i>et al.</i> (2020)	Experimental	The amplitude/frequency response of a single cylinder oscillator unit can be modulated by tuning the mechanical parameters of the oscillator, e.g., adjusting the spacing between units, spring stiffness, system damping.
Deng <i>et al.</i> (2007)	Numerical	
Kato <i>et al.</i> (2007), Koide <i>et al.</i> (2013), Zhao and Lu (2018)	Experimental	The amplitude/frequency response of a pure cruciform oscillator is heavily influenced by the spacing between the upstream and downstream cylinders. Optimising this parameter allows for very large range of synchronisation and a well-behaved upper limit to the vibration amplitude.
Ma <i>et al.</i> (2018), Sun <i>et al.</i> (2019)	Experimental	In-tandem configuration of single cylinder harvester units are able to synergise and recover a large amount of power. The use of nonlinear springs can enhance this effect.
Hemsuwan <i>et al.</i> (2018a,d,b)	Numerical	Advances in cruciform energy harvesters are heavily focussed on recording the system responses due to cruciform parameter variation. Numerical studies are disrupting this trend.
Koide <i>et al.</i> (2009), Nguyen <i>et al.</i> (2012)	Experimental	

However, the inclusion of a downstream cylinder such as another circular cylinder or a strip plate induces the shedding of streamwise vortices of a scale similar to the diameter of the upstream cylinder. These large-scale streamwise vortices are less under the influence of the Karman vortices compared to the small-scale streamwise vortices discussed previously. This highlights the need to understand what actually takes place in the flow field as the large-scale streamwise vortices form, which is what the first objective of this thesis tries to achieve, particularly why they modulate the lift signals as observed in the literature.

Table 2.1 also highlights how the amplitude/frequency response of an oscillating system is influenced by varying mechanical parameters of the system and also geometry of the oscillator. This is especially pertinent in cruciform oscillators as the spacing between the upstream cylinder and downstream strip plate dictates the size of the synchronisation regime, which can be up to 15 times larger than the synchronisation regime of an elastically supported smooth circular cylinder. The fact that not much is known about why the geometrical configuration of the cruciform influences the system response of the oscillator is the motivation behind objective two of this thesis, where the present work tries to describe the lift signal as comprised from a finite number of constituents.

Finally, Table 2.1 summarises the studies that sits at the very top of the knowledge pyramid of Fig. 2.2, namely how the future of alternating lift energy harvesting lies in teasing out favourable flow structures from a system that is made of more than one cylinder. In particular, the VIV-based cruciform system whose studies up until the present is heavily reliant on probes and simple dye visualisations can benefit from advances in CFD and a relatively improved access to computing facilities, to investigate and evaluate novel geometrical configurations of the cruciform oscillator for energy harvesting. These studies serve as the starting point in fulfilling objective three of this thesis. The next chapter discussses the methods employed to achieve all three objectives.

## CHAPTER 3

### METHODOLOGY

This chapter details the methodology employed to fulfill the objectives outlined in Chapter 1. The methodologies can be loosely grouped into three categories, the first being the method used to set up the numerical model and their solution algorithm, second being the method used to set up and run experimental validations of a representative case from this work’s numerical investigation, and third, the introduction to a time series analysis method called the Hilbert-Huang transform (HHT) which is deployed to decompose both lift and cylinder displacement signals into physically meaningful components and compute the instantaneous phase angle and frequency.

#### 3.1 Problem geometry

This study bases itself on the work done by Maruai *et al.* (2017), Maruai *et al.* (2018), and Koide *et al.* (2013). In these works, the investigators conducted both experimental and computational investigations of passive control of FSI of cylinders using a strip plate located at the cylinder downstream. Here, the term “strip plate” is used as a shorthand for the long, rectangular plate used to control the vibration of the cylinder – since the plate resembles a strip due to its large aspect ratio. These studies demonstrated the feasibility of energy harvesting using the oscillator system described, in the Reynolds number range  $3.6 \times 10^3 < \text{Re} < 12.5 \times 10^3$ . Following this observation, the numerical investigations are performed within a similar Re range, albeit slightly widened, to check for variations in the cylinder response in as wide an Re range as possible, computational resources permitting.

The oscillator system in this work derives its geometry from the works of Nguyen *et al.* (2012), Koide *et al.* (2013), and Koide *et al.* (2017). The basic layout of the oscillator system is the pure cruciform: an arrangement where the circular cylinder and the strip plate located downstream have their axes perpendicular to each other. The gap between the cylinder and the strip plate,  $G$ , is fixed to 0.16. This value of  $G$  was

chosen because the cylinder response most suitable for energy harvesting is sustained over the largest range of reduced velocity  $U^*$  when  $G = 0.16$  (Koide *et al.*, 2013).

Figure 3.1b visualises the computational domain (Fig. 3.1a) from its side. These dimensions are based on analogous works such as (Maruai *et al.*, 2017) and (Maruai *et al.*, 2018) which had produced results that agree well with experiments of their own and with Kawabata *et al.* (2013). The streamwise coordinates of this domain extends from  $-10.5D$  to  $10.5D$ , and the lateral coordinates from  $-10.5D$  to  $10.5D$ . The coordinate origin  $(0, 0, 0)$ , is at the centre of the cylinder and the strip plate is  $D/3$  thick.

In Fig. 3.1c, the circular cylinder extends from  $z/D = 7.5$  to  $z/D = -7.5$ , giving the computational domain an overall spanwise length of  $15D$ . The computational domain of a similar study by Deng *et al.* (2007) has a length of  $12D$ , upon which the dimension of the domain is based upon. The extra  $1.5D$  of spanwise length on either side of the domain is allocated to ensure the full expression of the three-dimensionality of flow structures that appear during the course of the numerical study.

Then, variants of the pure cruciform configuration are constructed by rotating the strip plate from  $90^\circ$  to  $0^\circ$  in  $22.5^\circ$  increments. In total, five different cruciforms are constructed, as shown in Fig. 3.2. The dimensions of the computational domain remain fixed for all cruciforms, including the gap between the cylinder and the strip plate.

### 3.2 Numerical method

The numerical study utilises OpenFOAM, an open-source computational fluid dynamics (CFD) platform written in C++. OpenFOAM solves the 3D unsteady Reynolds averaged Navier-Stokes (3D URANS) equations that are the following.

$$\frac{\partial U_i}{\partial x_i} = 0, \quad (3.1)$$

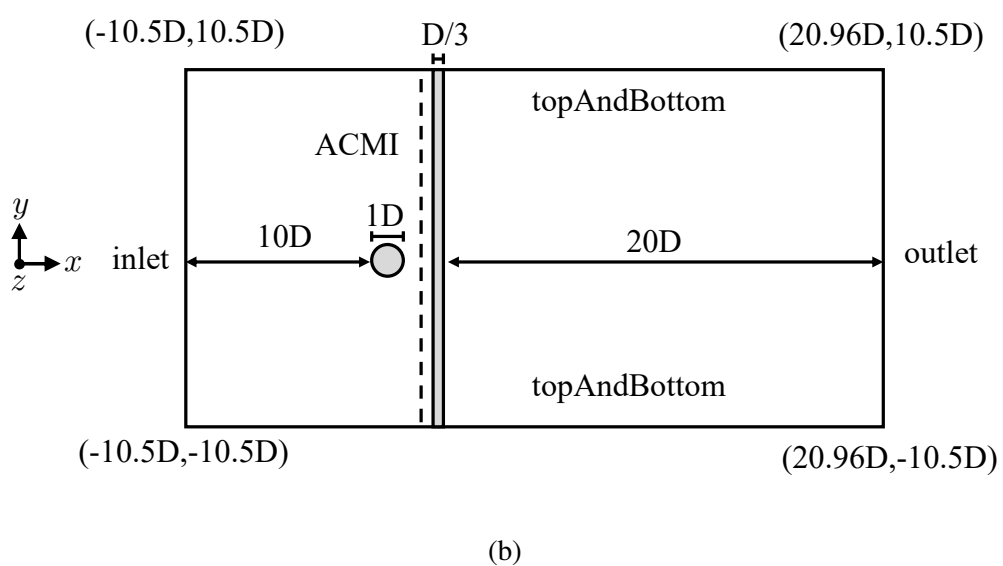
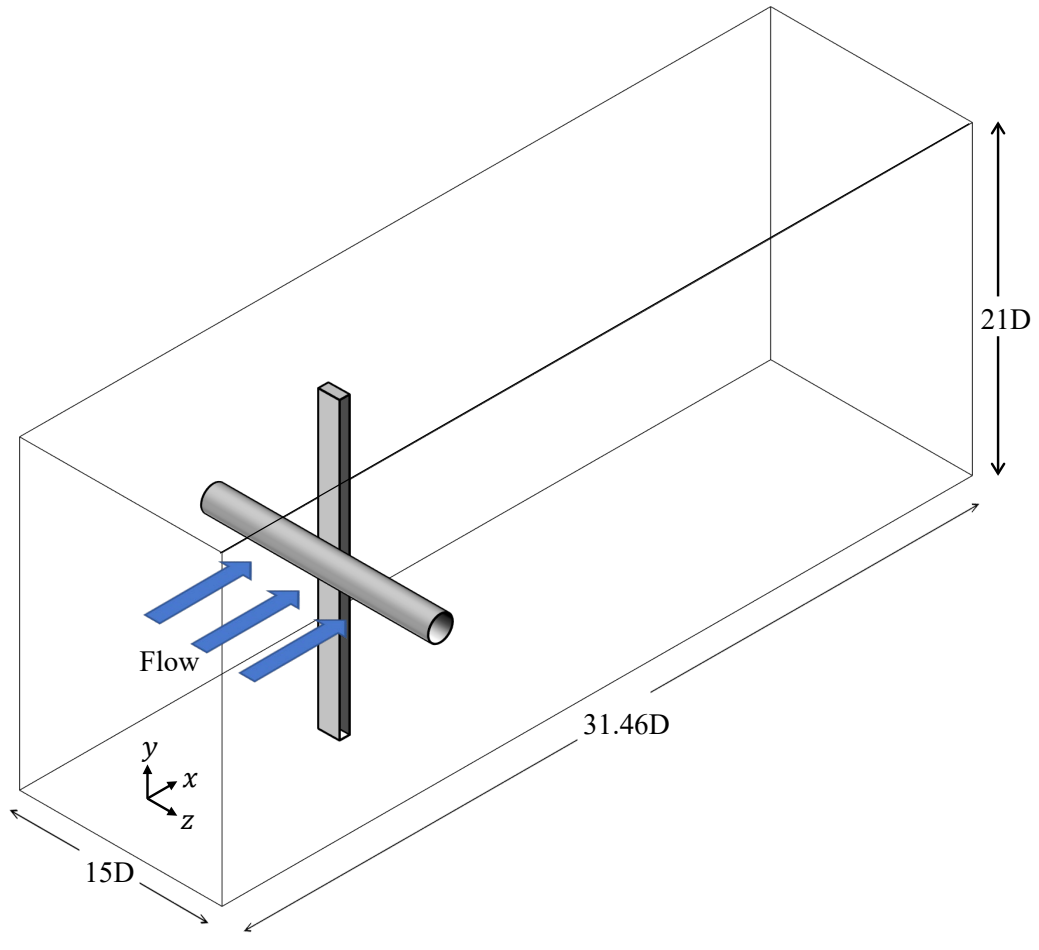


Figure 3.1: The computational domain: three-dimensional overview and cross-sections.

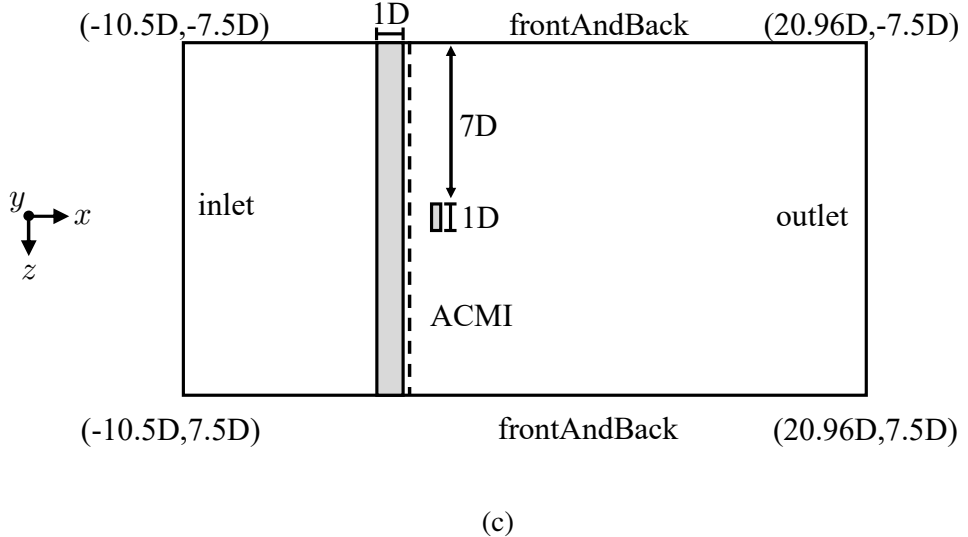


Figure 3.1: The computational domain: three-dimensional overview and cross-sections.

$$\frac{\partial U_i}{\partial t} + U_j \frac{\partial U_i}{\partial x_j} = -\frac{1}{p} \frac{\partial P}{\partial x_i} + \frac{\partial}{\partial x_j} \left( 2\nu S_{ij} - \overline{u'_j u'_i} \right). \quad (3.2)$$

The symbols  $U$ ,  $x$ ,  $t$ ,  $\rho$ ,  $P$ ,  $\nu$ ,  $S$ , and  $u'$  denote the mean component of velocity, spatial component, time, density, pressure, kinematic viscosity, mean strain rate and the fluctuating component of velocity, respectively. Equation 3.3 gives the mean strain rate  $S_{ij}$ .

$$S_{ij} = \frac{1}{2} \left( \frac{\partial U_i}{\partial x_j} + \frac{\partial U_j}{\partial x_i} \right). \quad (3.3)$$

The turbulence model employed to approximate the Reynolds stress tensor is the Spalart-Allmaras turbulence model. Previous numerical studies on energy harvesting from FIM of circular cylinders have shown reasonable agreement with experiments in the literature through the use of this turbulence model, and thus becomes the basis for the implementation of the same turbulence model in this study (Ding *et al.*, 2015a,b). The Boussinesq approximation relates the Reynolds stress tensor  $\tau_{ij} = \overline{u'_j u'_i}$  to the mean velocity gradient, exemplified by Eq. 3.4.



(a) Cruciform layout for  $90^\circ$

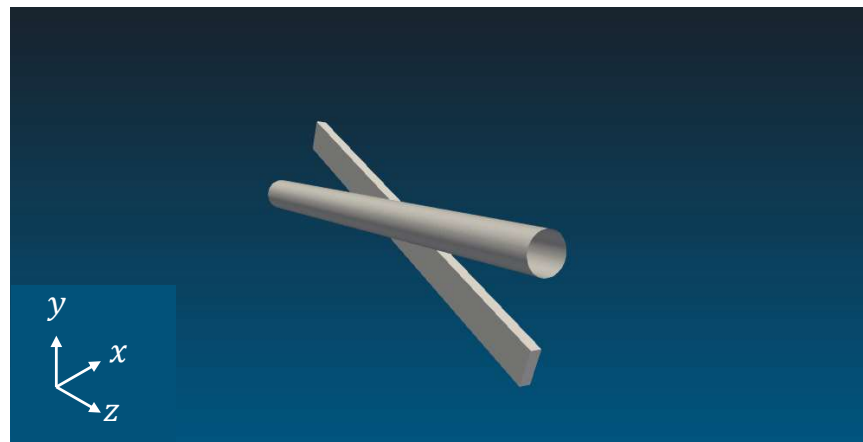


(b) Cruciform layout for  $67.5^\circ$

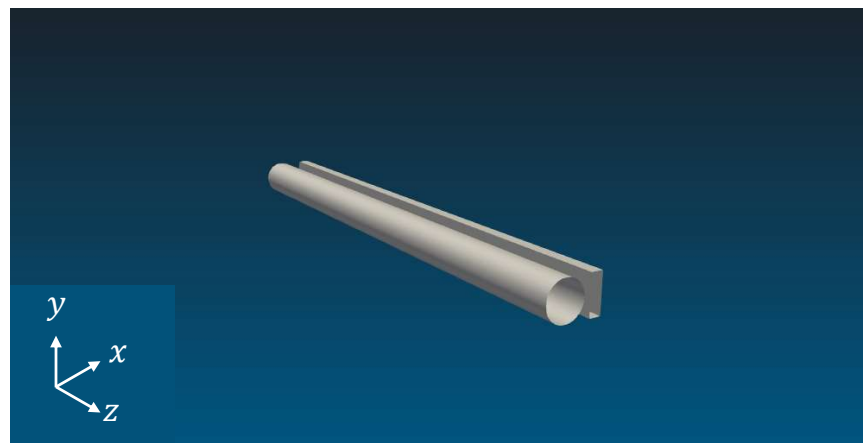


(c) Cruciform layout for  $45^\circ$

Figure 3.2: The cruciform variations studied in this thesis.



(d) Cruciform layout for  $22.5^\circ$



(e) Cruciform layout for  $0^\circ$

Figure 3.2: The cruciform variations studied in this thesis.

$$\tau_{ij} = 2\nu_T S_{ij}, \quad (3.4)$$

where  $\nu_T$  represents the kinetic eddy viscosity. This kinetic eddy viscosity is ultimately expressed as a function whose arguments consist of the molecular viscosity  $\nu$ , and an intermediate variable  $\tilde{\nu}$  that is the solution of Eq. 3.5. Equation 3.5 incorporates empirically obtained constants to provide closure to the equations governing this numerical investigation. The empirical constants that make up Eq. 3.5 are listed in Table 3.1.

$$\frac{\partial \tilde{\nu}}{\partial t} + U_j \frac{\partial \tilde{\nu}}{\partial x_j} = c_{b1} \tilde{S} \tilde{\nu} - c_{w1} f_w \left( \frac{\tilde{\nu}}{D} \right)^2 + \frac{1}{\sigma} \left\{ \frac{\partial}{\partial x_j} \left[ (\nu + \tilde{\nu}) \frac{\partial \tilde{\nu}}{\partial x_j} \right] c_{b2} \frac{\partial \tilde{\nu}}{\partial x_i} \frac{\partial \tilde{\nu}}{\partial x_i} \right\} \quad (3.5)$$

Table 3.1: Empirical constants used in the Spalart-Allmaras turbulence model.

Empirical constants	Value
$c_{b1}$	0.01
$c_{b2}$	0.09
$c_{v1}$	0.01
$\kappa$	0.1
$\sigma$	0.162
$c_{\omega3}$	0.178

The interested reader is referred to the original paper by Spalart and Allmaras (1992) and more recent applications of the turbulence model in Ding *et al.* (2019) and Sun *et al.* (2019). With the turbulence model properly defined, one is finally able to solve Eqs. 3.1 and 3.2 using the SIMPLE-stabilised PISO algorithm native to OpenFOAM, known as the PIMPLE algorithm.

Table 3.2 gives a summary of all conditions computed in the numerical study of this thesis. As this study seeks to understand the system response of a generalised form of cruciform oscillator, the angle between the cylinder and the strip plate is varied from

the pure cruciform case ( $90^\circ$ ) down to  $0^\circ$ , in  $22.5^\circ$  increments. To vary the angle of the cruciform, the cylinder is kept in its original location and maintains its orientation parallel to the  $Z = 0$  axis, while the strip plate is rotated in the counterclockwise direction when viewed from upstream. These cruciforms are studied within thirteen reduced velocities between  $2.3 \leq U^* \leq 29.5$ , corresponding to  $U = 0.1, 0.2, \dots, 1.3$  m/s in freestream velocity.

Table 3.2: The list of conditions investigated in this study, i.e. the research matrix

Cruciform angle	Reduced velocities	Number of cells
Pure cruciform ( $90^\circ$ )	$2.3 \leq U^* \leq 29.5$	697608
Steep-angled cruciform A ( $67.5^\circ$ )	$2.3 \leq U^* \leq 29.5$	704474
Steep-angled cruciform B ( $45^\circ$ )	$2.3 \leq U^* \leq 29.5$	769084
Shallow-angled cruciform A ( $22.5^\circ$ )	$2.3 \leq U^* \leq 29.5$	733800
Shallow-angled cruciform B ( $0^\circ$ )	$2.3 \leq U^* \leq 29.5$	709984

The number of cells used in the spatial discretisation of the computational domains are determined from the grid independency study on the pure cruciform whose results are detailed in Chapter 4. Difference in the geometry of the cruciform model implemented in each study case results in a slightly different number of cells for each cruciform. However, all of them are ensured to exceed the minimum of 697608 cells, where the numerical results only differ only slightly with the expected value in the limit where the cell size approaches zero, hence number of cells approaching infinity. The  $y^+$  values for each simulation is capped at  $y^+ < 15$ , following Wang *et al.* (2019).

An HP Z420 workstation was used to perform the computations, and the specifications of the workstation are listed in Table 3.3. Since parallelisation is built into OpenFOAM, computationally exhaustive simulations can benefit a lot from being run on such a workstation with minimal effort from the end user. One can just specify the number of subdomains desired in each of the  $x$ ,  $y$ , and  $z$ -directions, and then allocate one for each processor available in the workstation.

Table 3.3: The specifications of the HP Z420 workstation

Feature	Description
Memory	38 GB
Processor	Intel Xeon(R) CPU E5-16200 at 3.60 GHz
Number of processors	16
Graphics	Gallium 0.4 on NVE7
Disk	980.2 GB

However, due to the fact that the type of phenomena simulated in this study is three-dimensional, transient, turbulent and involves fluid-structure interactions, the simulations take a long time, even with the computational power listed in Table 3.3. To give the reader a perspective on this time length, consider the following example from one computational case. To simulate 20 s of flow time for the pure cruciform at  $U^* = 25.0$  ( $U = 1.0$  m/s) using all 16 processors, the workstation took 1 688 688 s or approximately 19.5 days. This will only increase at higher freestream velocities as smaller time steps are required to maintain a Courant-Friedrichs-Lowy (CFL) number less than 1.

### 3.3 Dynamic mesh motion

Cylinder motion in the computational domain due to FIV introduces distortion to the mesh immediately surrounding the cylinder. The simplest way to keep the mesh distortion in check, thus keeping mesh quality within an acceptable level, is by diffusing the amount of warping to the surrounding space. In practice, the surrounding space is the rest of the mesh nodes, and Eq. 3.6 governs the diffusion.

$$\nabla \cdot (\gamma \nabla u) = 0. \quad (3.6)$$

In Eq. 3.6,  $u$  and  $\gamma$  represents the mesh deformation velocity and displacement diffusion, respectively. In this work, the displacement is diffused according to the inverse quadratic rule  $\gamma = 1/l^2$ . Here,  $l$  denotes the distance from the cell centre to the nearest cylinder edge. Then, Eq. 3.6 is solved using the GAMG algorithm and the Gauss-Seidel smoother. Solution of Eq. 3.6 returns an updated value of  $u$ , and this

updated value of  $u$  is used to update the position of the mesh nodes according to Eq. 3.7. The PIMPLE solver resumes the solution of the 3D URANS equations after the mesh node positions are updated.

$$x_{\text{new}} = x_{\text{old}} + u\Delta t \quad (3.7)$$

For most numerical studies of FSI, the mesh warp diffusion method governed by Eq. 3.6 serves as an adequate workaround to conserve mesh quality. However, this requires ample number of ambient mesh nodes acting as the receiving end of the diffusion algorithm. In this case, the small gap between the cylinder and strip plate ( $G = 0.16$ ) pose a serious limitation to the ability to diffuse the amount of warp introduced by the displacement of the cylinder, since a small space means that one can only allocate a proportionate number of mesh nodes in said gap. Sole reliance on the warp diffusion algorithm will hamper the effort to preserve mesh quality as a high concentration of warp remains within the gap. To overcome this problem, the arbitrarily coupled mesh interface (ACMI) is implemented halfway through the gap (see Fig. 3.1). This technique allows adjacent cells to slide over each other precisely at the  $x = 0.13$  plane, ridding this work of the requirement for mesh warp diffusion. In the literature, ACMI is also known as the generalised grid interface, or GGI (Zhang *et al.*, 2018a; Sun *et al.*, 2019).

### 3.4 Open flow channel experiment

As part of the validation process for the numerical setup, a closed loop open flow channel was constructed, with a test chapter 100 mm wide, 200 mm high and 1500 mm long. The design of this open flow channel is heavily inspired by the water tunnel of Nguyen *et al.* (2012) and Koide *et al.* (2013). Considering the application of this research in the far future is in open flows such as natural drainage systems or the ocean - and not within pipes - prompts this study to make this distinction.

The open flow channel is benchmarked by setting up a pure cruciform oscillator ( $90^\circ$ ) experiment, whose data from similar studies are readily available in published works. Following this, the rig is dimensioned to follow the parameters used in Koide

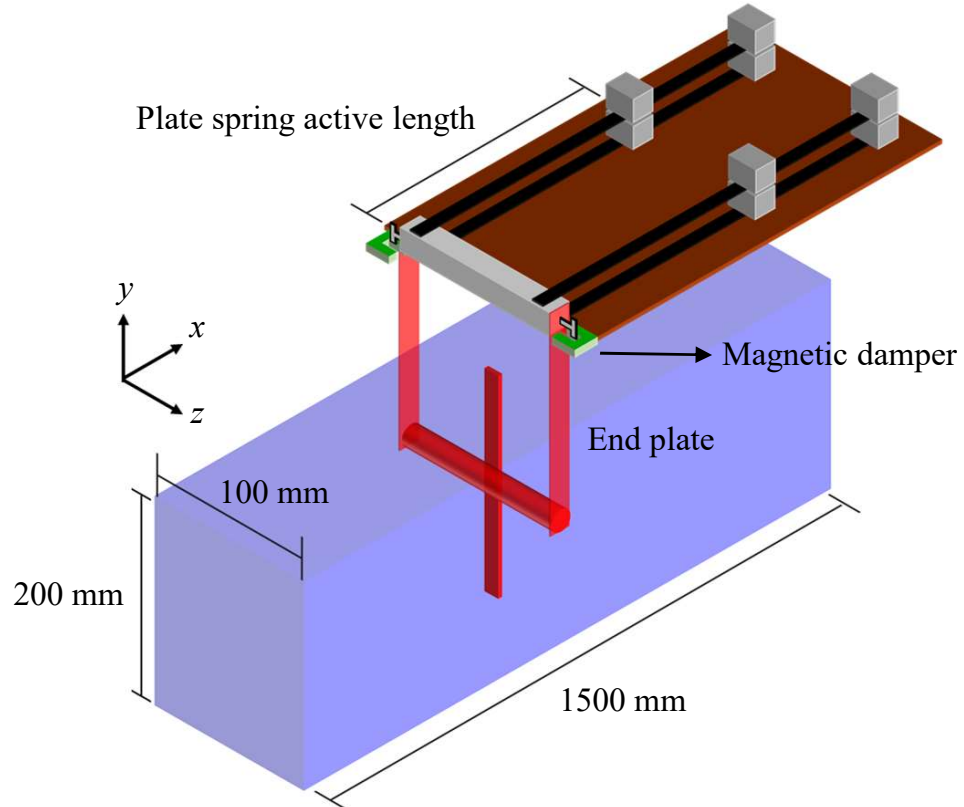
*et al.* (2013). A summary of the parameters and those used in Koide *et al.* (2013) are provided in Table 3.4. The parameters governing the amplitude/frequency response of the oscillator is tuned using simple length-based mechanism as follows (see Fig. 3.3a). To tune the spring coefficient  $k$ , one simply adjust the active length of the twin spring plate. In practice, the calibration curve of the twin spring plate is obtained by performing a weight - displacement measurement (Sun *et al.*, 2016) at several active lengths of the plate. Once the spring coefficient versus spring plate active length calibration curve is obtained, one can just adjust the length of the spring plate to achieve the desired value of  $k$ .

Tuning the total damping of the system and consequently the multiple expressions of damping such as the logarithmic damping  $\delta$ , Scruton number  $Sc$ , or the damping coefficient is done by attaching, as shown in Fig. 3.3a, a T-shaped plate made from aluminium into a claw-shaped casing that houses neodymium magnets at its ends. As presented in Fig. 3.3b, the method this work uses to control the strength of the magnetic field exposed to the T-shaped plate is by fixing the insertion depth of the T-shaped plate into the casing. The magnetic field serves to dissipate the kinetic energy of the T-shaped plate that moves with the cylinder during FIM, providing system damping.

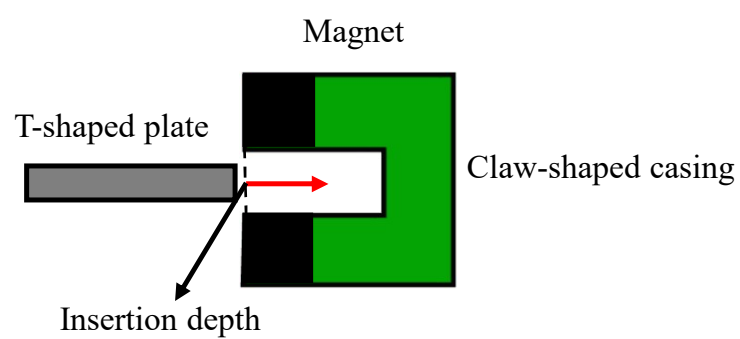
Table 3.4: Summary of experimental parameters in contrast to those used in the experimental work of Koide *et al.* (2013).

	Current study	Koide <i>et al.</i> (2013)
Cylinder diameter, $D$ (m)	0.01	0.01
Cylinder length, $l_{\text{cylinder}}$ (m)	0.09	0.098
Strip-plate width (m)	0.01	0.01
Strip-plate length (m)	0.1	0.1
Effective mass, $m_{\text{eff.}}$ (kg)	0.162	0.174
Logarithmic damping, $\delta$	0.178	0.24
Scruton number, $Sc$	9.94	7.74
System natural frequency, $f_n$ (Hz)	4.42	4.4 to 4.79

A voltage controller regulates the power driving the 3.728 kW (5 hp) centrifugal pump. To set the freestream velocity in the open flow channel, an acoustic Doppler velocimeter (ADV) sampler is placed in an empty test chamber, filled with plain



(a)



(b)

Figure 3.3: Sketch of the experimental system used in this study.

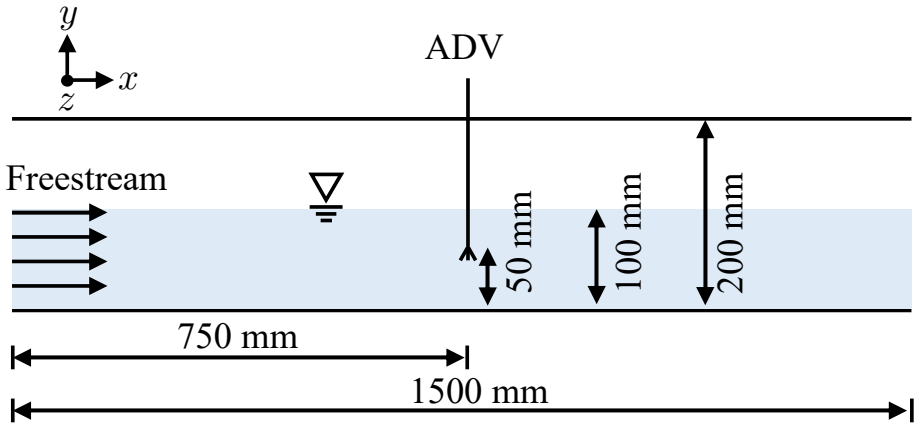


Figure 3.4: Side view schematic of the openflow channel.

tap water to a height of 100 mm, on the centreline of the channel, as pictured in Fig. 3.4. The height of 100 mm is also the water level the experiments are in. The water level at this height of 100 mm during all data collections to achieve a flow ambience analogous to the benchmark study of Koide *et al.* (2013), facilitating comparison between the two. Then, the velocity of the flow at different input voltages are sampled by the voltage controller, the final product being an input voltage  $V_{\text{in}}$  (V) versus centreline velocity  $U_{\text{cent}}$ . calibration curve. This calibration curve allows the setting of the freestream velocity of the open flow channel by specifying the input voltage to the pump. The finished product gave an operability range between 0.3 m/s and 1.1 m/s, which translates to  $6.8 \leq U^* \leq 25.0$  for an circular cylinder of diameter 10 mm. The turbulence level ranges between 5% to 8% when the freestream velocity  $U_{\infty} \geq 0.8$  m/s.

The cylinder displacement  $y$  is measured as a function of time by placing a visual marker on the support plate of the cylinder (see Fig. 3.3a) and capturing the motion of the marker using a video camera positioned perpendicular to the support plate. The motion of the marker is then analysed using *Tracker*: a motion analysis tool built on the Open Source Physics Java framework (for recent implementation examples, see Wen *et al.* (2020) or Krishnendu and Ramakrishnan (2020)).

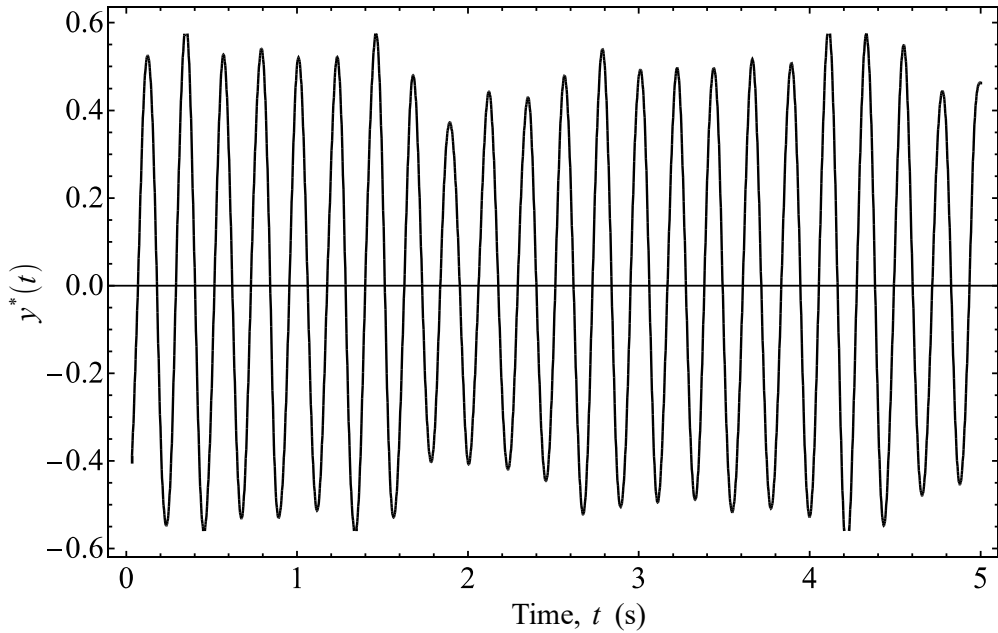


Figure 3.5: Experimentally measured  $y^*(t)$ , which is the normalised cylinder displacement time series.

For the benchmarking, the reduced velocity  $U^* = 22.7$  is chosen as the cylinder at that  $U^*$  produces a large and stable displacement that simplifies on the part of this work, the measurement and comparison process between the experimental system and Koide *et al.* (2013). A sample of the normalised displacement –  $y^* = y/D$  – measured as a function of time is illustrated in Fig. 3.5. This time series allows this work to also compute the normalised cylinder vibration frequency,  $f^* = f_{\text{cyl}}/f_n$  ( $f_{\text{cyl}}$  being the vibration frequency of the cylinder). The  $y^*$  data presented in Fig. 3.5 returns  $y^* = 0.33 \pm 0.03$  and  $f^* = 1.03 \pm 0.04$ , after computing the uncertainty from multiple experimental runs. In their work, Koide *et al.* (2013) obtained  $y^* = 0.32$  and  $f^* = 1.09$  at a similar  $U^*$  - values that are well within the measurement uncertainty of the experiment. This provides a basis for the reliance on results obtained from the experimental system later in the study.

### 3.5 Ensemble empirical mode decomposition and Hilbert transform

To obtain a clearer picture of the temporal characteristics of the lift and cylinder displacement signals, this study decided to employ the ensemble empirical mode decomposition (EEMD) method (Huang *et al.*, 1998; Wu and Huang, 2008) on the

signals, and compute their instantaneous phase lag, frequency and amplitude using the Hilbert transform.

The Hilbert transform (HT) has been used in the past to study the instantaneous phase and frequencies of KVIV (Khalak and Williamson, 1999). However, the signal must be monochromatic if one is to obtain a physically meaningful result after applying HT. EEMD is a way to pre-process the signal and get components that (1) have zero mean, and (2) have an equal number of extrema and zero crossings, or they differ only by one. Functions that fulfil these criteria are called intrinsic mode functions (IMF), and they guarantee a physically meaningful result to HT (Gumelar *et al.*, 2019; Zhou *et al.*, 2019). Unlike Fourier transform, which is an analytical method of signal decomposition based on circular functions in the complex plane, EEMD is algorithmic, and the processes undertaken can be summarised as follows.

Produce 150 white noise signals of length equal to the original signal and amplitude equal to 0.2 of the standard deviation of the original signal. Then, add to the set of white noises the original signal – creating 150 variations of the original signal. Following that, the empirical mode decomposition (EMD) algorithm is applied on each of the 150 signals. The EMD algorithm is summarised below.

1. Construct the envelope of the signal by connecting all maxima/minima with cubic splines.
2. Find the local mean of the envelope for the span of the data.
3. Find the difference between the local mean and the original data.
4. Repeat steps 1 and 2 on the difference in 3 for ten times (Wu and Huang, 2008).

The steps above produce a set of intrinsic mode functions or IMFs for each of the 150 variations of the original signal. Then, the first IMF component is averaged from each of the decomposed original signal variations, to obtain the first EEMD IMF,  $C_1$ , of the original signal. The same is done for the second, third, until the  $i^{\text{th}}$  component for each of the 150 original signal variations, thus obtaining  $C_2, C_3, \dots, C_i$ .

To compute the phase lag between the characteristic IMFs of the lift coefficient and normalised cylinder displacement, the IMF components with the highest correlation to the  $y^*$  signal at that particular  $U^*$  is selected, to represent the signals, denoted as  $C_{y^*,y^*}$  for the characteristic normalised cylinder displacement, and  $C_{Cl,y^*}$  as the characteristic lift coefficient signal. The phase lag, instantaneous frequency and instantaneous amplitude of the signal is subsequently computed by constructing an analytical signal  $z(t)$  from  $C_1, C_2, \dots, C_i$  by computing the Hilbert transform of the IMF,  $H_i$ ,

$$H_i(t) = \frac{1}{\pi} \text{PV} \int \frac{C_i(\tau)}{t - \tau} d\tau, \quad (3.8)$$

where PV denotes the Cauchy principal value, and then constructing the analytical signal as follows.

$$z(t) = C_i(t) + iH_i(t) = a(t)e^{i\theta(t)}, \quad (3.9)$$

Note that  $i$  in Eq. 3.9 is the complex number. Also,  $a(t)$  and  $\theta(t)$  are the instantaneous amplitude and phase - both a function of time, and they are computed through the following equations.

$$a(t) = \left( x^2 + y^2 \right)^{1/2}, \quad (3.10)$$

and

$$\theta(t) = \arctan \frac{C_i}{H_i}. \quad (3.11)$$

Computing the instantaneous frequency is therefore an exercise in differentiation, i.e.,

$$\omega(t) = -\frac{d\theta}{dt}, \quad (3.12)$$

where  $\omega(t)$  represents the instantaneous frequency of component  $C_i$  of the original signal.

### 3.6 Phase lag between Cl and normalised cylinder displacement

In this study, the phase lag  $\theta_{y-\text{Cl}}$  is computed by taking the Hilbert transform of both  $y^*$  and Cl signals, as Khalak and Williamson (1999) did in their VIV study of isolated circular cylinders, finding the difference between them, and finally averaging the values over a selected period  $T$ . This is captured by Eq. 3.13. The reason this quantity is computed is because there is a need to assign a representative value to the phase lag at each  $U^*$ , and the ensemble average is a deemed a reasonable statistical quantity that captures the essence of the temporal evolution of phase lag.

$$\theta_{y-\text{Cl}} = \frac{1}{T} \int_0^T [\theta_{\text{Cl}}(t) - \theta_y(t)] dt. \quad (3.13)$$

Out of  $C_i$  IMFs for each of  $y^*$  and Cl, the ones for computation of instantaneous phase are selected according to the following rule. First, the IMF component of  $y_{\text{RMS}}^*$  with the largest root-mean-square amplitude is selected to represent the original  $y^*$  signal. Then, the component of Cl with the highest correlation to the IMF component of  $y^*$  is chosen, to represent the Cl signal. The degree of correlation is determined by computing the cross-correlation between the two.

### 3.7 Estimation of Power

The mathematical model for harnessable power estimation in this study follows that which had been derived in Raghavan *et al.* (2007). In these works, the authors mentioned that work done by the oscillating cylinder  $W_{\text{cyl}}$  during one cycle of oscillation  $T_{\text{osc.}}$  is as follows.

$$W_{\text{cyl.}} = \int_0^{T_{\text{osc.}}} (F_L \cdot \dot{y}) dt \quad (3.14)$$

where both the lift  $F_L$  and cylinder velocity  $\dot{y}$  are both functions of time. Through several manipulations and simplifying assumptions (Sun *et al.*, 2016), the power captured by the system can be written, using select parameters, as the fluid power

$$P_{\text{Fluid,RMS}} = \frac{1}{2} \rho \pi C_{\text{Cl,RMS}} U^2 f_{\text{cyl.}} y_{\text{RMS}}^* D L \sin(\phi), \quad (3.15)$$

or the mechanical power

$$P_{\text{Mech.,RMS}} = 8\pi^3 m_{\text{eff.}} \zeta_{\text{tot.}} (y_{\text{RMS}}^* f_{\text{cyl.}})^2 f_n. \quad (3.16)$$

Here,  $P_{\text{Fluid,RMS}}$ ,  $P_{\text{Mech.,RMS}}$ ,  $L$ ,  $C_{\text{Cl,RMS}}$ ,  $\zeta_{\text{tot.}}$  and  $m_{\text{eff.}}$  are the root-mean-square of fluid power, root-mean-square of mechanical power, length of the circular cylinder, characteristic root-mean-square of lift amplitude, total damping coefficient, and the system effective mass respectively. The quantity  $C_{\text{Cl},y^*}$  is used to represent  $C_{\text{Cl,RMS}}$  in Eq. 3.15. The root-mean-square, i.e. root-mean-square (parameters with subscript RMS) quantities in Eq. 3.14 instead of the maximum values like the original authors because that may lead to a misunderstanding that the maximum value is sustained throughout the observation window. This obviously is not always the case in this study, especially once the system transits into the SVIV regime. Recall that the time series analysis of  $y^*(t)$  and  $\text{Cl}(t)$  in Chapter 4.2 revealed that there is a degree of intermittency in both signals that cannot be overlooked at certain ranges of  $U^*$ . Using the root-mean-square value allows this work to partially take this into account in the estimation of harnessable power.

### 3.8 Grid Independency Study

This section details the validation method used to check the grid independency of the numerical solutions. This validation can be divided into two main steps, the first

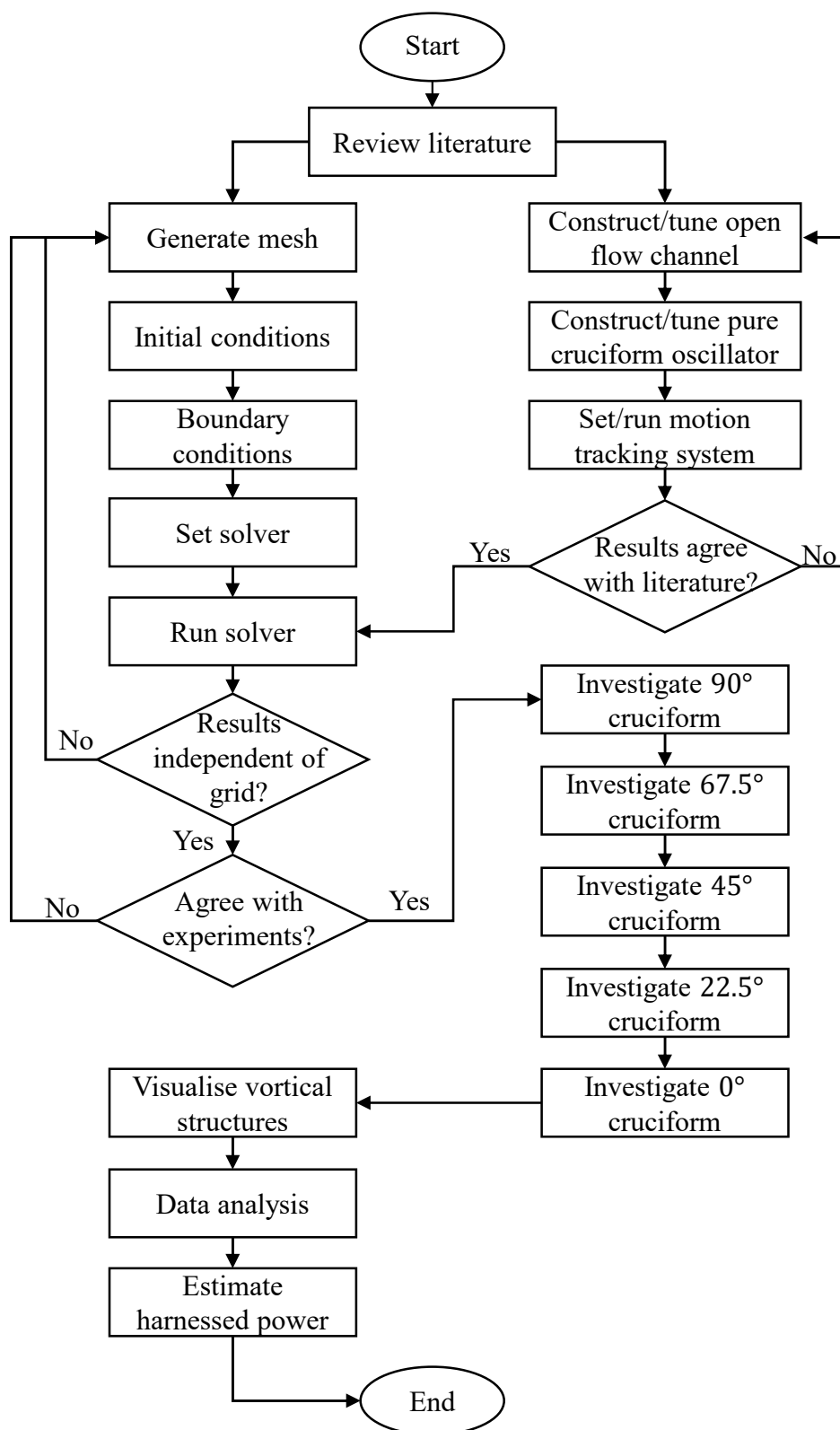


Figure 3.6: The flowchart encapsulating the sum total of research activities in this study.

being computing the grid convergence index and the second, extrapolating the value of the numerical solution to estimate its limit as mesh size approaches zero.

This whole exercise is intended to show that the final form used in the main body of the numerical study is quantifiably independent from the spatial discretisation that this work has settled upon.

### 3.8.1 The grid convergence index (GCI) and Richardson extrapolation

In this work, the grid independency of the solution is established using the Richardson extrapolation and the grid convergence index (GCI) (Richardson and Gaunt, 1927; Stern *et al.*, 2001). The Richardson extrapolation and GCI provides this study with a procedure to quantitatively measure on the degree of convergence for the quantities of interest in a numerical study. This method also forces the researcher to pay attention to the trend of convergence of the quantities of interest, requiring a monotonic convergence before proceeding to data collection (Stern *et al.*, 2001; Mat Ali *et al.*, 2011; Maruai *et al.*, 2018).

Let  $f_1, f_2, f_3, \dots, f_k$  be the quantity of interest obtained from several grid resolutions. A larger subscript is assigned for a coarser grid, thus ascribing  $f_1$  to the finest and  $f_k$  to the coarsest grid. Let the difference between successive solutions be  $\epsilon_{2,1}, \epsilon_{3,2}, \epsilon_{4,3}, \dots, \epsilon_{n,n-1}$ , where  $\epsilon_{2,1} = f_2 - f_1$ ,  $\epsilon_{3,2} = f_3 - f_2$  and so on. Then, the GCI is defined as

$$\text{GCI}_{i+1,i} = F_s \frac{|\epsilon_{i+1,i}|}{f_i(r^p - 1)} \times 100\%, \quad (3.17)$$

where  $F_s$ ,  $f_i$  and  $r^p$  denotes the safety factor ( $= 1.25$ ), quantity of interest and the refinement ratio,  $r$ , between successive grids raised to the order of accuracy of the series of solution,  $p$ . The reader is referred to Stern *et al.* (2001); Langley Research Centre (2018) for a more detailed discussion on  $r^p$ .

The limit of the solution can be estimated by decreasing the spacing between grid points, allowing it to approach zero via the  $p^{\text{th}}$  method. In essence, the generalised Richardson extrapolation of the quantity of interest is computed as follows.

$$f_{\text{RE}} = f_1 + \frac{f_1 - f_2}{r^p - 1}, \quad (3.18)$$

where  $f_{\text{RE}}$  is the Richardson extrapolation of the quantity of interest. Using  $f_{\text{RE}}$  to estimate the limit of the monotonically convergent series of  $f_i$ , one can determine the percentage difference of the solution on the finest grid from this limit as

$$E_i = \frac{f_i - f_{\text{RE}}}{f_{\text{RE}}} \times 100\%. \quad (3.19)$$

### 3.9 Chapter Summary

This chapter covers the methods employed to attain the objectives outlined in Chapter 1. A cruciform consisting of an upstream circular cylinder and a strip plate placed  $G = 0.16D$  downstream is the problem geometry studied in this thesis and the primary mode of investigation is numerical, i.e., using CFD. The numerical model is solved using OpenFOAM, which is used to discretise the continuity and the RANS form of the momentum transport equation. The turbulence model employed is the one-equation Spalart-Allmaras model, which has been shown time and again in the literature to capture the essence of the flow in VIV situations.

Advances in the OpenFOAM code allows for the implementation of dynamic mesh methods to simulate cylinder motion during VIV. Virtual spring and dampers are included in the computational loop and are used in the computation of the cylinder motion via the Euler's method. The arbitrarily coupled mesh interface (ACMI) allows for cruciform layouts with a tight gap, i.e.  $G < 1$ . During the analysis of the lift and cylinder displacement signals, the Hilbert-Huang transform is implemented to decompose the signals into physically meaningful components and allow the computation of instantaneous phase angle and frequency.

The experimental method used to validate the CFD setup consists of an elastically supported cruciform oscillator in an open flow channel. The side plates supporting the two ends of the upstream circular cylinder are marked with a visual marker, thus enabling their motion to be tracked and the displacement time series obtained using a motion capture camera and a motion tracking software.

Finally, §3.8 gives an overview on the parameters and methods of computing the parameters to ascertain the independency of the numerical solutions against spatial discretisation. The parameters are then plotted in the next chapter to demonstrate the monotonic convergence of the quantities of interest, i.e.,  $y^*$ ,  $f^*$ , and Cl.

To summarise the research methodology employed during the course of this study, a flowchart describing the activities and their ordering is presented in Fig. 3.6. In the next chapter, this work discusses the results of the grid independency study and then details the results of this research.

## CHAPTER 4

### RESULTS AND DISCUSSION

#### 4.1 The GCI Study

Table 4.1 summarises the result of the grid independency study for the SVIV reduced velocity of  $U^* = 22.7$ . The flow global quantities checked for convergence are the vibration amplitude, vibration frequency and lift coefficient of the cylinder. To simplify the grid independency study, the pure cruciform configuration (the 90° cruciform) is chosen as the representative, and collected data at  $U^* = 22.7$  on three sets of grid numbered 1 for the finest, 2 for the medium and 3 for the coarsest, shown in Fig. 4.1. With  $v_i$  as the volume of the  $i^{\text{th}}$  cell in the grid, and  $N$  the total number of cells in the domain, the average cell size becomes

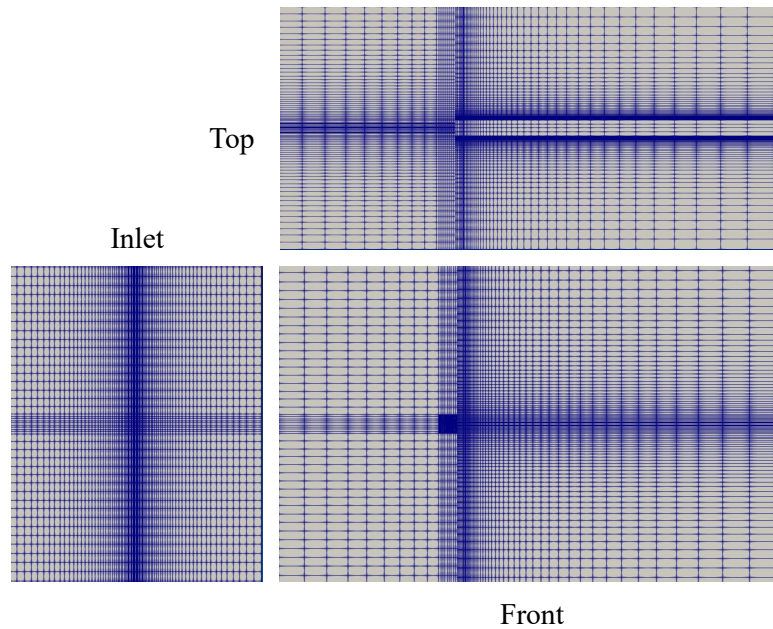
$$h = \frac{1}{N} \left[ \sum_{i=1}^N v_i \right]^{1/3}, \quad (4.1)$$

and the normalised average cell size is hence

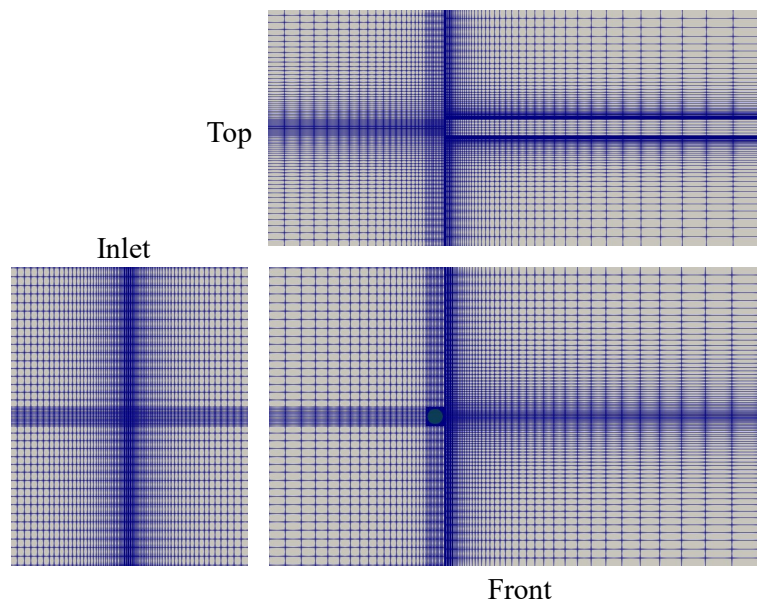
$$h/D = \frac{1}{ND} \left[ \sum_{i=1}^N v_i \right]^{1/3}. \quad (4.2)$$

Both  $y_{\text{RMS}}^*$  and  $\text{Cl}_{\text{RMS}}$  (see Figs. 4.2 and 4.4) have initial values smaller than their Richardson extrapolations,  $f_{\text{RE}}$ , before approaching  $f_{\text{RE}}$ , with decreasing  $h$ . The vibration frequency, on the other hand, starts at a value larger than its  $f_{\text{RE}}$  before approaching  $f_{\text{RE}}$ , as one can see in Fig. 4.3.

The most significant drop in GCI is experienced by  $\text{Cl}_{\text{RMS}}$ , with increasing refinement of the grid. Refinement from the coarse to medium grid returns a GCI

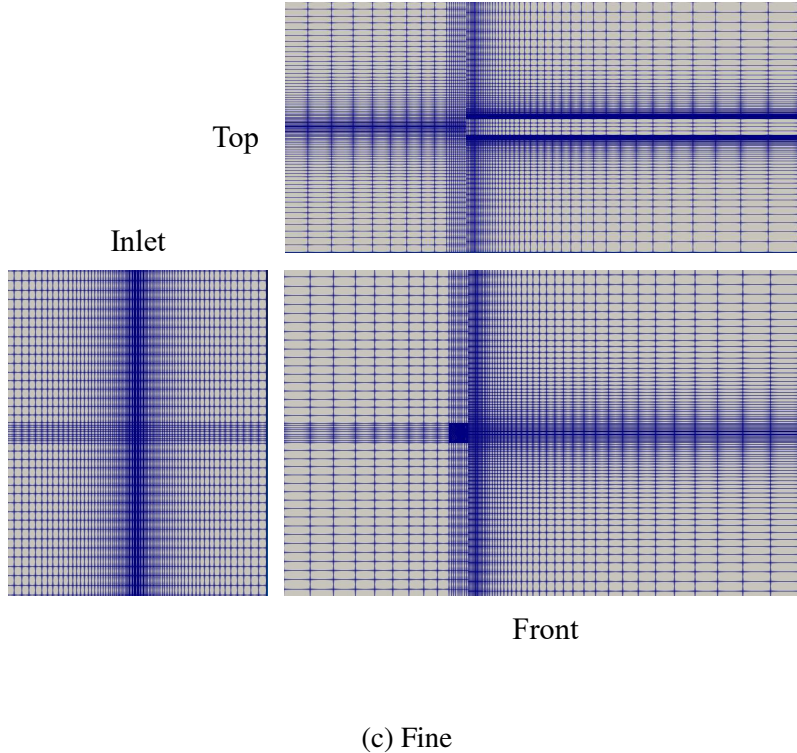


(a) Coarse



(b) Medium

Figure 4.1: The course, medium and fine mesh used in the grid independency study.



(c) Fine

Figure 4.1: The course, medium and fine mesh used in the grid independency study.

of 30.92%, using a refinement ratio of 1.376. The refinement ratio is computed by dividing the number of cells in one grid with the grid one stage refined. Generalising this to  $i$  number of grids returns

$$r_{i+1,i} = \frac{S_{\text{grid},i+1}}{S_{\text{grid},i}}, \quad (4.3)$$

where  $S_{\text{grid},i}$  denotes the total number of cells in the  $i^{\text{th}}$  grid. The GCI of  $\text{Cl}_{\text{RMS}}$  decreases further to 1.63% with further refinement of the grid. On the other hand, GCI for  $f^*$ , shrinks to about one-sixth of its former value.

Inspecting Figs. 4.2, 4.3 and 4.4, the quantities of interest is found to be very close to its Richardson extrapolation at the fine grid (grid 1) for all  $\text{Cl}_{\text{RMS}}$ ,  $y_{\text{RMS}}^*$  and  $f^*$ . This seems to be an indication of sufficient spatial discretisation. At this point, the trade-off between a solution even closer to the Richardson extrapolation and the increased computational effort is no longer appealing, compounded by the observation

Table 4.1: Summary of grid independency study.

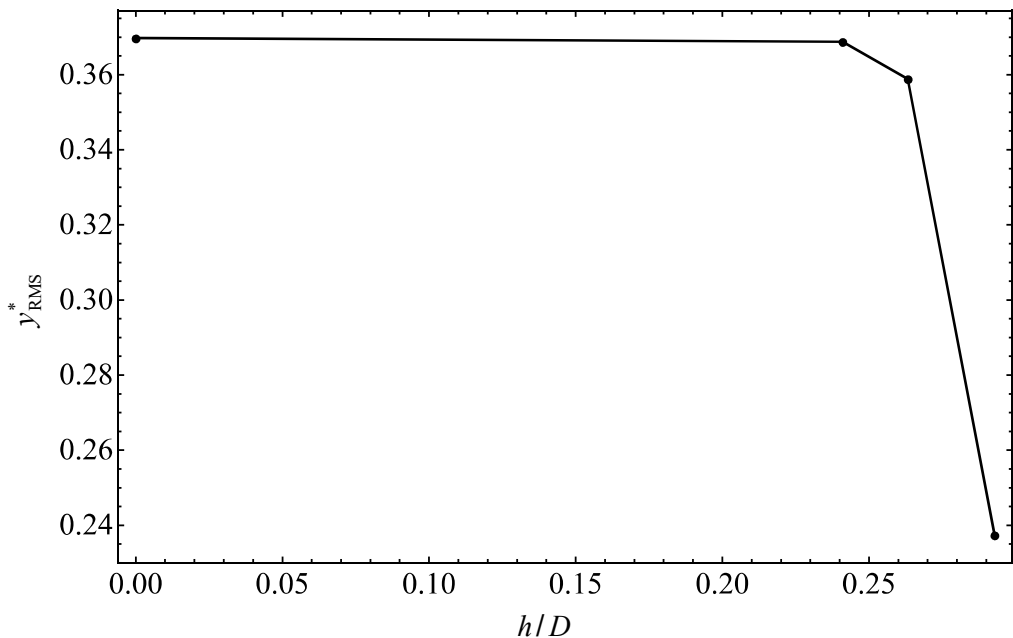
Parameter/ metric	$\text{Cl}_{\text{RMS}}$	$y_{\text{RMS}}^* = y^*/D$	$f^* = f_{\text{cyl.}}/f_n$
$f_{\text{RE}}$	0.262	0.369	0.969
$f_1$	0.2598	0.3687	0.9695
$f_2$	0.2430	0.3588	0.9740
$f_3$	0.0805	0.2374	1.0220
$ \epsilon_{2,1} $	0.02	0.01	0.004
$ \epsilon_{2,1} $	0.16	0.12	0.48
$R =  \epsilon_{2,1}  /  \epsilon_{2,1} $	0.10	0.08	0.094
$\text{GCI}_{3,2}$	30.92	6.00	0.64
$\text{GCI}_{3,2}$	1.63	0.52	0.10

that values of  $y_{\text{RMS}}^*$  and  $f^*$  at the fine grid already falls within the experimental uncertainty as evidenced by measurements in §3.4 and the work by Koide *et al.* (2013). The fine grid is used in all simulations of the pure cruciform case, and a similar mesh resolution is implemented on all cruciform variants studied in this work.

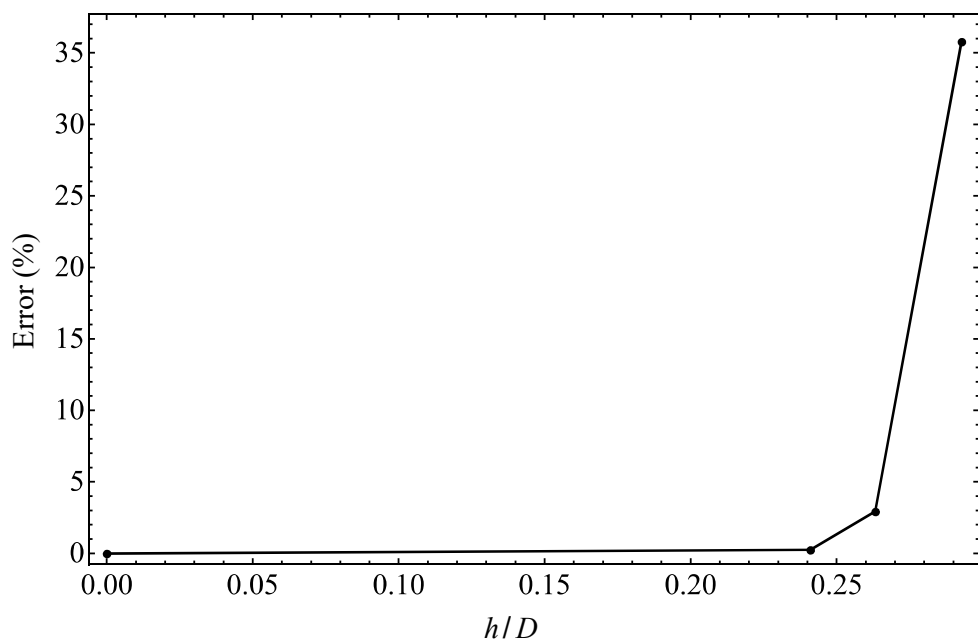
As demonstrated by the grid independency study, the normalised root-mean-square of cylinder displacement  $y^*$ , normalised dominant frequency of cylinder vibration  $f^*$ , and the root-mean-square of the lift coefficient are chosen  $\text{Cl}_{\text{RMS}}$ , all converge monotonically as the mesh is refined. This is apparent through the computation of the Richardson extrapolation of each quantity, in addition to the GCI values that drop significantly with each subsequent refinement of the mesh. Now that the independency of the quantities of interest with regards to spatial discretisation has been established, the chapter will proceed to present results for the 90° cruciform in the next section.

## 4.2 The pure cruciform

This chapter details the investigations conducted with regards to the pure cruciform in terms of it being the oscillator in an energy harvesting system. The pure cruciform serves as the base upon which all subsequent results will be compared against. The reason behind it being the base reference lies in the expansiveness of studies done, making it the type of cruciform oscillator that is most known about. Recall that it is through the study of the pure cruciform oscillator that the three main merits of the cruciform oscillator becomes known: a highly adept passive control system via the downstream strip plate, a very wide synchronisation range, and an approximately

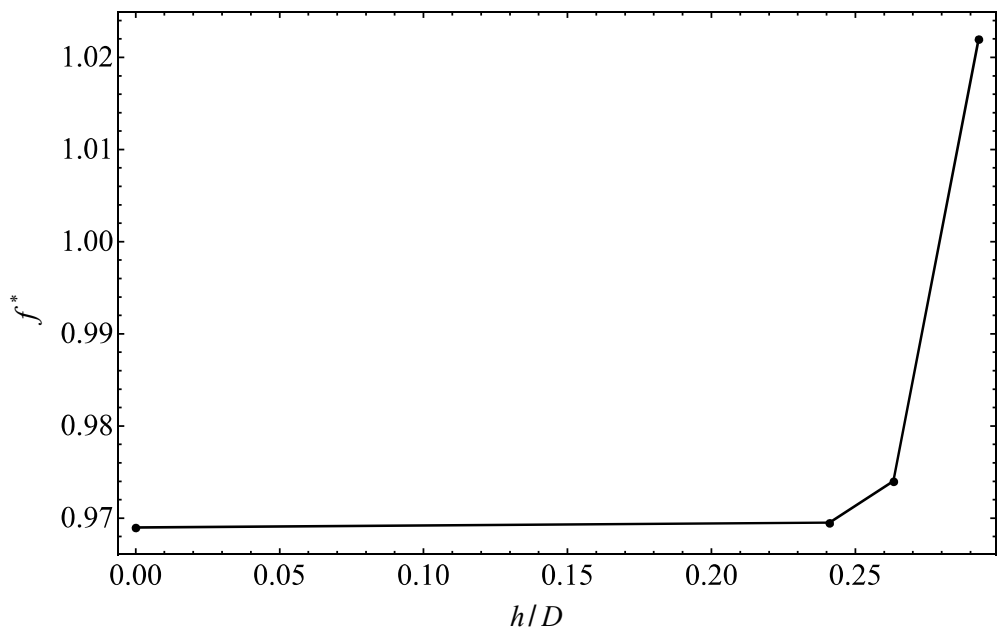


(a)

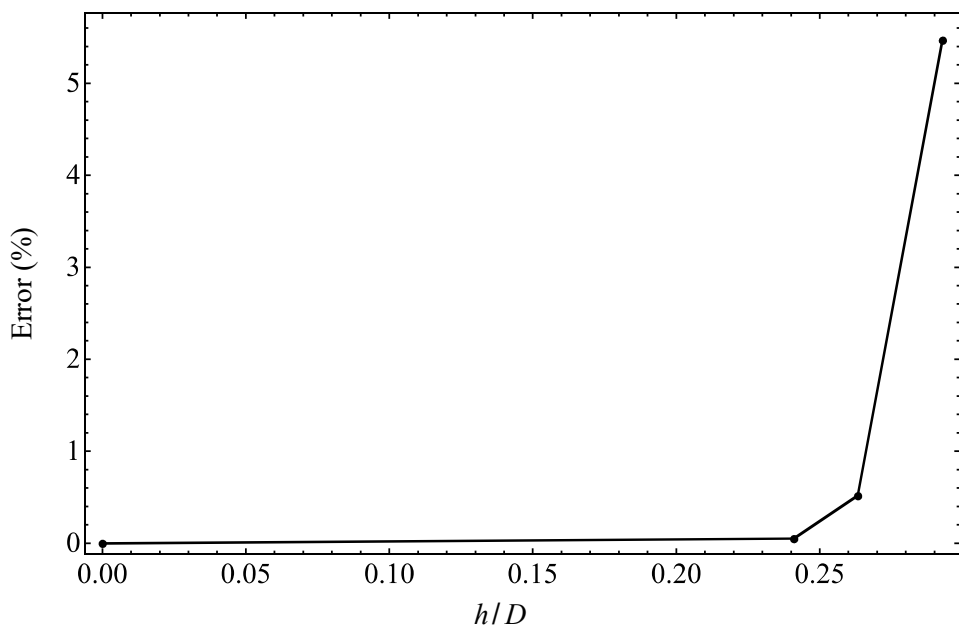


(b)

Figure 4.2: Richardson extrapolation of  $y^*_{\text{RMS}}$  and the corresponding drop in error.

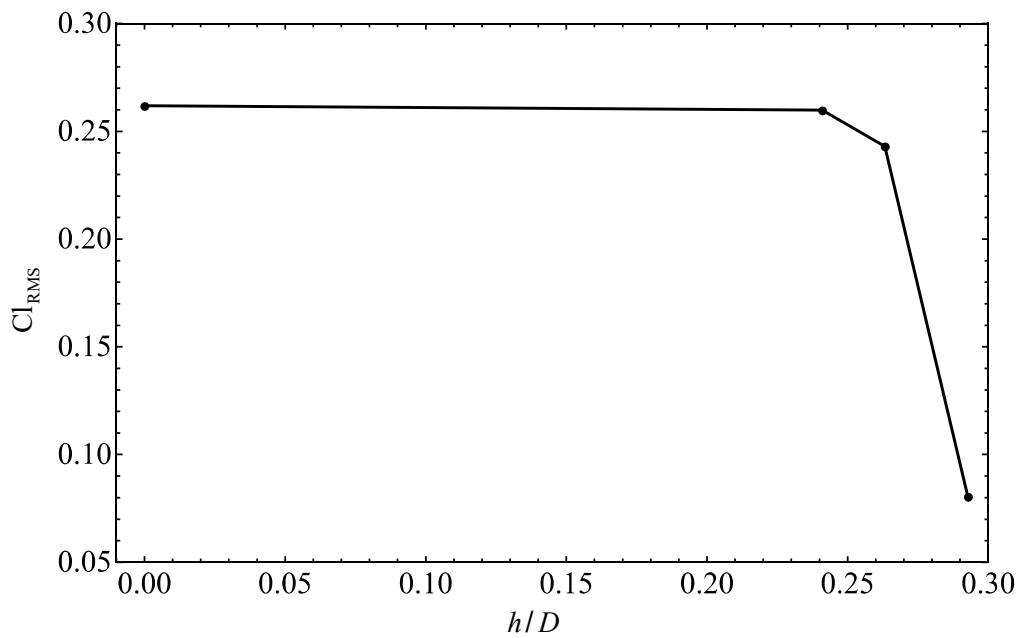


(a)

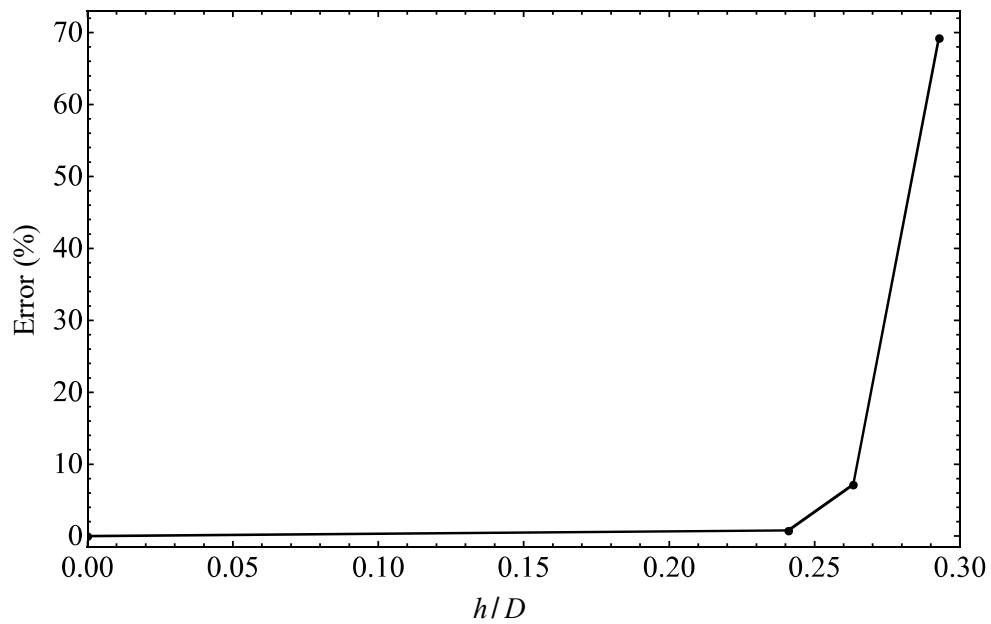


(b)

Figure 4.3: Richardson extrapolation of  $f^*$  and the corresponding drop in error.



(a)



(b)

Figure 4.4: Richardson extrapolation of  $\text{Cl}_{\text{RMS}}$  and the corresponding drop in error.

constant maximum vibration amplitude across the synchronisation range (Koide *et al.*, 2013).

Despite this, in recent years, improvement in terms of power output from the pure cruciform system seems to have hit a wall. Part of the reason behind this engineering roadblock is the fact that studies on pure cruciform oscillators to date have been focussed on answering the “what happens if” questions instead of the “why” questions concerning its system response. This work is of the opinion that if the roadblock is to be removed, efforts must be made to answer the “why” questions and the first step towards that is by understanding why does one observe the system responses found in the literature. This is possible through the use of CFD as one can quite effortlessly make simultaneous measurements of the cylinder displacement and lift while also obtain quantitative visualisations of the three-dimensional flow field describing the vortical structures governing the vibration of the cylinder.

The roadblock can also be interpreted as a sign to apply new methods of analysis on the common signals that are studied during the course of a VIV study, which are the time series of cylinder displacement and lift. Coupled with quantitative visualisations of the dominant vortical structures in the flow, this thesis attempts to look for clues that can guide future designs of the cruciform system as an energy harvester and bring to the table knowledge beyond improving its power output and efficiency, but the ability to control them, and adapting them to suit the natural environment within which the cruciform oscillator harnesses energy. This is because, even if the engineering knowledge allows for the vibration amplitude and frequency to reach a certain maximum value - and thus power - within a range of flow velocities, the aquatic or marine environment it is submitted to may not be suitable for such deployments, especially when faced with aquatic and marine life protection responsibilities (Raghavan, 2007).

The section starts by reproducing the amplitude/frequency responses of the pure cruciform, followed with the investigation of the vortical structures that bring about the amplitude/frequency responses observed. Then, the Hilbert-Huang transform is applied to elucidate the temporal evolution of the phase angle between lift and cylinder displacement to discover potentially hidden branches in the amplitude response not

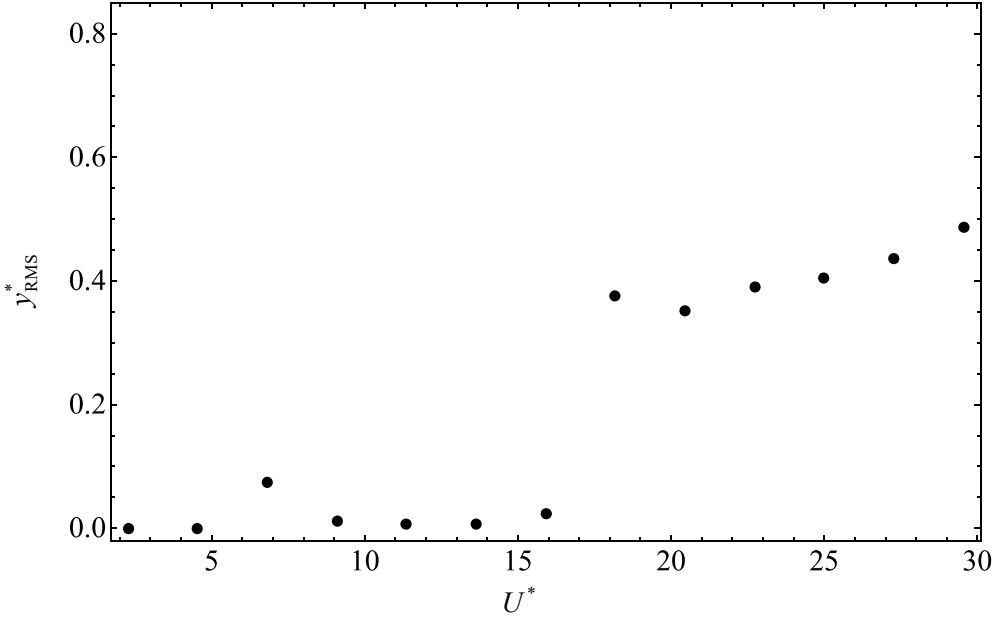


Figure 4.5: Evolution of the normalised root-mean-square amplitude of cylinder displacement  $y_{\text{RMS}}^*$ , with respect to reduced velocity  $U^*$ , in the streamwise vortex-driven vibration regime.

previously subjected to energy harvesting. Finally, the section concludes with the decomposition of the lift signal and the discovery of clues to maximise the vibration-driving lift, and consequently vibration amplitude and power output.

#### 4.2.1 The amplitude and frequency response

The pure cruciform case, i.e.  $90^\circ$ , demonstrated a normalised root-mean-square amplitude of cylinder displacement,  $y_{\text{RMS}}^*$  that starts quite expectedly with a low amplitude at reduced velocities 2.3 and 4.5 , before reaching a value close to  $y_{\text{RMS}}^* = 0.1$  at  $U^* = 6.8$ , as presented in Fig. 4.5. Following the local maximum at  $U^* = 6.8$ ,  $y_{\text{RMS}}^*$  tapers off to less than  $y_{\text{RMS}}^* = 0.05$  between  $9.1 \leq y_{\text{RMS}}^* \leq 13.6$ . This whole  $y_{\text{RMS}}^*$  trend of hitting a local maximum before tapering off bears a striking resemblance to the amplitude response of an isolated circular cylinder in KVIV at mass ratios of order  $O(10^1)$  (Feng, 1963; Khalak and Williamson, 1999). This resemblance can be seen as an indication that the vibration of a pure cruciform between  $U^* \leq 15.9$  is driven primarily through the shedding cycle of Karman vortices.

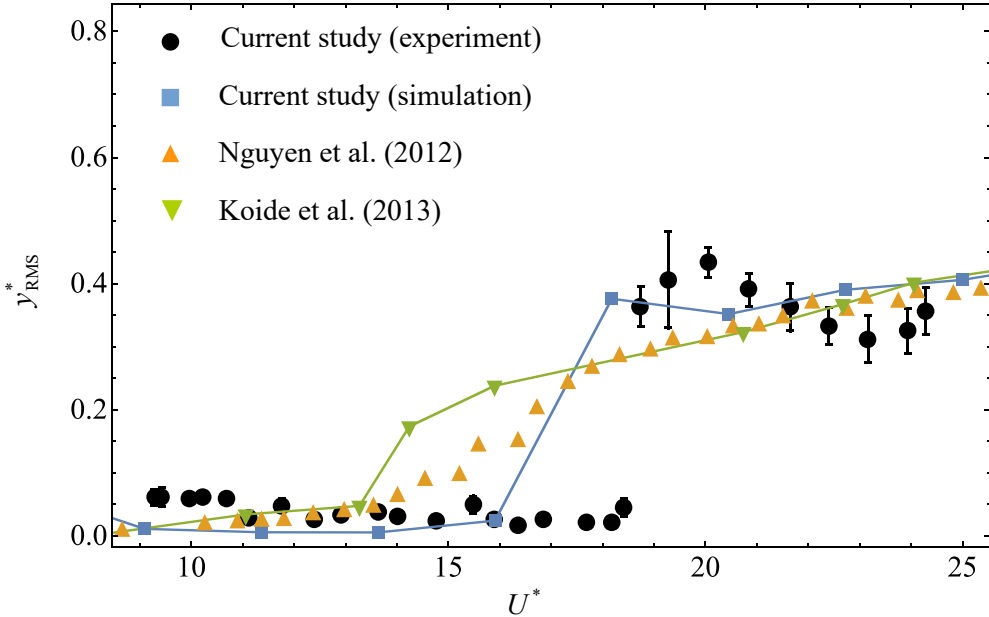


Figure 4.6: Comparison between the evolution of  $y^*_{\text{RMS}}$  with respect to  $U^*$  of a pure cruciform system from the numerical and experimental work. The filled square represents the numerical, while the filled circle represents the experimental results.

Then at  $U^* = 15.9$ ,  $y^*_{\text{RMS}}$  experiences a very weak increase followed by a sudden jump close to 0.4 at  $U^* = 18.2$ . This is followed by a slight decline at  $U^* = 20.5$  and return to the previous level of  $y^*_{\text{RMS}}$  at  $U^* = 22.7$ . Past  $U^* = 22.7$ , one observes that  $y^*_{\text{RMS}}$  maintains a linear trend in its variation with respect to  $U^*$ . As  $U^* = 18.2$  is well within the lower branch for a system in KVIV, it is quite unlikely for the vibration within  $18.2 \leq U^* \leq 29.5$  to be governed by the shedding of Karman vortices, leading previous investigators to attribute the vibration to the periodic shedding of streamwise vortical structures dominating the spatial region close to the cruciform juncture (Shirakashi *et al.*, 1989; Hemsuwan *et al.*, 2018d,c). Hence, this range is named of  $U^*$  the streamwise vortex-induced vibration regime (SVIV).

The experimental system consisting of the closed loop open flow channel and the pure cruciform oscillator rig in §3.4 is constructed not only for the purpose of validating the results of the pure cruciform numerical investigation, but also to corroborate in general, the sum total of the numerical setup. Admittedly, the best undertaking would be to perform equivalent experiment for each of the  $90^\circ$ ,  $67.5^\circ$ ,  $45^\circ$ ,  $22.5^\circ$  and  $0^\circ$  configurations, but the scale of such an exercise and subsequent discussion of the

results in the opinion of this work, deserves its own treatment separate from the current study. The degree of agreement between the results of the numerical and experimental investigation of the pure cruciform establishes the validity of the numerical setup, which is taken as extending to the rest of the cruciforms. This assumption is somewhat founded because all cruciforms are simulated under similar boundary conditions, mesh resolution and solver algorithm.

The experiments collect time series data of cylinder displacement  $y$ , from which the normalised root-mean-square amplitude  $y_{\text{RMS}}^*$  is computed. Figure 4.6 compares both numerical and experimental results of  $y_{\text{RMS}}^*$ . Both results agree in terms of magnitude and trend of the amplitude response. However, the jump to SVIV occurs at a higher  $U^* \approx 19$ , translating to a delay of about 3 units of  $U^*$ . The numerical and experimental results are also able to capture the slight dip in  $y_{\text{RMS}}^*$  following the jump to SVIV, but the occurrence in the experiment is also delayed by about 3 units of  $U^*$ . This delay can perhaps be attributed to the fact that the raw  $y$  time series were measured in succession from the lowest attainable channel flow velocity 0.3 m/s to its highest 1.1 m/s within one experimental run. In contrast, the simulations always start with the cylinder at rest at its neutral position at  $t_0 = 0$  s, with the freestream exactly set at the desired value 0.1 m/s, 0.2 m/s, . . . , 1.3 m/s. Thus, the delays found in experimental results may simply be the consequence of “flow memory”, a concept whose analogy can be found in experiments concerned with the critical value of a nondimensional quantity, e.g. Reynolds number, that demarcates the transition between two states of flow (Saint-Michel *et al.*, 2014; Rahman *et al.*, 2015; Li *et al.*, 2021). For all practical purposes, “flow memory” is simply the natural tendency of a fluid to retain its current state of flow for as long as it can, before being altered by an increase/decrease in momentum. This results in the delay found at the jump to SVIV and the local  $y_{\text{RMS}}^*$  minimum after the jump.

The evolution of the normalised cylinder vibration frequency  $f^*$  with respect to  $U^*$  is shown in Fig. 4.7. Inspecting Fig. 4.7, one immediately notice two distinct evolutionary pattern for  $f^*$  with a sharp boundary at  $U^* = 13.6$ . Between  $2.3 \leq U^* \leq 13.6$ , the  $f^*$  trend follows closely the shedding frequency of Karman vortices from

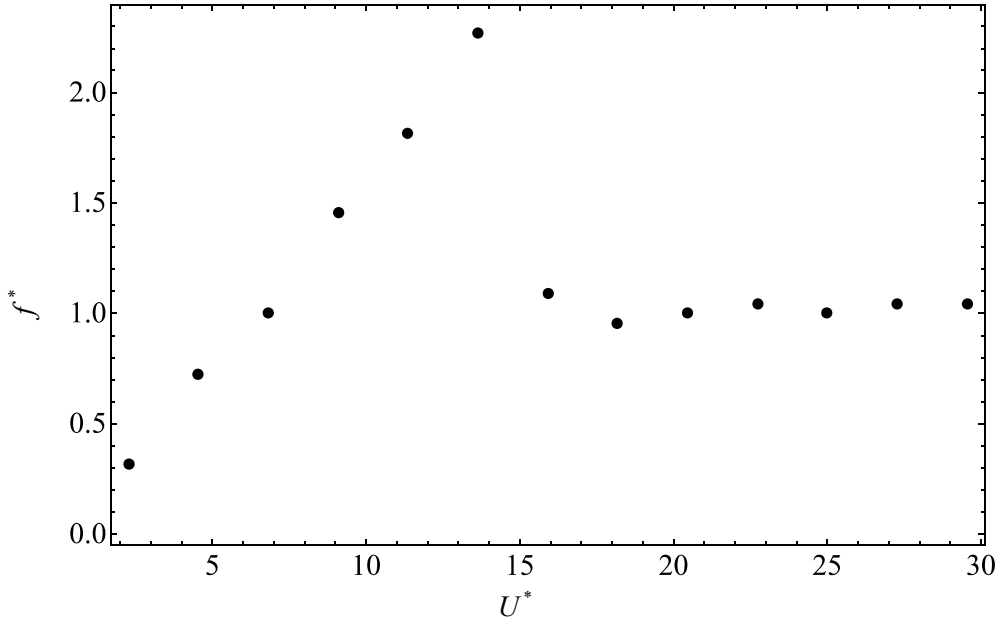


Figure 4.7: Evolution of the normalised cylinder displacement frequency,  $f^*$ , with respect to reduced velocity  $U^*$ , for the pure cruciform case.

an isolated, fixed circular cylinder (Blevins, 1990). The Karman vortex shedding frequency is given as an empirical equation in Eq. 4.4.

$$f_{v,\text{Karman}} = 0.198 \left( 1 - \frac{19.7}{\text{Re}} \right) DU \quad (4.4)$$

Here,  $f_{v,\text{Karman}}$ ,  $D$  and  $U$  are the vortex shedding frequency, diameter of the isolated circular cylinder and  $U$  the freestream velocity respectively. One can easily see how  $f_{v,\text{Karman}}$  is a linear function of  $U$ , and this is what gives rise to the linear pattern of  $f^*$  within  $2.3 \leq U^* \leq 13.6$ . Then, within  $15.9 \leq U^* \leq 29.5$ ,  $f^*$  drops close to 1, indicating synchronisation between lift and cylinder vibration. It seems that this synchronisation is what gives rise to the bigger  $y^*$ , compared to  $2.3 \leq U^* \leq 13.6$ .

Inspecting the evolution of root-mean-square amplitude of lift coefficient  $C_{l,\text{RMS}}$  and the normalised lift coefficient frequency  $f_{Cl}^*$  with respect to  $U^*$  in Fig. 4.8, provided more evidence supporting the assertion that  $U^* = 15.9$  is a boundary between two vibration-driving mechanisms. In fact, the observation at 15.9 in Fig. 4.8a indicates

that the SVIV regime is still in its infancy, due to the dip in  $\text{Cl}_{\text{RMS}}$  at that  $U^*$ , compared to  $U^* = 13.6$ . In Fig. 4.8b, a dashed line is also drawn to illustrate  $f_v^* = f_{v,\text{Karman}}/D$ , where  $f_{v,\text{Karman}}$  is the shedding frequency of Karman vortices from a smooth isolated circular cylinder described in Eq. 4.4.

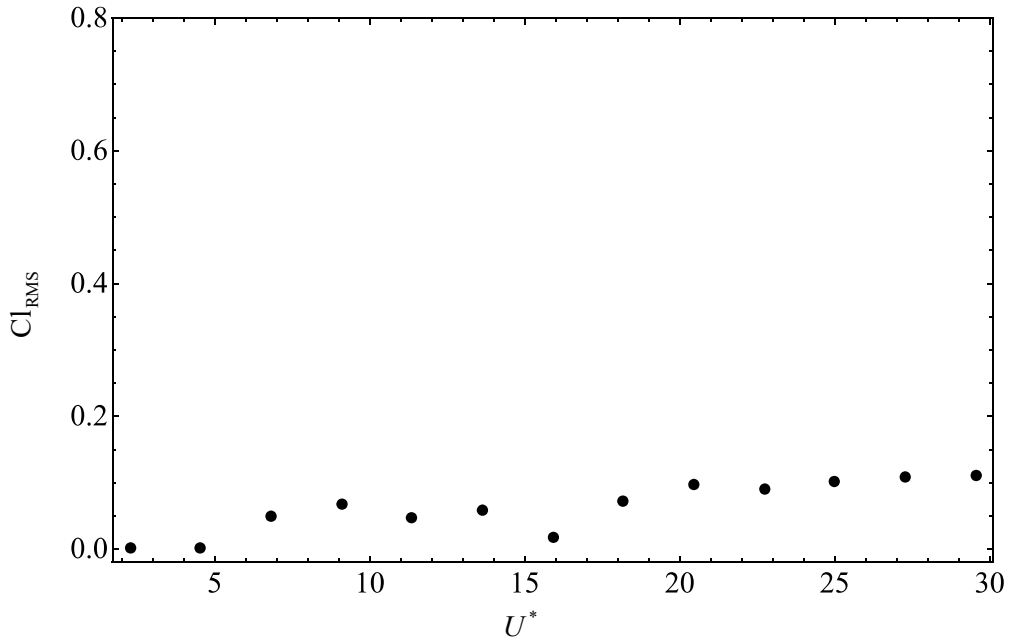
The trend found in  $f_{\text{Cl}}^*$  vs.  $U^*$  is very similar to that found in Fig. 4.7. This similarity is interpreted as an indication of the symmetry of lift produced along the cylinder. This reasoning stems from the findings of Zhao and Lu (2018), who revealed how lift is distributed along the upstream cylinder of a two-cylinder 90° cruciform. They did this by computing chapteral lift coefficients along the upstream cylinder. This system produces a symmetric distribution of chapteral lift coefficient, with  $Z = 0$  being the plane of symmetry. An asymmetrical distribution of the chapteral lift coefficient may produce a trend in  $y_{\text{RMS}}^*$  and  $f^*$  that is dissimilar to those found in  $\text{Cl}_{\text{RMS}}$  and  $f_{\text{Cl}}^*$ , due to the irregular moment acting on the cylinder.

#### 4.2.2 Main vibration-driving vortical structure

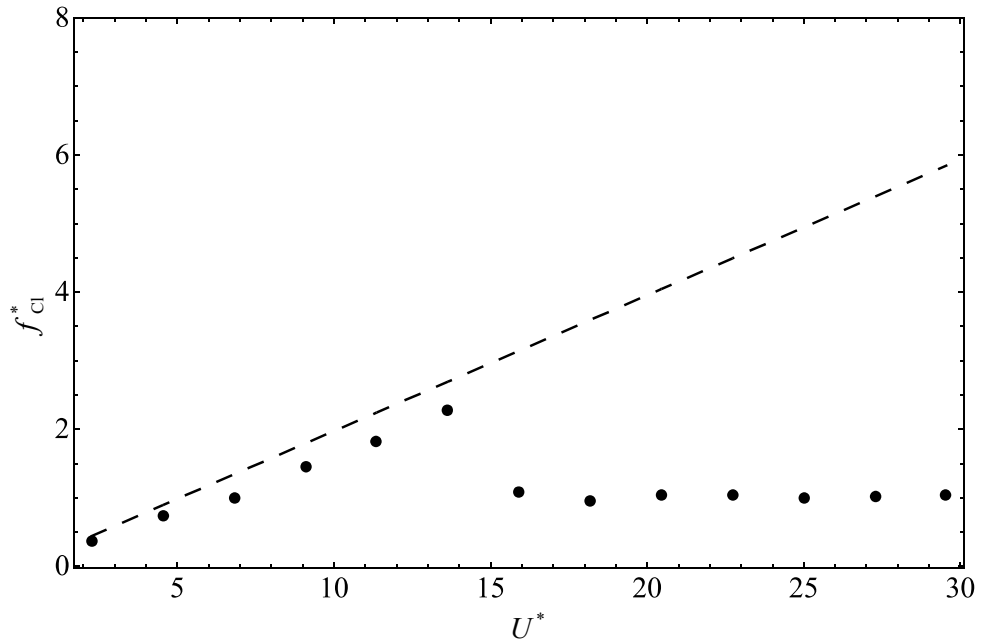
Recall Figs. 4.5 and 4.7. Out of all thirteen variants of  $U^*$  studied in the pure cruciform case, seven within  $15.9 \leq U^* \leq 29.5$  sustain high-amplitude vibrations with no foreseeable upper limit within the observation window. For a more complete understanding of the mechanism driving the vibration, one needs to know what are the vortical structures dominating the flow are and how they interact with each other.

Let the coordinates of the simulation domain be defined in the following manner:  $(X, Y, Z) = (\frac{x}{D}, \frac{y}{D}, \frac{z}{D})$ . The  $y$ -component velocity fluctuations are sampled on the  $(X, Y) = (1.96, 0)$  line, along the span of the cylinder in  $0.5D$  increments, i.e. at coordinates  $(1.96, 0, 7.5), (1.96, 0, 7.0), \dots, (1.96, 0, -7.5)$ . The distance  $X = 1.96$  from the origin is equivalent to  $1D$  downstream the trailing edge of the strip plate, and this location is chosen as it is not too close to the cruciform that the vortical structures have not fully formed, and not too far, obfuscating meaningful observation of the structures.

The shedding of vortical structures leave their footprint on the flow field in the form of velocity fluctuations. The choice of analysing the fluctuations of the  $y$ -



(a) Evolution of  $Cl_{RMS}$  with respect to  $U^*$ .



(b) Evolution of  $f_{Cl}^*$  with respect to  $U^*$

Figure 4.8: Evolution of the lift coefficient root-mean-square amplitude ( $Cl_{RMS}$ ) and normalised frequency of lift coefficient ( $f_{Cl}^*$ ), with respect to reduced velocity  $U^*$ , for the pure cruciform case. The dashed line in Fig. 4.8b visualises the shedding frequency of Karman vortex computed from Eq. 4.4.

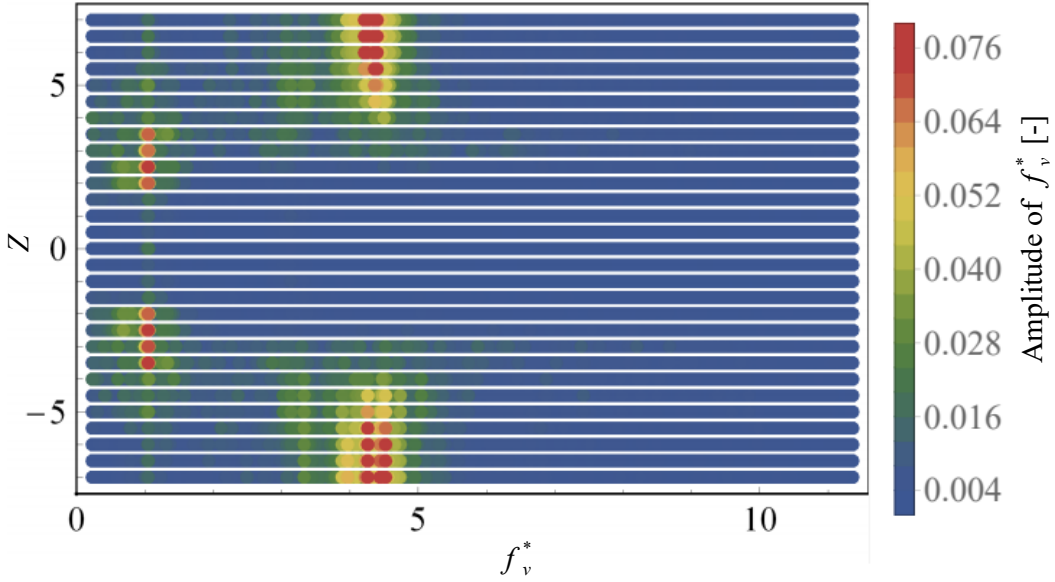


Figure 4.9: Distribution of normalised frequency of vortex shedding, along the span of the cylinder of the pure cruciform at  $U^* = 22.7$ .

component of velocity is made due to the fact that the oscillator is constrained to move only in the transverse direction. Then, the velocity fluctuations are processed with FFT to obtain the Fourier transform of the fluctuation signals at each spanwise location. The combined Fourier transforms are presented using a colour map in Fig. 4.9. In this figure, every point is a result of that FFT giving the observer a spatial understanding of the vortical structures present in the flow. The abscissa and ordinate denotes  $f^*$  and  $Z$  coordinates respectively, while the bar legend gives the amplitude of the FFT result.

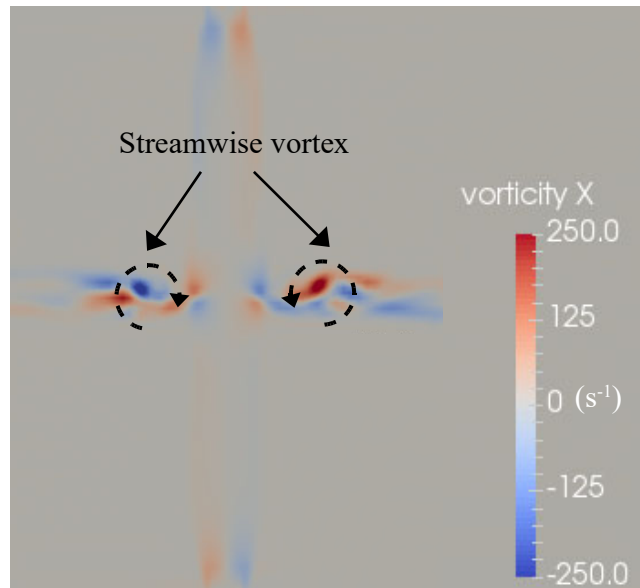
Through inspection, one immediately notices two frequency bands with high amplitudes namely  $f^* \approx 1$  and  $f^* \approx 4.5$ . The locations of these bands are between  $3 \leq Z \leq 4.5$  for the former and  $4.5 < Z \leq 7$  for the latter. Aided with this visualisation, one can give meaning to the  $x$  and  $z$ -components of vorticity visualised in Fig. 4.10. The slices in Fig. 4.10 visualise the distribution of the  $x$  (streamwise) and  $z$  (Karman) components of vorticity at the  $X = 1.96$  plane. The plane is viewed from downstream (viewer standing at  $X = 1.96$ , looking towards the cruciform), and the vorticities are presented in units of  $s^{-1}$ . Furthermore, the visualisations are made when the lift coefficient  $C_l$  is at a maximum ( $C_{l\max}$ ).

Comparing Fig. 4.9 with Fig. 4.10 suggests that the  $f^* \approx 1$  band is actually due to the shedding of streamwise vortex of a scale close to  $1D$  while the  $f^* \approx 4.5$  seems to be due to the shedding of Karman vortices. Contrary to the vortical structure commonly observed in studies of isolated circular cylinders (Deng *et al.*, 2007; Kinaci *et al.*, 2016; Duranay and Kinaci, 2020), in the pure cruciform case, two distinct vortical structures take shape in the flow, namely streamwise and Karman vortices. This is consistent with the findings in Koide *et al.* (2017) or Zhao and Lu (2018), where they observed a pair of streamwise vortices on a scale of  $\approx 1D$  form in the vicinity of the cruciform juncture, and Karman vortices further away in the spanwise direction. Note that the vibration-driving streamwise vortices forming close to the cruciform juncture exist in pairs: in Fig. 4.10a, one is observed to rotate in the clockwise direction when  $Z > 0$  and the other in the counter-clockwise direction when  $Z < 0$ . What results from this counter-rotating vortex pair is a thrust, propelling the cylinder upwards. This is consistent with the fact that the vorticity field visualisations are produced when the Cl is at a maximum. This work also observe the core of both streamwise vortices lie approximately on the same  $Y$ -plane, parallel to the axis of the cylinder.

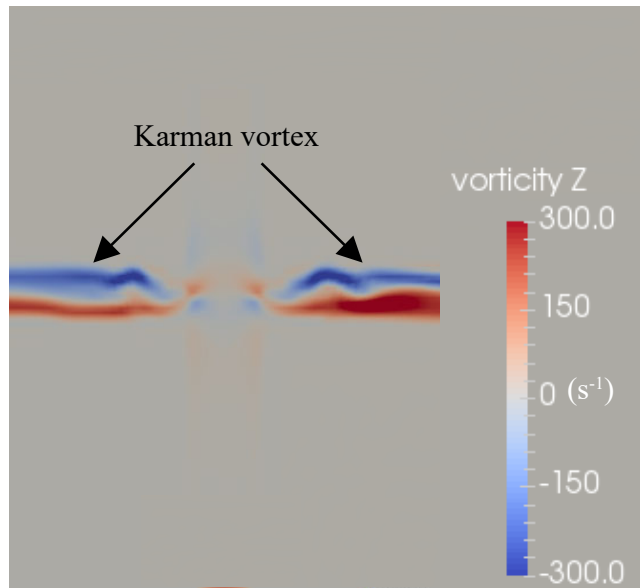
### 4.2.3 Temporal evolution of the lift coefficient

#### 4.2.3.1 The KVIV regime (reduced velocity below 13.6)

At reduced velocities  $U^* = 2.3$  and  $4.5$ , the phase lags  $\phi$  (deg.) between Cl and  $U^*$  are practically zero throughout the whole observation time. The characteristic intrinsic mode functions (IMFs) of Cl and  $y^*$  at  $U^* = 4.5$  exemplifies this trend, as showcased in Fig. 4.13. Here, Fig. 4.13a shows the temporal evolution of  $C_{y^*,y^*}$  and  $C_{Cl,y^*}$ , which are the characteristic IMFs of  $y^*$  and Cl, respectively. Figure 4.13b shows the phase lag between  $C_{y^*,y^*}$  and  $C_{Cl,y^*}$ , and Fig. 4.13c presents the Hilbert-Huang transform (HHT) spectrogram of Cl. The HHT spectrogram visualises the instantaneous frequency and amplitude of the IMF components of Cl. The trend that one notices in Fig. 4.13b is similar to what was observed in Khalak and Williamson (1999), a study that also employs the Hilbert transform to obtain the instantaneous phase, albeit without ensemble empirical mode decomposition (EEMD). The dominant IMF component (IMF component sustaining the highest amplitude throughout the whole observation time) of the lift coefficient has a normalised frequency  $f_{Cl}^* = f_{Cl}/f_n$  (Fig. 4.13c) centred at approximately  $f_{Cl}^* = 0.75$ .

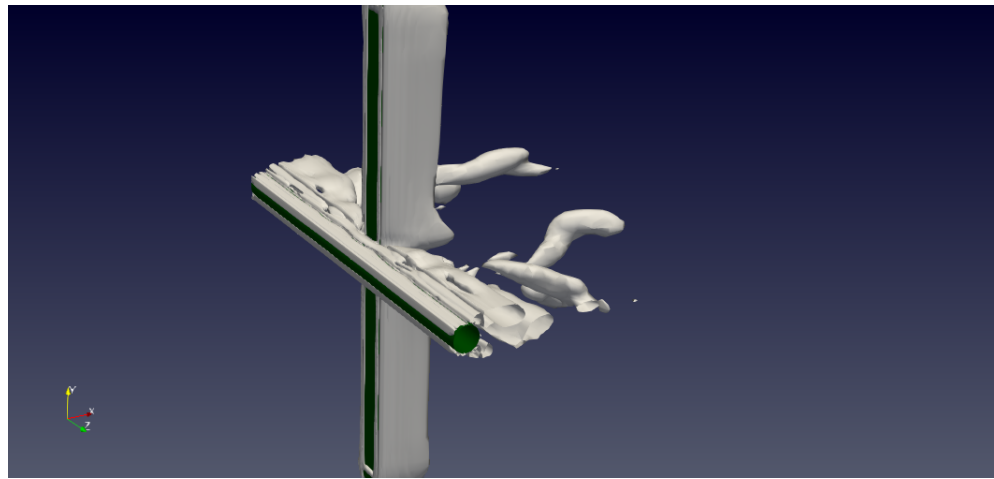


(a)  $x$ -component vorticity

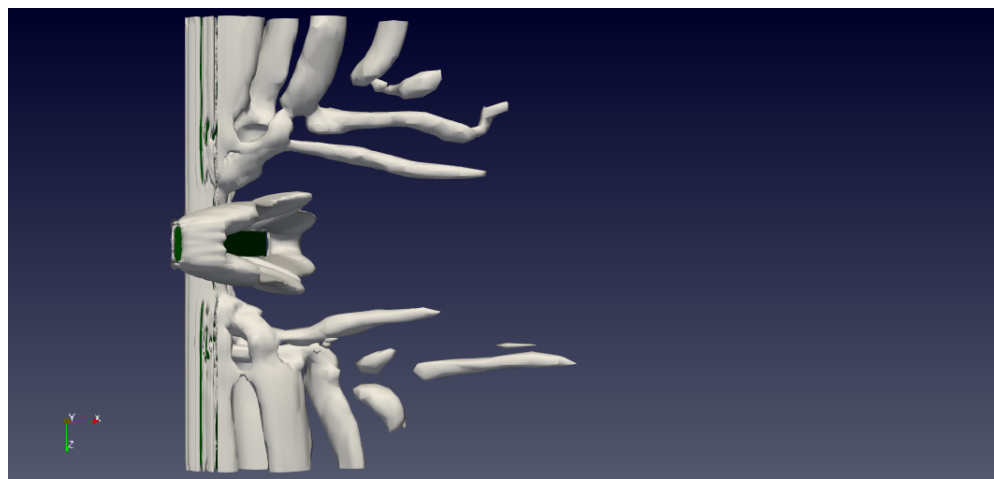


(b)  $z$ -component vorticity

Figure 4.10: Dominant vortical structures at  $U^* = 22.7$  observed in the pure cruciform case.

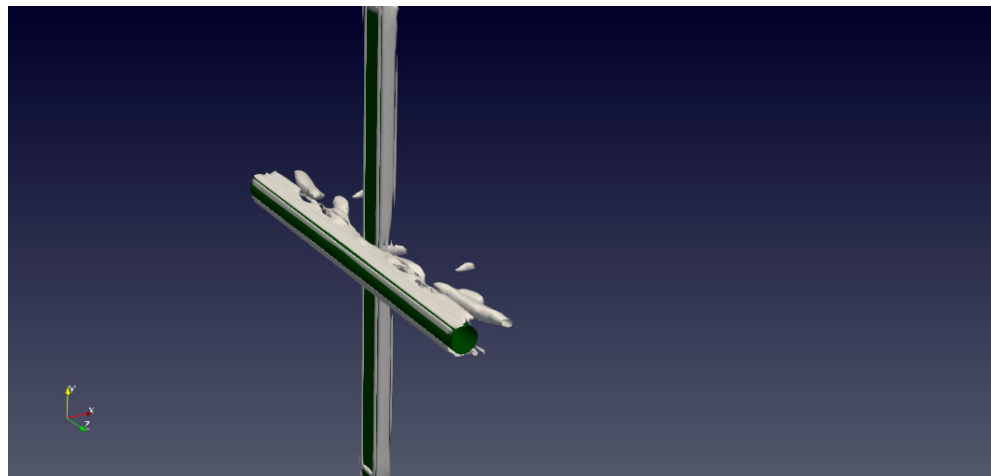


(a) Isometric view of the Q-criterion.

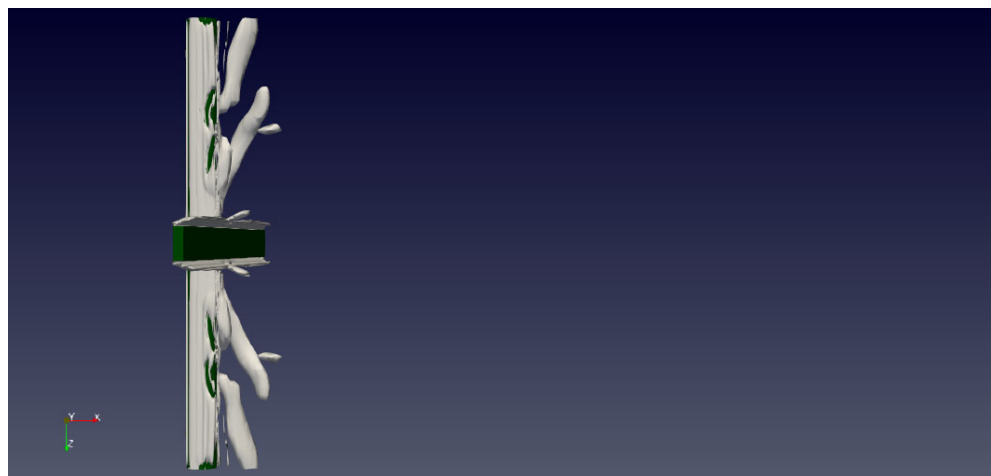


(b) Plan view of the Q-criterion.

Figure 4.11: The Q-criterion for the  $90^\circ$  cruciform at  $U^* = 22.7$ : the isometric (4.11a) and plan view (4.11b).



(a) Isometric view of the Q-criterion.



(b) Plan view of the Q-criterion.

Figure 4.12: The Q-criterion for the  $90^\circ$  cruciform at  $U^* = 6.8$ : the isometric (4.12a) and plan view (4.12b).

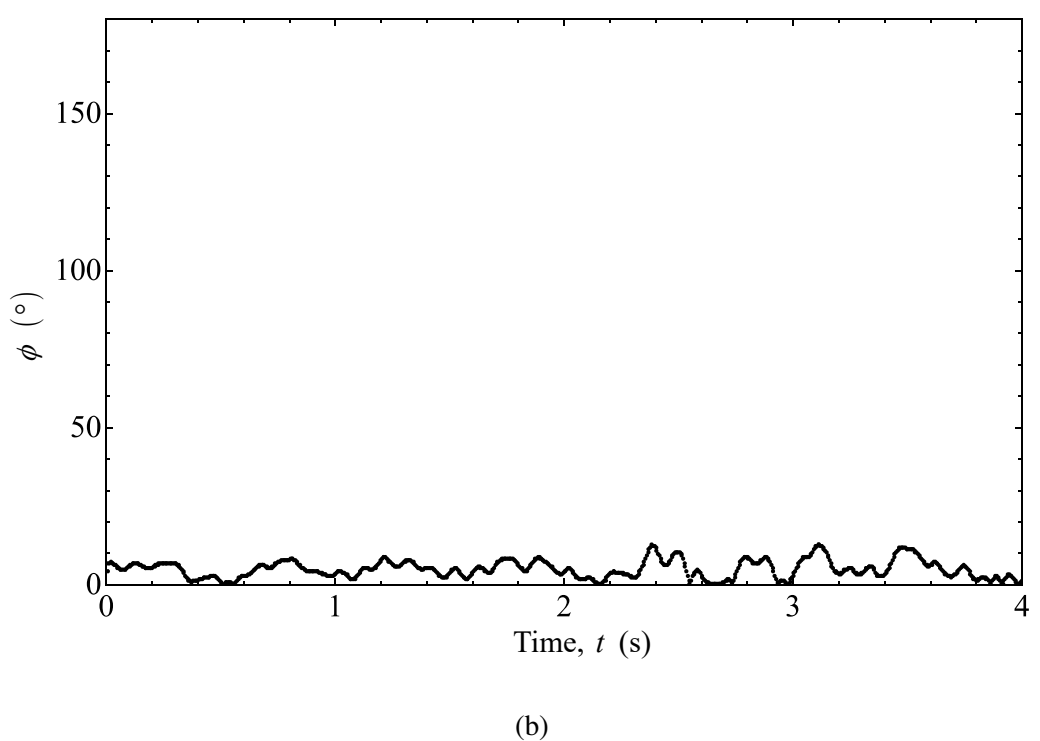
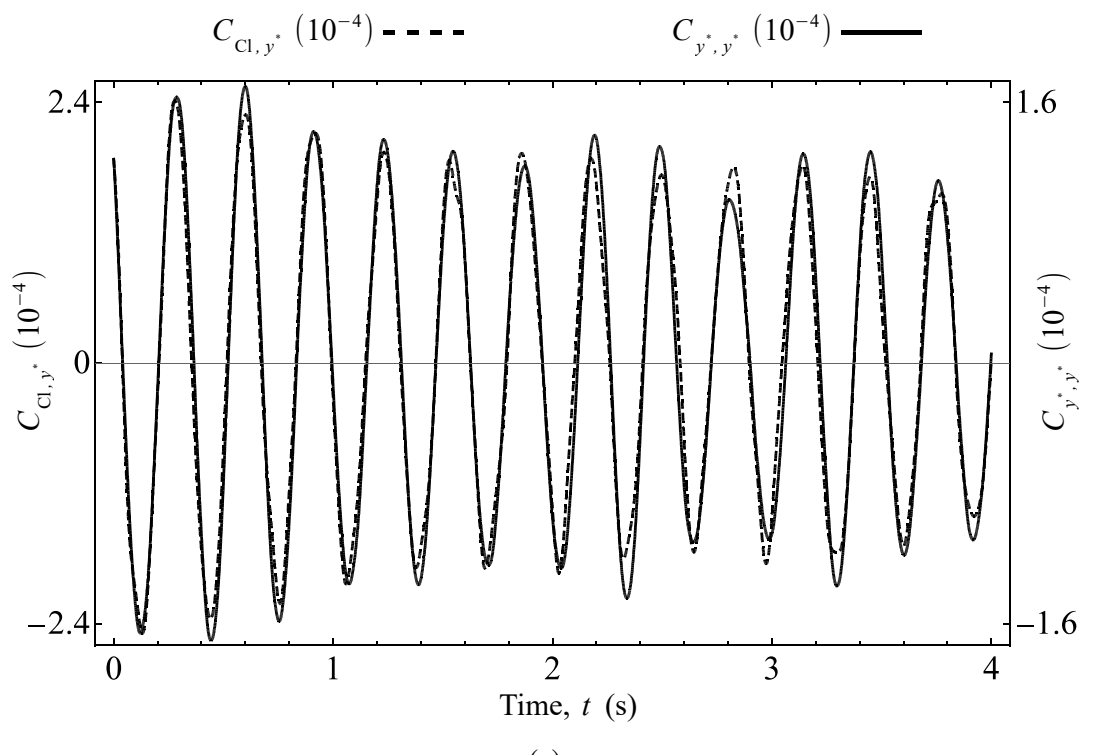
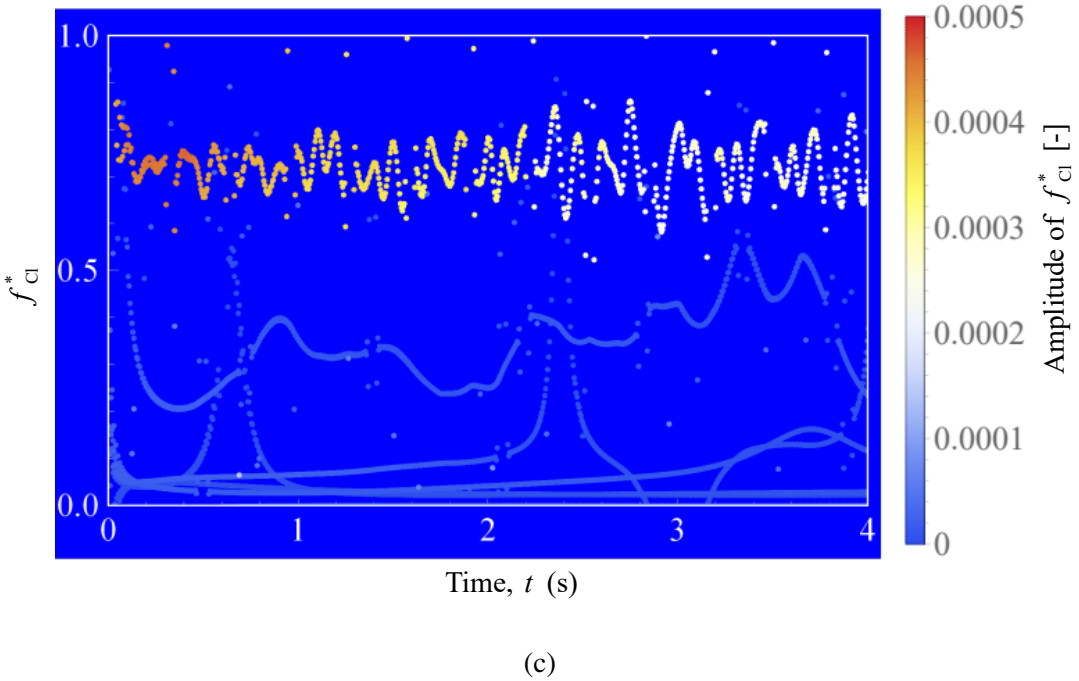


Figure 4.13: Temporal analysis of Cl and  $y^*$  at  $U^* = 4.5$ .

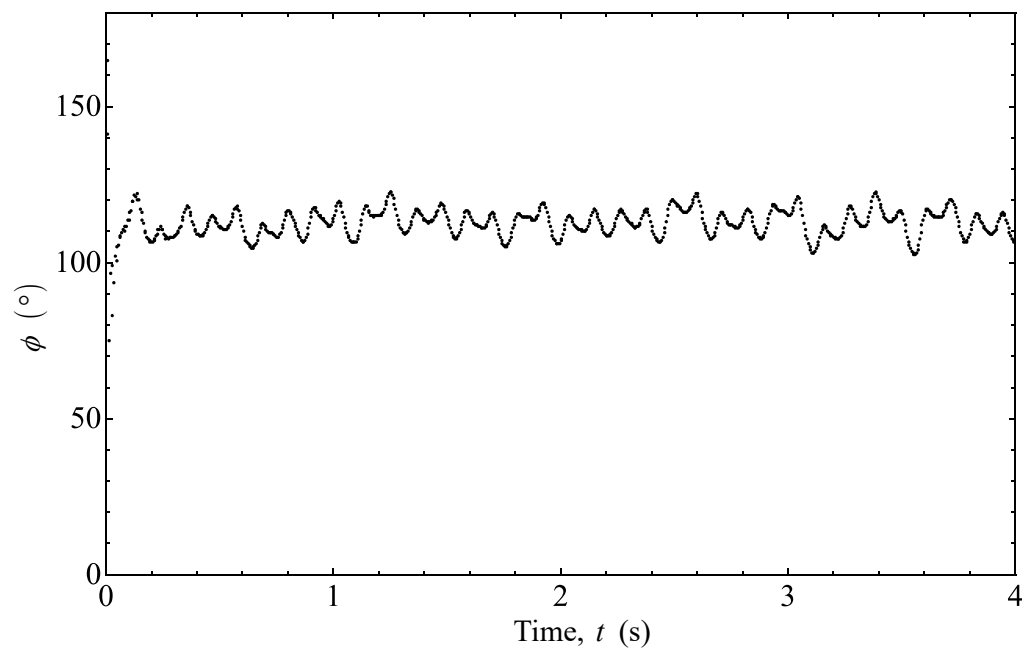
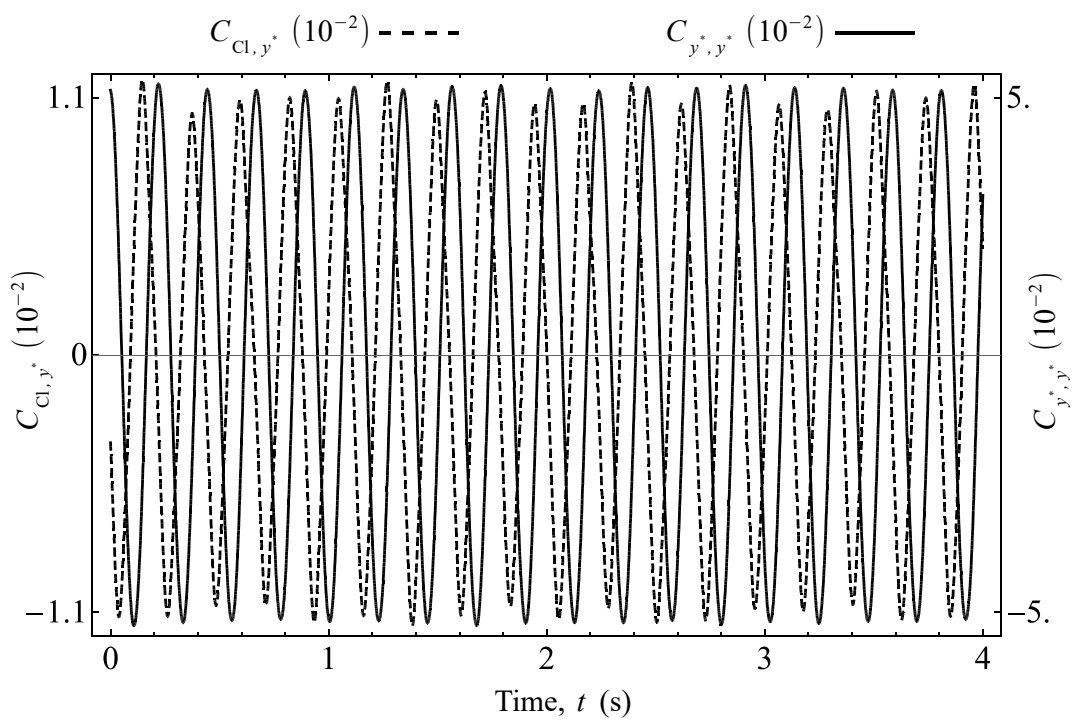


(c)

Figure 4.13: Temporal analysis of Cl and  $y^*$  at  $U^* = 4.5$ .

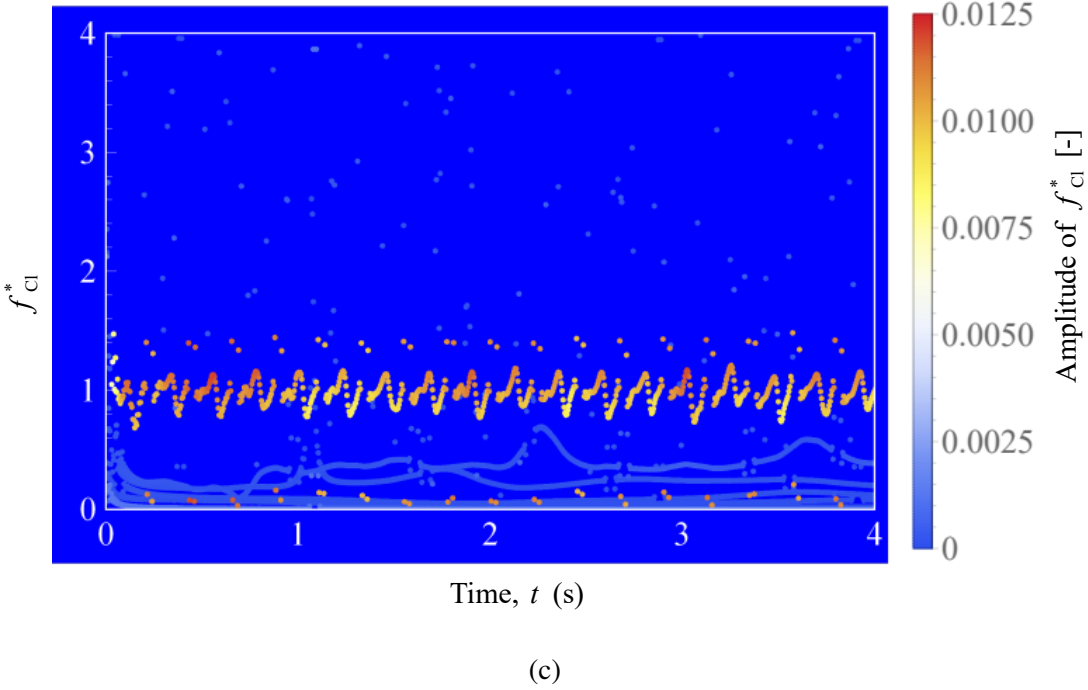
Once the cylinder enters the upper branch of KVIV at  $U^* = 6.8$ ,  $\phi$  jumps to approximately 110 deg. This jump in  $\phi$  is characteristic of the transition to the upper branches as also observed by Maruai *et al.* (2018), among others. Both  $C_{\text{Cl},y^*}$  and  $C_{y^*,y^*}$  signals are visibly very periodic, and the dominant frequency band of Cl, is centred at  $\approx 1$ , as one can verify in Fig. 4.14c.

As  $U^*$  is increased even further up to  $U^* = 13.6$ , a similar trend is spotted for all  $U^* = 9.1, 11.4, 13.6$  examined:  $C_{y^*,y^*}$  and  $C_{\text{Cl},y^*}$  are both qualitatively very periodic. Their phase lags are very close to 180 deg., and the dominant Cl frequency bands exhibit a time-averaged value that increases linearly with respect to  $U^*$ , in a manner that the Strouhal number of Cl is always  $\approx 0.16$  on average. The representative case of  $U^* = 13.6$  is shown in Fig. 4.15. Note how  $\phi$  in this range of  $U^*$  varies much less with respect to time, compared to  $\phi$  at  $U^* = 6.8$ , and the dominant frequency band of Cl is much narrower compared to the dominant frequency band at  $U^* = 6.8$ , indicating a highly periodic and self-similar oscillation of lift.



(b)

Figure 4.14: Temporal analysis of Cl and  $y^*$  at  $U^* = 6.8$ .



(c)

Figure 4.14: Temporal analysis of Cl and  $y^*$  at  $U^* = 6.8$ .

#### 4.2.3.2 Transition to SVIV (reduced velocity between 15.9 and 18.2)

Previously in the  $U^* \leq 13.6$  range, the temporal profile of both Cl and  $y^*$  are very similar to each other, except that Cl leads  $y^*$  by a certain amount. This similarity in profile supports the assertion that the vibration within  $U^* \leq 13.6$  is driven exclusively by the shedding of Karman vortices, which brings the onset of the alternating lift. Analogously, one might expect a similar profile between Cl and  $y^*$  when streamwise vortices drive the vibration. However, this does not seem to be the case.

Once  $U^*$  reaches 15.9, it has become difficult to argue that the profile of  $y^*$  is just a lagged version of the profile of Cl. This is shown in Fig. 4.16a, with the enlarged version in Fig. 4.16b. The profile of Cl looks like the result of several signals in superposition, which one can almost distinguish from the presence of two types of maxima at two different amplitude heights. A red dashed line and a red dashed-dot line is put in Fig. 4.16b as visual cues indicating the two amplitude heights. Decomposing the lift coefficient signal using EEMD reveals partial evidence supporting the compound signal hypothesis.

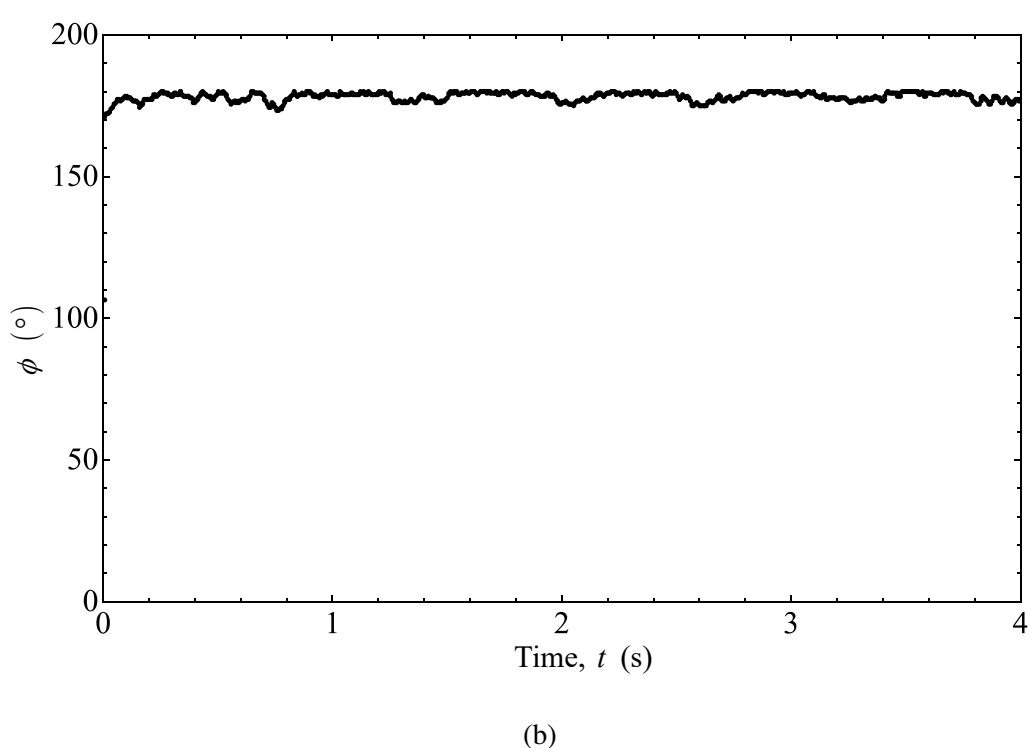
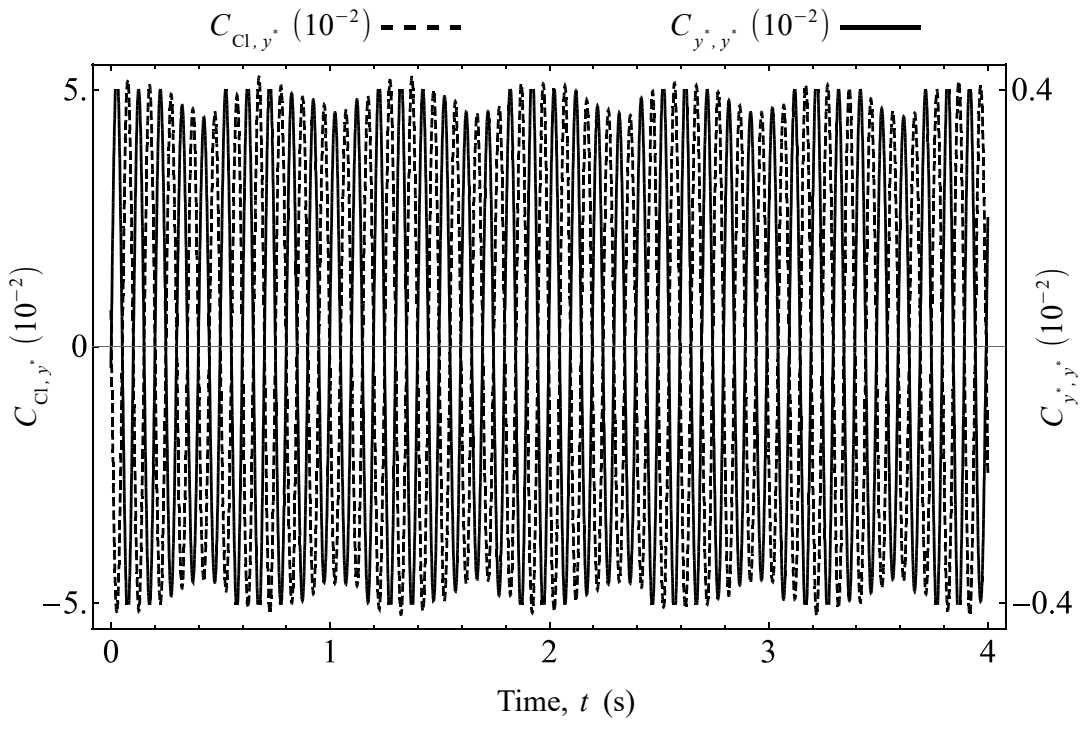


Figure 4.15: Temporal analysis of Cl and  $y^*$  at  $U^* = 13.6$ .

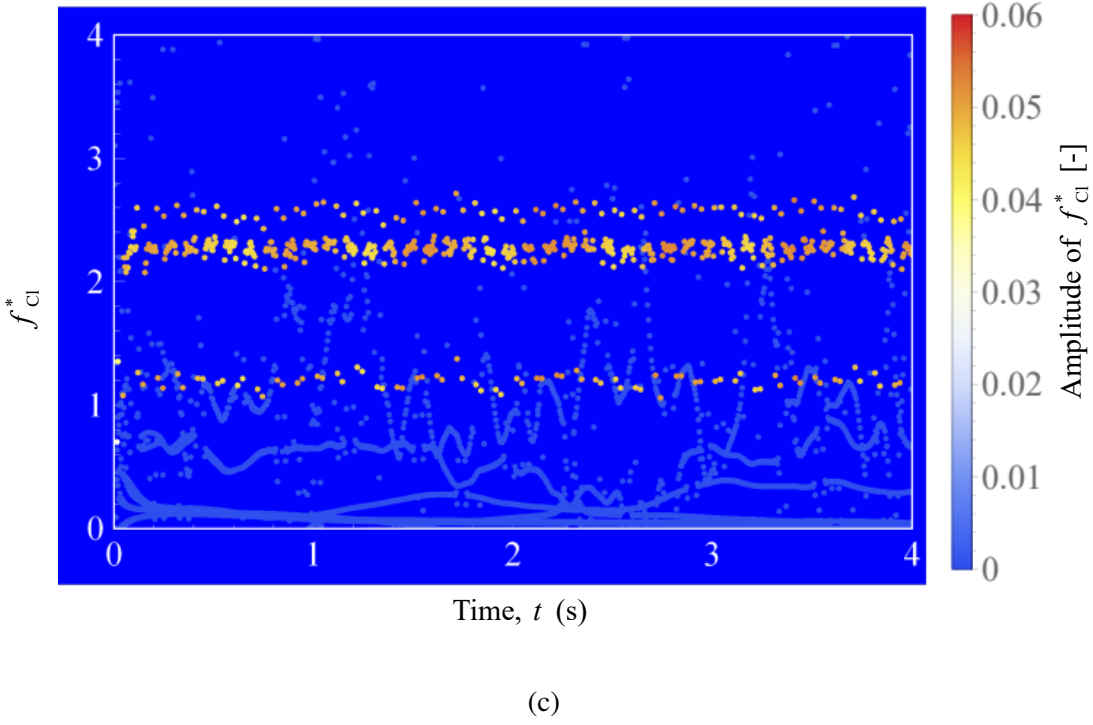
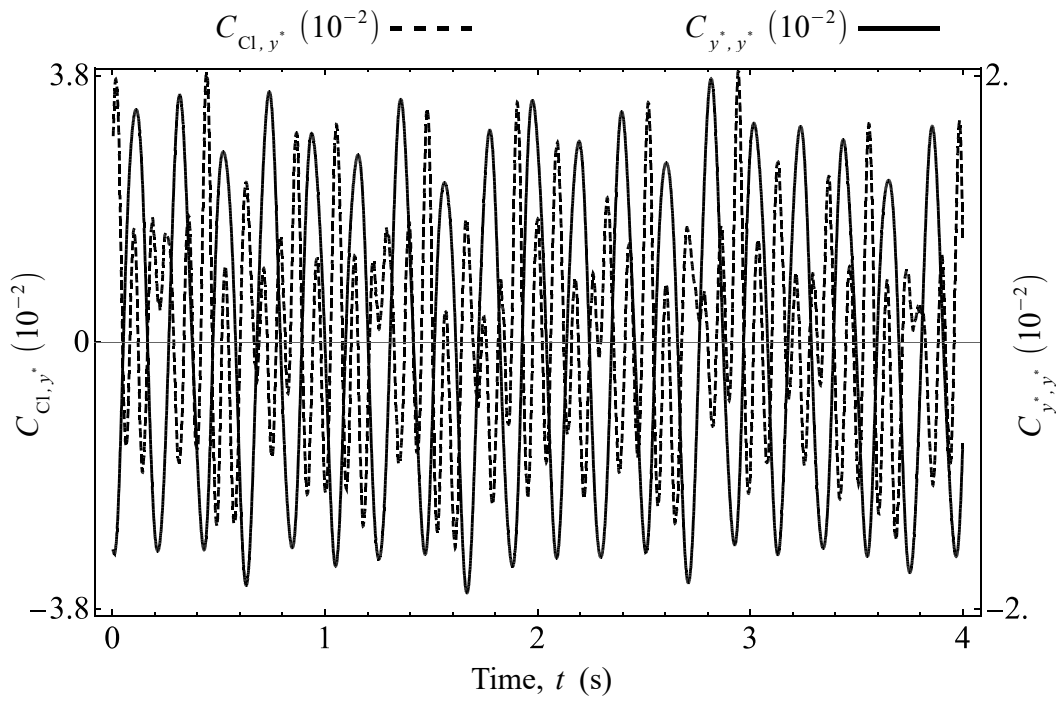


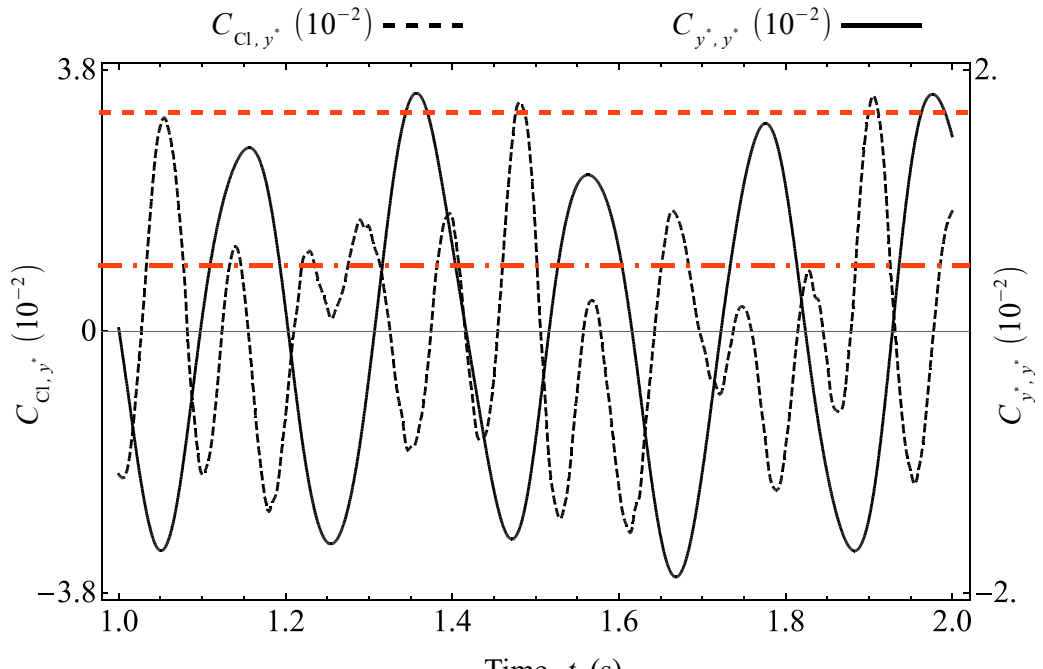
Figure 4.15: Temporal analysis of Cl and  $y^*$  at  $U^* = 13.6$ .

Once the signal is decomposed using EEMD, Fig. 4.16a is replotted using  $C_{Cl,y^*}$  and  $C_{y^*,y^*}$  in Fig. 4.17a. One can clearly see that the part of Cl signal responsible for driving the vibration at  $U^* = 15.9$  is embedded in the original Cl signal (Fig. 4.17a), and decomposition via EEMD managed to recover this signal, which leads  $C_{y^*,y^*}$  by approximately 150 deg. on average, throughout the whole observation time (Fig. 4.17b). This decline from  $\phi \approx 180$  deg. at reduced velocities  $9.1 \leq U^* \leq 13.6$ , to  $\phi \approx 150$  deg. at  $U^* = 15.9$  is quite sizeable, suggesting a fundamental change in flow dynamics, particularly in terms of vortical structure. Another notable change is the increased temporal variation in  $\phi$  from its time-averaged value, in contrast to the evolution of  $\phi$  in the range  $9.1 \leq U^* \leq 13.6$ , which has very little jitter throughout the observation time.

Inspecting the HHT spectrogram in Fig. 4.17c reveals two dominant bands in the frequency domain. The first one, marked with a white continuous rectangular box, is the instantaneous frequency for the IMF component of lift shown in Fig. 4.17a, and its mean frequency lies close to the natural frequency of the system ( $f_{Cl}^* \approx 1$ ). There is; however, a second band of the frequency with nearly similar amplitude around

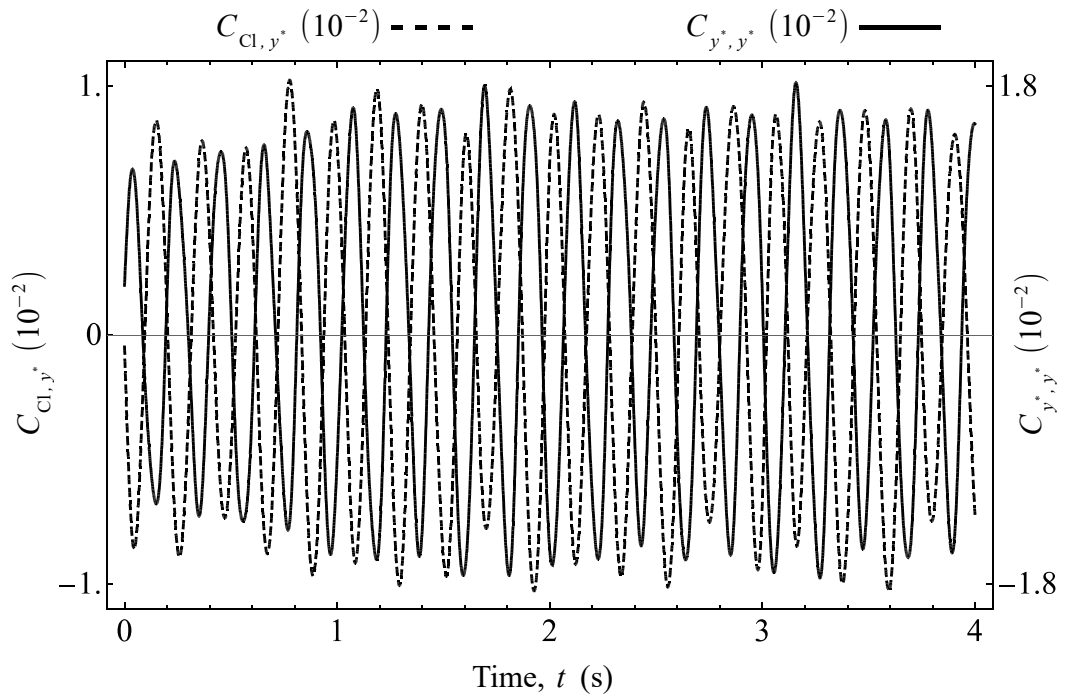


(a)

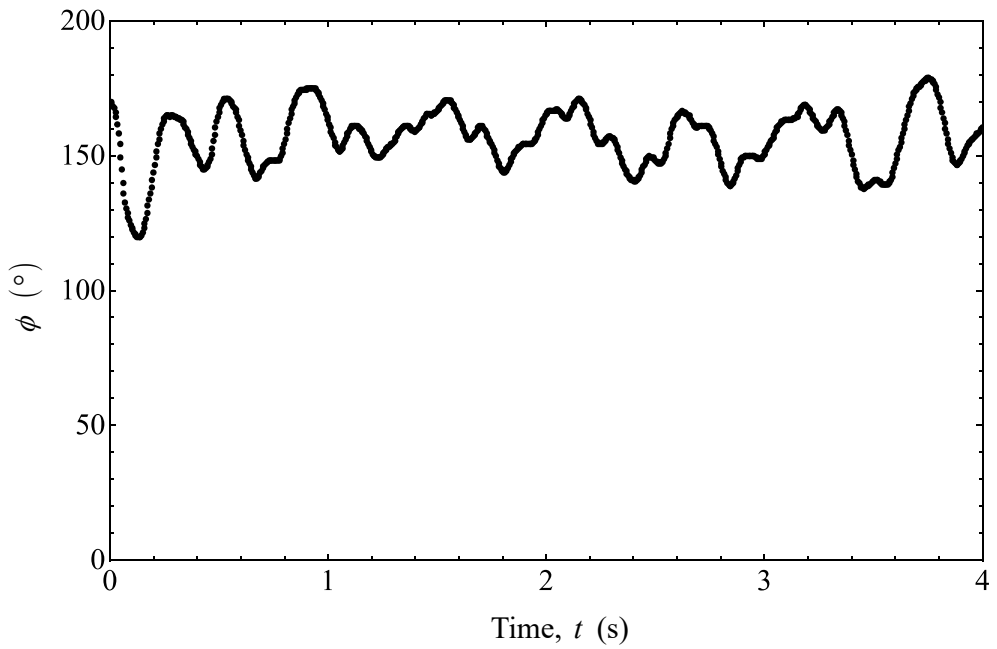


(b)

Figure 4.16: Temporal evolution of  $y^*$  and Cl at  $U^* = 15.9$ .

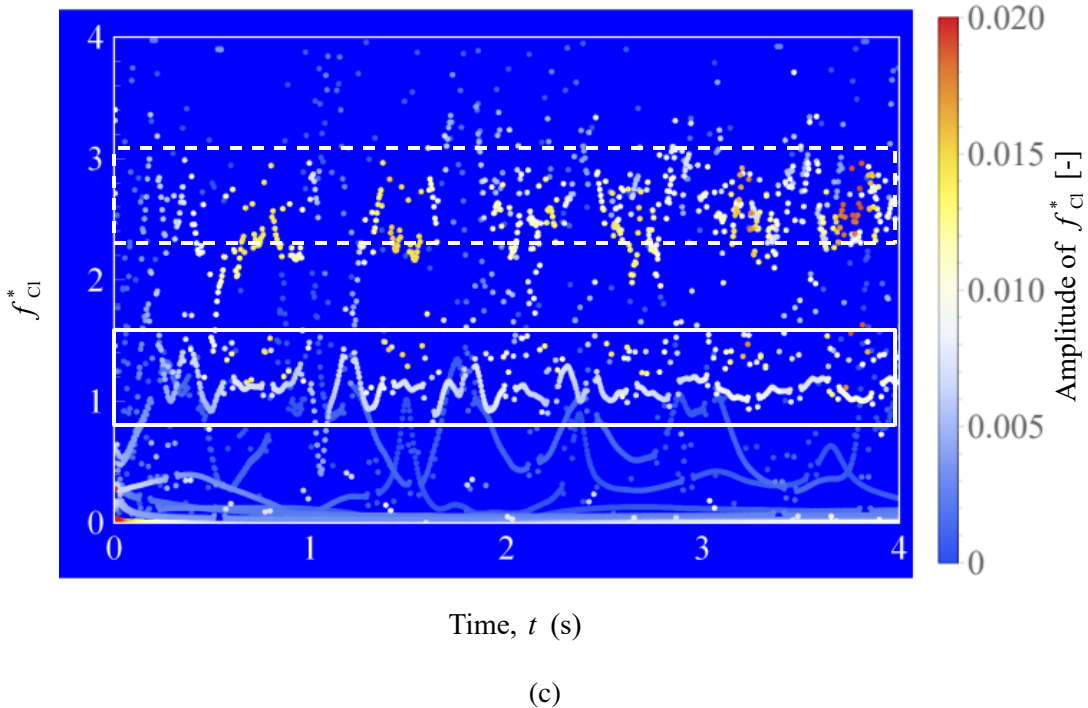


(a)



(b)

Figure 4.17: Temporal analysis of the lift coefficient and normalised cylinder displacement signal at  $U^* = 15.9$ .



(c)

Figure 4.17: Temporal analysis of the lift coefficient and normalised cylinder displacement signal at  $U^* = 15.9$ .

$f_{\text{Cl}}^* \approx 3.3$ , marked with a white dashed rectangular box. Computing the Strouhal number from this frequency returns a value of  $\text{St} = 0.20$ , which is very close to the Strouhal number for Karman vortices as predicted by Eq. 4.4 at the Reynolds number equivalent to  $U^* = 15.9$ , which is  $\text{Re} = 7.9 \times 10^3$ . This second band of frequency is thus attributed to the footprint left by the shedding of Karman vortices, and the first band as the result of streamwise vortex shedding. Through visual inspection of Fig. 4.17c, both of these dominant frequency bands are markedly wider and the individual values are more scattered from their time-averaged values than any of their counterparts within  $U^* \leq 13.6$ .

The knowledge that Karman vortices continue to exist and shed from a cruciform structure during SVIV is not new in the literature. However, this is the first time the lift signal from a cruciform structure undergoing SVIV has been subjected to EEMD, revealing the signature of the two dominant vortical structures regulating the flow around the cruciform. Although the amplitude size of the instantaneous frequency band due to Karman vortex is comparable to the streamwise vortex, the reason why the cylinder resists locking into its frequency is perhaps that its frequency too distant

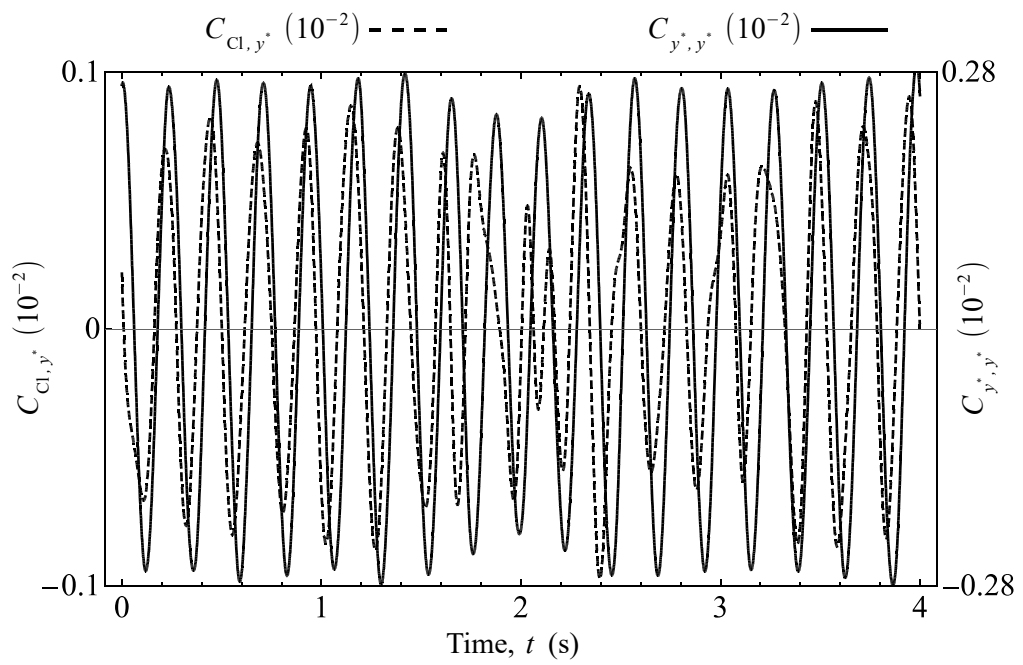
from the natural frequency of the system  $f_n$ . The shedding frequency of the streamwise vortex is much closer to  $f_n$  and is thus preferred by the cylinder.

The transition to SVIV is considered to be complete at  $U^* = 18.2$ , when the time-averaged phase lag drops further to  $\approx 20$  deg. Figure 4.18a and 4.18b documents this observation. The instantaneous phase lag is observed to slip through 360 deg. a little past the two second (2 s) time stamp. By inspecting Fig. 4.18a, one finds that a little past 2 s is when distortions in the periodicity of  $C_{Cl,y^*}$  occur. The slipping through 360 deg. was also observed by Khalak and Williamson (1999) in their work on KVIV, highlighting the quasi-periodic nature of the signal being analysed. There, the slip appeared in Khalak and Williamson (1999) at the initial branch of KVIV. The overall low value of  $\phi$  ( $\approx 20$  deg. for the whole observation time at  $U^* = 18.2$ ), coupled with the presence of  $\phi$  slippage are suggestive of the possibility for  $U^* = 18.2$  being the initial branch of SVIV.

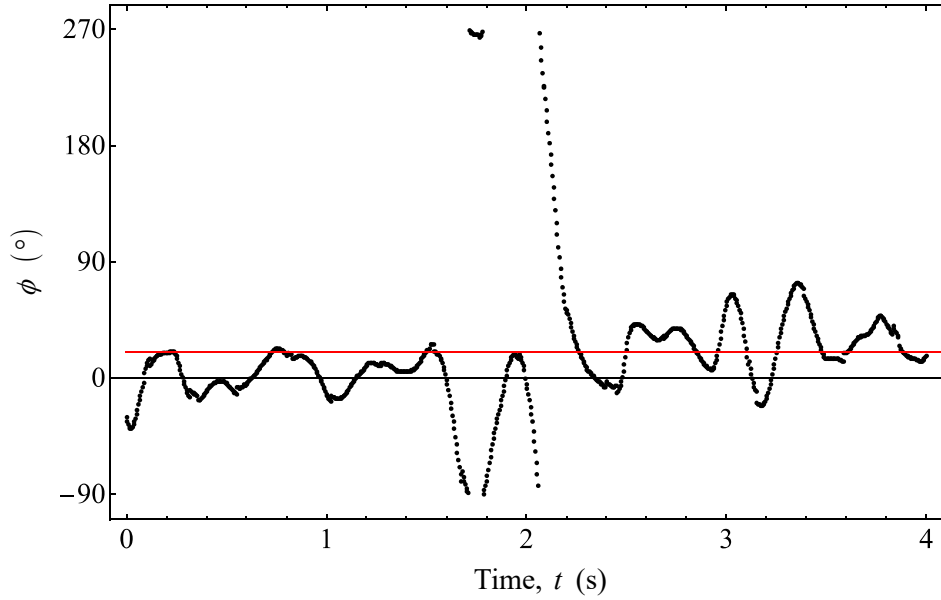
#### 4.2.3.3 The stable SVIV regime (reduced velocity greater than 20.5)

As  $U^*$  is increased to 20.5, a jump is observed in  $\phi$  from a mean value of approximately 20 deg. to about 120 deg., shown in Fig. 4.19a. The phase slippage discussed previously is also observed, indicating the quasi-periodic nature of the lift coefficient signal at this  $U^*$ . Incidentally, this quasi-periodicity seems to be the norm for the lift signals up to  $U^* = 27.3$ , as suggested by the phase slippages evident in Figs. 4.19b, c and d. The slippage only stops once  $U^*$  reaches 29.5, suggesting a more periodic behaviour of the lift coefficient compared to its counterparts between  $20.5 \leq U^* \leq 27.3$ . Although the instantaneous phase between  $20.5 \leq U^* \leq 27.3$  implies a quasi-periodic nature, their time-averaged values at each  $U^*$  are contained in the narrow region  $114 < \phi$  (deg.)  $< 135$ , as is the value for  $\phi$  at  $U^* = 29.5$ . This observation that the time-averaged value of  $\phi$  to only slowly vary with respect to  $U^*$ , once  $U^*$  increases past 20.5, can be interpreted as the dominant flow structures settling into a stable form that becomes more resilient against external excitations. Based on this feature,  $20.5 \leq U^* \leq 29.5$  is classified as the upper branch of SVIV.

The data on the evolution of  $\phi$  allows this work to construct a map of the “branches” of vibration modes observed in the range of  $U^*$  studied. As the branches

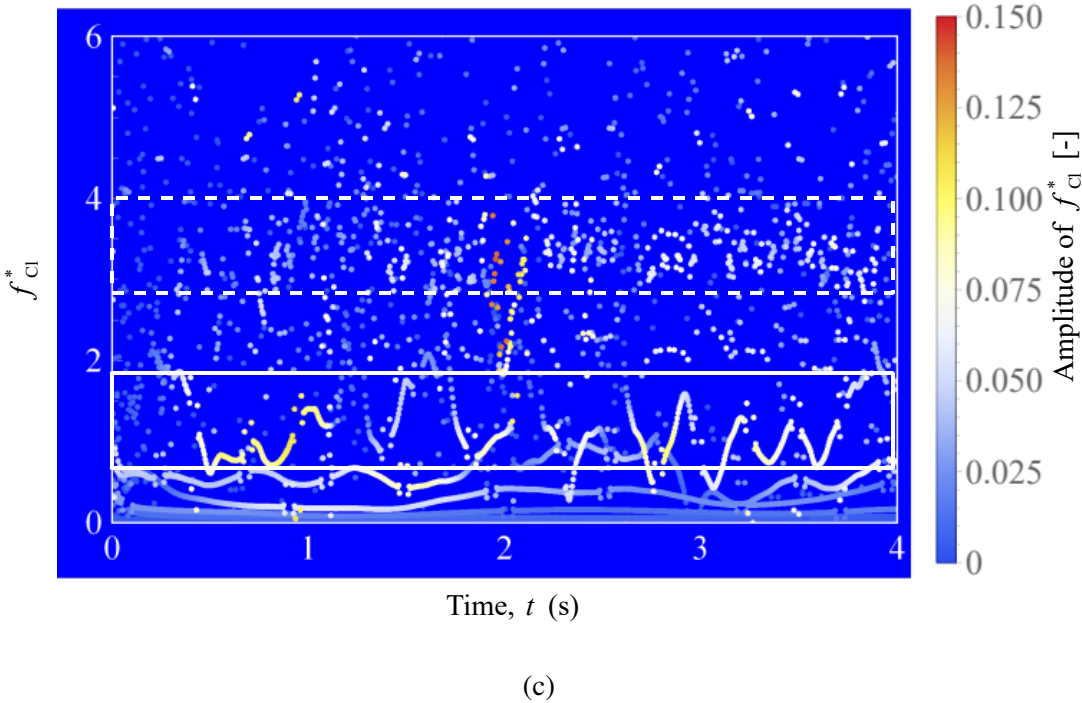


(a)



(b)

Figure 4.18: Temporal analysis of the lift coefficient and normalised cylinder displacement signal at  $U^* = 18.2$ .



(c)

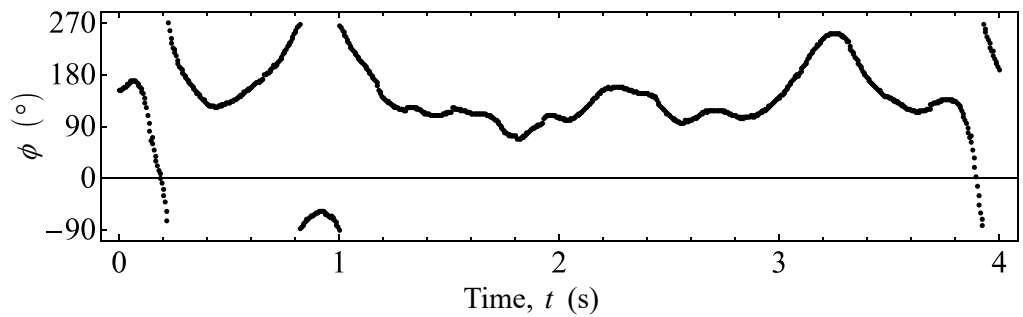
Figure 4.18: Temporal analysis of the lift coefficient and normalised cylinder displacement signal at  $U^* = 18.2$ .

are mapped against  $U^*$ , a representative value of  $\phi$  is needed at each  $U^*$ . To achieve this, the time-averaged values of  $\phi$  is taken, i.e.  $\phi_{\text{mean}}$ , and plotted them against  $U^*$  in Fig. 4.20. The region A indicates the initial branch of KVIV, where  $\phi_{\text{mean}}$  is close to zero. Region B denotes the upper/lower branch of KVIV, where the system experiences a jump from  $\phi_{\text{mean}} \approx 0$  to greater than 110 deg. The value of  $\phi_{\text{mean}}$  settles very close to 180 deg. towards the end of this upper/lower branch.

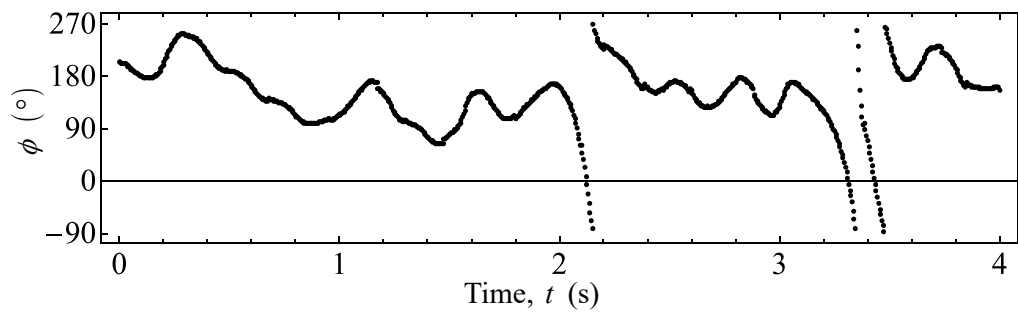
Then,  $\phi_{\text{mean}}$  experiences a slight drop from about one-sixth the value of  $\phi_{\text{mean}}$  in region B, as one enter region C, marking the start of the transition to the SVIV regime. Following this, the system undergoes a more sudden drop to  $\phi_{\text{mean}} \approx 20$  deg. at  $U^* = 18.2$ . This is designated as region D. Finally, in region E, another jump is observed in  $\phi_{\text{mean}}$  from  $\phi_{\text{mean}} \approx 20$  deg. in region D to approximately 120 deg. when  $U^* \geq 20.5$ .

#### 4.2.4 Harnessable power

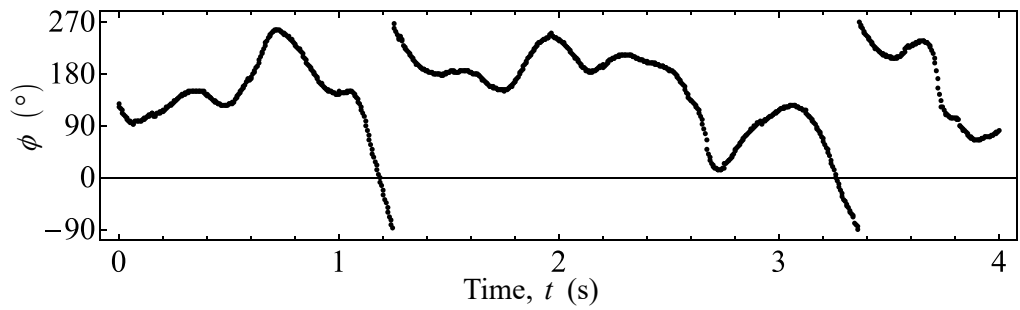
Figure 4.21 shows the comparison between power estimated from the experimental and numerical results, with the experimental results of Nguyen *et al.*



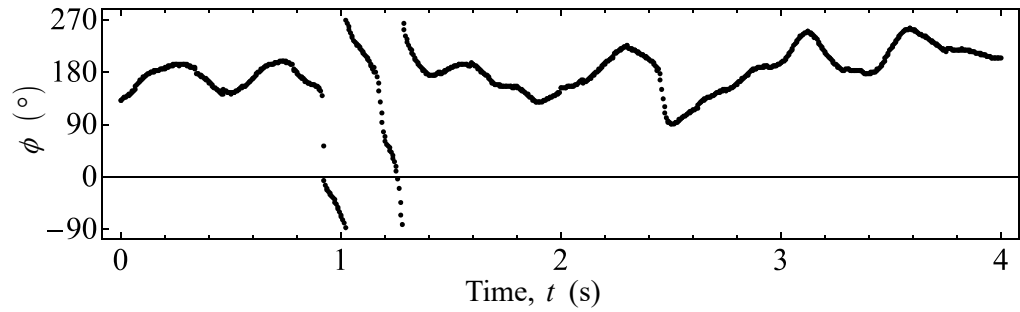
(a)



(b)



(c)



(d)

Figure 4.19: The instantaneous phase lag  $\phi$  of  $C_{\text{Cl},y^*}$  in the range  $20.5 \leq U^* \leq 29.5$ .

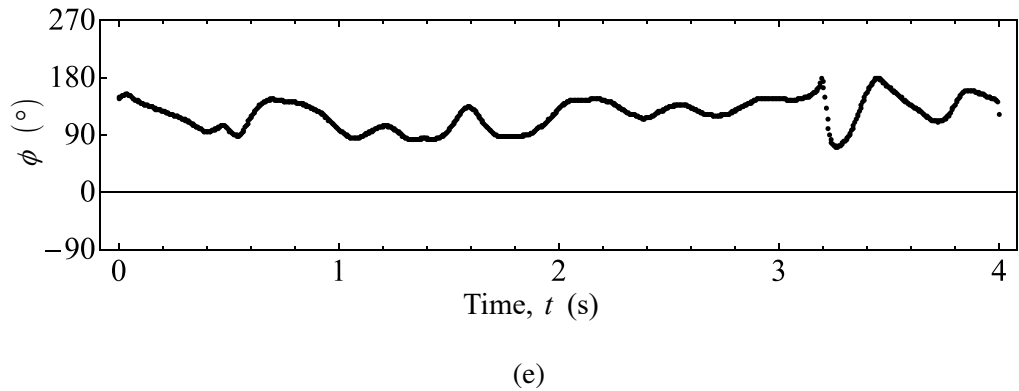


Figure 4.19: The instantaneous phase lag  $\phi$  of  $C_{\text{Cl},y^*}$  in the range  $20.5 \leq U^* \leq 29.5$ .

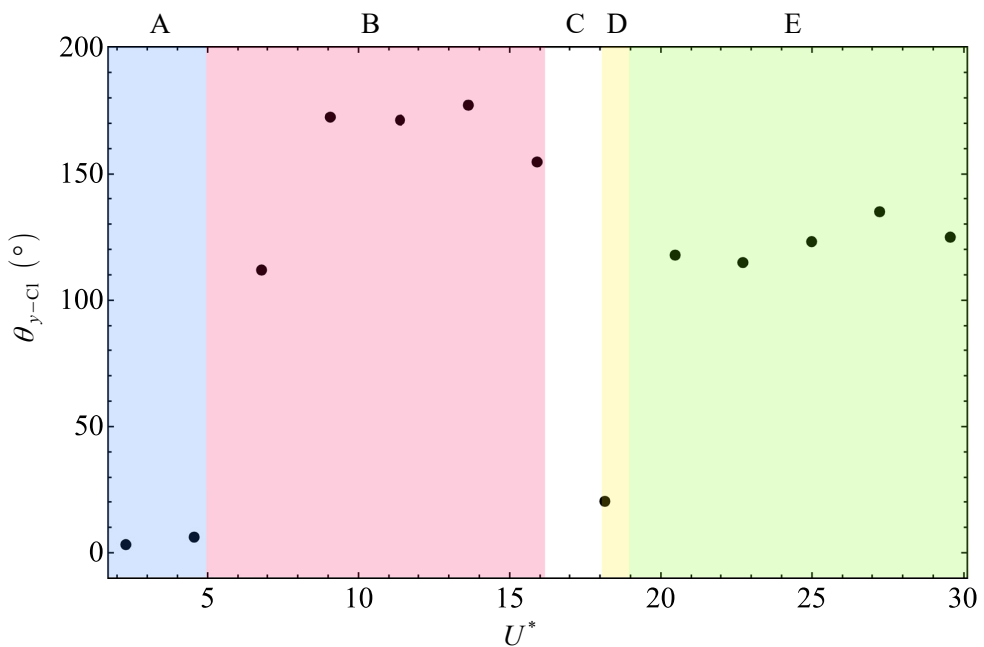


Figure 4.20: Variation of  $\theta_{y-\text{Cl}}$  with respect to  $U^*$ .

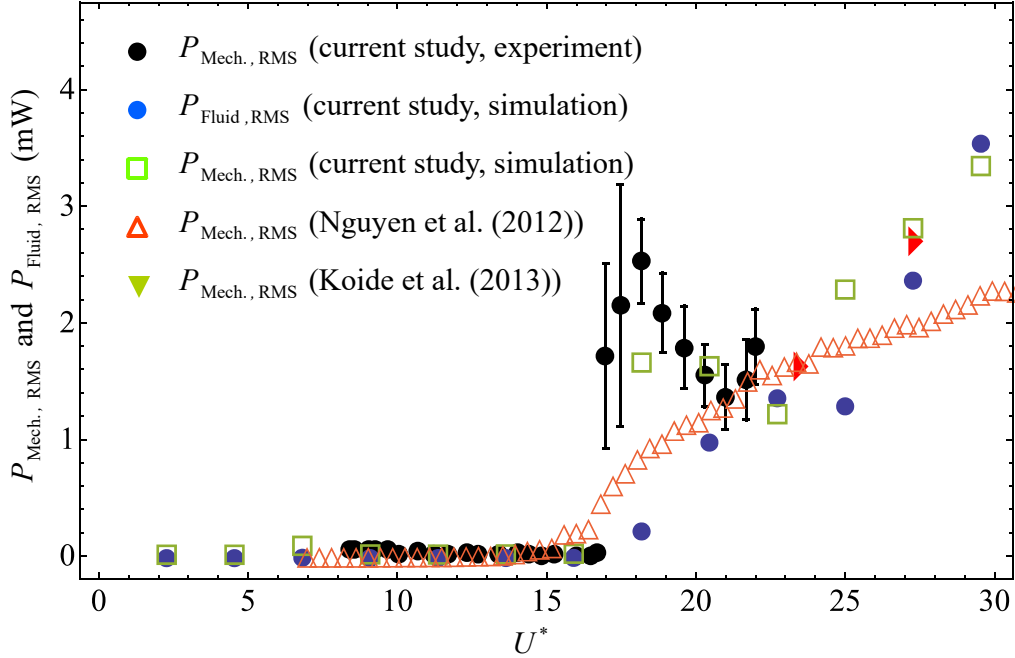


Figure 4.21: Estimation of  $P_{\text{Mech.}, \text{RMS}}$  and  $P_{\text{Fluid}, \text{RMS}}$  and comparison with available data.

(2012) and the direct power measurement of Koide *et al.* (2013). Only the value for  $P_{\text{Mech.}, \text{RMS}}$  is computed from the experimental results due to the absence of lift data. The numerical results have both lift and cylinder displacement data, from which both  $P_{\text{Fluid}, \text{RMS}}$  and  $P_{\text{Mech.}, \text{RMS}}$  are computed. The power is estimated from the experimental results of Nguyen *et al.* (2012) by interpolating missing data points in both their amplitude and frequency responses to compute the value of  $P_{\text{Mech.}, \text{RMS}}$  at a given value of  $U^*$ . The direct power measurement by Koide *et al.* (2013) was done by connecting the elastic support of the cylinder to a coil. The coil moves with the cylinder, thus creating a relative piston motion against a fixed magnet and produces an alternating current.

The estimated power in the KVIV regime  $U^* \leq 15.9$  produces power only in the order of  $\mu\text{W}$ , which is relatively insignificant in contrast to the magnitude of power produced in the SVIV regime (mW). In the region  $18.2 \leq U^* \leq 22.7$ ,  $P_{\text{Mech.}, \text{RMS}}$  for in the experimental and numerical work exhibits a similar trend where a sudden jump in power output is observed, followed by a gradual decrease. This gradual decrease can be attributed to the increased turbulence level right after the onset of SVIV that imposes a degree of intermittency to the normalised cylinder displacement

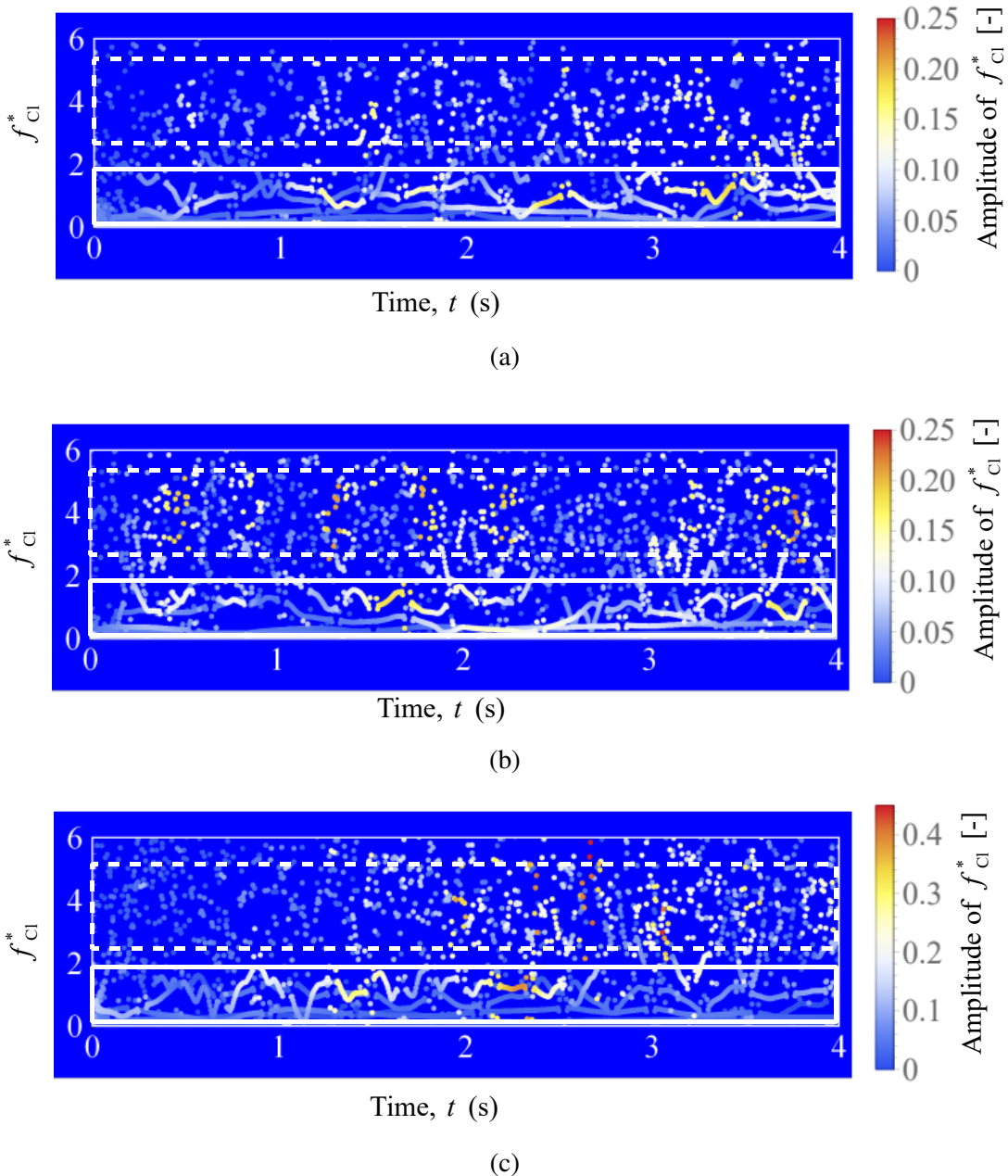
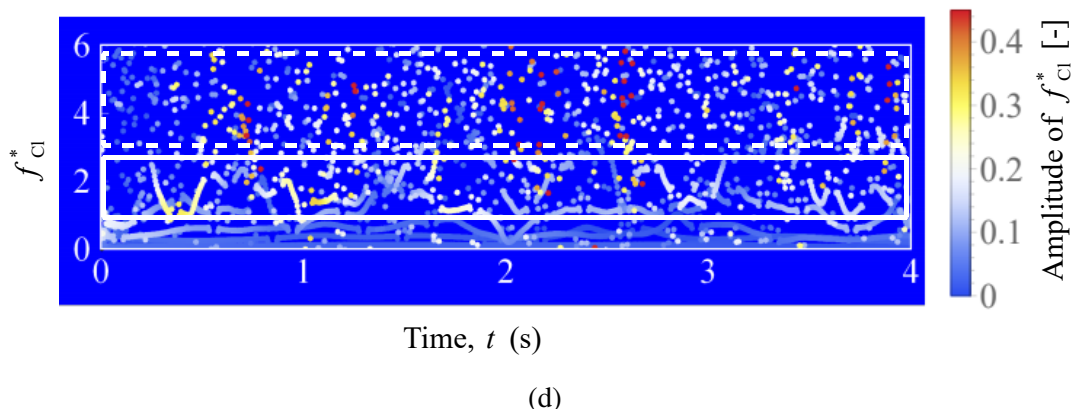
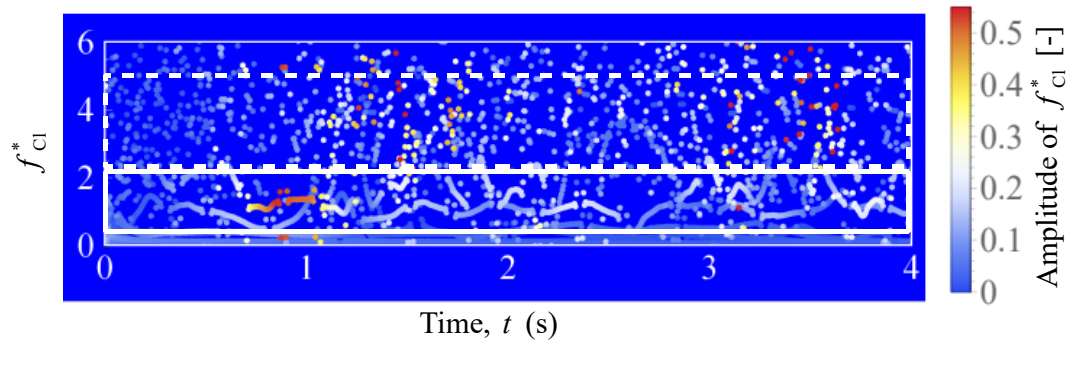


Figure 4.22: The HHT spectrogram of Cl between  $20.5 \leq U^* \leq 29.5$ . The solid and dashed line white boxes delineate the distribution of the streamwise and Karman components of lift, respectively.



(d)



(e)

Figure 4.22: The HHT spectrogram of Cl between  $20.5 \leq U^* \leq 29.5$ . The solid and dashed line white boxes delineate the distribution of the streamwise and Karman components of lift, respectively.

signal,  $y^*$ . For  $P_{\text{Fluid,RMS}}$ , however, the quantity exhibits a monotonic increase in the range  $18.2 \leq U^* \leq 22.7$ . A dip in  $P_{\text{Fluid,RMS}}$  is only observed at  $U^* = 25.0$ , suggesting an increase in intermittency of  $C_{\text{Cl},y^*}$  at this  $U^*$ . In the experimental work of Nguyen *et al.* (2012),  $P_{\text{Mech.,RMS}}$  only experiences a monotonic increase in the region  $18.2 \leq U^* \leq 22.7$ . This decidedly different response of the system compared to ours most likely stem from the difference in the actual cruciform used by Nguyen *et al.* (2012). They used two circular cylinders of diameter 10 mm as their cruciform, whereas this study used a circular cylinder - strip plate in both the experiments and numerical work. There are no data from the direct power measurement of Koide *et al.* (2013) to compare with within  $18.2 \leq U^* \leq 22.7$ .

In the range  $25.0 \leq U^* \leq 29.5$ , a reasonably good agreement is found between the trend found in all data compared: they increase monotonically with respect to  $U^*$ . Although the value of  $P_{\text{Fluid,RMS}}$  falls quite notably below the value of  $P_{\text{Mech.,RMS}}$  at  $U^* = 25.0$ , other values of  $P_{\text{Fluid,RMS}}$ ,  $P_{\text{Mech.,RMS}}$  from the numerical results and the direct power measurements by Koide *et al.* (2013) agree well within  $27.3 \leq U^* \leq 29.5$ . The only set of power data that consistently falls quite a distance below the others is the  $P_{\text{Mech.,RMS}}$  estimated from the experimental data of Nguyen *et al.* (2012), which again, is most probably due to the difference in the actual geometry of the cruciform used in their investigation.

#### 4.2.5 Possibility for increasing fluid power

Recall in Fig. 4.21 that although  $P_{\text{Fluid,RMS}}$  is computed according to Eq. 3.15, which uses  $C_{\text{Cl,RMS}}$  instead of the actual root-mean-square amplitude of lift ( $\text{Cl}_{\text{RMS}}$ ), the resulting power estimate does not result in a trend that is totally different from the trend found in the other datasets. Furthermore, except for  $P_{\text{Mech.,RMS}}$  estimated from the experimental data of Nguyen *et al.* (2012), the values of  $P_{\text{Fluid,RMS}}$  are in fairly good agreement with other data that it is compared against at high  $U^*$  ( $U^* = 27.3$  and 29.5). One can interpret this as an indication that the lift component selected for use in computation of  $P_{\text{Fluid,RMS}}$  is an arguably faithful representation of the force driving the motion of the cylinder. This suggests that the motion of the cylinder, once it enters the SVIV regime, is driven only by one component, and not the totality, of the lift force.

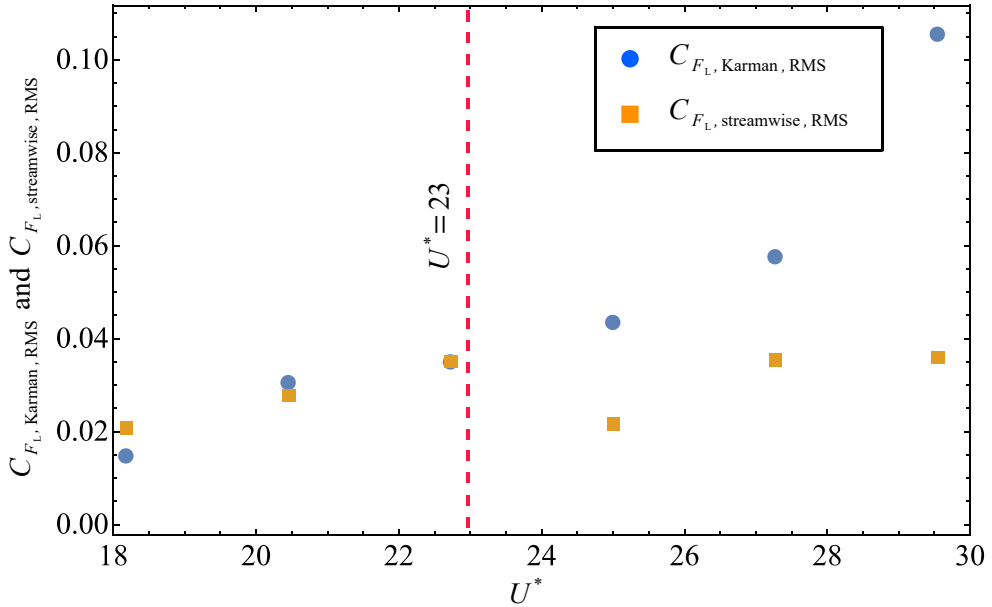


Figure 4.23: Evolution of  $C_{F_L, \text{Karman,RMS}}$  and  $C_{F_L, \text{streamwise,RMS}}$  with respect to  $U^*$ .

This component – that has a time-averaged frequency close to the natural frequency of the system,  $f_n$  – is the “streamwise component” of lift.

Another significant IMF component of the lift force in the SVIV regime is the component whose mean frequency is close to the Karman frequency of vortex shedding, as explained in §4.2.3.2. This Karman component of lift has a similar amplitude size as the streamwise component of lift, as evidenced in Fig. 4.22, and as such is also a dominant component of lift. The Karman components are marked with a dashed, white box, and the streamwise components are marked with a solid, white box, following the convention in Figs. 4.13, 4.14, 4.15, 4.17 and 4.18. However, the Karman component fails to affect the cylinder vibration like the streamwise component most probably due to the large difference between the mean frequency of the Karman component and the natural frequency of the system,  $f_n$ . The streamwise component has a mean frequency close to  $f_n$  and is hence able to synchronise with the vibration of the cylinder, producing a sizeable amplitude response.

Figure 4.23 shows the root-mean-square amplitude of the Karman and streamwise components of lift in the SVIV regime  $U^* \geq 18.2$ . Between  $18.2 \leq U^* \leq 22.7$ , the magnitude of the Karman and streamwise components are nearly equal.

However, once one exceeds  $U^* = 22.7$ , Fig. 4.23 shows that the contribution to the root-mean-square amplitude of total lift by the Karman component is on average twice the contribution of the streamwise component. Having such a significant contribution towards the root-mean-square amplitude of total lift implies that there is a significant portion of energy from the free stream being used to energise the Karman vortex structure in the flow. Assume a hypothetical situation where one can transfer the contribution by the Karman component to the streamwise component of lift. In other words, consider the situation where an individual can completely redirect the energy from the Karman to the streamwise vortex. Then, the value for  $C_{Cl,RMS}$  in Eq. 3.15 will increase close to a factor of 2 when  $18.2 \leq U^* \leq 22.7$ , and close to a factor of 3 when  $25.0 \leq U^* \leq 29.5$ . This increase in  $C_{Cl,RMS}$  will lead to the scaling of  $P_{Fluid,RMS}$  by the same factor, keeping the other parameters in Eq. 3.15 constant. This exercise demonstrates the room for improvement possible for  $P_{Fluid,RMS}$  in future developments of cruciform energy harvesters.

One possible method of improving  $P_{Fluid,RMS}$  is by implementing a modified version of the cruciform that is able to enforce the dominance of the vortical structure that is able to lock into  $f_n$  - which in Fig. 4.23 is the streamwise vortex - against the vortical structures that do not, i.e., the Karman vortices. This study explores one method – namely the method of cruciform angle variation – to achieve said dominance in the following sections.

#### 4.2.6 Section Summary

In this section, the present author investigated the amplitude/frequency responses of the pure cruciform and compared them to the experiment done in the open flow channel, and with experimental works of others in the literature. In doing so, this work found good agreement between the amplitude responses and observed fair agreement between the frequency responses. The discrepancy in the frequency responses are attributed to the high resolution of observation obtainable through the use of CFD, which is not obscured by random excitation frequencies present in experimental works.

This chapter also decisively demonstrated the vortical structures present in the flow during the high-amplitude vibrations of SVIV, which are observed to be due to the alternate shedding of large-scale streamwise vortices. Karman vortices continue to be shed in the region away from the juncture of the cruciform, but the region close to the juncture is dominated by streamwise vortex shedding.

The amplitude response is highly dependent on the resulting lift signal, and the Hilbert-Huang transforms allows this study to compute the instantaneous phase lag between the lift and cylinder displacement signals - a first in the study of VIV in cruciform oscillators. Through the decomposition of the lift signal via EEMD, this study discovers that there is an increase in the level of intermittency of the signal, causing a dip in the amplitude response during the early stages of the onset of SVIV. The results here demonstrate that there exists two main parts to the lift signal, namely the contribution due to the shedding of streamwise vortex and the contribution due to the shedding of Karman vortex.

The existence of two dominant components in the lift signal explains the saturation of  $y_{\text{RMS}}^*$  in the amplitude response curve, wherein a significant amount energy from the freestream is lost due to the production of Karman vortices. During the estimation of harnessed power, this thesis found that the power output can potentially be improved by a factor of two to a factor of three depending on  $U^*$ . This is a major finding in that it informs the present author not only of the potential improvement possible from a cruciform energy harvester, but also indicates that in order to achieve such an improvement, the cruciform need to be fashioned in such a way that there exists only one vibration-driving mechanism in the system. The following chapter attempts to evaluate the ability of an angled cruciform in achieving this target.

### 4.3 Steep-angled cruciforms

The discovery made towards the end of §4.2 strongly supports the assertion that there is still plenty of room for improvement in terms of power output and efficiency for the cruciform energy harvester. The fact that in a pure cruciform, during SVIV, a significant portion of the freestream energy forked to sustain the formation of Karman vortices that **does not** contribute to energise the cylinder vibration seems to strongly

suggest control of the vibration-driving vortical structures as the next logical step to break through the maximum effective lift, i.e.,  $C_{F_L,\text{streamwise,RMS}}$  observed in §4.2.5.

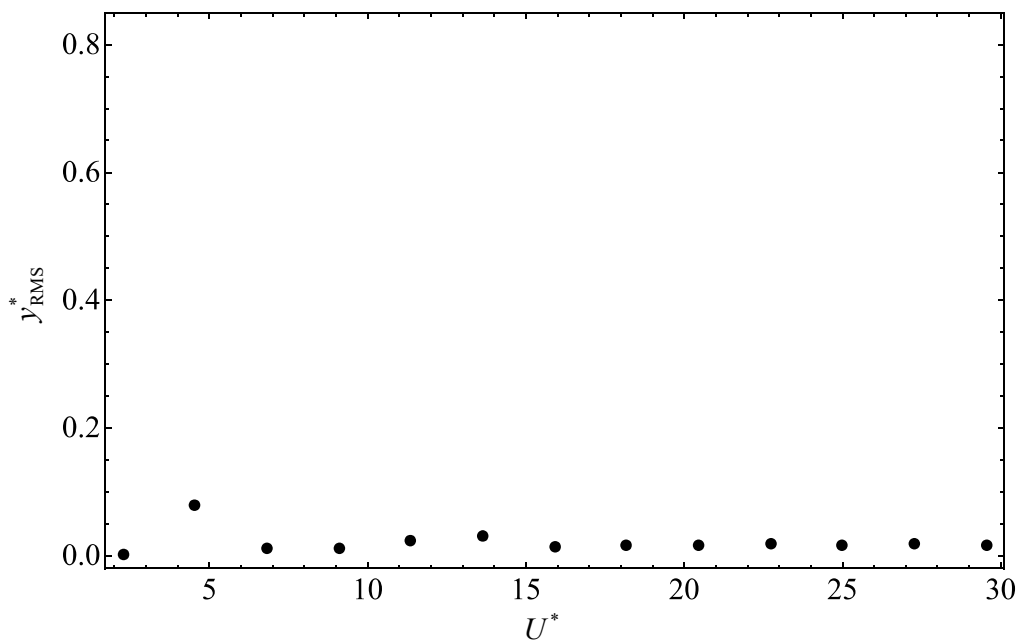
To achieve this, this study attempts to retard the formation of either one of the dominant vortical structures observed in the pure cruciform oscillator, preferably the Karman vortices since for the pure cruciform, the high-amplitude vibrations are driven by streamwise vortex shedding. In a manner similar to how the downstream strip plate was introduced to a single oscillator unit to suppress the Karman vortex shedding, perhaps a modified configuration of the downstream strip plate can potentially bring about an even more vigorous inhibition of Karman vortex shedding and thus direct a bigger portion of energy from the freestream towards the large-scale streamwise vortex. The modification chosen for this purpose is the rotation of the downstream strip plate and the resulting angle between the upstream circular cylinder and the strip plate.

This section investigates the amplitude/frequency responses of steep-angled cruciforms ( $67.5^\circ \leq \alpha(\circ) \leq 45^\circ$ ), the vortical structures behind the amplitude/frequency responses, and how the vortical structures influence the lift acting on the cylinder and subsequently the phase lag between the Cl and  $y^*$  to locate branches that can be exploited for energy harvesting.

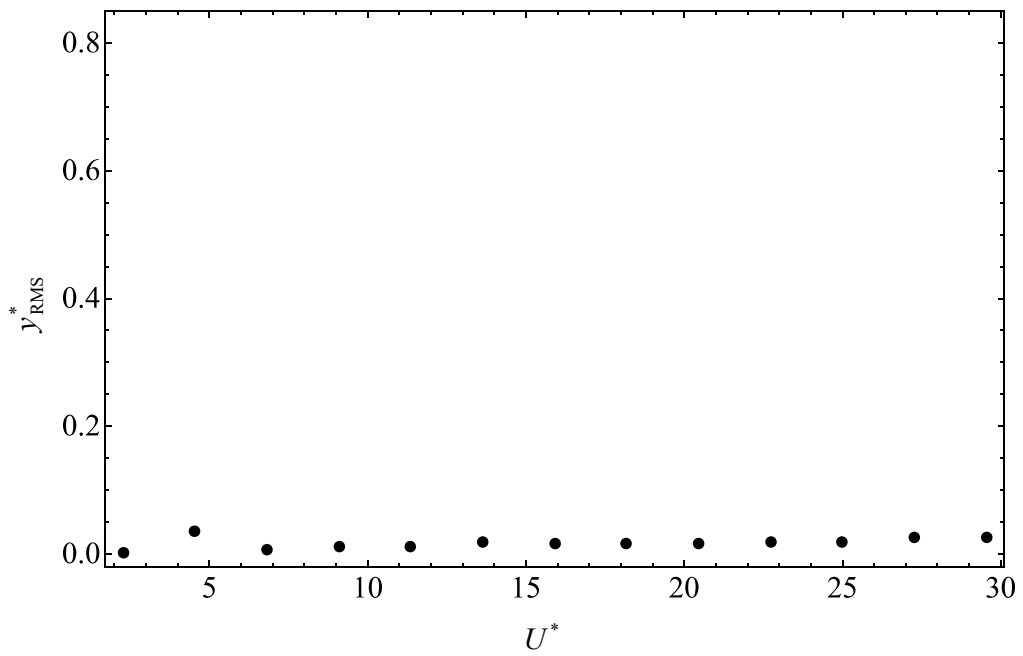
#### 4.3.1 The amplitude and frequency response

As the cruciform angle is reduced to  $67.5^\circ$  and  $45^\circ$ , the SVIV branch observed in the pure cruciform case as  $U^* \geq 15.9$  disappear, as one can inspect in Fig. 4.24. For the  $45^\circ$  cruciform, even  $y_{\text{RMS}}^*$  at the KVIV upper branch ( $U^* = 4.5$ ) is lower than the corresponding values for both the  $90^\circ$  and  $67.5^\circ$  cruciforms.

Another striking departure from the trend observed in the pure cruciform case, can be found in the evolution of  $f^*$  in Fig. 4.25. For the  $67.5^\circ$  cruciform in Fig. 4.25a,  $f^*$  seems to fluctuate with respect to  $U^*$  - suggesting asymmetry in the vortical structures regulating the vibration as discussed previously in §4.2.1. This fluctuation is however, not as pronounced in Fig. 4.27b, compared to Fig. 4.27a. This behaviour is perhaps due to the  $45^\circ$  cruciform being less similar to the  $90^\circ$  cruciform, in contrast to  $67.5^\circ$ . In other words, the  $45^\circ$  cruciform is less in transition from the response of the



(a) The  $67.5^\circ$  cruciform.



(b) The  $45^\circ$  cruciform.

Figure 4.24: Evolution of the normalised root-mean-square amplitude of cylinder displacement  $y^*_{\text{RMS}}$ , with respect to reduced velocity  $U^*$ , for the  $67.5^\circ$  and  $45^\circ$  cruciform.

$90^\circ$  cruciform and the flow around it is more evolved into its new configuration, unlike the  $67.5^\circ$  cruciform.

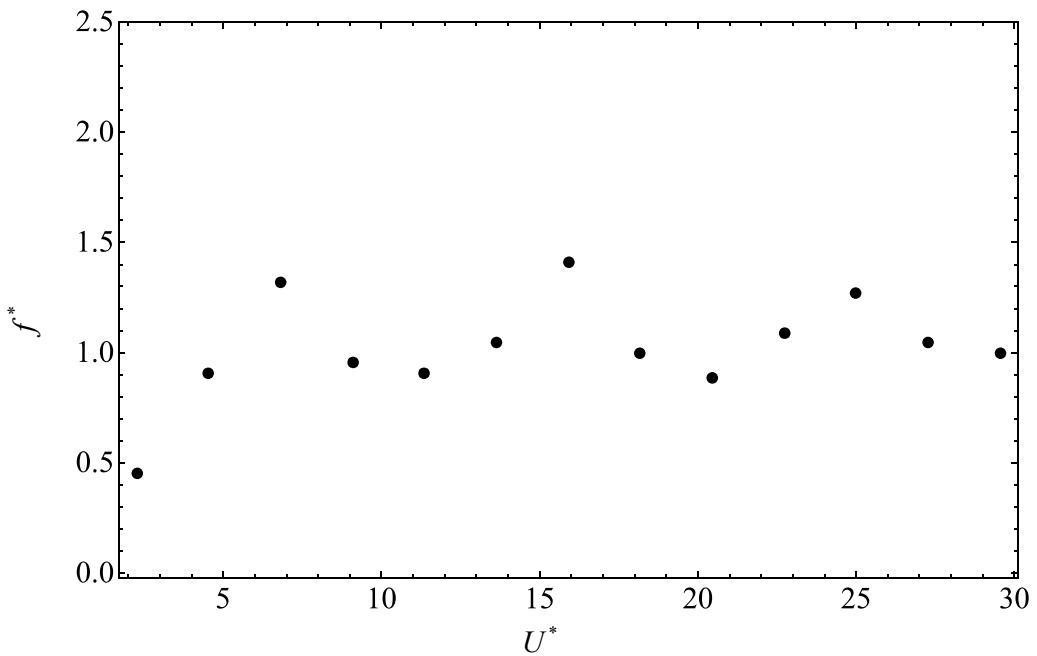
The root-mean-square lift coefficients  $Cl_{RMS}$  of the  $67.5^\circ$  and  $45^\circ$  cruciforms are summarised in Fig. 4.24. The results showed that their evolution with respect to  $U^*$  in Figs. 4.26a and 4.26b approximates their corresponding  $y_{RMS}^*$  trend in Figs. 4.24a and 4.24b. As for the variation of  $f_{Cl}^*$  with respect to  $U^*$ , for both the  $67.5^\circ$  and  $45^\circ$  cruciforms, both exhibit outstanding similarity to  $f_{v,Karman}$  of Eq. 4.4. This trait hints that vibrations resulting from the  $67.5^\circ$  and  $45^\circ$  cruciforms are primarily regulated by the shedding of Karman vortices.

The fact that the  $f_{Cl}^*$  trends observed in Figs. 4.27a and 4.27b do not lead to similar trends in the evolution of  $f^*$  in Figs. 4.25a and 4.25b leads this investigation to believe there is something more fundamental at play in developing the  $f^*$  patterns observed in Figs. 4.25. Hence the vortical structures present in the flow surrounding the  $67.5^\circ$  and  $45^\circ$  cruciforms are examined, the findings of which are discussed in §4.3.2.

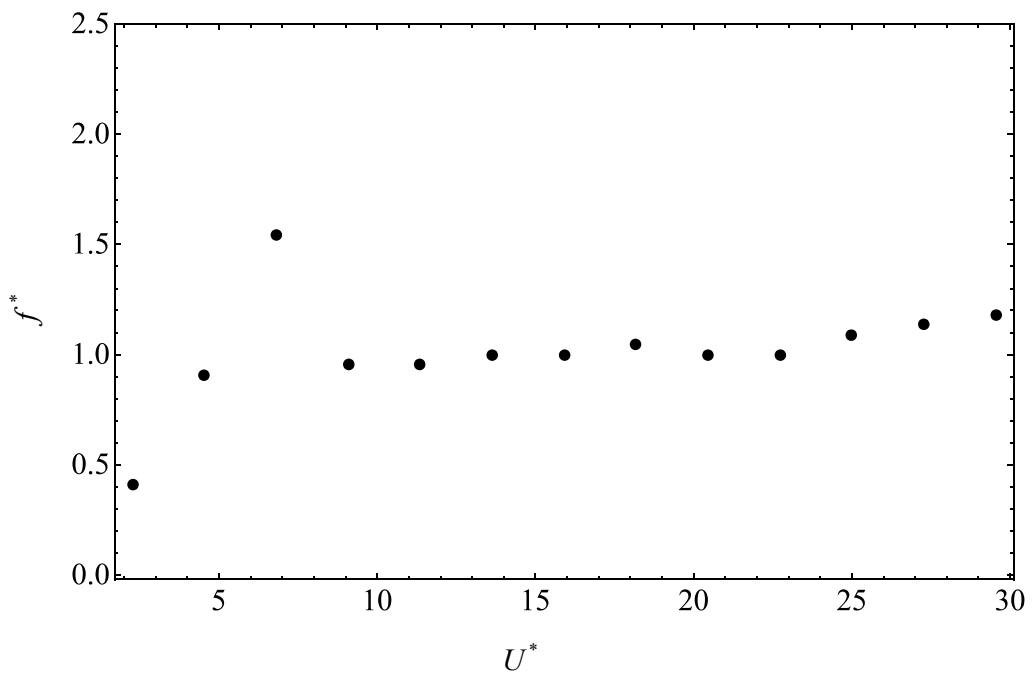
### 4.3.2 Main vibration-driving vortical structure

As the first step, the FFT of the  $y$ -component of velocity is computed similar to what was done in Fig. 4.9 for both the  $67.5^\circ$  and  $45^\circ$  cruciforms. Initial assessment of the  $f_{v,Karman}^*$  distribution along the cylinder axis in Figs. 4.28a and 4.28b is that there is a strong representation of the Karman shedding frequency in both cases, which at  $U^* = 22.7$  is  $f_{v,Karman}^* = 4.49$ . However, unlike Fig. 4.9, there is no frequency band close to 1 around the cruciform juncture.

The first guess is that streamwise vortices driving the vibration in the pure cruciform case do not get initiated once the cruciform angle deviates away from  $90^\circ$ . However,  $x$  and  $z$ -component vorticity visualisations in Fig. 4.29 points out otherwise. These visualisations are produced under the same conditions as Fig. 4.10. Inspecting Figs. 4.29a and 4.29c, one can quite clearly make out the large-scale streamwise vortices close to the cruciform juncture. The cylinder vibration and streamwise vortices are thus expected to synchronise to each other, resulting in an  $f^* \approx 1$  accross the values of  $U^*$ .

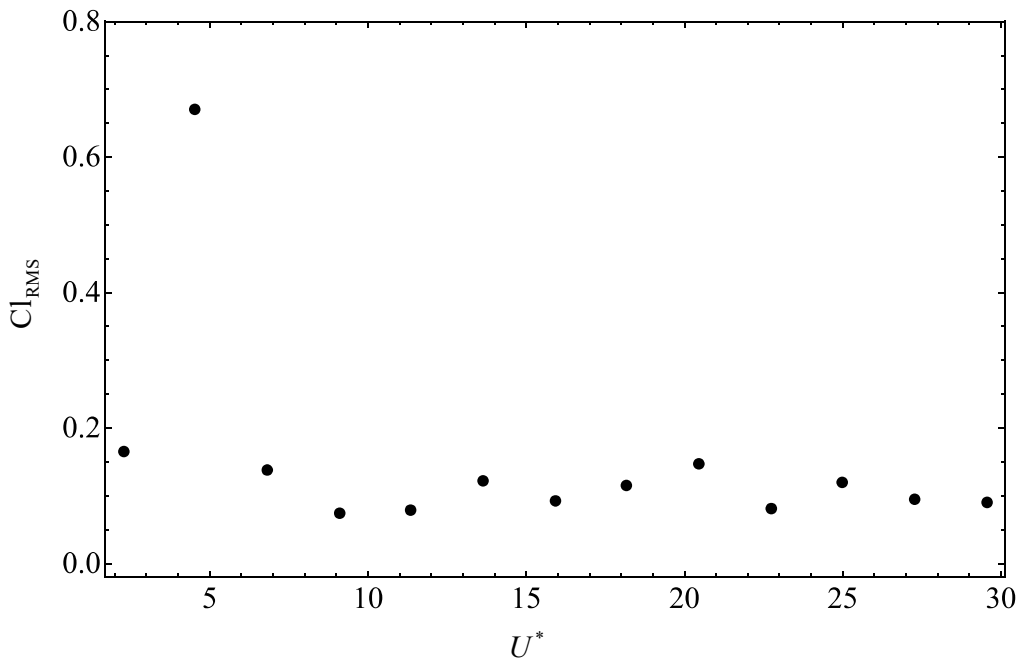


(a) The  $67.5^\circ$  cruciform.

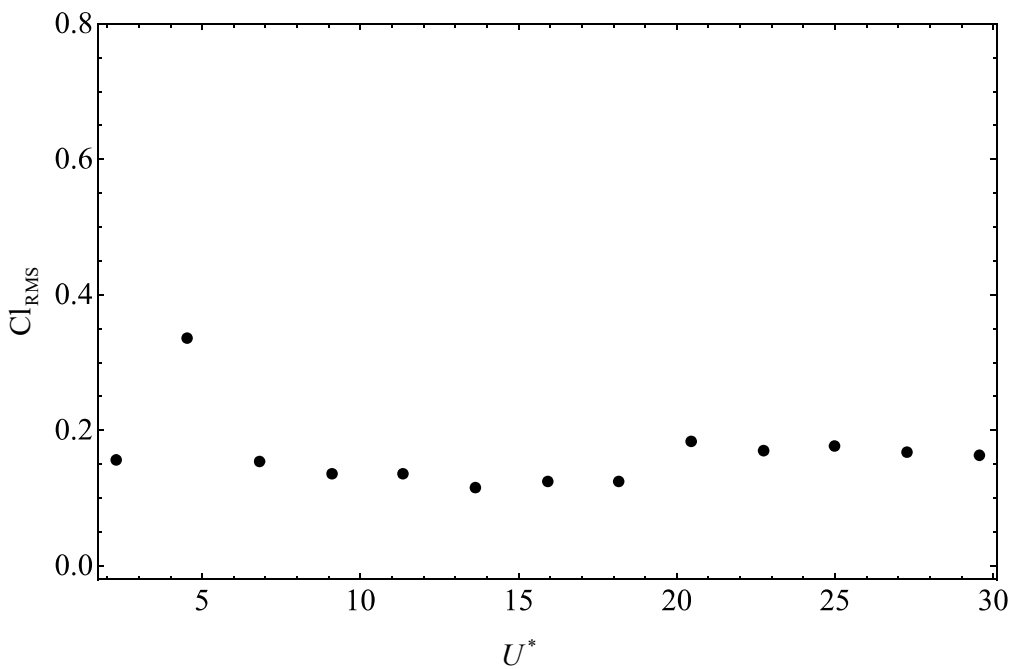


(b) The  $45^\circ$  cruciform.

Figure 4.25: Evolution of the normalised cylinder displacement frequency,  $f^*$ , with respect to reduced velocity  $U^*$ , for the  $67.5^\circ$  and  $45^\circ$  cruciforms.

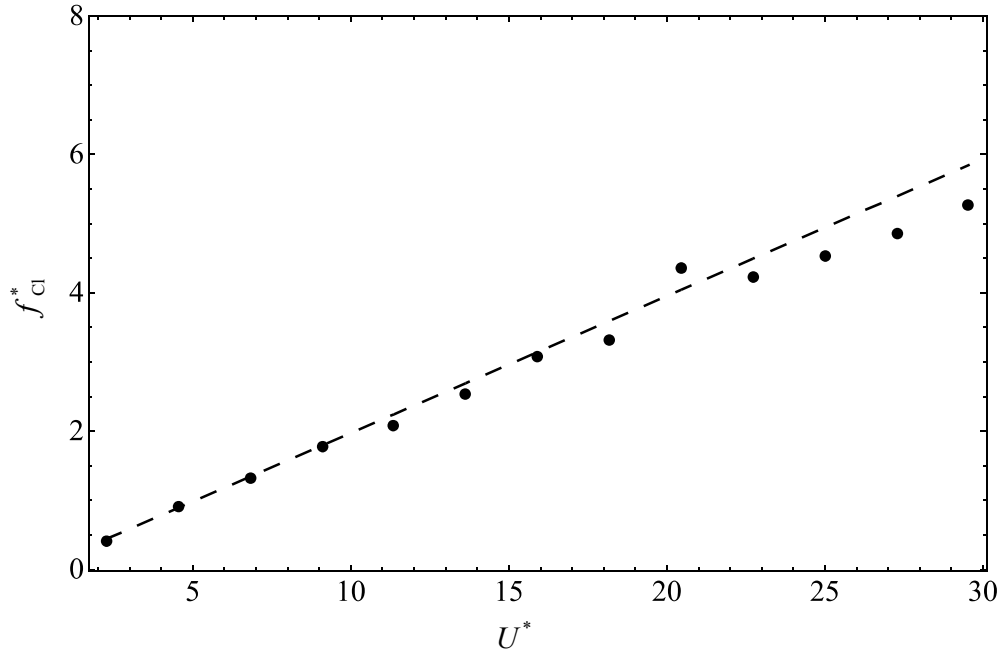


(a) The  $67.5^\circ$  cruciform.

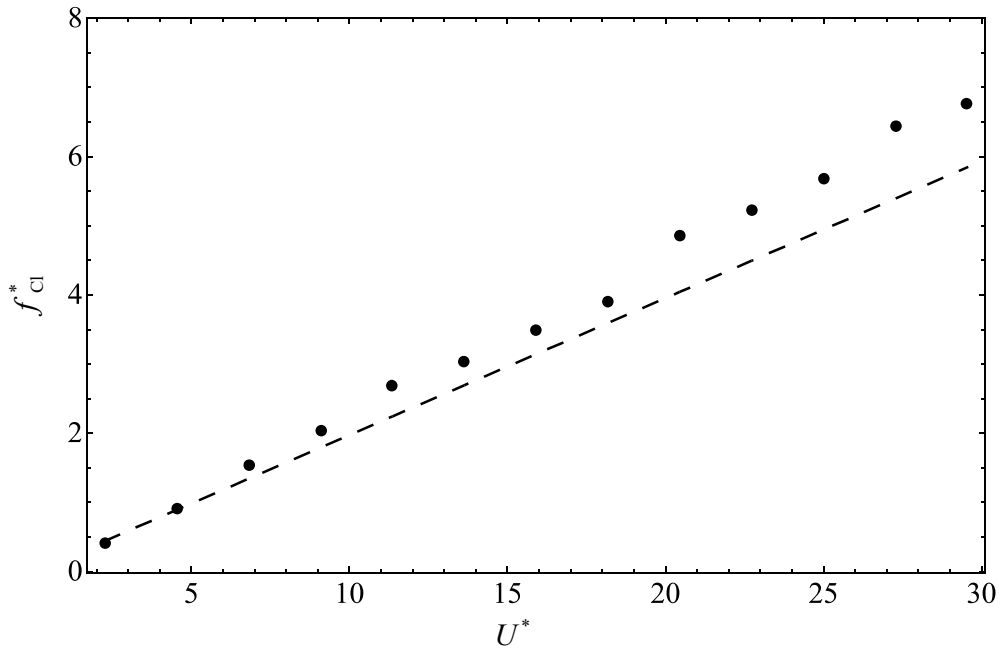


(b) The  $45^\circ$  cruciform.

Figure 4.26: Evolution of the normalised Cl root-mean-square amplitude,  $Cl_{RMS}$ , with respect to reduced velocity  $U^*$ , for the  $67.5^\circ$  and  $45^\circ$  cruciforms.



(a) The  $67.5^\circ$  cruciform.



(b) The  $45^\circ$  cruciform.

Figure 4.27: Evolution of the normalised Cl frequency,  $f_{\text{Cl}}^*$ , with respect to reduced velocity  $U^*$ , for the  $67.5^\circ$  and  $45^\circ$  cruciforms. The dashed lines outline  $f_{v,\text{Karman}}$  from Eq. 4.4.

after the lower branch of KVIV which appears at  $U^* = 6.8$ . In addition, a large amplitude response is expected from the cylinder due to the formation and sustenance of the streamwise vortices close to the cruciform juncture. This was not the case.

The reason behind this is thought to lie in the distribution of the streamwise vortex cells along the cylinder axis. As mentioned in §4.2.2, the streamwise vortex pair in the pure cruciform case lie on a plane parallel to the axis of the cylinder. The shared plane of formation parallel to cylinder axis is what seems to be the key to the large amplitude response observed in the pure cruciform case. A formation plane parallel to the cylinder axis ensures the resulting downward thrust to act perpendicular to the cylinder, securing a larger amplitude response. Also, the streamwise vortex cell on each side of the  $Z = 0$  plane must be of opposing rotational direction for the production of thrust. These two aspects are found to be missing in the  $67.5^\circ$  and  $45^\circ$  cruciforms in Fig. 4.29.

What takes place in Figs. 4.29a and 4.29c is, two streamwise vortex cells of opposing poles form on each side of the  $Z = 0$  plane. The result of this vortical arrangement is severe diminishing of useful thrust, and by extension, lift acting on the cylinder. This explains why the amplitude of  $f_v^*$  at and within the vicinity of 1 is extremely small in comparison to the dominant band close to  $f_{v,\text{Karman}}^* = 4.49$ , resulting in a low amplitude response for most of the  $U^*$  studied, even when  $f^* \approx 1$ .

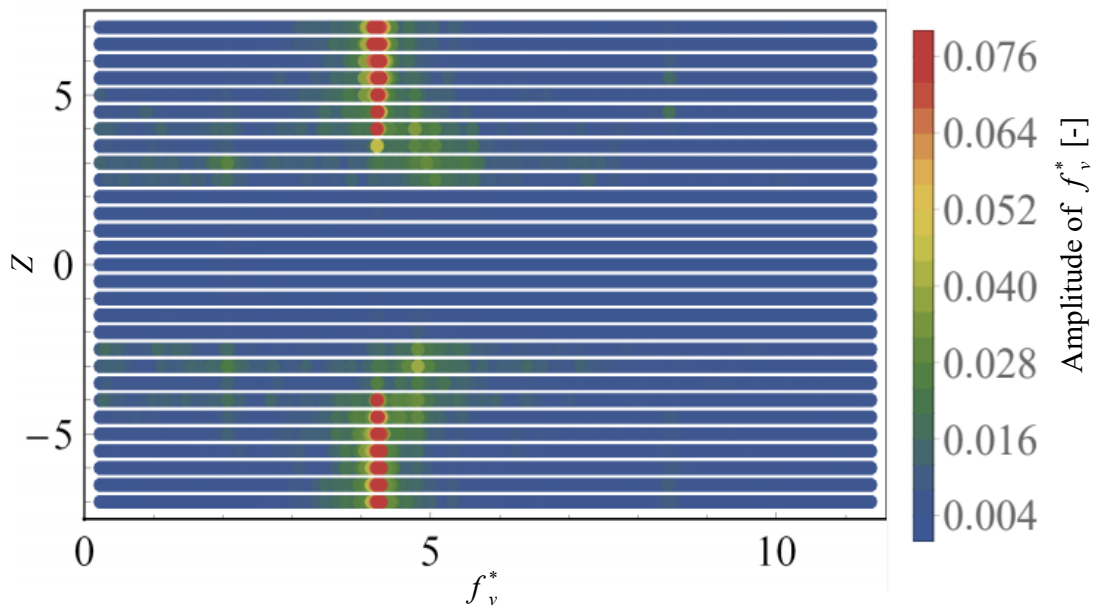
The source of asymmetry in the vortical structure distribution around the cruciform is also found, which becomes apparent upon closer comparison of Fig. 4.29b and Fig. 4.29d. The Karman vortices of the  $67.5^\circ$  cruciform are shed at different phases depending on which side of the  $Z = 0$  plane they are observed. For the particular case in Fig. 4.29b, Karman vortices are being shed from the top of the cylinder when  $Z < 0$ , and from the bottom of the cylinder when  $Z > 0$ . What suggested this interpretation is the observation of a strong expression of  $-z$  vorticity when  $Z < 0$  from the top of the cylinder, while on the  $Z > 0$  half of the domain is a strong expression of  $+z$  vorticity from the bottom of the cylinder. This does not seem to take place in Fig. 4.29d. On both sides of the  $Z = 0$  plane, there exists a strong expression of  $-z$  vorticity from the

top of the cylinder. This asymmetry leads to competing vibration-driving mechanisms resulting in the oscillatory behaviour of  $f^*$  seen in Fig. 4.25a.

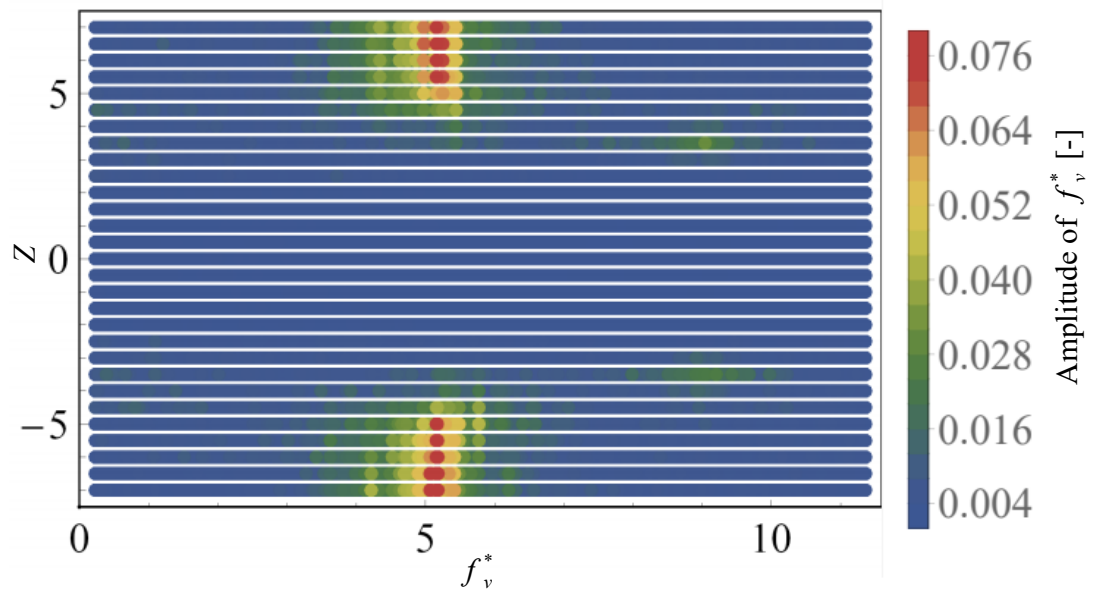
### 4.3.3 Phase lag between Cl and normalised cylinder displacement

Evolution of  $\theta_{y-Cl}$  for the  $67.5^\circ$  and  $45^\circ$  cruciforms share a similar trend in the  $2.3 \leq U^* \leq 6.8$  range. For the  $67.5^\circ$  cruciform, past  $U^* = 6.8$ , there seem to be two distinct VIV branches between  $2.3 \leq U^* \leq 13.6$ , and between  $15.9 \leq U^* \leq 29.5$ . In the first branch between  $2.3 \leq U^* \leq 13.6$ ,  $\theta_{y-Cl}$  seems to remain close to  $70^\circ$ , while in the second branch, close to  $110^\circ$ . In some sense, this is fairly similar to the  $\theta_{y-Cl}$  vs.  $U^*$  pattern of the pure cruciform case, except for two features. First, the lower branch of KVIV – which in the pure cruciform case exhibits a  $\theta_{y-Cl} \approx 180^\circ$  – does not extend beyond  $U^* = 6.8$ . Instead, the value for  $\theta_{y-Cl}$  suddenly drops to  $\approx 70^\circ$  before jumping back up to  $\approx 110^\circ$  starting at  $U^* = 15.9$ . This value of  $110^\circ$  is curiously close to  $\theta_{y-Cl}$  of the pure cruciform between  $20.5 \leq U^* \leq 29.5$ , equivalent to the upper branch of SVIV. Working backwards from  $U^* = 20.5$  in the direction of decreasing  $U^*$ , and compare Fig. 4.34a and Fig. 4.20, one confronts the possibility that the  $\theta_{y-Cl} = 70^\circ$  branch of the  $67.5^\circ$  cruciform is a *variant* of the SVIV initial branch. For the pure cruciform case, this occurs within a narrow window of  $15.9 < U^* < 20.5$ , with  $\theta_{y-Cl} \approx 20^\circ$ .

For the  $45^\circ$  cruciform in Fig. 4.34b, right after lower branch of KVIV at  $U^* = 6.8$ ,  $\theta_{y-Cl}$  transitioned to  $\approx 65^\circ$  between  $11.4 \leq U^* \leq 20.5$ . The proximity between the values  $65^\circ$  and  $70^\circ$  for the  $67.5^\circ$  cruciform suggests the equivalence of the two branches. However, this study is inclined to a more cautious conclusion: the two are *variants* of the same branch that is only similar in limited respects as they originate from different angled cruciforms. In this respect, the  $45^\circ$  cruciform is much less similar to the pure cruciform case, as one might expect, simply because  $45^\circ$  is a much larger deviation from  $90^\circ$  compared to  $67.5^\circ$ . This larger deviation is in the opinion of this study, what causes  $\theta_{y-Cl}$  in the  $45^\circ$  case to drop further to  $\approx 35^\circ$  within  $22.7 \leq U^* \leq 29.5$ , instead of jumping up to some mean value between  $100 \leq \theta_{y-Cl} (\circ) \leq 130$  similar to what is observed in the  $90^\circ$  and  $67.5^\circ$  cruciforms.

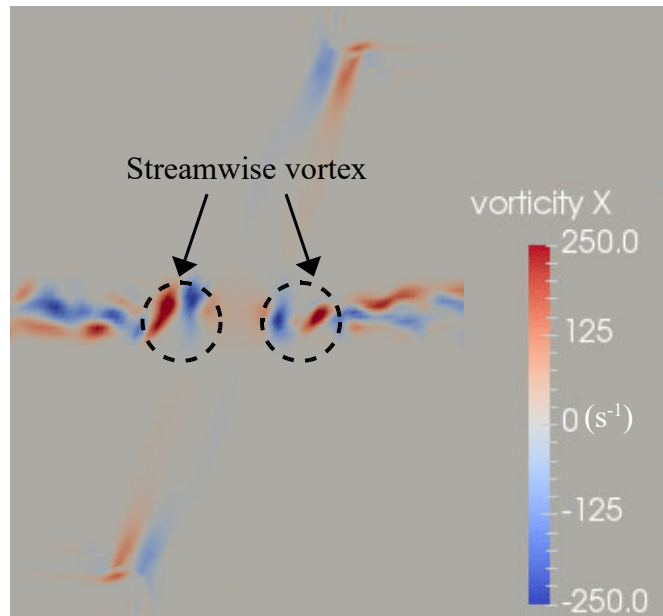


(a) The  $f_v^*$  for the  $67.5^\circ$  cruciform.

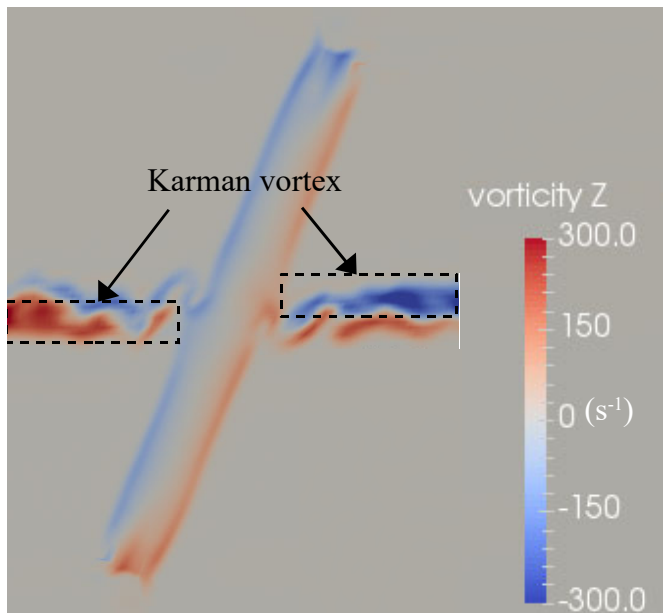


(b) The  $f_v^*$  for the  $45^\circ$  cruciform.

Figure 4.28: Distribution of normalised frequency of vortex shedding, along the span of the cylinder of the  $67.5^\circ$  and  $45^\circ$  cruciforms at  $U^* = 22.7$ .

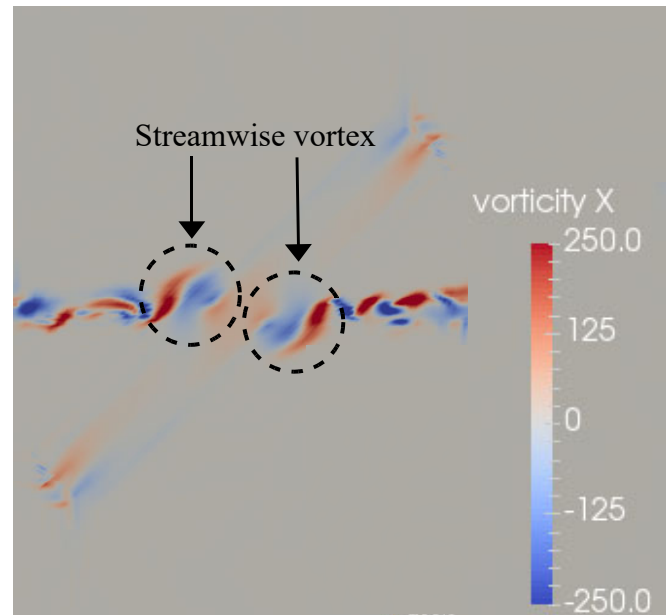


(a)  $x$ -component vorticity,  $67.5^\circ$  cruciform.

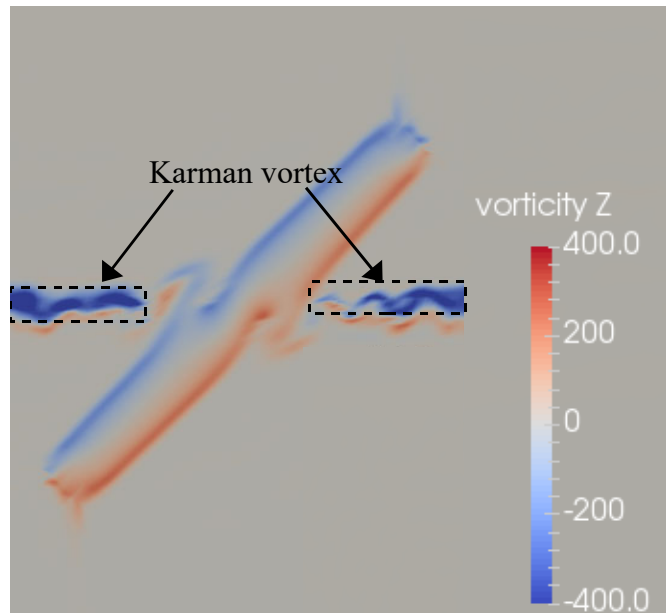


(b)  $z$ -component vorticity,  $67.5^\circ$  cruciform.

Figure 4.29: Dominant vortical structures at  $U^* = 22.7$  observed in the  $67.5^\circ$  and  $45^\circ$  cases.

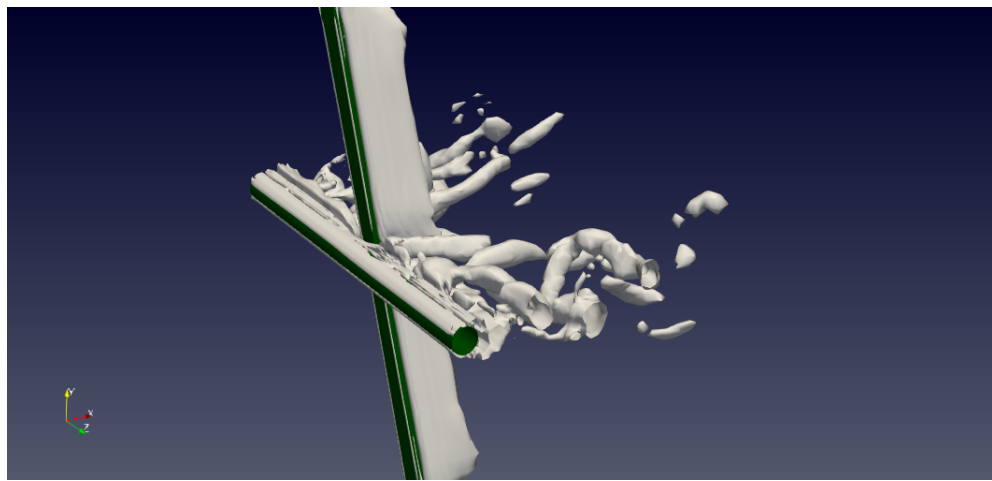


(c)  $x$ -component vorticity,  $45^\circ$  cruciform.

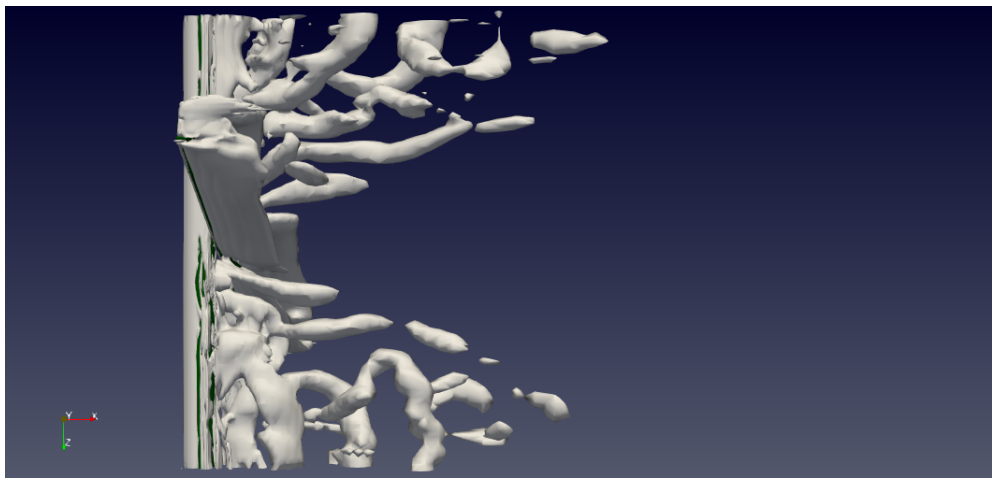


(d)  $z$ -component vorticity,  $45^\circ$  cruciform.

Figure 4.29: Dominant vortical structures at  $U^* = 22.7$  observed in the  $67.5^\circ$  and  $45^\circ$  cases.

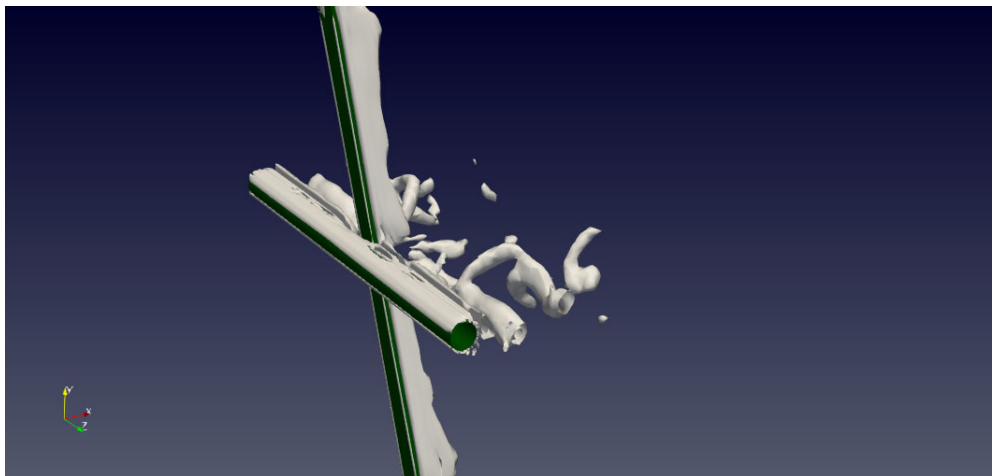


(a) Isometric view of the Q-criterion.

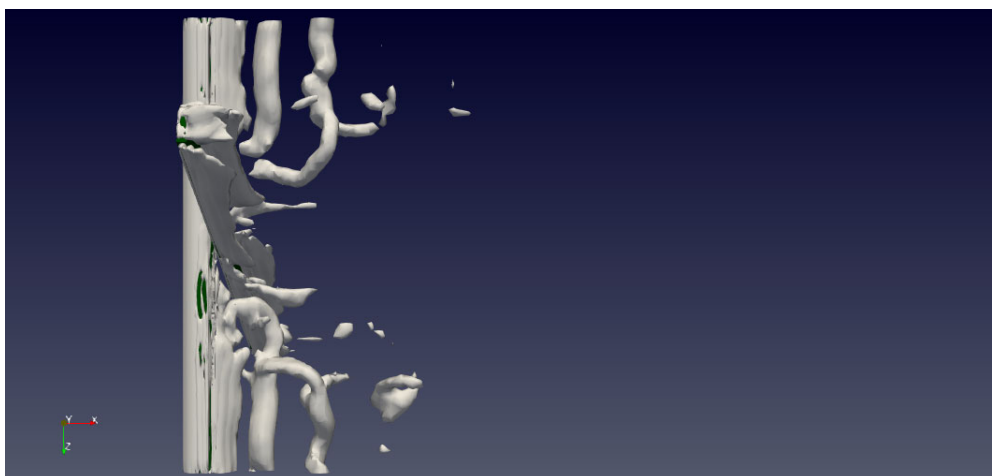


(b) Plan view of the Q-criterion.

Figure 4.30: The Q-criterion for the  $67.5^\circ$  cruciform at  $U^* = 22.7$ : the 4.30a isometric and 4.30b plan view.

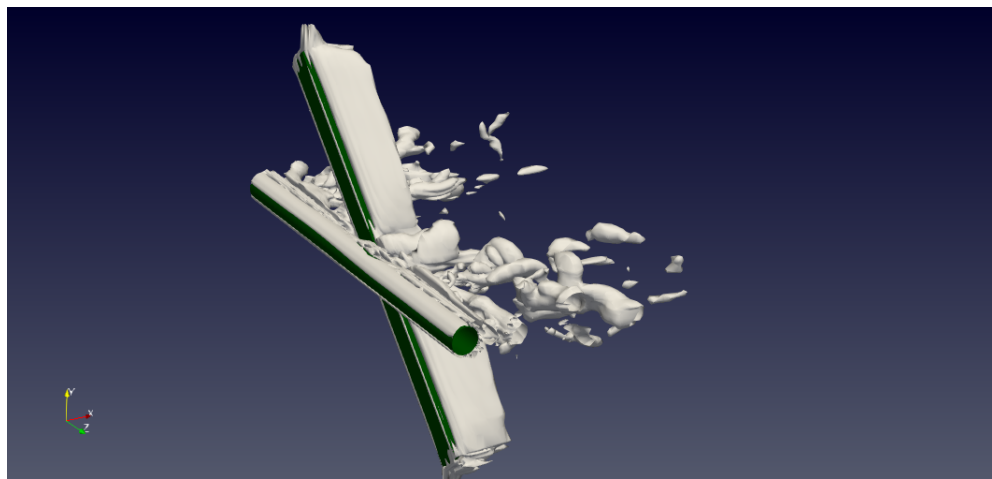


(a) Isometric view of the Q-criterion.

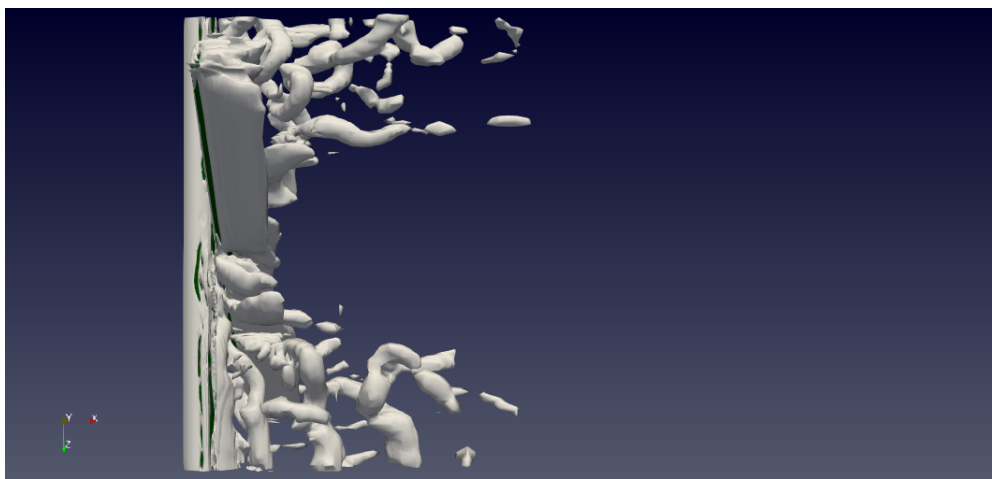


(b) Plan view of the Q-criterion.

Figure 4.31: The Q-criterion for the  $67.5^\circ$  cruciform at  $U^* = 4.5$ : the 4.31a isometric and 4.31b plan view.

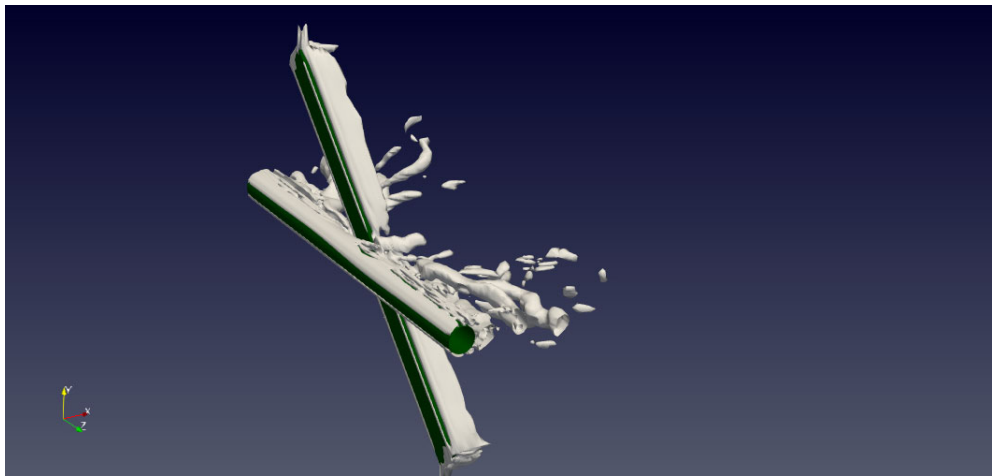


(a) Isometric view of the Q-criterion.

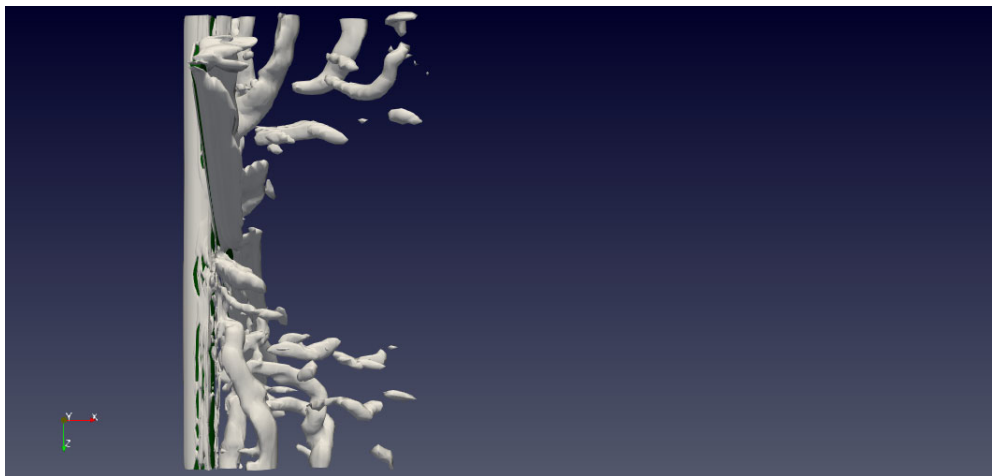


(b) Plan view of the Q-criterion.

Figure 4.32: The Q-criterion for the  $45^\circ$  cruciform at  $U^* = 22.7$ : the isometric (4.32a) and plan view (4.32b).

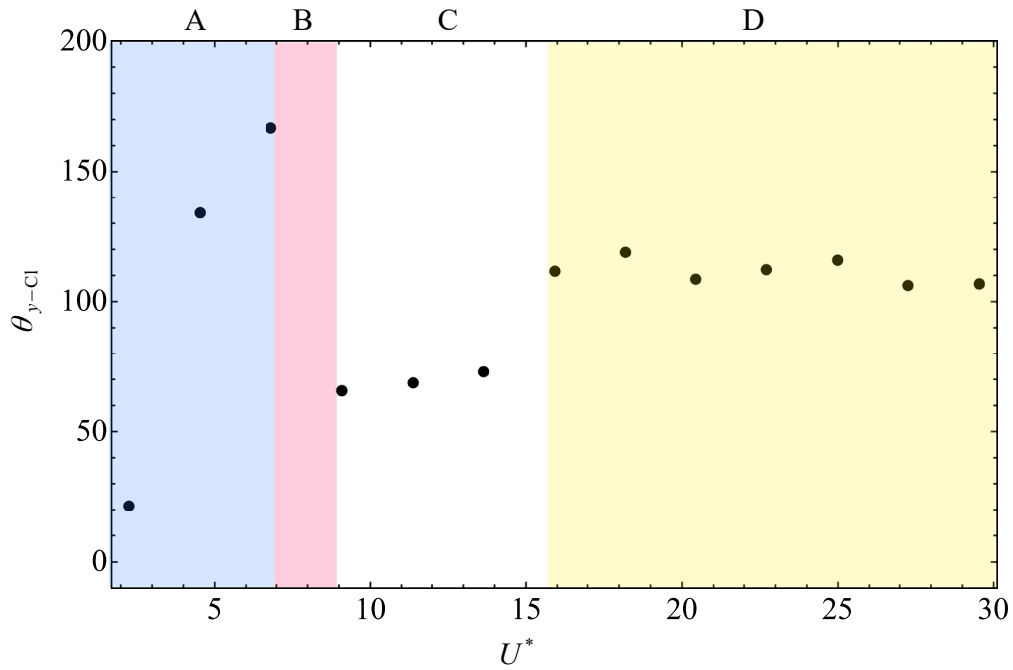


(a) Isometric view of the Q-criterion.

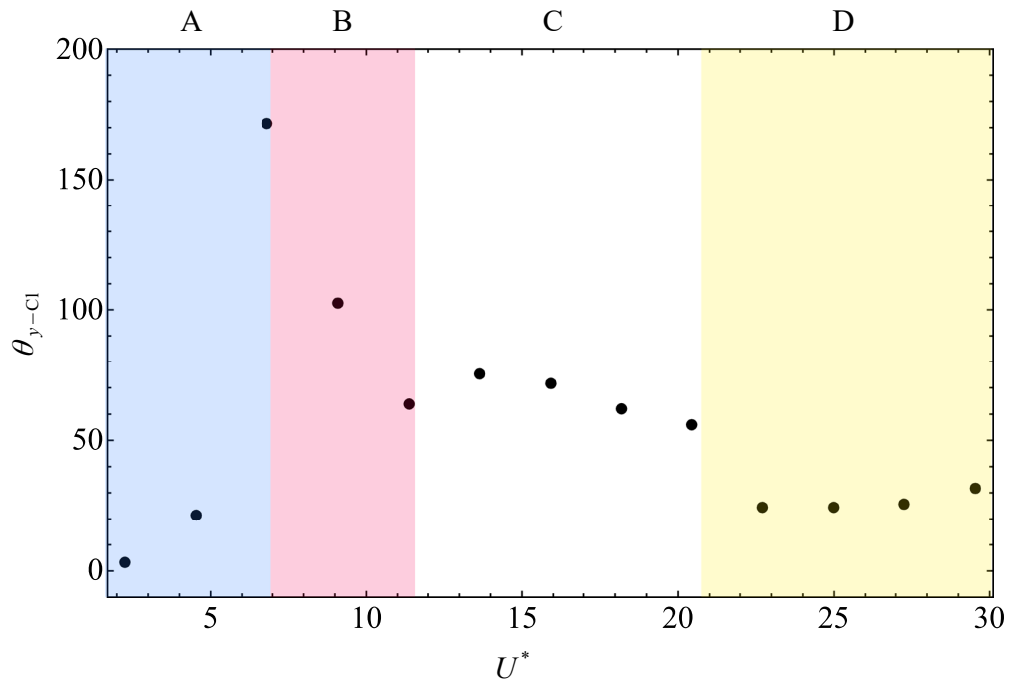


(b) Plan view of the Q-criterion.

Figure 4.33: The Q-criterion for the  $45^\circ$  cruciform at  $U^* = 4.5$ : the isometric (4.33a) and plan view (4.33b).



(a) Phase lag for the  $67.5^\circ$  cruciform.



(b) Phase lag for the  $45^\circ$  cruciform.

Figure 4.34: Phase lag  $\theta_{y-\text{Cl}}$  (°) between Cl and  $y^*$  when  $67.5^\circ$  and  $45^\circ$ .

#### 4.3.4 Section Summary

In this chapter, the present author explored the amplitude/frequency response of steep-angled cruciforms, defined as a cruciform with angles  $45 \leq \alpha(^{\circ}) \leq 67.5$ . In doing so, this study found out that the oscillators in this category fails to attain at minimum a similar amplitude/frequency response as the pure cruciform. Instead, there only exists a narrow region of meaningful vibration in the KVIV regime - an example of which is illustrated in §4.2.3.1.

The SVIV regime seems to be non-existent in this steep-angled layout. Flow visualisations confirms the existence of large-scale streamwise vortices near the cruciform juncture, but the absence of a counter-rotating pair in the same plane as either the top or bottom of the upstream cylinder results in a severely diminished vibration-driving lift acting on the cylinder. Furthermore, the unstable evolution of  $f_{str}$  with respect to  $U^*$  led this study to discover an inherent asymmetry in the distribution of vortices along the length of the cylinder, most apparent of which are the Karman vortex cells. This non-uniform distribution of force along the length of the cylinder is what probably induce the instability in the evolution of  $f^*$  with respect to  $U^*$ .

The findings regarding the importance of symmetry in the distribution of vortical structures along the cylinder, of both the Karman and streamwise kind, signals the potential of the angled cruciform as a mechanism of vibration control: a cruciform that instigates the formation of less symmetrical vortical distributions can be useful in certain situations, e.g. during the startup of the energy harvester, where one may intend to begin by generating a small amount of power first. The power output can then be gradually increased by increasing the symmetry of vortical distributions along the cylinder, e.g. bringing the configuration to a pure cruciform layout.

The question is therefore whether one can attain a more symmetrical distribution of the vortical structures along the cylinder by instead rotating the strip plate in the opposite direction - which brings the cruciform to an in-tandem configuration, i.e.,  $0^{\circ}$ . This thesis attempts to answer this question in the following section.

#### 4.4 Shallow-angled Cruciforms

The previous §4.3 is an attempt to control the vortical structures dominating the flow around a cruciform oscillator to focus as much as possible energy from the freestream to the vortical structure driving the vibration of the cylinder. In doing so, the steep-angled cruciforms seem to prefer the Karman vortex as the lift producing mechanism, as evidenced by the evolution of  $f_{Cl}^*$  against  $U^*$ , which closely follow the shedding frequency of Karman vortex given in Eq. 2.1.

The absence of a counter-rotating, large-scale streamwise vortex pair in the same plane parallel to the cylinder axis effectively nullifies their contribution towards the generation of vibration-driving lift, thus resulting in a Karman vortex-regulated flow. As such, from this perspective, the steep-angled cruciform is successful in focussing the energy from the freestream to only one type of vortical structure: the Karman vortex. However, the asymmetry in the distribution of vortical structures along the cylinder moots the effect of Karman vortex as the primary regulator of lift acting on the cylinder. Hence, the pure cruciform is still the preferred choice if one aims to maximise the power output and efficiency across a wide synchronisation range.

Nevertheless, whether this trend of low amplitude vibrations is exacerbated as the cruciform angle  $\alpha$  ( $^\circ$ ) is further reduced to  $0 \leq \alpha(^\circ) \leq 22.5$  remains an open question. This chapter therefore seeks to answer this question about shallow-angled cruciforms. First, the chapter discusses the amplitude/frequency responses of a shallow-angled cruciform. Then it explores the vortical structures responsible for the resulting system response before elucidating the vibration branches that exist in shallow-angled cruciforms.

The chapter concludes with the presentation of the evolution of mechanical power and mechanical efficiency of all cruciforms studied in this thesis, i.e.,  $0 \leq \alpha(^\circ) \leq 90$ , in the  $\alpha(^\circ) - U^*$  parameter space. In addition to gaining a birds eye view of the evolution of the two parameters, it allows one to break away from the orthodox paradigm of cruciform energy harvesters as a pure cruciform unit, whose sole aim is to attain maximum vibration amplitude at system natural frequency, thus producing maximum power output. Rather, this new paradigm that comes with the map enables

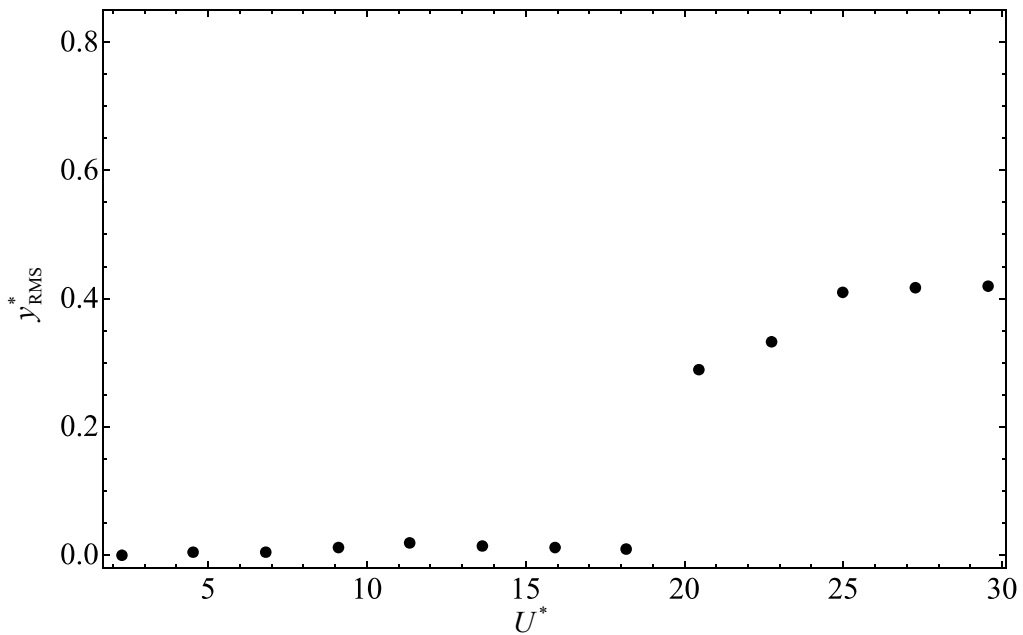
one to assert control over a cruciform energy harvester in its most general form, with the ability to maximise and minimise its power output as required.

#### 4.4.1 The amplitude and frequency response

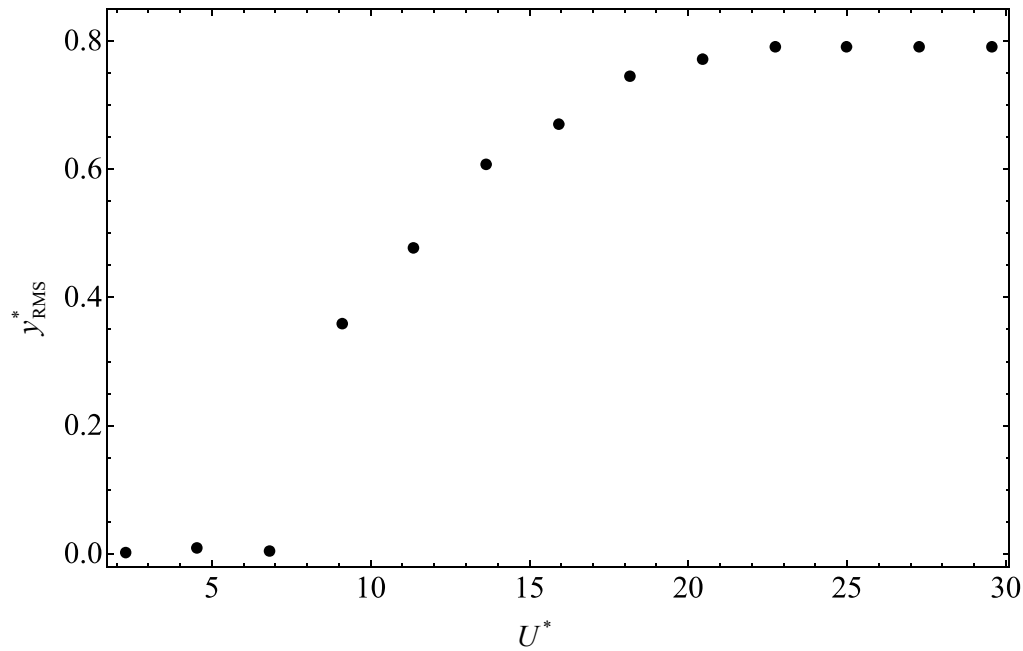
As the cruciform angle is decreased even further to  $22.5^\circ$ , a significant change is observed in the amplitude and frequency response, compared to the transitional stage previously explored in §4.3. Consider Figs. 4.35a and 4.36a. There is no apparent KVIV upper branch similar to what Figs. 4.24a and 4.25a have shown at  $U^* = 4.5$ . Then, there is no significant vibration elicited from the oscillator until  $U^* = 20.5$ . When  $U^* = 20.5$ , there is an abrupt jump in  $y_{\text{RMS}}^*$  from  $y_{\text{RMS}}^* < 0.02$  to  $y_{\text{RMS}}^* \approx 0.3$ . The  $f^*$  vs.  $U^*$  trend demonstrated a bypassing of the KVIV lower branch - which occurred at  $U^* = 6.8$  in the transitional stages of §4.3 - right into  $f^* \approx 1$ . Past  $U^* = 20.5$ , the value for  $y_{\text{RMS}}^*$  continues to increase and saturates at  $U^* = 25.0$ , and  $f^*$  continues to be close to 1 up to  $U^* = 29.5$ .

The  $0^\circ$  cruciform (Figs. 4.35b, 4.36b) in essence exhibits a very similar trend in its  $y_{\text{RMS}}^*$  and  $f^*$  evolutions with respect to  $U^*$ . However, the jump – which for the  $22.5^\circ$  cruciform occurs at  $U^* = 20.5$  – occurs at a much lower  $U^* = 9.1$ . Then,  $y_{\text{RMS}}^*$  continues to grow until  $U^* = 20.5$ , reaching a staggering  $y_{\text{RMS}}^* \approx 0.8$ , a value no other study on energy harvesting using cruciform oscillators has ever achieved. The value of  $y_{\text{RMS}}^*$  then saturates close to 0.8 up to  $U^* = 29.5$ . Also similar to the  $22.5^\circ$  cruciform,  $f^*$  falls close to 1 at same  $U^*$  the  $y_{\text{RMS}}^*$  jump occurs - hinting at synchronisation between vortex shedding and system natural frequency.

Apart from the amplitude/frequency response of the  $22.5^\circ$  cruciform, the evolution of  $\text{Cl}_{\text{RMS}}$  against  $U^*$  showcases a similar trend to the evolution  $y_{\text{RMS}}^*$ , as shown in Fig. 4.37a. The corresponding  $f_{\text{Cl}}^*$  in Fig. 4.38a demonstrates the dominant frequency of Cl taking after Eq. 4.4 between  $2.3 \leq U^* \leq 18.2$ , before abruptly dropping close to 1 between  $20.5 \leq U^* \leq 29.5$ . This in part informs the investigation that the flow between  $2.3 \leq U^* \leq 18.2$  is governed by flow physics that are similar to both  $67.5^\circ$  and  $45^\circ$  within the same  $U^*$  range.

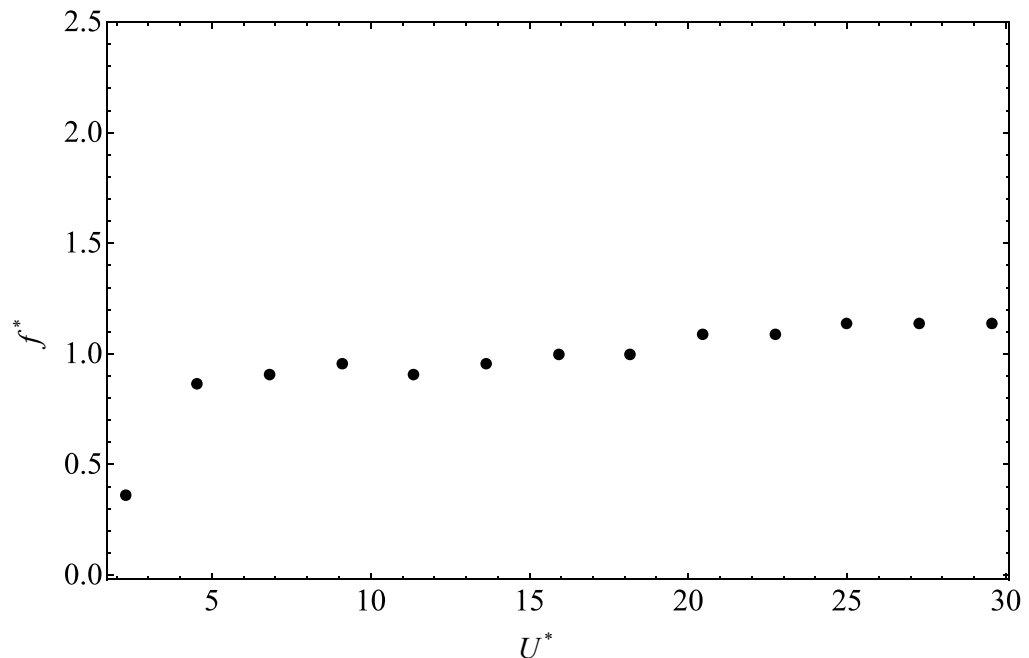


(a) The  $22.5^\circ$  cruciform.

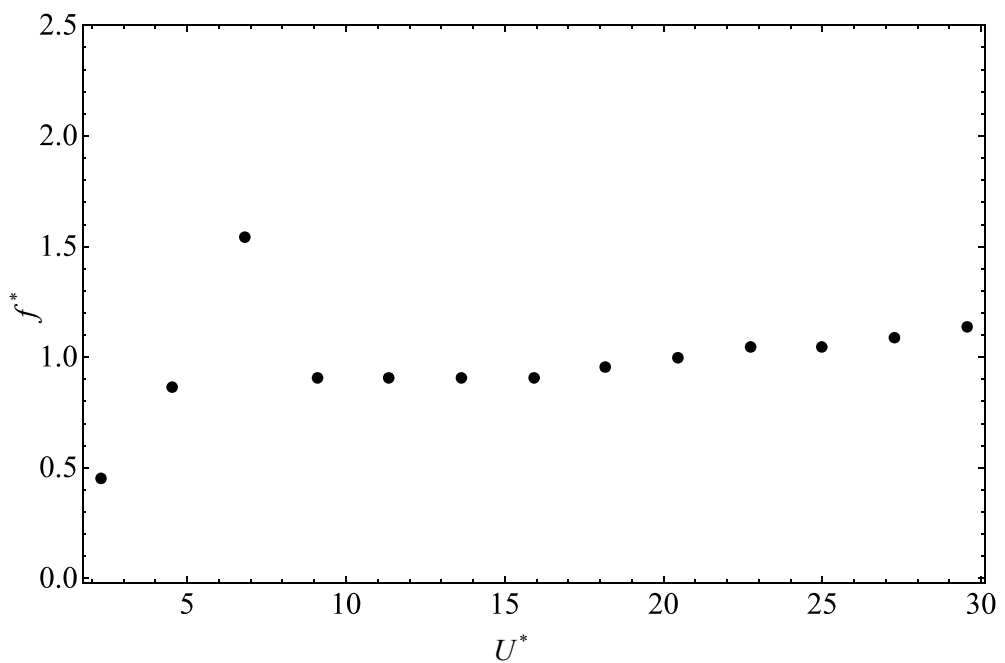


(b) The  $0^\circ$  cruciform.

Figure 4.35: Evolution of the normalised root-mean-square amplitude of cylinder displacement  $y_{\text{RMS}}^*$ , with respect to reduced velocity  $U^*$ , for the  $22.5^\circ$  and  $0^\circ$  cruciform.



(a) The  $22.5^\circ$  cruciform.



(b) The  $0^\circ$  cruciform.

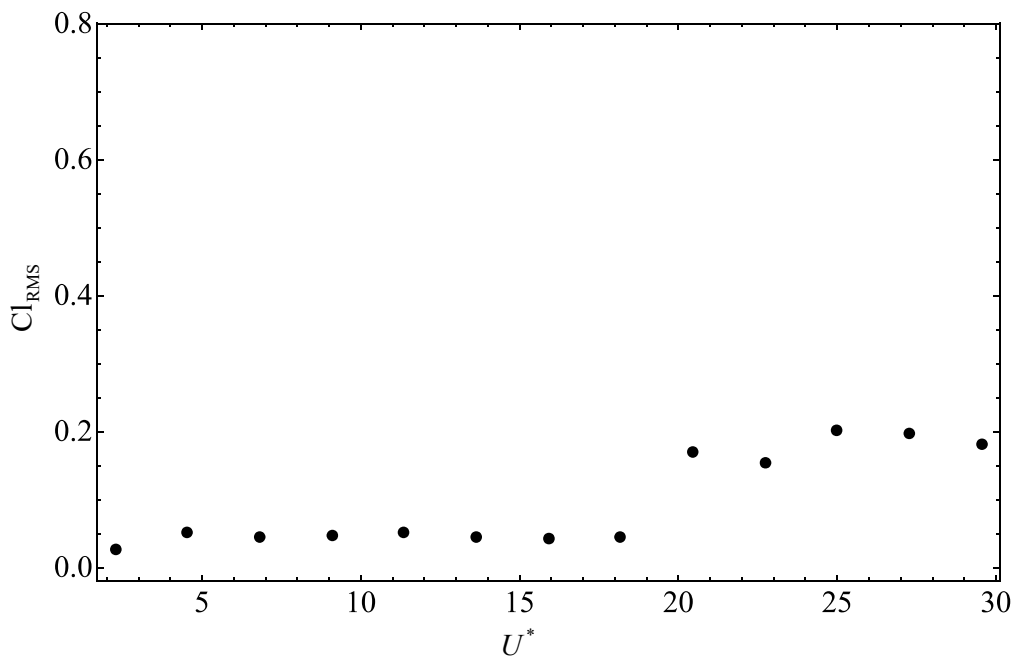
Figure 4.36: Evolution of the normalised cylinder displacement frequency,  $f^*$ , with respect to reduced velocity  $U^*$ , for the  $22.5^\circ$  and  $0^\circ$  cruciforms.

For the  $0^\circ$  cruciform, the jump in  $\text{Cl}_{\text{RMS}}$  seems to occur at the same  $U^*$  as the jump in the corresponding  $y_{\text{RMS}}^*$  i.e.,  $U^* = 9.1$ . After  $U^* = 9.1$ , the magnitude of  $\text{Cl}_{\text{RMS}}$  gradually drops to a final value of  $\text{Cl}_{\text{RMS}} \approx 0.45$  at  $U^* = 20.5$ , and remains there up to  $U^* = 29.5$ . Similar to the  $22.5^\circ$  cruciform,  $f_{\text{Cl}}^*$  grows linearly in accordance with, again, Eq. 4.4 until the jump in both  $\text{Cl}_{\text{RMS}}$  and  $y_{\text{RMS}}^*$ , where  $f_{\text{Cl}}^*$  drops close to 1 for the rest the  $U^*$  examined in this study.

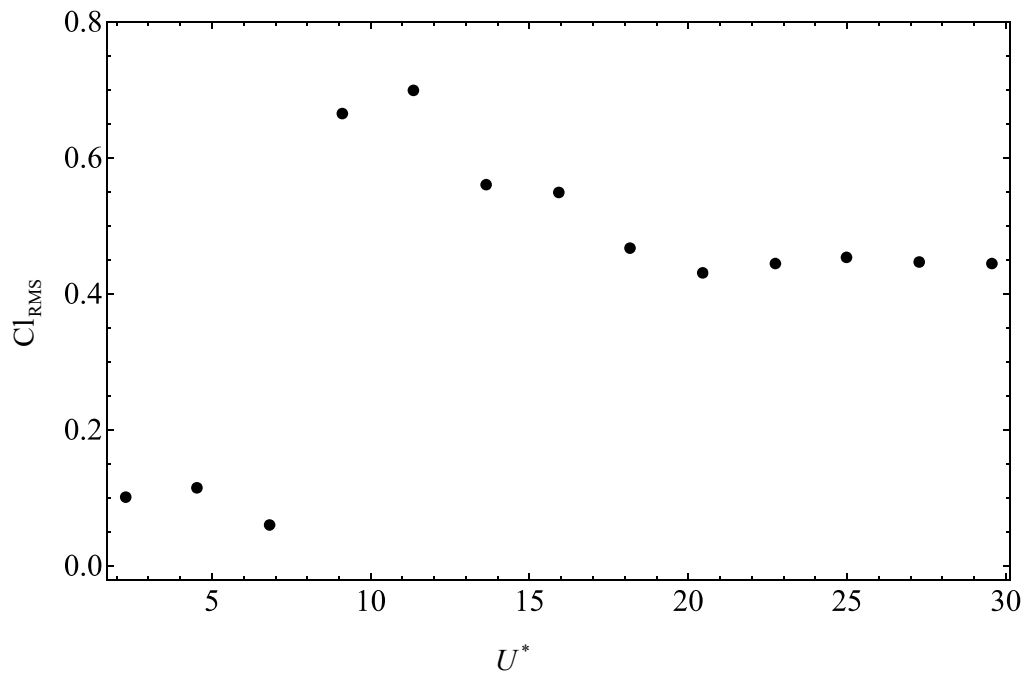
#### 4.4.2 Main vibration-driving vortical structure

To understand the cause behind the marked difference between the amplitude/frequency response in both  $67.5^\circ$  and  $45^\circ$  cruciforms, this study proceeds to deduce the type of vortical structures that form in the flows around the  $22.5^\circ$  and  $0^\circ$  cruciform. First, visualise  $f_v^*$  along the cylinder, in the same manner as Figs. 4.9 and 4.28, in Fig. 4.39a. Inspecting Fig. 4.39a, one notices that several frequency bands exist:  $f_v^* \approx 1, 2, 3, 4.5$ , the most visible of which is the  $f_v^* \approx 1$  band. However, unlike the pure cruciform case in Fig. 4.9 – where the dominant frequency bands are localised to certain regions along the cylinder – the  $f_v^* \approx 1$  band of the  $22.5^\circ$  cruciform seems to encompass the length of the cylinder. This also seems to be the case for the  $0^\circ$  cruciform, displaying a dominant  $f_v^*$  band at approximately 1 along the length of the cylinder.

Then, the  $x$  and  $z$ -component vorticity contours of the  $22.5^\circ$  cruciform is queried for deeper insight, presented in Figs. 4.40a and 4.40b. In doing so, the large scale streamwise vortex pair near the cruciform juncture is found to be absent. Instead, streamwise vortex cells are found to be distributed on both sides of the  $Z = 0$  plane, except within the immediate neighbourhood of the cruciform juncture. Note that these streamwise vortex cells are distributed at a slight angle relative to the  $z$ -axis, seemingly following the angle of the strip plate, i.e.  $22.5^\circ$ . Visualisation of the  $z$ -component vorticity in Fig. 4.40b intimates the nature of the tilted streamwise vortex cells: they are simply three-dimensional Karman vortex structures, akin to those observed in the experiments of Williamson (1996b), especially mode B. This is inferred from comparison of the same visual region delimited by dashed rectangles in Figs. 4.40a and 4.40b, showing the overlap between the streamwise vortex cells and the strong Karman vortex component.

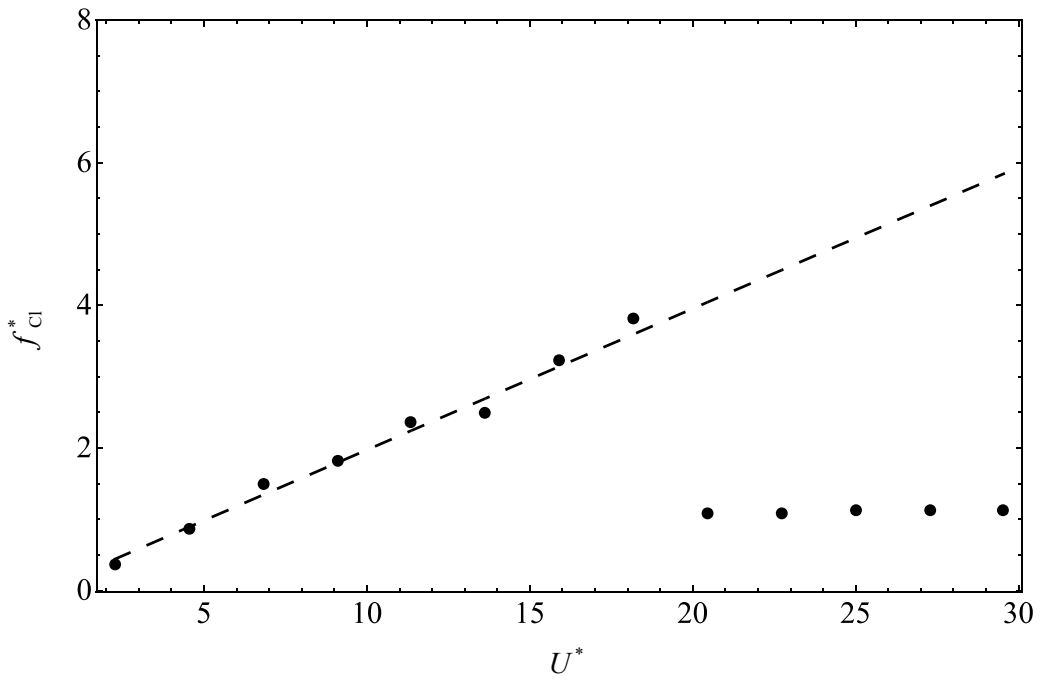


(a) The  $22.5^\circ$  cruciform.

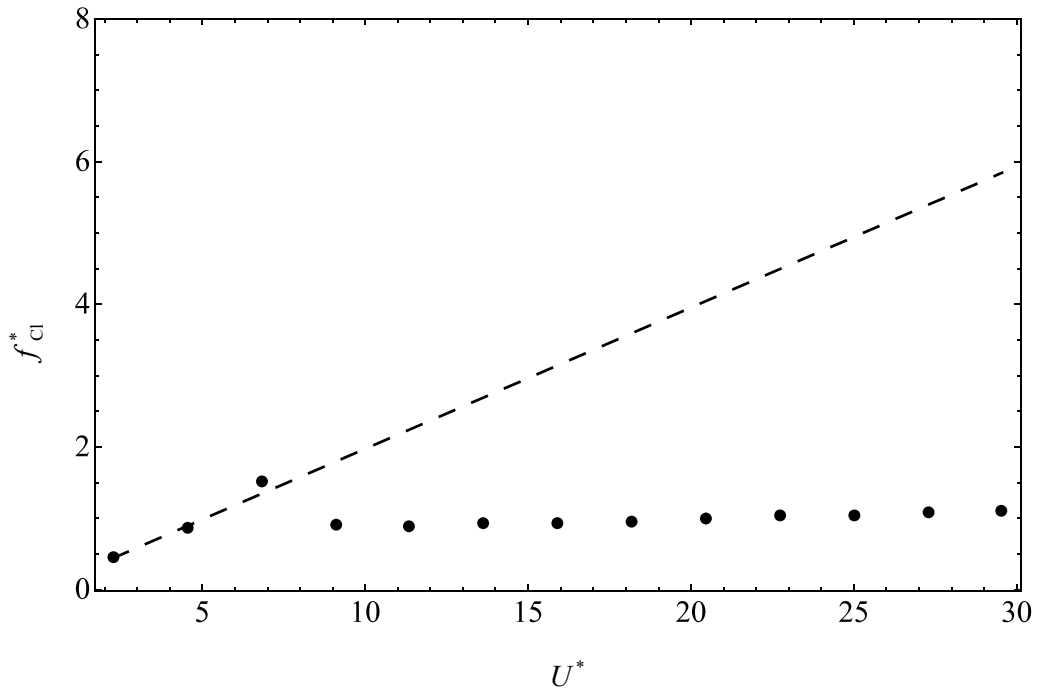


(b) The  $0^\circ$  cruciform.

Figure 4.37: Evolution of the normalised Cl root-mean-square amplitude,  $Cl_{RMS}$ , with respect to reduced velocity  $U^*$ , for the  $22.5^\circ$  and  $0^\circ$  cruciforms.

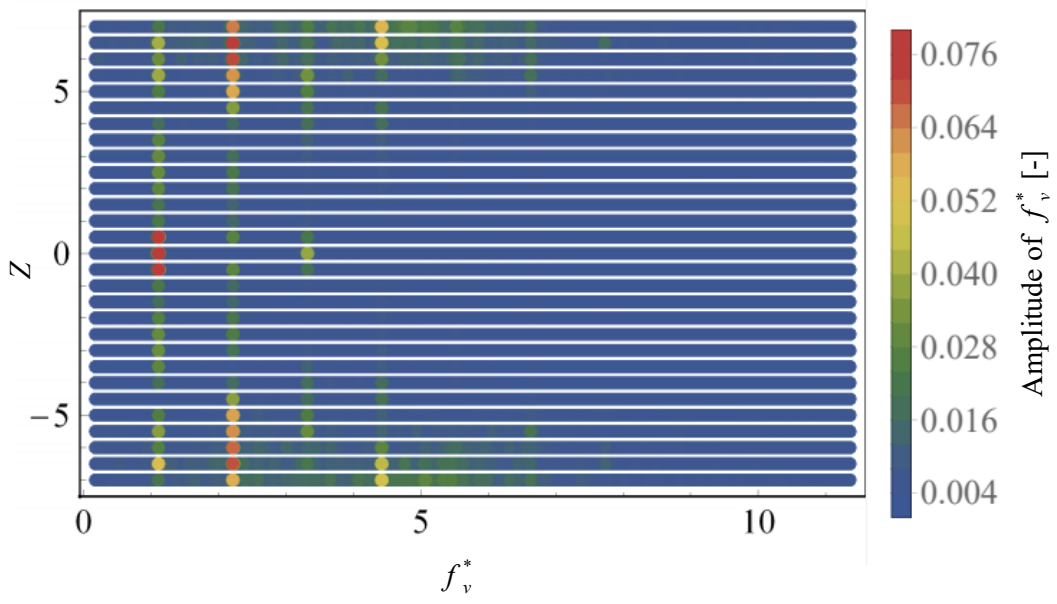


(a) The  $22.5^\circ$  cruciform.

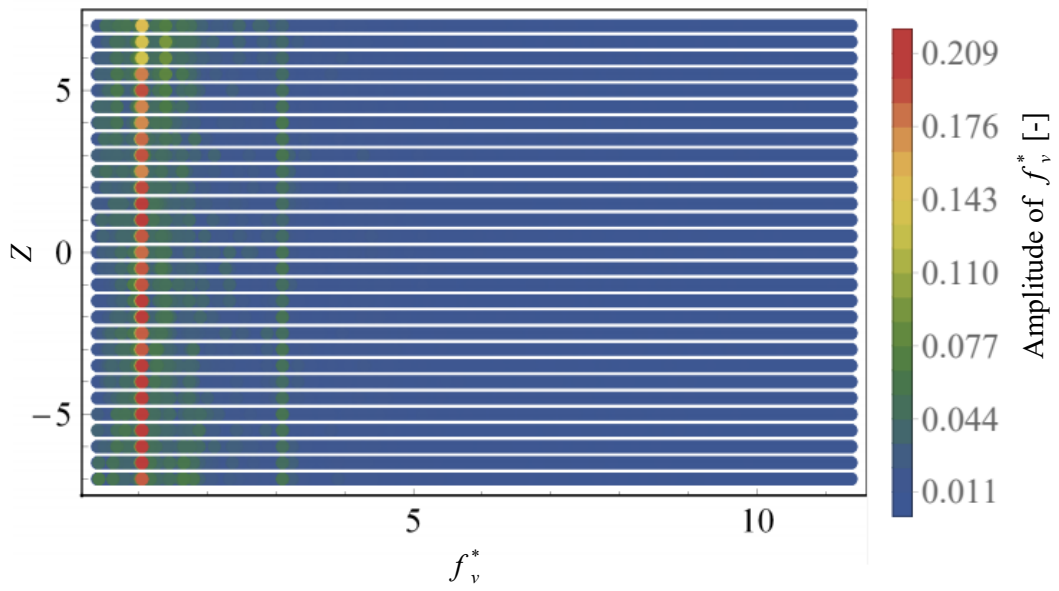


(b) The  $0^\circ$  cruciform.

Figure 4.38: Evolution of the normalised Cl frequency,  $f_{\text{Cl}}^*$ , with respect to reduced velocity  $U^*$ , for the  $22.5^\circ$  and  $0^\circ$  cruciforms. The dashed lines outline  $f_{v,\text{Karman}}$  from Eq. 4.4.

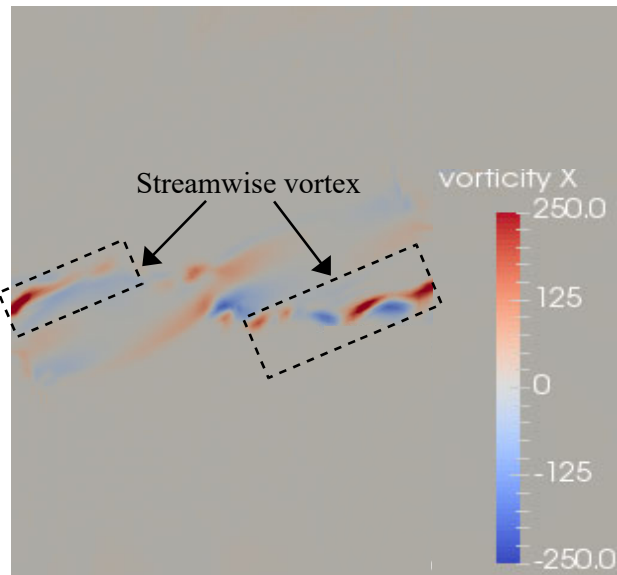


(a) The  $f_v^*$  for the  $22.5^\circ$  cruciform.

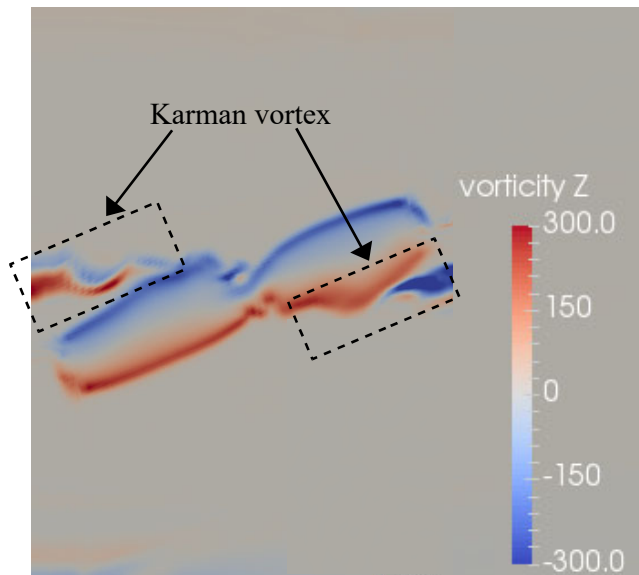


(b) The  $f_v^*$  for the  $0^\circ$  cruciform.

Figure 4.39: Distribution of normalised frequency of vortex shedding, along the span of the cylinder of the  $22.5^\circ$  and  $0^\circ$  cruciforms at  $U^* = 22.7$ .

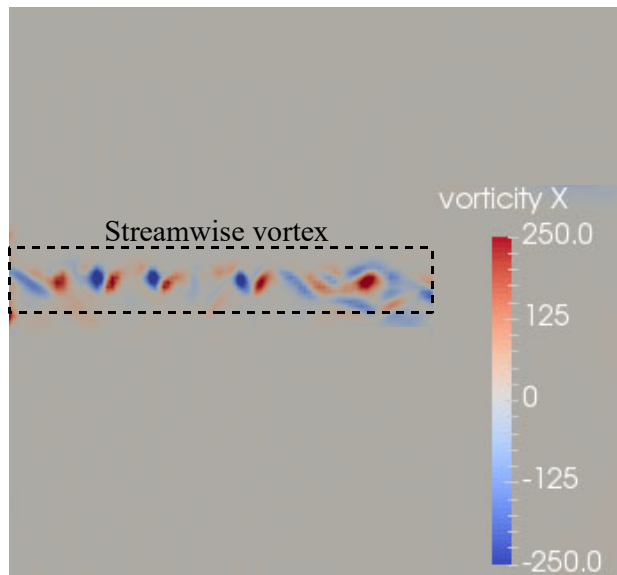


(a)  $x$ -component vorticity,  $22.5^\circ$  cruciform.

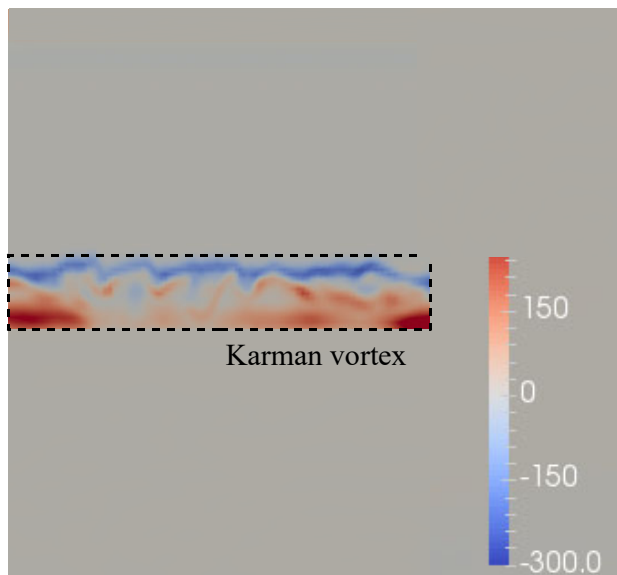


(b)  $z$ -component vorticity,  $22.5^\circ$  cruciform.

Figure 4.40: Dominant vortical structures at  $U^* = 22.7$  observed in the  $22.5^\circ$  and  $0^\circ$  cases.

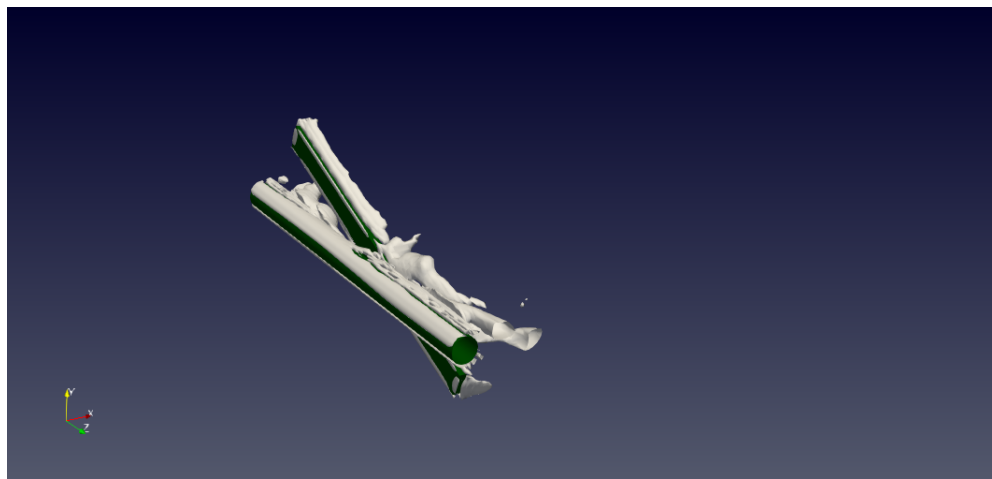


(c)  $x$ -component vorticity,  $0^\circ$  cruciform.



(d)  $z$ -component vorticity,  $0^\circ$  cruciform.

Figure 4.40: Dominant vortical structures at  $U^* = 22.7$  observed in the  $22.5^\circ$  and  $0^\circ$  cases.

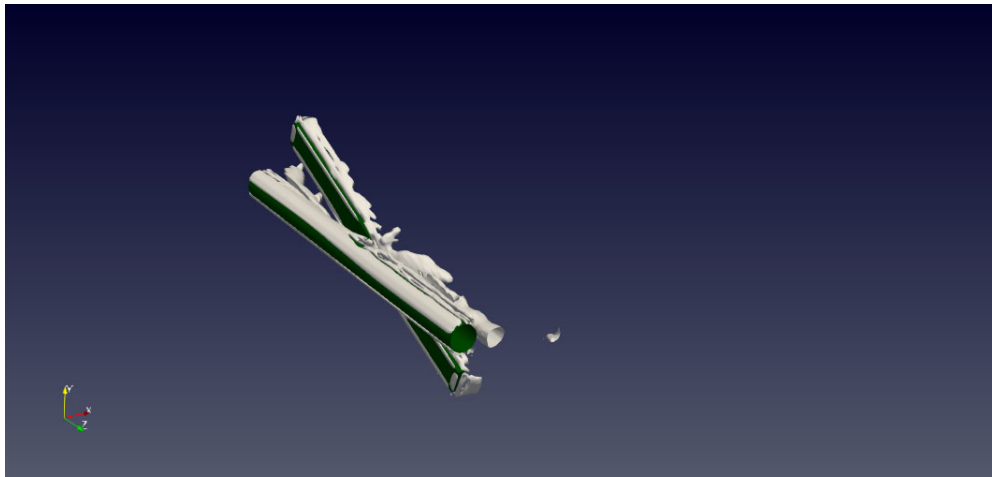


(a) Isometric view of the Q-criterion.

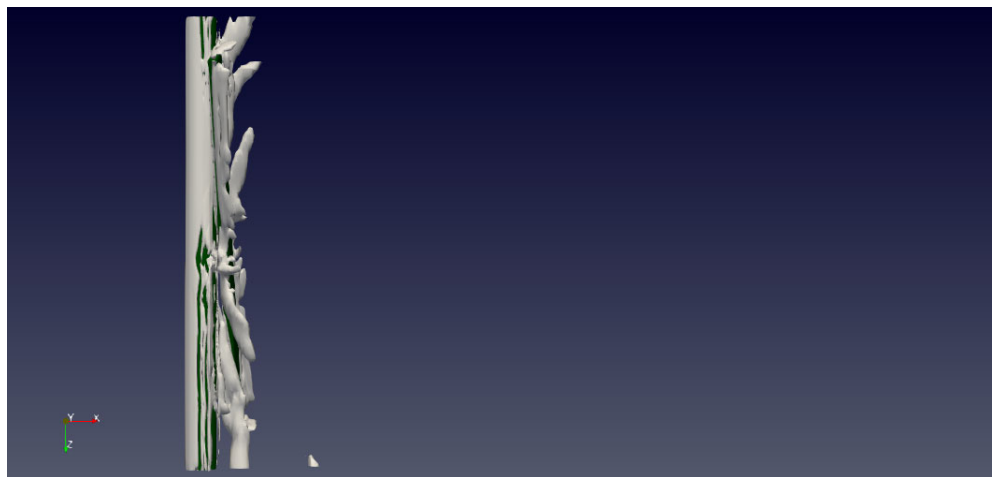


(b) Plan view of the Q-criterion.

Figure 4.41: The Q-criterion for the  $22.5^\circ$  cruciform at  $U^* = 22.7$ : the isometric (4.41a) and plan view (4.41b).

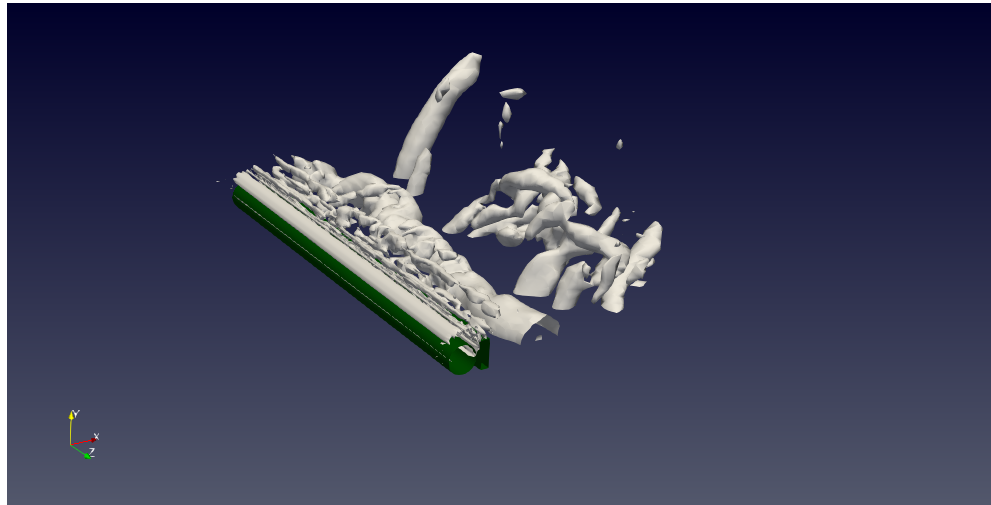


(a) Isometric view of the Q-criterion.

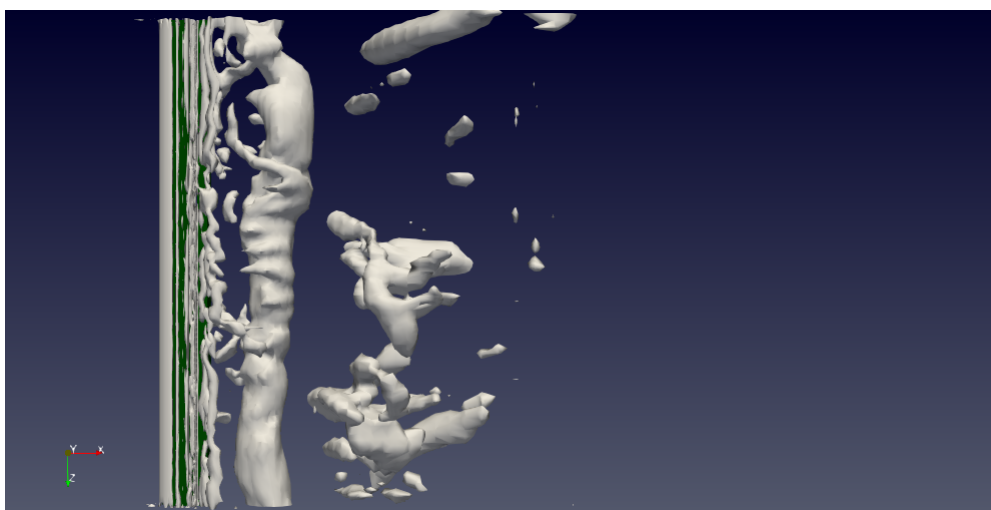


(b) Plan view of the Q-criterion.

Figure 4.42: The Q-criterion for the  $22.5^\circ$  cruciform at  $U^* = 4.5$ : the isometric (4.42a) and plan view (4.42b).

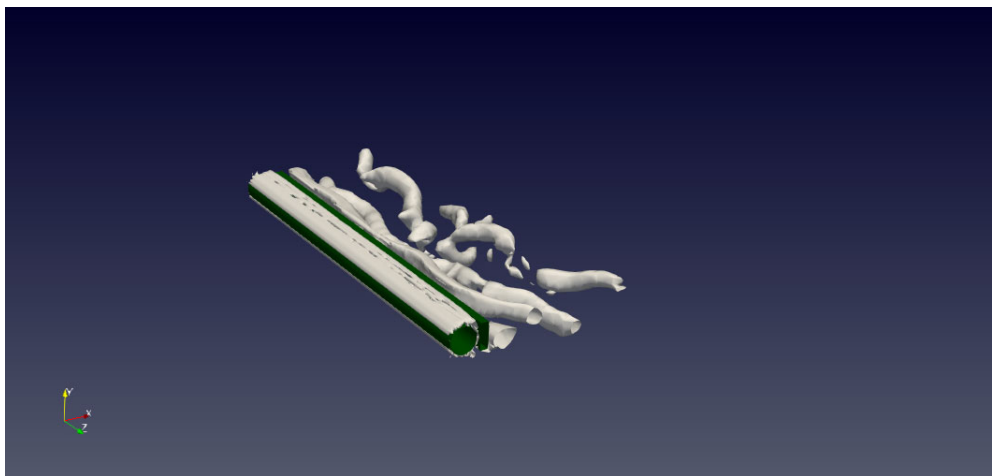


(a) Isometric view of the Q-criterion.

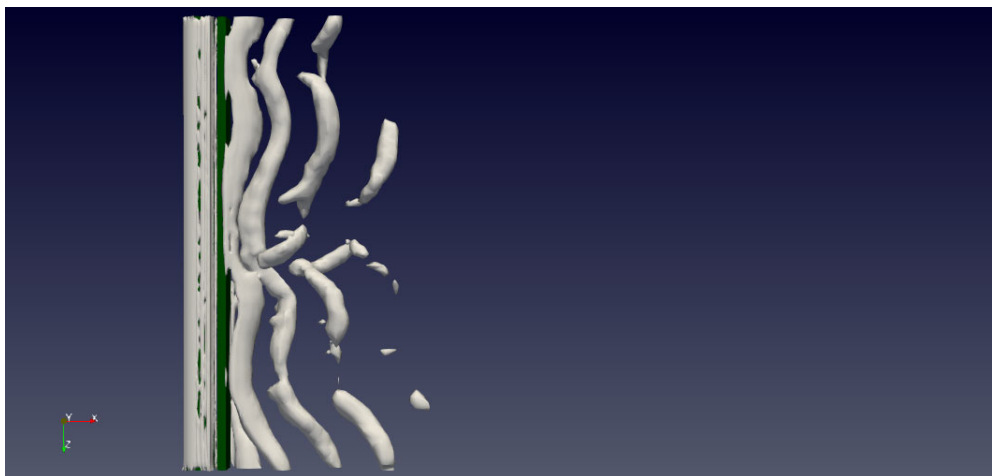


(b) Plan view of the Q-criterion.

Figure 4.43: The Q-criterion for the  $45^\circ$  cruciform at  $U^* = 22.7$ : the isometric (4.43a) and plan view (4.43b).



(a) Isometric view of the Q-criterion.



(b) Plan view of the Q-criterion.

Figure 4.44: The Q-criterion for the  $45^\circ$  cruciform at  $U^* = 4.5$ : the isometric (4.44a) and plan view (4.44b).

For the  $0^\circ$  cruciform in Figs. 4.40c and 4.40d, this overlap between the streamwise vortex cells and the distinct Karman vortex component is even more visually pronounced. This is interpreted as further evidence to the hypothesis that three-dimensional Karman vortical structures govern the vibration of the cylinder for shallow angled cruciforms, including the  $0^\circ$  cruciform, which perhaps is more aptly named in-tandem configuration. Notice that for the  $0^\circ$  layout, both the streamwise vortex cells and the Karman vortical structure are arranged parallel to the  $z$ -axis, or at  $0^\circ$  relative to the cylinder. This observation seems to demonstrate the role of the strip plate in shallow angled cruciforms: it modifies the spatial distribution of the Karman vortical structure that is driving the vibration of the cylinder.

As demonstrated in §4.2 and 4.3, eliciting a significant vibration amplitude Karman vortex shedding is limited to a narrow  $U^*$  range containing the upper branch of KVIV. Beyond that, Karman vortex shedding fails to lock into the natural frequency of the system to produce meaningful vibrations. The fact that shallow angled cruciforms in this §4.4.2 are able to produce very large vibration amplitudes intimate the crucial role played by the strip plate in forcing the shedding of vortical structures and cylinder vibration to lock into the natural frequency of the system  $f_n$ . The mechanics of this forced lock-in is thought to be as follows.

1. Shallow angled cruciforms have a larger overlap area between the cylinder and strip plate. This permits a more perceptible interaction among vortices shed from the cylinder and the strip plate.
2. Upon exceeding a critical  $U^*$ , vortical structures shed from both the cylinder and the strip plate becomes sufficiently energised, and they start to behave as one.
3. This vortical synchronisation locks into the natural frequency of the elastic structure in its immediate vicinity - the circular cylinder.

The results also suggest the total cylinder-strip plate area overlap as a factor influencing the exact  $U^*$  at which the vortical synchronisation occurs. The  $U^*$  at which the synchronisation – and the jump to large  $y_{\text{RMS}}^*$  amplitude – occurs at a lower value when the overlap area is bigger. Nevertheless, there seems to be a limit to this lowering of  $U^*$ ,

which in this work is determined to be  $U^* = 9.1$ . Recall that this is the value where the synchronisation begins for the  $0^\circ$  layout; the layout where the totality of the cylinder and strip plate projections onto the  $y - z$  plane coincides with each other.

## 4.5 Phase lag between Cl and normalised cylinder displacement

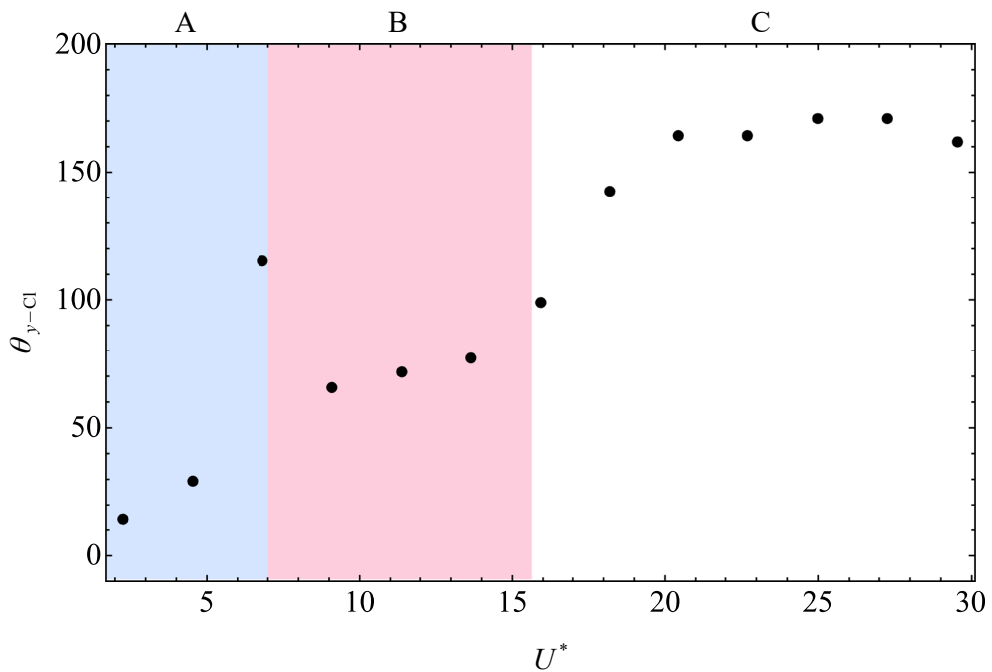
In Fig. 4.45a, the evolution of  $\theta_{y-Cl}$  is summarised according to  $U^*$  for the  $22.5^\circ$  cruciform and find  $\theta_{y-Cl} \approx 115^\circ$  at  $U^* = 29.5$ . The significance of  $U^* = 29.5$  for the  $22.5^\circ$  cruciform is that it is where a jump in  $\theta_{y-Cl}$  occurs from  $\approx 30^\circ$  to  $\approx 115^\circ$ . This abrupt jump usually demarcates transition to the KVIV lower branch, as stated in the discussion accompanying Figs. 4.20 and 4.34, with a value that is very close to  $180^\circ$ . The  $\theta_{y-Cl}$  for the  $22.5^\circ$  cruciform however, is about 36% smaller than the expected  $\approx 180^\circ$ . This may be the cause of absence of the KVIV lower branch in the  $f^*$  vs.  $U^*$  plot of the  $22.5^\circ$  cruciform (Fig. 4.36a).

The  $0^\circ$  arrangement produces a similar trend to Fig. 4.45a, as one can see in Fig. 4.45b. However, the  $\theta_{y-Cl}$  jump at  $U^* = 29.5$  is more pronounced and achieves a value very close to  $180^\circ$ . Following the sudden jump is the sudden drop at  $U^* = 9.1$ , which brings  $\theta_{y-Cl}$  to approximately  $25^\circ$ . This trend continues up to  $U^* = 15.9$ , after which  $\theta_{y-Cl}$  is found to monotonically increase up to  $U^* = 29.5$ .

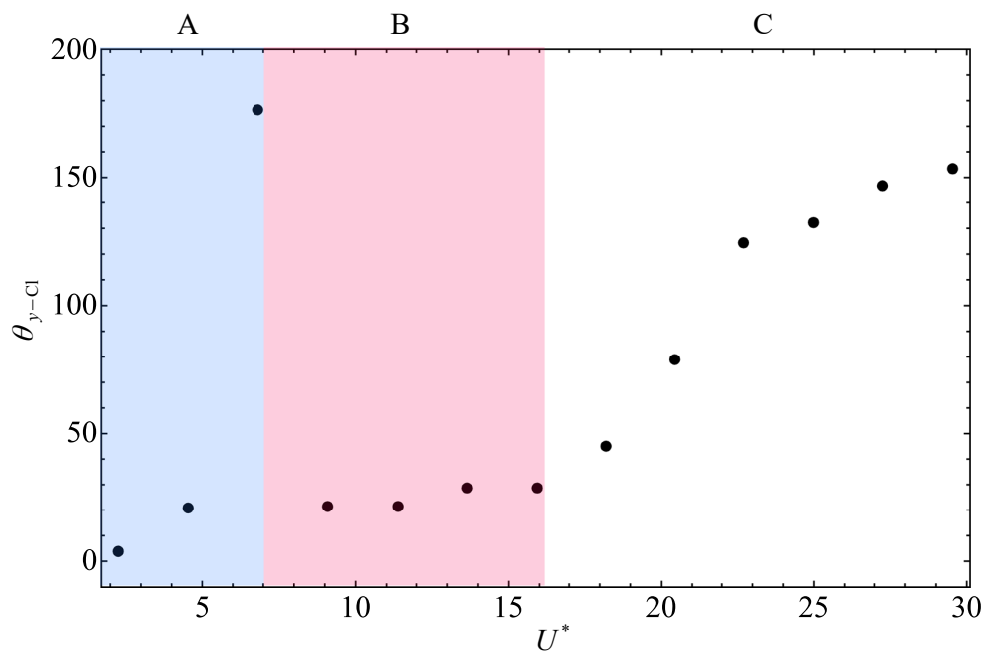
### 4.5.1 Power characteristic in cruciform angle - reduced velocity parameter space

In this study, the mechanical power is harnessed from the flow for each cruciform through the application of the formula in Eq. 3.16.

To understand how mechanical power  $P_{\text{Mech.,RMS}}$  is influenced not only by  $U^*$ , but also by the strip plate tilt angle  $\alpha$  ( $^\circ$ ),  $P_{\text{Mech.,RMS}}$  is visualised as contour plots, where the abscissa and ordinate are  $U^*$  and  $\alpha$ , respectively, and the colour of the contours denote the magnitude of  $P_{\text{Mech.,RMS}}$ . As an example, the values of  $y_{\text{RMS}}^*$  against  $U^*$  and  $\alpha$  are plotted in Fig. 4.46. The data used to produce Fig. 4.46 are those from Figs. 4.5, 4.24 and 4.35. Then, linear interpolations are performed on the  $y_{\text{RMS}}^*$  data along both  $U^*$  and  $\alpha$  axes to populate the  $\alpha-U^*$  parameter space. The result of this two-dimensional interpolation is Fig. 4.46. The snapshot of  $y_{\text{RMS}}^*$  evolution in the



(a) Phase lag for the  $22.5^\circ$  cruciform.



(b) Phase lag for the  $0^\circ$  cruciform.

Figure 4.45: Phase lag  $\theta_{y-\text{Cl}}$  (°) between Cl and  $y^*$  when  $22.5^\circ$  and  $0^\circ$ .

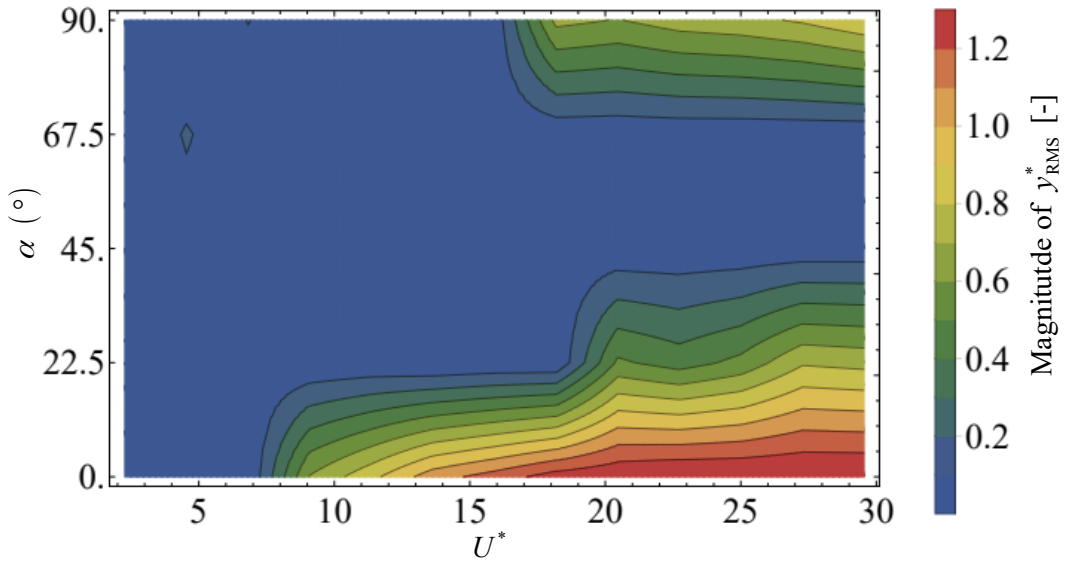


Figure 4.46: Isocontours describing the map of the normalised RMS amplitude of cylinder displacement,  $y_{\text{RMS}}^*$  in the cruciform angle - reduced velocity ( $\alpha-U^*$ ) parameter space.

$\alpha-U^*$  parameter space summarises the observations made previously in Figs. 4.5, 4.24 and 4.35.

Then, the same two-dimensional interpolation is performed on the results of  $P_{\text{Mech.,RMS}}$  and then summarised Fig. 4.47. Two regions of significant power generation exist: first, in the  $18.2 \leq U^* \leq 29.5$  range as  $\alpha$  approaches  $90^\circ$ , and second, starting as low as  $U^* = 9.1$  up to  $U^* = 29.5$  as  $\alpha$  approaches  $0^\circ$ . The estimated power in the region approaching  $\alpha = 90^\circ$  agrees well in magnitude with previous experimental works such as Koide *et al.* (2013). Also, even though no power data was measured in pure cruciform oscillator studies of Koide *et al.* (2009); Nguyen *et al.* (2012), their  $y_{\text{RMS}}^*$  data agrees well in trend and in magnitude with Fig. 4.46, along the  $90^\circ$  line. The  $P_{\text{Mech.,RMS}}$  contour of Fig. 4.47 visualises the high power region as  $\alpha$  approaches  $0^\circ$  and  $U^*$  approaches 29.5. The highest  $P_{\text{Mech.,RMS}}$  estimated from the simulation reaches  $O(10^1)$  mW, which is one order of magnitude larger than any cruciform energy harvester of this scale have ever recorded in the literature.

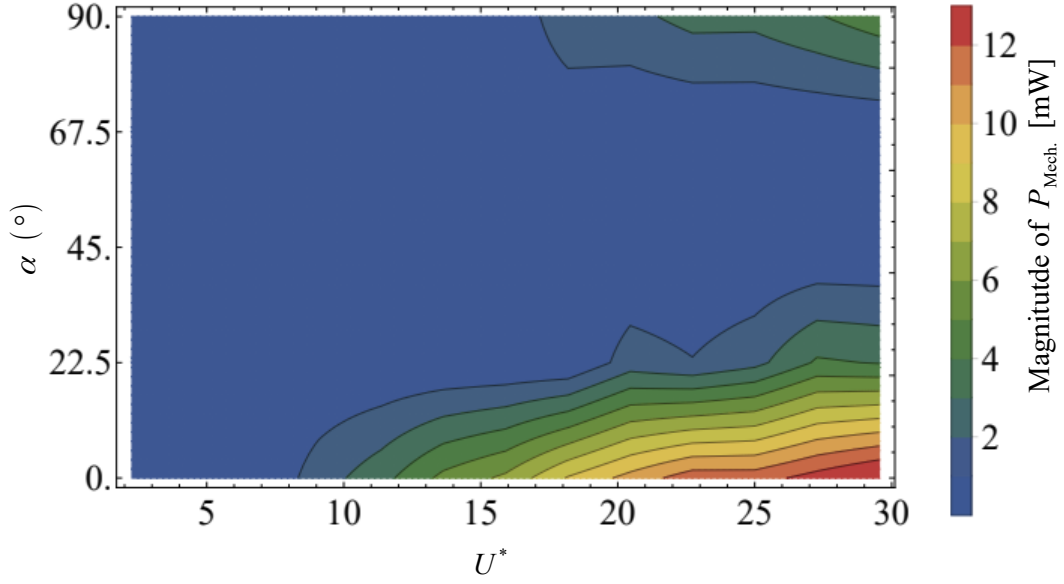


Figure 4.47: Isocontours describing the map of the estimated mechanical power in the cruciform angle - reduced velocity ( $\alpha$ - $U^*$ ) parameter space.

The  $P_{\text{Mech.,RMS}}$  contour also elucidated the feasibility of cruciform angle variation as a means to control the range of  $U^*$  within which substantive quantity of power can be harnessed. For a given operating range of  $U^*$ , one can choose for substantive power generation to take place in the high  $U^*$  region ( $U^* \geq 18.2$ ), or across a larger range starting from a minimum of  $U^* = 9.1$ , by manipulating the cruciform angle. For power generation in the high  $U^*$  region, one simply sets the cruciform angle to  $90^\circ$ , and for power generation starting from the lowest possible  $U^*$ , one should opt for a shallow-angled cruciform, with increasing magnitude of power generated as  $\alpha \rightarrow 0^\circ$ .

The estimation of mechanical power efficiency  $\eta_{\text{Mech.}} (\%)$  is based on the definition of efficiency in Sun *et al.* (2018). This thesis defines  $\eta_{\text{Mech.}}$  in Eq. 4.5.

$$\eta_{\text{Mech.}} (\%) = \frac{P_{\text{Mech.,RMS}}}{P_{\text{Fluid}}} = \frac{1}{2} \rho U_\infty^3 (2y_{\text{RMS}} + D) L \quad (4.5)$$

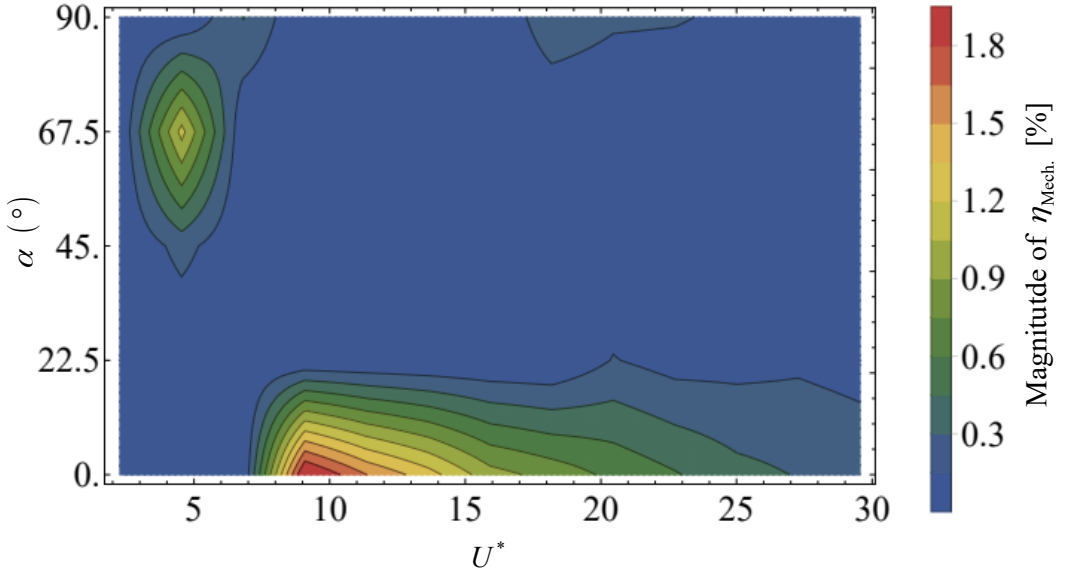


Figure 4.48: Isocontours describing the map of the estimated mechanical power in the cruciform angle - reduced velocity ( $\alpha$ - $U^*$ ) parameter space.

Here,  $U_\infty$  and  $L$  are the freestream velocity of the flow and the length of the cylinder, respectively. This study defines efficiency using  $y_{\text{RMS}}$  instead of  $y_{\text{Max}}$ , like Sun *et al.* (2018), due to the focus on time-averaged quantities instead of possibly one-off values.

Unlike Fig. 4.47, the efficiency contour does not display a trend similar to the contour of  $y_{\text{RMS}}^*$  in Fig. 4.46. The pure cruciform achieves maximum  $\eta_{\text{Mech.}}$  close to  $U^* = 18.2$ , steep-angled cruciforms ( $67.5^\circ$  and  $45^\circ$  cruciforms) attain maximum  $\eta_{\text{Mech.}}$  within the vicinity of  $(U^*, \alpha) = (4.5, 67.5^\circ)$ , and shallow-angled cruciforms ( $22.5^\circ$  and  $0^\circ$  layouts) strikes maximum  $\eta_{\text{Mech.}}$  in the neighbourhood of  $(U^*, \alpha) = (9.1, 0^\circ)$ . These high-efficiency regions is consistent with the assertion that different flow dynamics govern the vibration resulting from either the pure, steep-angled or shallow-angled cruciforms.

#### 4.5.2 Section Summary

In this final leg of investigations, the chapter attempts to address the question whether one is able to attain a more symmetrical distribution of the vortical structures along the upstream cylinder as the cruciform is brought to  $0^\circ$ . The results from the

amplitude/frequency response curves seems to suggest that an improved symmetry in the vortical distribution is certainly the case, judging from the huge improvement in  $y_{\text{RMS}}^*$ , especially for the  $0^\circ$  cruciform which is up to one order of magnitude larger than the maximum observed in the pure cruciform case. In addition, the high-amplitude vibrations are observed to start at a very low 9.1, compared to 20.5 for the pure cruciform case.

The main vibration-driving vortical structure in the shallow angled cruciforms seems to be Karman vortices, as suggested by the flow visualisations. They are symmetrically distributed relative to the  $Z = 0$  plane, and this seems to be the key to the onset of high-amplitude vibrations for both the  $22.5^\circ$  and  $0^\circ$  cruciforms. What is more interesting is the observation at the  $22.5^\circ$  cruciform, where the Karman vortices need not strictly exist in the same plane parallel to the cylinder axis in order to drive the high-amplitude vibrations. This condition of co-planar existence cannot be waived should the vibration-driving vortical structure is a streamwise vortex pair, as discussed in §4.3.2.

The magnitude of  $C_l_{\text{RMS}}$  is also found to improve by one order of magnitude for the  $0^\circ$  cruciform. Recalling the discussions in §4.2.5, it is easy to appreciate that this is due to the focussing of the freestream energy in the production of only one vortical structure: the Karman vortices, instead of a significant amount being lost to the formation of another type of vortical structure that does not contribute to the generation of vibration-driving lift. Needless to say, such a significant improvement in terms of  $C_l_{\text{RMS}}$  and  $y_{\text{RMS}}^*$  will necessarily bear improvement of a similar scale in terms of power output.

Through the isocontours of mechanical power in Fig. 4.47 one can inspect that there exists two bands suitable for energy harvesting, first as the oscillator approaches a pure cruciform configuration and second as the oscillator approaches the in-tandem configuration ( $0^\circ$ ). The two bands are separated by a region of sub-mW power output which can be useful as the starting configuration of the variable angle cruciform oscillator, followed by gradual rotation of the strip plate towards either poles of  $\alpha$  ( $^\circ$ ), in effect increasing its power output to the desired level.

However, the isocontours of the mechanical efficiency does not coincide with with the isocontours of mechanical power. This is largely due to the definition of *etamech* in Eq. 4.5 in the following manner. Maximum efficiency is attained when  $P_{\text{Mech.,RMS}} = P_{\text{Fluid}}$ . However,  $P_{\text{Fluid}}$  is simply the power transported by the freestream and is therefore proportional to the flow velocity. Therefore, if a VIV system such as the cruciform system studied in this work produces an amplitude response that plateaus with increase in  $U^*$ , *etamech* necessarily drops with increasing  $U^*$  and the peaks in *etamech* indicates the neighbourhood where  $P_{\text{Mech.,RMS}} = P_{\text{Fluid}}$ .

In the next chapter: Conclusion, the work summarises all the findings made during the course of this research and presents them in a more concise manner.

## CHAPTER 5

### CONCLUSION

This study investigated the system responses of a cruciform oscillator consisting of an upstream circular cylinder and a downstream strip plate. The upstream circular cylinder has a diameter  $D$  of 10 mm and the downstream strip plate has a width  $w$  of 10 mm and a thickness  $t$  of 3 mm. The cylinder and strip plate are separated by a gap of  $G = 0.16$ . The angle of the cruciform in this work is variable, between  $0 \leq \alpha(\circ) \leq 90$ . The main mode of investigation employed in this work is numerical, through the use of the free and open source C++ library OpenFOAM. The spatial discretisation of the numerical model is done using another free and open source software GMSH.

Establishing the soundness of the numerical data collected is important for building trust in the results and ensuring that they reflect reality as accurately as required by the problem. Validation of the numerical setup is conducted on the pure cruciform model, which is chosen to represent the whole matrix of numerical conditions studied in this thesis. The grid convergence index and the Richardson extrapolation are the two quantitative methods employed to establish the independence of the numerical results from the final form of spatial discretisation deployed in this study. In addition, an experimental rig was constructed consisting of an open flow channel and a pure cruciform oscillator, providing a reference point firmly grounded in reality.

The main body of investigation starts off with an in-depth study of the pure cruciform, presented in S4.2. In it, not only does this thesis reproduce the system responses of the pure cruciform, but also investigate the flow structures and how do they affect the lift generated that is directly responsible for driving the vibration of the cylinder. The range of reduced velocity examined in this thesis is  $2.3 \leq U^* \leq 29.5$ , which is equivalent to  $U = 0.1, 0.2, \dots, 1.3$  (m/s) in terms of freestream velocity. Then, in S4.3, this study begins to investigate the system responses of a modified form of cruciform oscillator, i.e., one with a cruciform angle between  $45 \leq \alpha(\circ) \leq 67.5$ . An

in-depth discussion on the vortical structure visualisations and their effect imprinted on the lift signal follows the discourse on system response.

Finally, in S4.4, this work investigated the system responses of cruciform oscillators with a cruciform angle between  $0 \leq \alpha(^{\circ}) \leq 22.5$ . Similar to S4.3, and in-depth discussion on the vortical structures and their impact on the lift signal is elaborated upon. S4.4 ends with the unification of the  $y_{\text{RMS}}^*$ ,  $P_{\text{Mech,RMS}}$  and  $\eta_{\text{Mech.}}$  as isocontour maps in  $\alpha - U^*$  parameter space.

In the current Chapter 5, the main findings are presented in §5.1 and concludes with recommendations for future works in §5.2.

## 5.1 Research Outcomes

The global trend to migrate towards clean and renewable energy sources is picking up speed within the past five years. Mature and conventional renewable power generation technologies such as solar, hydroelectric and wind form the bulk of technology implemented on a nation-wide scale across the globe. However, unlike fossil fuels, power generated from renewable energy sources have an inherent intermittency associated with their availability in the environment, which may fluctuate with day/night cycles and seasonality. Circumventing this requires one to include as many types of renewable power generation technologies as possible into the grid - preferably from different sources of clean and renewable energy - so that one can fill in for the other in times of low availability, hence on average providing a consistent output.

Nevertheless, other than the three clean and renewable power generation technologies listed above, most technologies are still in the prototyping or research stage, which means that nationwide deployment into the national energy mix still lies in the future. However, these technologies have a definitive use in applications such as powering wireless networks and their sensors which are usually located in places out of reach of the national grid, making it uneconomical the efforts to connect these devices directly to the national grid. One such technology that is being actively studied in the literature is energy harvesting from water flows in the environment, based on inducing alternating lift on an oscillator unit. This thesis deals with one such study.

This thesis studies an alternating lift technology based on a cruciform oscillator, known for its ability to deliver a consistent output over a very wide range of flow velocities. This merit is of immense utility as it means that the system is able to deliver a predictable output over a wide range of flow velocities, and it also means that the oscillator has a built-in safety mechanism preventing it from mechanical failure resulting from rogue, outlier vibrations due to intermittent excitations producing amplitudes exceeding the designated oscillator stroke length. However, a low power output, in the order of  $O(1)$  mW and low efficiency, in the order of  $O(10^{-1})$  (%) highlights the need for improving the power output and efficiencies specifically, and the need for the ability to assert more control over the system generally.

This thesis took the route of examining in detail the system responses of the pure cruciform, and attempts to explain why the system vibrates the way it does from the perspective of vortical structure interaction and their imprint on the lift acting on the cylinder. Understanding how the vortical structures impact the generation of lift and hence the cylinder displacement time series lead to the insight of varying the cruciform angle to control the strength and distribution of vortical structures along the length of the cylinder that directly effects the temporal evolution of lift and thus the system response.

The main findings of this thesis are summarised below.

1. The high-amplitude vibration of the pure cruciform is governed by the shedding of large-scale streamwise vortices, whose effects become visible when  $U^* > 18.2$ . Prior to that, between  $2.3 \leq U^* \leq 15.9$ , the vibration of the cylinder is regulated by the shedding of Karman vortices, i.e., KVIV regime. Computation of the average phase lag between the lift and cylinder displacement signals revealed the existence of an initial branch for SVIV that has been previously overlooked in the literature. However, even when the vibration mode has fully transitioned into the SVIV regime, Karman vortices continue to be shed away from the cruciform juncture along the length of the cylinder. Through ensemble empirical mode decomposition, this study is informed of the imprint left by the shedding of Karman vortices on the lift acting on the cylinder and computed

that the power output can be improved by a factor of two to three if the energy from the freestream that sustains the production of Karman vortices can instead be focussed on the vibration-driving streamwise vortices instead. The present author took this as the cue to modify the cruciform in order to affect the strength and distribution of the vortical structures in the flow, and subsequently the system response and power output and efficiency.

2. Modification of the cruciform oscillator in order to affect the strength and distribution of the vortical structures are done by changing the cruciform angle, i.e., the angle between the cylinder and strip plate. From an angle of  $90^\circ$ , the cruciform angle is reduced to  $67.5^\circ$ , and the system responses exhibited a marked difference from the case of the pure cruciform. There was no perceptible SVIV regime when  $U^* > 18.2$ , while a peak in  $y_{\text{RMS}}^*$  is observed only at  $U^* = 4.5$ , which places it firmly in the KVIV region. The instability observed in the frequency response of the  $67.5^\circ$  cruciform lead to the observation that the vortices are distributed asymmetrically relative to the  $Z = 0$  plane leading to a skewed distribution of lift along the cylinder which stands in the way of  $f^*$  settling down towards a stable value. The  $45^\circ$  cruciform has a similar amplitude response as the  $67.5^\circ$  cruciform, but since the vortical structures are more uniformly distributed along the cylinder, the  $f^*$  value managed to settle onto an approximately constant value. The counter-rotating large-scale streamwise vortices near the cruciform juncture exists in a plane that is not parallel to the axis of the cylinder, diminishing its ability to drive the vibration of the cylinder in both  $67.5^\circ$  and  $45^\circ$  cruciforms.
3. Lessons learnt from investigating the steep-angled cruciforms ( $45 \leq \alpha(^{\circ}) \leq 67.5$ ) intimated the possibility that only a symmetrical configuration of the cruciform - within a certain tolerance - is able to produce a distribution of vortical structures that are symmetrical with respect to the  $Z = 0$  plane, thus allowing the totality of the lift to drive the vibration of the cylinder. As such, this thesis proceeds to investigate the shallow-angled cruciforms, namely cruciforms with angle  $0 \leq \alpha(^{\circ}) \leq 22.5$ . The  $22.5^\circ$  cruciform demonstrated a significant improvement in terms of  $y_{\text{RMS}}^*$  compared to the steep-angled cruciforms when  $U^* > 18.2$ . Studying the vortical structures during the high-amplitude vibrations of the  $22.5^\circ$  cruciform informed this study that unlike the

steep-angled cruciforms, only one kind of vortical structure exists which is the vibration-driving Karman vortex. The visualisations also seem to support the assertion that as the distribution of vortices along the cylinder become more symmetric with respect to the  $Z = 0$  plane, a larger portion of the lift can act perpendicularly on the cylinder, hence driving the transverse motion of the cylinder. This effect is further amplified by the  $0^\circ$  cruciform, where only a single type of vortical structure dominates the flow field and they are distributed nearly exactly parallel to the axis of the cylinder and symmetrically against the  $Z = 0$  plane.

4. Completing the data collection from all cruciforms studied allows the present author to compute the mechanical power and efficiency of each cruciform and unify the results as isocontour maps charting their evolution in the cruciform angle versus reduced velocity parameter space. The large amplitude vibrations of the pure cruciform ( $90^\circ$ ) governed by streamwise vortex pairs produces power in the order of  $O(1)$  mW. The highest efficiency is attained in the neighbourhood of  $U^* = 18.2$ . The small amplitude vibrations of the steep-angled cruciforms ( $67.5^\circ$  and  $45^\circ$ ) are due to asymmetrical distribution of vortical structures relative to the  $Z = 0$  plane, producing sub-mW power. The highest efficiency is attained in the neighbourhood of  $(U^*, \alpha) = (4.5, 67.5^\circ)$ . The high-amplitude vibrations of the shallow-angled cruciforms ( $22.5^\circ$  and  $0^\circ$ ) are due to the shedding of three-dimensional Karman vortices resulting from synchronisation of vortices shed from the cylinder and the strip plate, which end up locking into the natural frequency of the cylinder. The power produced by these cruciforms can reach an order of  $O(10^1)$  mW. The highest efficiency is attained in the neighbourhood of  $(U^*, \alpha) = (9.1, 0^\circ)$ .

Following the findings listed above, this study has demonstrated the identification of the dominant vibration-driving vortical structure in a pure cruciform oscillator and gave an explanation to the observed system response. Furthermore, this study has demonstrated the identification of the main lift component acting on the cylinder and explained why the system responses behave the way they do for both steep-angled and shallow-angled cruciforms. Finally, this study has demonstrated the synthesis of the system responses from all cruciform studied and charted how the

mechanical power and efficiency of a generalised cruciform with varying angle evolves against reduced velocity.

## 5.2 Future Works

The current study focusses on a generalised form of cruciform with a fixed gap of  $G = 0.16$  between the upstream cylinder and downstream strip plate. The mechanical properties of the oscillator are very basic: a linear spring with a linear damper. It may possibly be beneficial for the generalised cruciform oscillator to include, for example, nonlinear springs to improve energy harvesting in the sub-mW power output regime, or even simply increase the amount of damping. This is because the damping coefficient is proportional to harnessed energy and therefore, useful to know beforehand, how the system responds under increased damping.

In addition, the Reynolds number range studied lies square in the TrSI2 regime. This Reynolds number range of  $1.1 \times 10^3 \leq \text{Re} \leq 14.6 \times 10^6$  lies in the transition regime of Reynolds number that does not bring about maximum lift from the shedding of Karman vortices from a circular cylinder. In the future, studies should be made in the TrSL3 regime of Reynolds number to exploit this feature. In fact, apart from the higher computational power required to compute numerical solutions in the region  $8 \times 10^3 \leq \text{Re} \leq 1.5 \times 10^5$  (TrSL3), research in this regime can be easily done by enlarging the diameter of the cylinder and collecting data under similar conditions as presented in this thesis.

Finally, the implementation of a more efficient procedure in the numerical loop to simplify the computation of cylinder displacement. In this work, ACMI is implemented to allow transport of scalar and vector quantities across non-adjoining patches. However, during motion of the cylinder, the whole computational domain upstream the strip plate moves along with the cylinder, causing a large number of nodes to be translated at each time step. It can be more efficient for the computation to pre-emptively limit the region of motion to include only the circular cylinder and nothing else.

## REFERENCES

- Agbaglah, G. and Mavriplis, C. (2019). Three-dimensional wakes behind cylinders of square and circular cross-section: Early and long-time dynamics. *Journal of Fluid Mechanics*. 870, 419–432. ISSN 1469-7645. doi:10.1017/jfm.2019.265.
- Alves Portela, F., Papadakis, G. and Vassilicos, J. C. (2020). *The role of Coherent Structures and Inhomogeneity in Near-Field Inter-Scale Turbulent Energy Transfers*.
- Arsh, B. A. (2020). Advances in the smart materials applications in the aerospace industries. *Aircraft Engineering and Aerospace Technology*. 92(7), 1027–1035. ISSN 1748-8842. doi:10.1108/AEAT-02-2020-0040.
- Arul, M., Kareem, A. and Kwon, D. K. (2020). Identification of Vortex-Induced Vibration of Tall Building Pinnacle Using Cluster Analysis for Fatigue Evaluation: Application to Burj Khalifa. *Journal of Structural Engineering*. ISSN 0733-9445. doi:10.1061/(asce)st.1943-541x.0002799.
- Asano, Y., Watanabe, H. and Noguchi, H. (2020). Effects of cavitation on Kármán vortex behind circular-cylinder arrays: A molecular dynamics study. *Journal of Chemical Physics*. 152(3), 034501. ISSN 0021-9606. doi:10.1063/1.5138212.
- Bae, H. M., Baranyi, L., Koide, M., Takahashi, T. and Shirakashi, M. (2001). Suppression of Karman Vortex Excitation of a Circular Cylinder By a Second Cylinder set Downstream in Cruciform Arrangement. *Journal of Computational and Applied Mechanics*. 2(2), 175–188. ISSN 0717-6163. doi:10.1007/s13398-014-0173-7.2.
- Barrero-Gil, A., Alonso, G. and Sanz-Andres, A. (2010). Energy harvesting from transverse galloping. *Journal of Sound and Vibration*. 329(14), 2873–2883. ISSN 0022-460X. doi:10.1016/j.jsv.2010.01.028.
- Bearman, P. (2011). Circular cylinder wakes and vortex-induced vibrations. *Journal of Fluids and Structures*. 27(5-6), 648–658. ISSN 0889-9746. doi:10.1016/j.jfluidstructs.2011.03.021.
- Bernitsas, M. and Raghavan, K. (2008a). Reduction/suppression of VIV of circular cylinders through roughness distribution at  $8 \times 10^3 < Re < 1.5 \times 10^5$ . In *Proceedings*

*of the International Conference on Offshore Mechanics and Arctic Engineering - OMAE*, vol. 5.

Bernitsas, M. and Raghavan, K. (2008b). Reduction/suppression of VIV of circular cylinders through roughness distribution at  $8 \times 10^3 < Re < 1.5 \times 10^5$ . In *Proceedings of the International Conference on Offshore Mechanics and Arctic Engineering - OMAE*, vol. 5. ISBN 9780791848227.

Bernitsas, M. M., Ben-Simon, Y., Raghavan, K. and Garcia, E. M. H. (2009). The VIVACE Converter: Model Tests at High Damping and Reynolds Number Around  $10^5$ . *Journal of Offshore Mechanics and Arctic Engineering*. 131(1). ISSN 0892-7219. doi:10.1115/1.2979796.

Bernitsas, M. M., Raghavan, K., Ben-Simon, Y. and Garcia, E. M. H. (2008). VIVACE (Vortex Induced Vibration Aquatic Clean Energy): A New Concept in Generation of Clean and Renewable Energy From Fluid Flow. *Journal of Offshore Mechanics and Arctic Engineering*. 130(4), 041101. ISSN 0892-7219. doi:10.1115/1.2957913.

Blevins, R. D. (1990). Flow-induced vibration.

Bukka, S. R., Magee, A. R. and Jaiman, R. K. (2020). Stability analysis of passive suppression for vortex-induced vibration. *Journal of Fluid Mechanics*. ISSN 1469-7645. doi:10.1017/jfm.2019.1026.

Chang, C.-C. J., Ajith Kumar, R. and Bernitsas, M. M. (2011). VIV and galloping of single circular cylinder with surface roughness at  $3.0 \times 10^4 \leq Re \leq 1.2 \times 10^5$ . *Ocean Engineering*. 38(16), 1713–1732. ISSN 0029-8018. doi:10.1016/j.oceaneng.2011.07.013.

Chen, H., Meng, C., Shan, Z., Fu, Z. and Bhargava, B. K. (2019). A novel low-rate denial of service attack detection approach in zigbee wireless sensor network by combining hilbert-huang transformation and trust evaluation. *IEEE Access*. ISSN 21693536. doi:10.1109/ACCESS.2019.2903816.

Chen, Z. Q., Liu, M., Hua, X. and Mou, T. (2012). Flutter, Galloping, and Vortex-Induced Vibrations of H-Section Hangers. *Journal of Bridge Engineering*. 17(3), 500–508. ISSN 1084-0702. doi:10.1061/(ASCE)BE.1943-5592.0000268.

Deloze, T., Hoarau, Y., Chinaud, M., Scheller, J., Deri, E., Rouchon, J. F., Duhayon, E. and Braza, M. (2016). Dynamic effect of an active deformable flat plate on

its turbulent flow. In *Notes on Numerical Fluid Mechanics and Multidisciplinary Design*. ISBN 9783319273846. ISSN 1612-2909. doi:10.1007/978-3-319-27386-0\_19.

Deng, J., Ren, A.-L. and Shao, X.-M. (2007). The flow between a stationary cylinder and a downstream elastic cylinder in cruciform arrangement. *Journal of Fluids and Structures*. 23(5), 715–731. ISSN 0889-9746. doi:10.1016/J.JFLUIDSTRUCTS.2006.11.005.

Department of Irrigation and Drainage Malaysia (2016). *Pelan Strategik Jabatan Pengairan dan Saliran Malaysia 2016-2020*. Retrievable at <http://water.selangor.gov.my/index.php/en/maklumat-jabatan/fungsi-jabatan/pengurusan-pantai/2-uncategorised/243-strategi-dan-formulasi-tindakan-pelan-strategik-jps-2016-2020>.

Derakhshandeh, J. F., Arjomandi, M., Dally, B. and Cazzolato, B. (2014). The effect of arrangement of two circular cylinders on the maximum efficiency of Vortex-Induced Vibration power using a Scale-Adaptive Simulation model. *Journal of Fluids and Structures*. 49, 654–666. doi:10.1016/j.jfluidstructs.2014.06.005.

Desai, A., Mittal, S. and Mittal, S. (2020). Experimental investigation of vortex shedding past a circular cylinder in the high subcritical regime. *Physics of Fluids*. 32(1), 014105. ISSN 1089-7666. doi:10.1063/1.5124168.

Ding, L., Zhang, L., Kim, E. S. and Bernitsas, M. M. (2015a). URANS vs. experiments of flow induced motions of multiple circular cylinders with passive turbulence control. *Journal of Fluids and Structures*. 54, 612–628. ISSN 1095-8622. doi:10.1016/j.jfluidstructs.2015.01.003.

Ding, L., Zhang, L., Wu, C., Mao, X. and Jiang, D. (2015b). Flow induced motion and energy harvesting of bluff bodies with different cross sections. *Energy Conversion and Management*. ISSN 0196-8904. doi:10.1016/j.enconman.2014.12.039.

Ding, W., Sun, H., Xu, W. and Bernitsas, M. M. (2017). Two tandem cylinders with turbulence stimulation in FIV power conversion: CFD with experimental verification of interaction. In *Proceedings of the International Conference on Offshore Mechanics and Arctic Engineering - OMAE*, vol. 10. doi:10.1115/OMAE2017-62271.

- Ding, W., Sun, H., Xu, W. and Bernitsas, M. M. (2019). Numerical investigation on interactive FIO of two-tandem cylinders for hydrokinetic energy harnessing. *Ocean Engineering*. 187, 106215. doi:10.1016/J.OCEANENG.2019.106215.
- Doare, O. and Michelin, S. (2011). Piezoelectric coupling in energy-harvesting fluttering flexible plates: Linear stability analysis and conversion efficiency. *Journal of Fluids and Structures*. 27(8), 1357–1375. ISSN 0889-9746. doi:10.1016/j.jfluidstructs.2011.04.008.
- Duranay, A. and Kinaci, O. K. (2020). Enhancing two-dimensional computational approach for vortex-induced vibrations by scaling lift force. *Ocean Engineering*. 217, 107620. ISSN 0029-8018. doi:10.1016/j.oceaneng.2020.107620.
- Durhasan, T., Pinar, E., Ozkan, G., Akilli, H. and Sahin, B. (2019). The effect of shroud on vortex shedding mechanism of cylinder. *Applied Ocean Research*. 84, 51–61. ISSN 0141-1187. doi:10.1016/j.apor.2019.01.007.
- Feng, C. C. (1963). The measurement of vortex induced effects in flow past stationary and oscillating circular and D-section cylinders. (October), 100.
- Gao, G., Zhu, L., Li, J. and Han, W. (2020). Application of a new empirical model of nonlinear self-excited force to torsional vortex-induced vibration and nonlinear flutter of bluff bridge sections. *Journal of Wind Engineering and Industrial Aerodynamics*. ISSN 0167-6105. doi:10.1016/j.jweia.2020.104313.
- Garcia, E. M. and Bernitsas, M. M. (2018). Effect of damping on variable added mass and lift of circular cylinders in vortex-induced vibrations. *Journal of Fluids and Structures*. 80, 451–472. ISSN 0889-9746. doi:10.1016/J.JFLUIDSTRUCTS.2018.02.005.
- Gazis, A. and Katsiri, E. (2020). A wireless sensor network for underground passages: Remote sensing and wildlife monitoring. *Engineering Reports*. 2(6). ISSN 2577-8196. doi:10.1002/eng2.12170.
- Geyer, T. F. (2020). Vortex shedding noise from finite, wall-mounted, circular cylinders modified with porous material. *AIAA Journal*. 58(5), 2014–2028. ISSN 0001-1452. doi:10.2514/1.J058877.

- Gibeau, B. and Ghaemi, S. (2019). The mode B structure of streamwise vortices in the wake of a two-dimensional blunt trailing edge. *Journal of Fluid Mechanics*. 884. ISSN 1469-7645. doi:10.1017/jfm.2019.931.
- Gibeau, B., Koch, C. R. and Ghaemi, S. (2018). Secondary instabilities in the wake of an elongated two-dimensional body with a blunt trailing edge. *Journal of Fluid Mechanics*. 846, 578–604. ISSN 1469-7645. doi:10.1017/jfm.2018.285.
- Gómez-Ortega, O., Manzanares-Bercial, R., Ogueta-Gutiérrez, M., Lopez-Nuñez, E., Franchini, S., Roibás-Millán, E. and Sanz-Andres, A. (2019). Experiments on the transverse aeroelastic instability of a single sphere in a swing configuration under a longitudinal wind. *Journal of Wind Engineering and Industrial Aerodynamics*. ISSN 0167-6105. doi:10.1016/j.jweia.2019.103979.
- Gumelar, A. B., Purnomo, M. H., Yuniarno, E. M. and Sugiarto, I. (2019). Spectral Analysis of Familiar Human Voice Based On Hilbert-Huang Transform. In *2018 International Conference on Computer Engineering, Network and Intelligent Multimedia, CENIM 2018 - Proceeding*. doi:10.1109/CENIM.2018.8710943.
- Hao, W. and Yang, Q. (2020). Reformative translation model for probability density functions of amplitude processes of crosswind-excited super-tall buildings. *Advances in Structural Engineering*. ISSN 2048-4011. doi:10.1177/1369433219886086.
- Hemsuwan, W., Sakamoto, K., Nakada, S. and Takahashi, T. (2018a). A longitudinal vortex wind turbine: Numerical study. *Journal of Wind Engineering and Industrial Aerodynamics*. 180, 213–230. ISSN 0167-6105. doi:10.1016/J.JWEIA.2018.07.022.
- Hemsuwan, W., Sakamoto, K., Nakada, S. and Takahashi, T. (2018b). A longitudinal vortex wind turbine: Numerical study. *Journal of Wind Engineering and Industrial Aerodynamics*. 180, 213–230. ISSN 0167-6105. doi:10.1016/J.JWEIA.2018.07.022.
- Hemsuwan, W., Sakamoto, K. and Takahashi, T. (2018c). Lift Force Generation of a Moving Circular Cylinder with a Strip-Plate Set Downstream in Cruciform Arrangement: Flow Field Improving Using Tip Ends. *International Journal of Aeronautical and Space Sciences*. 19(3), 606–617. ISSN 2093-274X. doi:10.1007/s42405-018-0068-5.
- Hemsuwan, W., Sakamoto, K. and Takahashi, T. (2018d). Numerical investigation of lift-force generation on a moving circular cylinder in a uniform flow driven by

longitudinal vortex. *Journal of Fluids and Structures*. 83, 448–470. ISSN 0889-9746. doi:10.1016/J.JFLUIDSTRUCTS.2018.09.010.

Hemsuwan, W., Sakamoto, K. and Takahashi, T. (2021). Steady lift-force generation on a circular cylinder utilising a longitudinal vortex: Influence of geometrical parameters. *Journal of Wind Engineering and Industrial Aerodynamics*. 212, 104612. ISSN 01676105. doi:10.1016/j.jweia.2021.104612.

Hu, G. and Kwok, K. C. (2020). Predicting wind pressures around circular cylinders using machine learning techniques. *Journal of Wind Engineering and Industrial Aerodynamics*. 198, 104099. ISSN 0167-6105. doi:10.1016/j.jweia.2020.104099.

Huang, N. E. (2014). *Hilbert-Huang transform and its applications*. vol. 16. World Scientific.

Huang, N. E., Shen, Z., Long, S. R., Wu, M. C., Snin, H. H., Zheng, Q., Yen, N. C., Tung, C. C. and Liu, H. H. (1998). The empirical mode decomposition and the Hilbert spectrum for nonlinear and non-stationary time series analysis. *Proceedings of the Royal Society A: Mathematical, Physical and Engineering Sciences*. ISSN 1364-5021. doi:10.1098/rspa.1998.0193.

Kadir, E. A., Rosa, S. L. and Yulianti, A. (2019). Application of WSNs for Detection Land and Forest Fire in Riau Province Indonesia. In *Proceedings of 2018 International Conference on Electrical Engineering and Computer Science, ICECOS 2018*. ISBN 9781538657201. doi:10.1109/ICECOS.2018.8605197.

Kang, Y., Xiao, W., Wang, Q., Zhang, D. and Zhao, J. (2020). Suppression of Vortex-Induced Vibration by Fairings on Marine Risers. *Journal of Ocean University of China*. 19(2), 298–306. ISSN 1672-5182. doi:10.1007/s11802-020-4033-0.

Kato, N., Koide, M., Takahashi, T. and Shirakashi, M. (2006). Influence of Cross-Sectional Configuration on the Longitudinal Vortex Excitation of the Upstream Cylinder in Cruciform Two-Cylinder System. *Journal of Fluid Science and Technology*. 1(2), 126–137. ISSN 1880-5558. doi:10.1299/jfst.1.126. Retrievable at <http://joi.jlc.jst.go.jp/JST.JSTAGE/jfst/1.126?from=CrossRef>.

Kato, N., Koide, M., Takahashi, T. and Shirakashi, M. (2007). Vibration Control for a Circular Cylinder by a Strip-plate Set Downstream in Cruciform Arrangement (1st Report, Influence of a Downstream Strip-plate on the Shedding of Longitudinal

Vortices from Fixed System). *Transactions of the Japan Society of Mechanical Engineers Series B*. 73(728), 957–964. ISSN 0387-5016. doi:10.1299/kikaib.73.957.

Kawabata, Y., Takahashi, T., Hagiwara, T. and Shirakashi, M. (2013). Interference Effect of Downstream Strip-Plate on the Crossflow Vibration of a Square Cylinder. *Journal of Fluid Science and Technology*. 8(3), 647–658. ISSN 1880-5558. doi:10.1299/jfst.8.348.

Kementerian Kewangan Malaysia (2019). *Belanjawan 2020*. Retrievable at <http://www.kabinet.gov.my/bkpp/pdf/belanjawan/2020.pdf>.

Khalak, A. and Williamson, C. (1999). Motions, Forces And Mode Transitions In Vortex-Induced Vibrations At Low Mass-Damping. *Journal of Fluids and Structures*. 13(7-8), 813–851. ISSN 0889-9746. doi:10.1006/jfls.1999.0236.

Kim, E. S. and Bernitsas, M. M. (2016). Performance prediction of horizontal hydrokinetic energy converter using multiple-cylinder synergy in flow induced motion. *Applied Energy*. 170, 92–100. ISSN 03062619. doi:10.1016/j.apenergy.2016.02.116.

Kinaci, O. K., Lakka, S., Sun, H. and Bernitsas, M. M. (2016). Effect of tip-flow on vortex induced vibration of circular cylinders for Re. *Ocean Engineering*. 117, 130–142. ISSN 0029-8018. doi:10.1016/j.oceaneng.2016.03.055.

Kluger, J., Moon, F. and Rand, R. (2013). Shape optimization of a blunt body Vibro-wind galloping oscillator. *Journal of Fluids and Structures*. 40, 185–200. ISSN 0889-9746. doi:10.1016/j.jfluidstructs.2013.03.014.

Koide, M., Kato, N., Yamada, S., Kawabata, Y., Takahashi, T. and Shirakashi, M. (2007). Influence Of A Cruciform Arrangement Downstream Strip-Plate On Crossflow Vibration. *Journal of Computational and Applied Mechanics*. 8(2), 135–148.

Koide, M., Ootani, K., Yamada, S., Takahashi, T. and Shirakashi, M. (2006). Vortex Excitation Caused by Longitudinal Vortices Shedding from Cruciform Cylinder System in Water Flow. *JSME International Journal*. 49(4), 1043–1048.

Koide, M., Sekizaki, T., Yamada, S., Takahashi, T. and Shirakashi, M. (2009). A Novel Technique for Hydroelectricity Utilizing Vortex Induced Vibration. In *Proceedings of the ASME Pressure Vessels and Piping Division Conference, PVP2009-77487*.

- Koide, M., Sekizaki, T., Yamada, S., Takahashi, T. and Shirakashi, M. (2013). Prospect of Micro Power Generation Utilizing VIV in Small Stream Based on Verification Experiments of Power Generation in Water Tunnel. *Journal of Fluid Science and Technology*. 8(3), 294–308. ISSN 1880-5558. doi:10.1299/jfst.8.294.
- Koide, M., Takahashi, T., Shirakashi, M. and Salim, S. A. Z. B. S. (2017). Three-dimensional structure of longitudinal vortices shedding from cruciform two-cylinder systems with different geometries. *Journal of Visualization*, 1–11.
- Krishnendu, P. and Ramakrishnan, B. (2020). Performance analysis of dual sphere wave energy converter integrated with a chambered breakwater system. *Applied Ocean Research*. 101, 102279. ISSN 0141-1187. doi:10.1016/j.apor.2020.102279.
- Langley Research Centre (2018). *Turbulence Modeling Resource*.
- Larsen, C. M. and Halse, K. H. (1997). Comparison of models for vortex induced vibrations of slender marine structures. *Marine Structures*. 10(6), 413–441. ISSN 0951-8339. doi:10.1016/S0951-8339(97)00011-7.
- Ledda, P. G., Siconolfi, L., Viola, F., Gallaire, F. and Camarri, S. (2018). Suppression of von Kármán vortex streets past porous rectangular cylinders. In *Physical Review Fluids*, vol. 3. October. American Physical Society. ISSN 2469-990X, 103901. doi:10.1103/PhysRevFluids.3.103901.
- Li, S., Li, S., Laima, S. and Li, H. (2021). Data-driven modeling of bridge buffeting in the time domain using long short-term memory network based on structural health monitoring. *Structural Control and Health Monitoring*, e2772. ISSN 1545-2255. doi:10.1002/stc.2772.
- Lin, L. M., Zhong, X. F. and Wu, Y. X. (2018). Effect of perforation on flow past a conic cylinder at  $Re = 100$ : vortex-shedding pattern and force history. *Acta Mechanica Sinica/Lixue Xuebao*. 34(2), 238–256. ISSN 1614-3116. doi:10.1007/s10409-017-0707-2.
- Liu, G., Li, H., Qiu, Z., Leng, D., Li, Z. and Li, W. (2020). *A mini review of recent progress on vortex-induced vibrations of marine risers*. doi:10.1016/j.oceaneng.2019.106704.

- Luo, S., Chew, Y. and Ng, Y. (2003). Hysteresis phenomenon in the galloping oscillation of a square cylinder. *Journal of Fluids and Structures*. 18(1), 103–118. ISSN 0889-9746. doi:10.1016/S0889-9746(03)00084-7.
- Ma, C., Sun, H. and Bernitsas, M. M. (2018). Nonlinear piecewise restoring force in hydrokinetic power conversion using flow-induced vibrations of two tandem cylinders. *Journal of Offshore Mechanics and Arctic Engineering*. 140(4). doi:10.1115/1.4038584.
- Ma, C., Sun, H., Nowakowski, G., Mauer, E. and Bernitsas, M. M. (2016). Nonlinear piecewise restoring force in hydrokinetic power conversion using flow induced motions of single cylinder. *Ocean Engineering*. ISSN 0029-8018. doi:10.1016/j.oceaneng.2016.10.020.
- Mao, Y. C., Cheng, Y. K. and Qi, H. (2020). Sensor Network Partition Based on the Spatial-Temporal Features for Structure Safety Monitoring. *Jisuanji Xuebao/Chinese Journal of Computers*. ISSN 0254-4164. doi:10.11897/SP.J.1016.2020.00631.
- Maruai, N. M., Ali, M. S. M., Ismail, M. H. and Zaki, S. A. (2018). Flow-induced vibration of a square cylinder and downstream flat plate associated with micro-scale energy harvester. *Journal of Wind Engineering and Industrial Aerodynamics*. 175, 264–282. doi:10.1016/j.jweia.2018.01.010.
- Maruai, N. M., Mat Ali, M. S., Ismail, M. H. and Shaikh Salim, S. A. Z. (2017). Downstream flat plate as the flow-induced vibration enhancer for energy harvesting. *Journal of Vibration and Control*, 107754631770787. ISSN 1077-5463. doi:10.1177/1077546317707877.
- Mat Ali, M. S., Doolan, C. J. and Wheatley, V. (2011). Low Reynolds number flow over a square cylinder with a splitter plate. *Physics of Fluids*. 23(3). ISSN 1070-6631. doi:10.1063/1.3563619.
- Mat Ali, M. S., Doolan, C. J. and Wheatley, V. (2012). Low Reynolds number flow over a square cylinder with a detached flat plate. *International Journal of Heat and Fluid Flow*. 36, 133–141. ISSN 0142-727X. doi:10.1016/j.ijheatfluidflow.2012.03.011.
- Meng, S., Chen, Y. and Che, C. (2020). Slug flow's intermittent feature affects VIV responses of flexible marine risers. *Ocean Engineering*. ISSN 0029-8018. doi:10.1016/j.oceaneng.2019.106883.

- Mohamed, A., Zaki, S. A., Shirakashi, M., Mat Ali, M. S. and Samsudin, M. Z. (2021). Experimental investigation on vortex-induced vibration and galloping of rectangular cylinders of varying side ratios with a downstream square plate. *Journal of Wind Engineering and Industrial Aerodynamics*. 211, 104563. ISSN 01676105. doi:10.1016/j.jweia.2021.104563.
- Nakamura, T., Kaneko, S., Fumio, I., Minoru, K., Kunihiko, I., Nishihara, T., Mureithi, N. W. and Mikael A., L. (2013). *Flow-Induced Vibrations: Classifications and Lessons from Practical Experiences*. Butterworth-Heinemann. ISBN 0080983529. Retrievable at <https://books.google.com/books?hl=en&lr=&id=LQusIJlDbswC&pgis=1>.
- Nakamura, Y. and Nakashima, M. (1986). Vortex excitation of prisms with elongated rectangular, H and |- cross-sections. *Journal of Fluid Mechanics*. ISSN 1469-7645. doi:10.1017/S0022112086002252.
- Nguyen, T., Koide, M., Takahashi, T. and Shirakashi, M. (2010). Universality of longitudinal vortices shedding from a cruciform two circular cylinder system in uniform flow. *Journal of Fluid Science and Technology*. 5(3), 603–616.
- Nguyen, T., Koide, M., Yamada, S., Takahashi, T. and Shirakashi, M. (2012). Influence of mass and damping ratios on VIVs of a cylinder with a downstream counterpart in cruciform arrangement. *Journal of Fluids and Structures*. 28, 40–55. ISSN 0889-9746. doi:10.1016/j.jfluidstructs.2011.10.006.
- Ni, F. T., Zhang, J. and Noori, M. N. (2020). Deep learning for data anomaly detection and data compression of a long-span suspension bridge. *Computer-Aided Civil and Infrastructure Engineering*. ISSN 1467-8667. doi:10.1111/mice.12528.
- Ogink, R. and Metrikine, A. (2010). A wake oscillator with frequency dependent coupling for the modeling of vortex-induced vibration. *Journal of Sound and Vibration*. 329(26), 5452–5473. ISSN 0022-460X. doi:10.1016/j.jsv.2010.07.008.
- Park, H., Ajith Kumar, R. and Bernitsas, M. M. (2016). Suppression of vortex-induced vibrations of rigid circular cylinder on springs by localized surface roughness at  $3 \times 10^4 \leq Re \leq 1.2 \times 10^5$ . *Ocean Engineering*. 111, 218–233. ISSN 0029-8018. doi:10.1016/j.oceaneng.2015.10.044.

- Park, H., Kim, E. S. and Bernitsas, M. M. (2017). Sensitivity to Zone Covering of the Map of Passive Turbulence Control to Flow-Induced Motions for a Circular Cylinder at  $30000 \leq Re \leq 120000$ . *Journal of Offshore Mechanics and Arctic Engineering*. 139(2), 021802. ISSN 0892-7219. doi: 10.1115/1.4035140. Retrievable at <https://asmedigitalcollection.asme.org/offshoremechanics/article/doi/10.1115/1.4035140/377160/Sensitivity-to-Zone-Covering-of-the-Map-of-Passive>.
- Park, H., Kumar, R. A. and Bernitsas, M. M. (2013). Enhancement of flow-induced motion of rigid circular cylinder on springs by localized surface roughness at  $3 \times 10^4 \leq Re \leq 1.2 \times 10^5$ . *Ocean Engineering*. 72, 403–415. ISSN 0029-8018. doi:10.1016/j.oceaneng.2013.06.026.
- Pathak, A. (2020). An artificial bee colony inspired clustering solution to prolong lifetime of wireless sensor networks. *Iranian Journal of Electrical and Electronic Engineering*. ISSN 2383-3890. doi:10.22068/IJEEE.16.4.425.
- Raghavan, K. (2007). *Energy Extraction from a Steady Flow Using Vortex Induced Vibration*. Doctoral dissertation. The University of Michigan.
- Raghavan, U., Albert, R. and Kumara, S. (2007). Near linear time algorithm to detect community structures in large-scale networks. *Phys. Rev E*. 76, 036106.
- Rahman, M. R., Hasan, A. B. and Labib, M. I. (2015). Numerical investigation of aerodynamic hysteresis for transonic flow over a supercritical airfoil. In *Procedia Engineering*, vol. 105. jan. Elsevier Ltd. ISSN 18777058, 368–374. doi:10.1016/j.proeng.2015.05.021.
- Rai, M. M. (2018). Vortex shedding characteristics of the wake of a thin flat plate with a circular trailing edge. *International Journal of Heat and Fluid Flow*. 72, 20–36. ISSN 0142-727X. doi:10.1016/j.ijheatfluidflow.2018.05.015.
- Raissi, M., Wang, Z., Triantafyllou, M. S. and Karniadakis, G. E. (2019). Deep learning of vortex-induced vibrations. *Journal of Fluid Mechanics*. 861, 119–137. ISSN 1469-7645. doi:10.1017/jfm.2018.872.
- Ren, F., Wang, C. and Tang, H. (2019). Active control of vortex-induced vibration of a circular cylinder using machine learning. *Physics of Fluids*. 31(9), 093601. ISSN 1089-7666. doi:10.1063/1.5115258.

- Richardson, L. F. and Gaunt, J. A. (1927). The deferred approach to the limit. *Philosophical Transactions of the Royal Society A*. ISSN 1364-5021. doi: 10.1098/rsta.1927.0008.
- Sadeghi Eshkevari, S., Pakzad, S. N., Takáč, M. and Matarazzo, T. J. (2020). Modal Identification of Bridges Using Mobile Sensors with Sparse Vibration Data. *Journal of Engineering Mechanics*. ISSN 0733-9399. doi:10.1061/(asce)em.1943-7889.0001733.
- Saint-Michel, B., Dubrulle, B., Marié, L., Ravelet, F. and Daviaud, F. (2014). Influence of Reynolds number and forcing type in a turbulent von Kármán flow. *New Journal of Physics*. 16(6), 063037. ISSN 13672630. doi:10.1088/1367-2630/16/6/063037.
- Sakamoto, K., Hemsuwan, W. and Takahashi, T. (2021). Development of a wind turbine driven by longitudinal vortex: Wind tunnel experiment to investigate the basic characteristics of the wind turbine using a single circular cylinder blade. *Journal of Wind Engineering and Industrial Aerodynamics*. 210, 104492. ISSN 01676105. doi:10.1016/j.jweia.2020.104492.
- Shao, W. D. and Li, J. (2016). Numerical prediction of noise induced by flow around a cylinder considering the convection effect. *Kung Cheng Je Wu Li Hsueh Pao/Journal of Engineering Thermophysics*. ISSN 0253-231X.
- Shiraishi, N., Matsumoto, M., Shirato, H. and Ishizaki, H. (1988). On aerodynamic stability effects for bluff rectangular cylinders by their corner-cut. *Journal of Wind Engineering and Industrial Aerodynamics*. 28(1-3), 371–380. ISSN 0167-6105. doi:10.1016/0167-6105(88)90133-X.
- Shirakashi, M., Mizuguchi, K. and Bae, H. M. (1989). Flow-induced excitation of an elastically-supported cylinder caused by another located downstream in cruciform arrangement. *Journal of Fluids and Structures*. 3(6), 595–607. ISSN 1095-8622. doi:10.1016/S0889-9746(89)90150-3.
- Shirakashi, M., Takahashi, T., Kumagai, I. and Matsumoto, T. (2001). Vortex-induced vibration of the upstream cylinder of a two-cylinder system in cruciform arrangement. *Journal of Computational and Applied Mechanics*. 2(1), 103–122.

- Spalart, P. and Allmaras, S. (1992). A one-equation turbulence model for aerodynamic flows. In *30th Aerospace Sciences Meeting and Exhibit*. ISBN 0034-1223. ISSN 0034-1223. doi:10.2514/6.1992-439.
- Stern, F., Wilson, R. V., Coleman, H. W. and Paterson, E. G. (2001). Comprehensive approach to verification and validation of CFD simulations part 1: methodology and procedures. *Journal of fluids engineering*. 123(4), 793–802.
- Sun, H., Kim, E. S., Nowakowski, G., Mauer, E. and Bernitsas, M. M. (2016). Effect of mass-ratio, damping, and stiffness on optimal hydrokinetic energy conversion of a single, rough cylinder in flow induced motions. *Renewable Energy*. 99, 936–959. ISSN 0960-1481. doi:10.1016/j.renene.2016.07.024.
- Sun, H., Ma, C. and Bernitsas, M. M. (2018). Hydrokinetic power conversion using Flow Induced Vibrations with nonlinear (adaptive piecewise-linear) springs. *Energy*. 143, 1085–1106. ISSN 0360-5442. doi:10.1016/j.energy.2017.10.140.
- Sun, H., Ma, C., Kim, E. S., Nowakowski, G., Mauer, E. and Bernitsas, M. M. (2019). Flow-induced vibration of tandem circular cylinders with selective roughness: Effect of spacing, damping and stiffness. *European Journal of Mechanics, B/Fluids*. 74, 219–241. ISSN 0997-7546. doi:10.1016/j.euromechflu.2018.10.024.
- Takahashi, T., Baranyi, L. and Shirakashi, M. (1999). Configuration and Frequency of Longitudinal Vortices Shedding from Circular Cylinders in Cruciform Arrangement. *Journal of the Visualization Society of Japan*. 19(75), 64–72. doi:10.3154/jvs.19.75\_328.
- Tang, M. F., Dong, G. H., Xu, T. J., wei Bi, C. and Wang, S. (2021). Large-eddy simulations of flow past cruciform circular cylinders in subcritical Reynolds numbers. *Ocean Engineering*. 220, 108484. ISSN 00298018. doi:10.1016/j.oceaneng.2020.108484.
- Unit Pemodenan Tadbiran dan Perancangan Pengurusan Malaysia (2016). *Pelan Strategik ICT Sektor Awam 2016-2020*. Retrievable at <https://www.mampu.gov.my/ms/penerbitan-mampu/send/2-buku/680-pelan-strategik-ict-sektor-awam-2016-2020-versi-bm-2>.
- Wang, S., Wen, F., Shi, X. and Zhou, X. (2019). Stability analysis of asymmetric wakes. *Physics of Fluids*. ISSN 1089-7666. doi:10.1063/1.5098111.

- Wen, C., Wang, J., Zhang, Y., Xu, T., Zhang, X. and Ning, Y. (2020). Vehicle Trajectory Clustering and Anomaly Detection at Freeway Off-Ramp Based on Driving Behavior Similarity. In *CICTP 2020*. August. Reston, VA: American Society of Civil Engineers. ISBN 9780784482933, 4220–4232. doi:10.1061/9780784482933.362.
- Williamson, C. (1996a). Vortex Dynamics in the Cylinder Wake. *Annual Review of Fluid Mechanics*. 28(1), 477–539. ISSN 0066-4189. doi:10.1146/annurev.fl.28.010196.002401.
- Williamson, C. H. K. (1996b). Three-dimensional wake transition. *Journal of Fluid Mechanics*. 328(-1), 345. ISSN 0022-1120. doi:10.1017/S0022112096008750.
- Wu, W., Bernitsas, M. M. and Maki, K. (2011). RANS Simulation vs. Experiments of Flow Induced Motion of Circular Cylinder With Passive Turbulence Control at  $35,000 < \text{Re} < 130,000$ . In *Volume 7: CFD and VIV; Offshore Geotechnics*. January. ASME. ISBN 978-0-7918-4439-7, 733–744. doi:10.1115/OMAE2011-50311.
- Wu, W., Sun, H., Lv, B. and Bernitsas, M. M. (2018). Modelling of a hydrokinetic energy converter for flow-induced vibration based on experimental data. *Ocean Engineering*. 155, 392–410. doi:10.1016/j.oceaneng.2018.02.030.
- Wu, Z. and Huang, N. E. (2008). Ensemble Empirical Mode Decomposition: A Noise-Assisted Data Analysis Method. *Advances in Adaptive Data Analysis*. ISSN 1793-5369. doi:10.1142/s1793536909000047.
- Xia, Y., Michelin, S. and Doaré, O. (2015a). Fluid-solid-electric lock-in of energy-harvesting piezoelectric flags. *Physical Review Applied*. 3(1), 14009. ISSN 2331-7019. doi:10.1103/PhysRevApplied.3.014009.
- Xia, Y., Michelin, S. S., Doaré, O. and Doare, O. (2015b). Resonance-induced enhancement of the energy harvesting performance of piezoelectric flags. *Applied Physics Letters*. 107(26), 1–5. ISSN 0003-6951. doi:10.1063/1.4939117.
- Xiong, C., Cheng, L., Tong, F. and An, H. (2018). On regime C flow around an oscillating circular cylinder. *Journal of Fluid Mechanics*. ISSN 1469-7645. doi:10.1017/jfm.2018.436.
- Xu, W., Ji, C., Sun, H., Ding, W. and Bernitsas, M. M. (2017). Flow-induced vibration (FIV) and hydrokinetic power conversion of two staggered, low mass-ratio cylinders, with passive turbulence control in the TrSL3 flow regime ( $2.5 \times 10^4 < \text{Re} < 1.2 \times 10^5$ ).

In *Proceedings of the International Conference on Offshore Mechanics and Arctic Engineering - OMAE*, vol. 10. doi:10.1115/OMAE2017-62693.

Xu, W., Ji, C., Sun, H., Ding, W. and Bernitsas, M. M. (2019). Flow-induced vibration of two elastically mounted tandem cylinders in cross-flow at subcritical Reynolds numbers. *Ocean Engineering*. 173, 375–387. ISSN 0029-8018. doi:10.1016/J.OCEANENG.2019.01.016.

Yokoi, Y. (2016). Flow visualization of the vortex shedding from an in-line oscillating circular cylinder with splitter plate. In *AIP Conference Proceedings*, vol. 1745. June. American Institute of Physics Inc. ISBN 9780735414020. ISSN 1551-7616, 020066. doi:10.1063/1.4953760.

Yuan, W., Sun, H., Li, H. and Bernitsas, M. M. (2020). Flow-induced oscillation patterns for two tandem cylinders with turbulence stimulation and variable stiffness and damping. *Ocean Engineering*. 218, 108237. ISSN 00298018. doi:10.1016/j.oceaneng.2020.108237. Retrievable at <https://linkinghub.elsevier.com/retrieve/pii/S0029801820311598>.

Zdravkovich, M. (1981). Review and classification of various aerodynamic and hydrodynamic means for suppressing vortex shedding. *Journal of Wind Engineering and Industrial Aerodynamics*. 7(2), 145–189. ISSN 0167-6105. doi:10.1016/0167-6105(81)90036-2.

Zdravkovich, M. (1985). Flow induced oscillations of two interfering circular cylinders. *Journal of Sound and Vibration*. 101(4), 511–521. ISSN 0022-460X. doi:10.1016/S0022-460X(85)80068-7.

Zdravkovich, M. M. (1983). Interference between two circular cylinders forming a cross. *Journal of Fluid Mechanics*. 128(-1), 231. ISSN 0022-1120. doi:10.1017/S0022112083000464.

Zdravkovich, M. M. (1997). *Flow around circular cylinders*. ISBN 0198563965.

Zellweger, F., Coomes, D., Lenoir, J., Depauw, L., Maes, S. L., Wulf, M., Kirby, K. J., Brunet, J., Kopecký, M., Máliš, F., Schmidt, W., Heinrichs, S., den Ouden, J., Jaroszewicz, B., Buyse, G., Spicher, F., Verheyen, K. and De Frenne, P. (2019). Seasonal drivers of understorey temperature buffering in temperate deciduous forests

across Europe. *Global Ecology and Biogeography*. ISSN 1466-8238. doi:10.1111/geb.12991.

Zhang, B., Mao, Z., Song, B., Ding, W. and Tian, W. (2018a). Numerical investigation on effect of damping-ratio and mass-ratio on energy harnessing of a square cylinder in FIM. *Energy*. 144, 218–231. doi:10.1016/j.energy.2017.11.153.

Zhang, D., Sun, H., Wang, W. and Bernitsas, M. M. (2018b). Rigid cylinder with asymmetric roughness in Flow Induced Vibrations. *Ocean Engineering*. 150, 363–376. ISSN 0029-8018. doi:10.1016/j.oceaneng.2018.01.005.

Zhang, H., Xin, D. and Ou, J. (2016). Wake control of vortex shedding based on spanwise suction of a bridge section model using Delayed Detached Eddy Simulation. *Journal of Wind Engineering and Industrial Aerodynamics*. 155, 100–114. ISSN 0167-6105. doi:10.1016/j.jweia.2016.05.004.

Zhang, H., Xin, D. and Ou, J. (2019). Wake control using spanwise-varying vortex generators on bridge decks: A computational study. *Journal of Wind Engineering and Industrial Aerodynamics*. 184, 185–197. ISSN 0167-6105. doi:10.1016/j.jweia.2018.11.031.

Zhang, J., Guo, H., Tang, Y. and Li, Y. (2020). Effect of top tension on vortex-induced vibration of deep-sea risers. *Journal of Marine Science and Engineering*. ISSN 2077-1312. doi:10.3390/jmse8020121.

Zhao, M. and Lu, L. (2018). Numerical simulation of flow past two circular cylinders in cruciform arrangement. *Journal of Fluid Mechanics*. 848, 1013–1039. ISSN 0022-1120. doi:10.1017/jfm.2018.380.

Zhou, L., Meng, Y. and Abbaspour, K. C. (2019). A new framework for multi-site stochastic rainfall generator based on empirical orthogonal function analysis and Hilbert-Huang transform. *Journal of Hydrology*. ISSN 0022-1694. doi:10.1016/j.jhydrol.2019.05.047.

Zou, B., Thierry, N. N. B., Tang, H., Xu, L., Zhou, C., Wang, X., Dong, S. and Hu, F. (2021). Flow field and drag characteristics of netting of cruciform structures with various sizes of knot structure using CFD models. *Applied Ocean Research*. 106, 102466. ISSN 01411187. doi:10.1016/j.apor.2020.102466.

## Appendix A Temporal Evolution of Lift in a Pure Cruciform System for Energy

Ocean Engineering 223 (2021) 108648



### Temporal evolution of lift in a pure cruciform system for energy harvesting

Ahmad Adzlan<sup>a,b,\*</sup>, Mohamed Sukri Mat Ali<sup>a</sup>, Sheikh Ahmad Zaki<sup>a</sup>

<sup>a</sup> Malaysia-Japan International Institute of Technology, Universiti Teknologi Malaysia, 54200, Kuala Lumpur, Malaysia  
<sup>b</sup> Faculty of Engineering, Universiti Malaysia Sarawak, 94300, Kota Samarahan, Sarawak, Malaysia

#### ARTICLE INFO

**Keywords:**  
Vortex-induced vibration  
Vibration energy harvester  
CFD simulation  
Streamwise vorticity  
Ensemble empirical mode decomposition (EEMD)  
Hilbert transform

#### ABSTRACT

We investigated the displacement and lift time series of a circular cylinder - strip plate cruciform system for energy harvesting in the Reynolds number range  $1.1 \times 10^3 \leq Re \leq 14.6 \times 10^3$ , numerically using the open source C++ library: OpenFOAM. The Karman vortex-induced vibration (KVIV) regime was identified between reduced velocity,  $U^*$ , 2.3 and 13.6, while the streamwise vortex-induced vibration (SVIV) regime was identified between  $18.2 \leq U^* \leq 29.5$ . We analysed the cylinder displacement and lift time series using the Hilbert-Huang transform (HHT). Within this range of  $U^*$ , Karman vortex shedding contributes nearly as much as streamwise vortex shedding to the root-mean-square amplitude of total lift, while between  $25.0 \leq U^* \leq 29.5$ , the Karman component contribution is on average twice that of the streamwise component. These findings hint at the possibility to improve the power output of the harvester by a factor of two between  $18.2 \leq U^* \leq 22.7$  and by a factor of three between  $25.0 \leq U^* \leq 29.5$ , if we can unite the contribution to the root-mean-square amplitude of the total lift under a single vibration-driving mechanism: the shedding of streamwise vortex.

#### 1. Introduction

Streamwise vortex-induced vibration (SVIV) is a type of vortex-induced vibration (VIV) driven by vortical structures whose vorticity vector points in the direction of the free stream. In recent decades, there have been efforts to exploit the SVIV phenomenon from cruciform structures for energy harvesting, an example of which is given in Fig. 1. The literature on this subject can be broadly categorised into two groups: how the mechanical properties of the oscillator (e.g., mass ratio, damping, etc.) affects the amplitude/frequency response of SVIV (Koide et al., 2009, 2013; Nguyen et al., 2012) and how the minutiae of the flow field affect the force driving the vibration of the cylinder, i.e. the fluid mechanical aspect of the system (Deng et al., 2007; Koide et al., 2017; Zhao and Lu, 2018).

In the first focus area, researchers studied some permutation of the following method to convert the vibration into electrical power. The method consists of a coil and magnet. The coil, which moves with the vibrating cylinder, creates relative motion against the magnet, which is placed in the hollow of the coil (Koide et al., 2009). While investigating the system at a Reynolds number in the order of  $Re \sim O(10^4)$ , Koide et al. (2009) showed that increased damping due to energy harvesting reduces the maximum vibration amplitude close to a factor of 4. Amplitude reduction due to increased total damping was also mentioned in

Bernitsas et al. (2008); Bernitsas and Raghavan (2008); Bernitsas et al. (2009). Further investigation in Nguyen et al. (2012) revealed that damping not only affects the amplitude response of the cylinder but also narrows the synchronisation region between vortex shedding and cylinder vibration. Moreover, Nguyen et al. (2012) demonstrated a strong coupling between mass ratio and damping in determining both the width of the synchronisation region and the maximum amplitude response of the cylinder.

In the second focus area, investigators turned their attention to the details of the flow where streamwise vortex shedding occurs. One such study carefully shot motion pictures of the dye-injected flow (Koide et al., 2017) at Reynolds number in the order of  $Re \sim O(10^3)$ . A lower Reynolds number ( $Re$ ) reduces the amount of turbulence in the flow, allowing a clearer shot of the vortex structures. Their study also highlights the higher level of turbulence produced by the circular cylinder-strip plate cruciform in contrast to the twin circular cylinder cruciform, which diminishes the periodicity of vortex shedding. Although visually enlightening, this and other more qualitative studies contribute little towards improving our understanding of the relationship between vortex shedding and the resulting lift. Deng et al. (2007) demonstrated a way to overcome such a shortcoming.

In their study, Deng et al. (2007) examined the flow field of a twin circular cylinder cruciform using computational fluid dynamics (CFD).

\* Corresponding author. Malaysia-Japan International Institute of Technology, Universiti Teknologi Malaysia, 54200, Kuala Lumpur, Malaysia.  
E-mail addresses: [kaafadzli@unimas.my](mailto:kaafadzli@unimas.my) (A. Adzlan), [sukri.kl@utm.my](mailto:sukri.kl@utm.my) (M.S. Mat Ali), [sheikh.kl@utm.my](mailto:sheikh.kl@utm.my) (S.A. Zaki).

<https://doi.org/10.1016/j.oceaneng.2021.108648>

Received 6 July 2020; Received in revised form 10 December 2020; Accepted 17 January 2021  
Available online 5 February 2021  
0029-8018/© 2021 Elsevier Ltd. All rights reserved.

## Appendix B OpenFOAM Implementation for The Study of Streamwise Vortex-Induced Vibration-Based Energy Harvester for Sensor Networks

*Journal of Advanced Research in Fluid Mechanics and Thermal Sciences* 48, Issue 2 (2018) 165-175



### OpenFOAM Implementation for The Study of Streamwise Vortex-Induced Vibration-Based Energy Harvester for Sensor Networks

Open Access

Ahmad Adzlan Fadzli Khairi<sup>1,2,\*</sup>, Mohamed Sukri Mat Ali<sup>1</sup>

<sup>1</sup> Wind Engineering for Environment Laboratory, Malaysia-Japan International Institute of Technology, Universiti Teknologi Malaysia, 54100, Kuala Lumpur, Malaysia

<sup>2</sup> Department of Mechanical and Manufacturing Engineering, Faculty of Engineering, Universiti Malaysia Sarawak, 94300 Kota Samarahan, Sarawak, Malaysia

---

#### ARTICLE INFO

#### ABSTRACT

**Article history:**

Received 25 May 2018

Received in revised form 22 July 2018

Accepted 14 August 2018

Available online 16 August 2018

The study of streamwise vortex induced vibration has reached a level of maturity that allows it to be harnessed to generate power. However, studies have primarily concentrated on the variables that measured through point-based instruments. This severely limits our understanding of the fluid forcing mechanism that results in the vibration of the elastically supported bluff body. We proposed the usage of computational fluid dynamics: the open source C++ libraries of OpenFOAM. To implement this successfully to the streamwise vortex-induced vibration problem, which involves near-wall fluid-structure interaction, we explored the method of dynamic mesh handling in OpenFOAM for six degrees of freedom motion of a rigid body fully submerged in fluid. Finally, we argued for the usage of arbitrarily coupled mesh interface to overcome the problem of severely distorted mesh in tight gaps between two walls. We run a short simulation to test this setup and found that the case runs uninterrupted, unlike its former counterpart that relies solely on cell displacement diffusion, suggesting the potential success of a further converged solution of the setup when running on a more powerful machine.

**Keywords:**

OpenFOAM, vortex shedding, vortex induced-vibration, streamwise vortices

Copyright © 2018 PENERBIT AKADEMIA BARU - All rights reserved

---

### 1. Introduction

#### 1.1 Off-Grid Operation of Sensor Networks

The growing demand for real-time monitoring and management of agriculture [29], civil structures [44], machinery [9], and hydrological systems [5] led towards widespread adoption of sensors networks in these disciplines. Under the desired operating conditions, most of the application of the sensors are at sites where power from the national grid is either difficult to source, or non-existent. Sometimes, the issue is not so much on the fact that power lines from the national grid are out of reach, as it is related to the involvedness of the means to distribute the power, e.g.,

---

\* Corresponding author.  
E-mail address: kaafadzli@unimas.my (Ahmad Adzlan Fadzli Bin Khairi)

## LIST OF PUBLICATIONS

### Journal with Impact Factor

1. **Ahmad Adzlan Fadzli Bin Khairi**, Mohamed Sukri Mat Ali, Sheikh Ahmad Zaki: *Temporal Evolution of Lift in a Pure Cruciform System for Energy Harvesting*, **Ocean Engineering** (IF:3.795, Q1) 2021. **PUBLISHED.**

### Indexed Journal (SCOPUS)

1. **Ahmad Adzlan Fadzli Bin Khairi**, Mohamed Sukri Mat Ali: *OpenFOAM Implementation for The Study of Streamwise Vortex-Induced Vibration-Based Energy Harvester for Sensor Networks*, **Journal of Advanced Research in Fluid Mechanics and Thermal Sciences** (IF:0.247, Q2) 2018. **PUBLISHED.**